Multi-parameter Detection using Optical Spectroscopy for Monitoring and Control of Biomedical Anomalies, Food Adulteration and Environmental Pollution

THESIS

SUBMITTED FOR THE DEGREE OF

DOCTOR OF PHILOSOPHY (SCIENCE)

OF

JADAVPUR UNIVERSITY

BY

AMRITA BANERJEE

DEPARTMENT OF PHYSICS
JADAVPUR UNIVERSITY
KOLKATA-700032, INDIA

2023

CERTIFICATE FROM THE SUPERVISOR(S)

This is to certify that the thesis entitled "Multi-parameter Detection using Optical Spectroscopy for Monitoring and Control of Biomedical Anomalies, Food Adulteration and Environmental Pollution"

Submitted by ~~Sri~~ / Smt. Amrita Banerjee who got ~~his~~ / her name registered on 17.03.2023 for the award of Ph. D. (Science) Degree of Jadavpur University, is absolutely based upon his own work under the supervision of Prof. Subhadipta Mukhopadhyay and Prof. Samir Kumar Pal and that neither this thesis nor any part of it has been submitted for either any degree / diploma or any other academic award anywhere before.

Subhadipta Mukhopadhyay

Dr. Subhadipta Mukhopadhyay
Professor Dept. of Physics
Jadavpur University, Kolkata-700 032

23-08-23

(Signature of the Supervisor(s) date with official seal)

Dr. Samir Kumar Pal, FNAE
Senior Professor &
Abdul Kalam Technology Innovation National Fellow
S. N. Bose National Centre for Basic Sciences
Government of India
Block-JD, Sector-III, Salt Lake, Kolkata-700 106

To My Parents

Acknowledgements

Undertaking this PhD has been a truly life-changing experience for me and it would not have been possible to do without the support and guidance that I received from many people.

First of all I take this opportunity to express my sincere gratitude to my advisor Prof. (Dr.) Samir Kumar Pal, whom I am extremely grateful for being an exceptional mentor for me. His instrumental expertise, insight into various experimental problems, wisdom, and inspiration have allowed my research skills to develop, my creativity to flourish along with getting shaped as a working researcher. He has provided me with many opportunities to gain scientific experience, allowing me to explore new areas of research, interact and collaborate with talented researchers from a number of different national and international institutes. This thesis would not have been possible without his thoughtful guidance, warm encouragement, unconditional support, constructive criticism with simultaneous allocation to express my ideas to work independently and his inexhaustible help. He has taught me so much, inspired me to work hard, always taken time to listen to my crazy ideas, and made these years so enjoyable. I could not have wished for a better advisor. Thank you Sir, for everything you have done for me.

I would like to express my deepest gratitude also to my supervisor Dr. Subhadipta Mukhopadhyay for allowing me to pursue my journey of PhD under his guidance. Especially grateful for his constant availability, great interest and numerous helpful discussions for my work. He has provided me with many opportunities to gain scientific experience, allowing me to explore new areas of research, and interact and collaborate with talented researchers from many different institutes.

I am grateful to get the opportunity to actively collaborate with talented researchers across globe. I would like to cordially thank Dr. Arpita Chattopadhyay, Techno International, Kolkata, for her unconditional help and support all the time. I am also grateful for the fruitful collaboration with Prof. Dr. Saleh A. Ahmed, Umm Al-Qura University, Makkah, Saudi Arabia, Prof. Amitava Das, IISER Kolkata, Prof. Dr. Ranjan Das, West Bengal State University, Dr. Debasish Bhattacharya, NRSMH, India, Prof. Debjani Karmakar, Uppsala University, Sweden, Prof. Dr. Mala Mitra, Sister Nivedita University, Kolkata, Prof. Asim Kumar Mallick, NRS

Medical College and Hospital, India, Dr. Sudeshna S. Chowdhury, St. Xavier's College, India, and Dr. Tapan Adhikari, IISS, India. Great appreciation is extended to SNBNCBS and JU staffs and faculty members for their assistances in my research career.

I'd like to express my sincere thanks to all my seniors and colleagues for providing a stimulating and enriching environment. Special thanks to Dr. Soumendra Singh for helping me at the initial stage of my research work. I am grateful to Ria and Nur da, for helping me out from many difficulties during my research works. Special thanks to Nur Da for their assistance in formatting and proof-reading my thesis. My sincere appreciation goes to all my seniors: Dr. Damayanti Bagchi, Dr. Jayita Patwari, Dr. Priya Singh, Dr. Soumendra Singh, Dr. Animesh Halder, Dr. Anirudhha Adhikari, Dr. Pritam Biswas, Dr. Tuhin Kumar Maji, Dr. Arka Chatterjee, Dr. Tatini Rakshit, Dr. Soumendra Darbar, and all the other group members: Ria, Susmita, Dipanjan, Nivedita, Arpan Da, Lopa Di, Neha, and Monojit Da for providing a homely and a cheerful environment as well as assisting me in research. I'd like to extend a special vote of thanks to Dr. Nilanjana Ghosh for helping me unconditionally to work in hospital ambience and collecting humongous amount of data from vulnerable neonatal babies.

I would also like to thank all the teachers of my previous institute, university, college and schools for giving me the light of education and directing me towards my passion, holding the head high always, especially Prof. Sanatan Chattopadhyay, University of Calcutta and Dr. Dipayan Sanyal, CSIR-Central Glass and Ceramic Research Institute, Kolkata.

Finally, I would like to express my gratitude to my family who supports me through thick and thin, with loves and affections. I want them to know that I love them cordially. Without their sacrifices, moral supports and blessings the thesis would not have taken its shape.

Dated: 28.08.2023

Department of Physics,
Jadavpur University,
Jadavpur, Kolkata-700032, India

Amrita Banerjee

(Amrita Banerjee)

CONTENTS

CHAPTER 1

Introduction

1.1. BACKGROUND:

The optical spectroscopy has always been considered as a fascinating tool for the researchers to study and reveal fundamental properties of materials by analyzing the interaction of electromagnetic radiation with matter [1]. Multi-parameter measurements like absorption, emission, scattering and rotation of light by atoms or molecules provide important structural information and their chemical identification. The interaction of light with matter has started attracting human attention since ancient times. For thousands of years, people marvelled at the multicolour arc of visible light that frequently appears after rain showers. In order to understand the rainbow effect, the term 'spectroscopy' was originated in the 17th century through the study of visible light dispersion according to its specific wavelength, by a prism. The idea was later extended impressively to append any feasible interaction with radiative energy as a function of its frequency or wavelength. Spectroscopy is a fundamental exploratory tool in the fields of physics, chemistry, biomedical science and environmental science, allowing the compositional and structural information of matter to be investigated at atomic or molecular scale.

Application of spectroscopy in the field of biomedical science is popularised dramatically during early 20th century. However, from the earliest times to till now the diagnosis of medical diseases using spectroscopic tools is unavoidable. Primary medical diagnosis made by an expert physician based on what they could observe with their eyes and ears, which sometimes also included the examination of human specimens. The ancient Greeks believed that the health was affected due to disorders of bodily fluids called humors, and during the Late Middle Ages, doctors routinely performed uroscopy. Later on, the discovery of microscope was a revolution in medical science; it revealed not only the cellular structure of human tissue, but also the organisms that cause disease. After that, lots of sophisticated diagnostic tools and

techniques has been discovered and the clinical laboratory would become a standard fixture of medicine in the beginning of the 20th century using these sophisticated spectroscopic tools and techniques [2]. However, the current cost of clinical laboratory test is very high compared to the economic condition of the people in developing countries. Therefore, the development of low-cost and highly efficient spectroscopic device for disease diagnosis is still necessary to meet the increasing demand of people living in the low-income countries. Besides diagnosis, medicinal problems had been a major quest for all civilizations since prehistoric times. Even in the present era of advanced bio-medical technologies, worldwide burden of an aged population, threats of climate change, frequent incidence of new epidemic infections, the greater occurrence of chronic diseases, irregular and sedentary lifestyle along with shortcomings of conventional drugs, which include poor bioavailability, multi-drug resistance and undesired adverse effects have forced the researchers to look for alternative resources of medicines like nanomaterials (i.e., nanomedicines). The enthusiasm surrounding nanomedicines emerges from the unique possibility of precisely engineering their physicochemical properties such as size, shape, elasticity, surface charge, and surface functionalization to achieve desired in vivo behaviors [3, 4]. The term 'Nanomedicine' can be traced back to the late 1990s, and first appeared in scientific literature in the year 2000 (Institute for Scientific Information, Thompson, Philadelphia, PA, USA)[5]. Since then, various nanoscale materials have turned out to be useful for application in health and diseases. Some of the materials have already been approved by the US Food and Drug Administration (US FDA) for human use [6-8]. Despite having innovative functionality and versatility, the therapeutic use of nanomaterials is still in its infancy. Poor aqueous solubility, problem in large scale manufacturing, limited understanding about in vivo behaviour and concern over the biocompatibility and safety has limited their use as medicine.

On the other hand, optical spectroscopy has been used for centuries to find out the chemical composition of materials and making decisions by sensing properties and converting them into an optical signature. In the early 16th century, Georgius Agricola mentioned in the 'Ore Testing' section of his famous De re metallica that the differences in colour from heated materials provide the compositional information of

the materials [9]. At the same time, in 1565, Nicolàs Monardes examined a species of wood using fluorescence to use in the treatment of urinary and kidney infections. The spectral analysis was proposed to detect if the wood was counterfeited [10]. Since the 16th century, the chemical analysis has been carried out by studying the interaction of matter to radiative excitation, such as photo-acoustic spectroscopy, photothermal spectroscopy, Raman scattering and many others. But the invention of the LASER by Maiman in 1960 was a revolution in the field of chemical analysis [11]. As a spectroscopic tool it has several advantages and it rapidly has become a useful technology in laboratories, outdoor situations as well as within the industrial context. In order to be applied outside laboratories focusing on fundamental research, laser spectroscopy is confronted with the real world of sensing and chemical analysis. Furthermore, the aforementioned technologies have been used to integrate the instrumentation for both atomic and molecular spectroscopy. Now a days, the developed spectroscopic tools are used to monitor environmental pollutions, the progress of chemical processes and to assess the purity of products. However, the current cost of environmental pollution monitoring technologies, commercially available in the market is very high. Due to increasing human health problems with increasing environmental pollutions, the development of low-cost and highly efficient spectroscopic techniques is essential to monitor environmental pollutions.

Besides biomedical and environmental applications, optical spectroscopy finds an enormous applicability in food quality assessment since years. Adulteration of food commodities with substandard low-cost contaminants for higher monetary profit continues to be a long-standing global concern [12]. Spectroscopy is a quick, low cost, rapid, non-destructive, and emerging approach for verifying authenticity and toxicity of food products. However, instead of high-cost sophisticated lab grade instruments, portable and field deployable devices for food testing are the need of this hour.

Optical spectroscopy holds promise not only as clinical tool for diagnosing at the early stage of diseases or formulation of nanomedicine but also as sensing tool for the determination of environmental pollution and food adulteration by combining with available photonic technology and has been utilised throughout this thesis work.

1.2. SPECTROSCOPY IN BIOMEDICAL APPLICATIONS:

In view of recent scientific developments, photon-based detectors and optical fiber based light probes have made significant advancement towards the quality of measurements and diagnostic techniques, resulting in greater insight about the macromolecular light interactions on biologicals and meteorological targets. Better quality of receivers, spectroscopic advancements and novel electro-optical strategies have seen significant advancements in recent times. In the following sections few contemporary similar techniques with possible bio-medical applications have been discussed.

1.2.1. Spectroscopy in Medical Diagnosis:

Application of spectroscopy in diagnosis covers broad field of application from pulse oximetry to non-invasive optical biopsy. In this section we have represented the state-of-the-art diagnostic strategies based on different spectroscopic techniques. Ultraviolet/visible (UV/Vis) absorption spectroscopy has been used in the clinical laboratory for many years. The technique has appeal, as it is almost universal in its application. Absorption spectroscopy is usually performed with molecules dissolved in a transparent solvent, such as aqueous buffers. The absorbance of a solute depends linearly on its concentration and, therefore, absorption spectroscopy is ideally suited for quantitative measurements. The wavelength of absorption and the strength of absorbance of a molecule depend not only on the chemical nature but also on the molecular environment of its chromophores. Absorption spectroscopy is therefore an excellent technique for following ligand-binding reactions, enzyme catalysis, and conformational transitions in proteins and nucleic acids [13]. In this category the most popular diagnostic tool used in day to day basic for the measurement of oxygen saturation (SpO_2) is pulse oximetry. A blood-oxygen monitor displays the percentage of blood that is loaded with oxygen. More specifically, it measures what percentage of haemoglobin, the protein in blood that carries oxygen, is loaded. Acceptable normal ranges for patients without pulmonary pathology are from 95 to 99 percent. For a patient breathing room air at or near sea level, an estimate of arterial pO_2 can be made from the blood-oxygen monitor "saturation of peripheral oxygen" (SpO_2) reading.

Pulse oximeter works based on the Beer–Lambert law. It utilizes an electronic processor and a pair of small light-emitting diodes (LEDs) facing a photodiode through a translucent part of the patient's body, usually a fingertip or an earlobe. One LED is red, with wavelength of 660 nm, and the other is infrared with a wavelength of 940 nm. Absorption of light at these wavelengths differs significantly between blood loaded with oxygen and blood lacking oxygen. Oxygenated haemoglobin absorbs more infrared light and allows more red light to pass through. Deoxygenated haemoglobin allows more infrared light to pass through and absorbs more red light. The ratio of the red light measurement to the infrared light measurement is then calculated by the processor (which represents the ratio of oxygenated haemoglobin to deoxygenated haemoglobin), and this ratio is then converted to SpO_2 by the processor via a lookup table [14]. Absorbance spectroscopy has also been employed for the estimation of glycated hemoglobin in hemolysate samples of normal individuals and diabetic patients, which does not involve the use of external dyes or reagents. The optical fiber-based instrument used for recording absorption spectra in the spectral range 200–850 nm of glycated hemoglobin (HbA1c). The parameter ''area under the curve'' of each baseline corrected absorption spectrum was used for the estimation of HbA1c (%). The glycated hemoglobin values obtained by this spectroscopic method were compared with the values reported by the standard ion exchange HPLC method. It has been observed the aforementioned technique may be employed as a supplementary technique to other techniques that already exist [13].

Fluorescence spectroscopy is a complementary technique of absorption spectroscopy which analyzes fluorescence from a sample. It is primarily concerned with electronic and vibrational states of the fluorophores. Fluorescence spectroscopy is being used in many medical subspecialties as a diagnostic tool which extends from diagnostic studies for the determination of skin cancers to atheromatic plaques detection in coronary arteries. There are three main types of fluorophores used for cancer diagnostic studies: exogenous fluorophores, endogenous fluorophores, and fluorophores synthesized in the tissue from a precursor molecule that is given externally [15, 16]. Endogenous fluorophores give rise to autofluorescence phenomenon. Examples of endogenous fluorophores include collagen, elastin,

nicotinamide adenine dinucleotide (NADH), tryptophan, porphyrins, and flavin adenine dinucleotide (FAD) [17]. Collagen and elastin are mainly responsible for spectral changes associated with structural changes within the tissues and cells [17]. Other fluorophores like FAD, NADH, tryptophan, and porphyrins are mainly responsible for spectral changes associated with changes in cellular metabolism and functional processes [16]. Steady-state ultraviolet (UV) fluorescence spectroscopy can be utilised to separate malignant tumors from benign and normal breast, cervical, ovarian, and uterus tissues and tumors [16-18]. Upon exiting the tissue samples at 300 nm using a lamp-based spectrometer the emission can be recorded from 320 nm to 550 nm. The ratios of fluorescence intensities at 340 nm to 440 nm for cancerous breast tissues were found to be different from that of normal and benign tissues. In order to obtain further information on the chromophores responsible for the emission and to have a better physics picture of the heterogeneous nature of tissue fluorescence in cancerous and normal tissue, the kinetics of the physical processes occurring in tissues can be studied using time-resolved fluorescence. The key fluorescence relaxation decay parameters can be determined from the time-resolved fluorescence spectroscopic data of photo-excited tissues. The fluorescence kinetics from malignant and non-malignant breast tissues upon excitation at 310 nm and 353 nm, exhibit different double exponential decay profiles consisting of slow and fast components. Typical time-resolved fluorescence profiles at 340 nm emission band from a benign breast tissue, a benign tumor and a malignant tumor, photoexcited at 100 fs 310 nm pulse contain one slow and one fast component of fluorescence decay. The profiles for non-malignant (benign and normal) and malignant samples show a marked difference. The fast component seems to be more dominant in non-malignant tissues than in malignant tissues. The fluorescence decay curves for 440 nm band appear to contain one slow and one fast component of fluorescence lifetime. Unlike the 340 nm band, there is no marked dominance of either component for 440 nm [17]. Which further shows that the time resolved fluorescence is a novel way to obtain fundamental information on cancer. On the other hand, laser-induced fluorescence spectroscopy, a non-invasive real-time technique for evaluating neoplasia, measures the auto-fluorescence of tissue based on the amounts of naturally occurring

fluorophores present. With fluorescence spectroscopy, diagnostic algorithms can be derived that allow reasonable sensitivity and specificity for the diagnosis of squamous intraepithelial lesions (SILs) and work without a priori information about the abnormalities of the cervix [18]. New medical technologies can be evaluated using several measures, including sensitivity, specificity, positive and negative predictive values, receiver operating characteristic (ROC) curves, and areas under ROC curves. The ROC curve has the advantage of comparing test performance over several thresholds and can be used both in diagnostic settings, in which the prevalence of disease is high, and in screening settings, in which the prevalence of disease is low. Furthermore, fluorescence dye based detection of different diseases has also been reported. For an instance, fluorescence lifetime imaging of 4',6-diamidino-2-phenylindole (DAPI) stained nuclei has been utilised as a novel diagnostic tool for the detection and classification of B-cell chronic lymphocytic leukemia [19]. Conversely, the use of different dyes for the detection of cellular reactive oxygen species by fluorescence assay has also been reported [20].

Raman spectroscopy represents a molecular fingerprint of the sample and provides quantitative information regarding its chemical makeup. It is a powerful analytical technique that can measure the chemical composition of complex biological samples, such as biofluids, cells and tissues. Biochemical changes in cells and tissues, that may either be caused or are the cause of a disease, can lead to significant changes in the Raman spectra. The potential of Raman spectroscopy arises from its ability to detect such biochemical changes at a molecular level, and therefore, can be used for diagnostics, prognostics or as a tool for evaluating new therapies. Raman spectroscopy has several features that are advantageous for medical diagnostics. It has high chemical specificity and molecular information that can be obtained without any staining or labelling. Changes in the molecular composition of biological samples as measured by Raman spectroscopy can be used to build multivariate calibration and classification models, which allow quantitative and objective diagnosis for independent patients. Raman spectroscopy relies on scattering of light by molecules and information regarding the vibrational modes of the molecules can be obtained using visible or near-infrared lasers. Thus, Raman spectroscopy can take advantage of

the advanced optical microscopy technologies, optical fibres, miniaturised lasers and other photonic devices, to improve diagnostic performance and speed. Often the measurements are carried out in backscattering geometry without requiring transmission of light through the specimen. This feature is useful in particular for *in vivo* diagnostic and for examination of thick tissue specimens (e.g. surgical resections), without requiring micro-sectioning. The use of visible or near-infrared light for excitation also reduces the absorption effects of water, allowing measurements of body fluids or cells within water environments. Similar to other optical techniques, Raman spectroscopy can provide real-time (or near real-time) molecular information and high resolution imaging at relatively low cost compared to other well established medical imaging techniques (e.g. ultrasound, magnetic resonance imaging, etc.). This is an important feature as often the clinical implementation and translation of technologies are limited by practical, logistical and financial factors [21]. The application of Raman spectroscopy in medical diagnosis includes invasive detection of cancer (brain, barest, lung, skin, prostate, Colorectal); minimally invasive bio fluid analysis for the detection of asthma, inflammatory response, coagulant and anti-coagulant factors in human blood, malaria etc.

1.2.2. Spectroscopy in Medical Therapy:

Application of spectroscopy in medical science in not limited to medical diagnosis only. Along with diagnosis, the treatment or therapy has become a growing concern for the modern civilization. Spectroscopy has significant role in therapeutic applications including photodynamic therapy, atmospheric pressure plasma therapy even evaluating the action of a targeted cancer drug through magnetic resonance spectroscopy has also been reported.

Photo dynamic therapy (PDT) is a treatment that uses a drug, called a photosensitizer or photosensitizing agent, and a particular type of light. When photosensitizers are exposed to a specific wavelength of light, they produce a reactive form of oxygen that kills nearby cells. Each photosensitizer is activated by light of a specific wavelength. This wavelength determines how far the light can travel into the body. Thus, doctors use specific photosensitizers and wavelengths of light to treat

different areas of the body with PDT. In the first step of PDT for cancer treatment, a photosensitizing agent is injected into the bloodstream. The agent is absorbed by cells all over the body but stays in cancer cells longer than it does in normal cells. Approximately 24 to 72 hours after injection, when most of the agent has left normal cells but remains in cancer cells, the tumor is exposed to light. The photosensitizer in the tumor absorbs the light and produces an active form of oxygen that destroys nearby cancer cells. In addition to direct killing of cancer cells, PDT appears to shrink or destroy tumors in two other ways. Firstly, the photosensitizer can damage blood vessels in the tumour, thereby preventing the cancer from receiving necessary nutrients. Secondly, PDT also may activate the immune system to attack the tumour cells. The light used for PDT can come from a laser or other sources. Laser light can be directed through fiber optic cables (thin fibers that transmit light) to deliver light to areas inside the body. For example, a fiber optic cable can be inserted through an endoscope (a thin, lighted tube used to look at tissues inside the body) into the lungs or esophagus to treat cancer in these organs. Other light sources include light-emitting diodes (LEDs), which may be used for surface tumors, such as skin cancer. PDT is usually performed as an outpatient procedure. PDT may also be repeated and may be used with other therapies, such as surgery, radiation therapy, or chemotherapy. Extracorporeal photopheresis (ECP) is a type of PDT in which a machine is used to collect the patient's blood cells, treat them outside the body with a photosensitizing agent, expose them to light, and then return them to the patient. The U.S. Food and Drug Administration (FDA) has approved ECP to help lessen the severity of skin symptoms of cutaneous T-cell lymphoma that has not responded to other therapies. Studies are under way to determine if ECP may have some application for other blood cancers, and also to help reduce rejection after transplants.

Plasma medicine is an innovative and emerging field combining plasma physics, life sciences and clinical medicine to use physical plasma for therapeutic applications. Plasma, described as the fourth state of matter, comprises charged species, active molecules and atoms and is also a source of UV-photons [22]. These plasma-generated active species are useful for several bio-medical applications such as sterilization of implants and surgical instruments as well as modifying biomaterial

surface properties. Sensitive applications of plasma, like subjecting human body or internal organs to plasma treatment for medical purposes, are also possible. Initial experiments confirm that plasma can be effective in *in vivo* antiseptics without affecting surrounding tissue and, moreover, stimulating tissue regeneration [22]. Based on sophisticated basic research on plasma-tissue interaction, first therapeutic applications in wound healing, dermatology and dentistry will be opened [22].

Though nanoparticles are not directly related to the spectroscopic studies but the working of the nanoparticles can be confirmed by means of spectroscopic methods only. Hence, the application of the nanoparticles for drug delivery agent or as drug is indirectly related to the spectroscopy. However, in some cases the effective application of the nanoparticles could be enhanced through the application of external light or magnetic field which is in the domain of spectroscopy [23]. Nanometer-sized colloidal particles with small size and large surface area have many superior properties when used as magnetic resonance imaging (MRI) contrast agents, such as their ability to carry large payloads of active magnetic centers, easy penetration of biological membranes, long blood circulation times, and efficient conjugation to affinity molecules. Thus, they have the potential to allow us to visualize targets at low imaging-agent concentration with high sensitivity and specificity [24]. Furthermore, nanoparticles can be used in combination with therapeutic agents as bifunctional medical systems that enable simultaneous MRI diagnosis and drug treatment [25]. For example, superparamagnetic iron oxide nanoparticles have been developed as efficient T2 contrast agents and employed to image tumors, stem cell migration, and cancer metastases. Some colloidal nanoparticles containing gadolinium (III) or manganese(II) have recently been reported as potent T1 MRI contrast agents [26]. Very recently, reports on MnO nanoparticles as T1 contrast agents for MRI signal enhancement of the anatomic brain structure can also be found [26]. Conversely, manganese oxides have been widely exploited because of their promising applications in many fields, such as catalysis [27], molecular adsorption [28] and others [29], ion exchange [30], supercapacitors [31], magnetic applications [32], and secondary batteries. Among the manganese oxides, the hausmannite Mn_3O_4 is the most stable oxide at high temperature relative to other manganese oxides, such as MnO_2 and

Mn_2O_3. The compound is known to be an active catalyst for the oxidation of methane and carbon monoxide [33], decomposition of waste gases, the selective reduction of nitrobenzene [34], and the combustion of organic compounds at temperatures of the order of 373-773 K. These catalytic applications provide a powerful method of controlling air pollution. Most recently, hollow Mn_3O_4 nanoparticles have been utilized as positive MRI contrast agent (exploiting their room temperature paramagnetism) with enhanced relaxivity attributed to an increased water-accessible surface area and the flexibility of further functional surface modifications [35, 36].

Thus, spectroscopy can offer the necessary tools to investigate the relevant structure and function, but the size and complexity of biological systems is beyond that usually encountered in the physical and chemical sciences and therefore poses a particular challenge. The contemporary challenges in the mentioned fields include the design and realization of low-cost techniques without compromising the sensitivity and overall performance of the device or methodology. This challenge is met by extraordinary efforts to extend the sensitivity, specificity, information content, and in some cases spatial resolution of spectroscopic methods. Goal of this thesis is to exploit modern instrumentation and spectroscopic tools for the betterment of human life by developing novel diagnostic and therapeutic strategies which can further help to shape our understanding of living systems. The thesis also aims to give an overview about the spectroscopic and analytic tools, and to assess how novel developments may promise unprecedented insight into biomedical procedures.

1.3. SPECTROSCOPY IN ENVIRONMENTAL POLLUTION MONITORING:

Application of spectroscopy is not limited to medical science only. Spectroscopy has significant role on environmental pollution monitoring also. Environmental pollution is one of the most serious global problems that humanity and other life forms on our planet are facing today. Among all the environmental pollutants, chemical elements are the most hazardous one. Optical spectroscopy has been used for centuries for determining the chemical composition of materials and making decisions by sensing properties and converting them into an optical signature [37]. During the last quarter of the century, there has been a tremendous revolution in

the use of instrumentation and spectroscopic techniques in the field of environmental research. The dynamical change of environmental conditions by various pollutions has adverse effects on life, make it extremely important to detect and quantify. Various spectroscopic techniques and interferometers provide us greater insight about the composition of matter and suspended particulates. Therefore, the application of spectroscopy in the field of environmental pollution monitoring is unanimous. Ultraviolet and visible spectroscopic tools have been employed by environmental scientists for years. Common colorimetric tests that probe different water properties are now available in the market in simple kit forms, using portable colorimeters or visual colour matching [38]. Atomic absorption spectroscopy and emission spectroscopy are highly convenient techniques in the ultraviolet and visible regions to determine the chemical ions in water and solids samples. Sometimes, to analysis the samples using these techniques, immersion of the analyte into the solution is required. However, certain solid or semi-solid samples can be examined directly with atomic absorption spectrometry (by employing electrothermal atomization). Infrared spectroscopy is also one of the useful technique for environmental pollution monitoring to the environmental analysts [39]. Environmental scientists employed this technique to develop long-range infrared sensors for the determination of certain compound's concentration in the air mass. In addition, UV long-path methods are also tremendously used, albeit not as habitually as infrared spectroscopy. On the other hand, fluorescence spectroscopy, such as atomic fluorescence spectroscopy can be employed for the measurement of a compound present in air, water, or other media. In environmental pollution monitoring field, these techniques are extremely used for chemical ions detection, such as mercury, iron, fluoride etc. The X-ray methods (such as X-ray fluorescence spectroscopy) are also useful techniques for the measurement of atomic composition of solid materials. These methods can also be suitable for the detection of metal concentrations in particulate matter from the air, as well as in soil samples. In addition to all, sometime microwave region spectroscopy and magnetic resonance spectroscopy have also been implemented in some environmental research. On the other hand, even the nanomaterials or nanoparticles are not directly related to the spectroscopic studies but the working of the nanomaterials can be confirmed by

means of spectroscopic methods only. Hence, the application of the nanomaterials as environmental pollution monitoring agent is indirectly related to the spectroscopy. However, in some cases the effective application of the nanoparticles could be enhanced through the application of external light or magnetic field which is in the domain of spectroscopy [40]. The nanomaterials or nanoparticles are extensively used in the past few years for the environmental pollution monitoring agent using spectroscopic application. Strong absorption/emission of electromagnetic waves and tuneable optical properties induced by small changes in size, shape, surface nature and dielectric properties of the media make them suitable for the environmental pollution monitoring. Thus, spectroscopy can offer the necessary tools to investigate the relevant structure and function, but the complexity in biological systems as well as in environmental systems are beyond that usually encountered in the chemical and physical sciences and therefore poses a particular challenge. This challenge is met by extraordinary efforts to improve the specificity, sensitivity, information content and in some cases spatial resolution of spectroscopic methods. The key focus of this thesis is to exploit modern instrumentation and spectroscopic tools for the betterment of human life by developing not only novel disease diagnosis tools but also environmental pollution monitoring techniques, which can further help to shape our understanding of environmental systems.

1.4. SPECTROSCOPY IN FOOD QUALITY ASSESSMENT:

Exploration of newer optical methodologies for potential applications in food quality assessment is experiencing phenomenal growth and attracting huge interest over conventional techniques due to their versatility and inherent advantages including high sensitivity, little or no sample preparation, real-time monitoring, ease of use, requirement of less expertise, and non-invasive point-of-care diagnosis.

Adulteration of food commodities with substandard low-cost contaminants for higher monetary profit continues to be a long-standing global concern [12]. In recent times, adulteration of food in being done in sophisticated mode by substitution of specific substances (i.e., already present in the food), which are conventionally used as marker for food quality assessment, with low-grade chemical or biological

adulterant to manoeuvre the contemporary detection techniques. Detection of such health-hazardous adulterants demands cutting edge research and alternative methodologies, where optical techniques can play a pivotal role [41]. For example, β-carotene and Vitamin-A is used as biomarkers to assess quality of buffalo milk using easy spectroscopic techniques [42]. Likewise, the authenticity and origin of the floral type honey could be identified using front-face Fluorescence spectroscopy [43].

1.5. SCOPE AND OBJECTIVE:

Importance of spectroscopy in the field of biomedical, food and environmental applications is unanimous. Advent of nanotechnology further opens up the scope of optical spectroscopic techniques for the medical diagnosis and cure, environmental pollution monitoring and control along with food quality control applications. In recent years, spectroscopic techniques have come to be regarded as attractive and promising analytical tools for analyses conducted in research and industrial laboratories. These techniques are increasingly considered by researchers as an obvious solution. Daily, new applications of spectroscopic methods in the fields of biomedical, environmental and food applications are being demonstrated and published.

Development of cost-effective design and realization of highly sensitive spectroscopy-based instruments for potential applications in detecting and control biomedical anomalies, environmental pollution monitoring and food quality assessment to render a better quality of human life is the key objective of the works under the thesis. Following are the representative examples of the proposed achievements towards the said objective.

Spectroscopic investigation has taken an important role in diagnosis of different diseases including hypoxia [44], anemia, jaundice [45] and even cancer [46]. Among these diseases, anemia and hyperbilirubinemia are the most common global health problems affecting both developed and developing countries; it has far-reaching and severe adverse effects on human health, especially neonates and strongly affects socioeconomic development. Neonatal jaundice and anemia are the most

common health issues encountered by newborns globally and constitute a major percentage of infant mortality. The prevalence of neonatal jaundice and anemia is quoted to be between 50% and 60% among healthy term neonates [47-49]. According to the recent reports of World Health Organization, neonatal jaundice effects one in every two infants globally. Therefore, detection and control activities of these diseases should be an integral part of healthcare services, particularly because an early diagnosis of anaemia and hyperbilirubinemia in the neonatal population is one of the proven means of health promotion. Till date, the lack of a portable, easily operable, inexpensive and accurate device has hindered the widespread adaption of anemia and jaundice screening in neonatal health programs [50]. The contemporary method of measurement of serum bilirubin concentrations (TSB) hemoglobin levels (Hb) and arterial blood gas (for measurement of blood oxygen saturation) involves painful blood sampling [51-54] which suffers from multiple long term consequences like infection at the sampling site, osteomyelitis (though in rare cases), blood loss, etc.[52, 55, 56]. Although, some non-invasive methods (BiliCheck™ [57], JM-105™ [58], Rad 57™ [59] NBM-200, etc) [60] have been established as alternatives to repeated blood samplings for TSB and Hb measurement [61, 62] however, they suffer from certain inherent limitations that restrict their usage in widespread hospital settings [61, 63, 64]. Particularly, the accuracy of these non-invasive devices vary across races and have been found to be less accurate in Asian, Hispanic and African populations (having dark skin tone) because of the variation of melanin concentration in skin tissues [65]. So, to overcome the aforementioned limitations and to realize several crucial functions missing in the current non-invasive devices, a highly efficient spectroscopic device is extremely needed. In the above context, we developed a translational spectroscopic, non-invasive device (i.e. SAMIRA, Spectrum Assisted Medical Inoffensive Radiation Application) for simultaneous bilirubin and hemoglobin measurement at low-resource point-of-care settings in human neonatal subjects, independent of their skin color, age and sex, by measuring the optical spectrum of the blood flowing in the vascular bed of the distal subungual arcade and the superficial arcade area discarding the influence of melanin or skin colour. Incorporation of machine learning and artificial intelligence has improved the data accuracy of the proposed device stronger.

By virtue of the machine learning algorithm the developed device is capable of locking a data which is 98% accurate. Studies on a huge number of neonatal populations helped in exact incident light dosage determination, data acquisition time optimization etc., making the device highly precise and accurate for point of care settings.

On the other hand, World Health Organization (WHO) has declared antimicrobial-resistant (AMR) infections as one of the top 10 global public health threats [66]. It was reported that in 2019 alone, the AMR organisms were the primary cause of 1.27 million deaths worldwide [67]. Amongst antimicrobial-resistant bacteria, the emergence of multidrug-resistant (MDR) bacteria species is of great concern, primarily because of their ability to mutate genes and to reduce drug action. Poor drug binding capacity and low cell penetration [68] make multidrug-resistant bacteria responsible for almost 65% infections spread from contaminated surfaces which are linked with HealthCare-Associated disease [69]. Emerging MDR strains of MRSA are clinically notorious because of their lack of response to conventional antimicrobial therapy. Previously it was pointed out that the combination of two different drugs linked through a selectively chosen drug carrier, improves the efficacy of the system against AMR activities [70, 71].The present thesis work explores the co-localization of an antituberculosis drug rifampicin (RF) with another drug benzothiazole (BT) in an organized assembly of Cetyl Triethyl Ammonium Bromide (CTAB) micelles, and their highly potential prospect as an antibacterial spray against MRSA.

In this thesis, antimicrobial activity of citrate-CuO NPs was examined on *S. Hominis* bacteria strain. The citrate functionalized NPs were found to generate reactive oxygen species (ROS) upon photo-excitation, which is responsible for their anti-microbial action as ROS has the ability to destroy the active substances in the bacterial inner and outer membrane [72-74]. This phenomenon establishes the credentials of citrate CuO NPs for applications like antibacterial photo dynamic therapy (PDT) with enhanced efficacy. We have also used computational biology strategy in order to rationalize the antibiotic resistant bacterial remediation found in our experimental studies. Immediately after the establishment of the CuO nano-hybrid to be a potential

antibacterial agent, we have also explored the use of copper mine tailings as a source of raw materials for the nano-hybrid synthesis in order to cater low-cost antibiotics to wider population across the globe and to remediate the burden from the copper mines simultaneously.

A good quality of drinkable water is essential for human health, socio-economic development and ecosystems. Besides growing population and rapid urbanization, the high use of harmful chemicals in manufacturing, construction and other industries, fertilizers in farms and their direct disposal to nearby water bodies have significantly worsened the water quality available to people [75]. A minimum of 2 billion people worldwide consumes water for drinking, contaminated with faecal matter [76]. The root cause of many deadly diseases such as cholera, diarrhoea, dysentery as well as typhoid is consumption of contaminated water and the consumption results in more than half million deaths due to diarrhoea annually [77]. These statistics are indication of the urgent need for quantitative assessment of water quality including lakes [78] and large water bodies with online determination of results indicating the readiness of consumption of available drinking water. The quality of water is primarily determined by its physical, chemical, and biological content [79-81]. Traditional water drinkability assessments are generally performed manually where water samples are sent for examination to the laboratories, conventionally following chemical and other methods of analysis [82]. The processes are complex and require trained personnel [83]. Moreover, they are time-consuming and non-real time measurement techniques [84]. With the advent and development of sensor-based systems, substantial research has been carried out to automate and real-time monitor the water quality and Internet of Things (IoT) enabled devices are in demand for immediate intimation of human remedial interventions needed anywhere [85, 86]. But such sensor-based systems mainly focus on the total dissolved solvents (TDS) and pH properties of water and few such sensors have been made commercially available also. Some alternate experimental methods [87] were also tried by researchers like using the bio-screen microbiological growth analyser [88] and underwater imaging systems [89, 90]. While online sensors ensure immediate data availability and trigger the need for urgent action, their calibration, reliability, and

water-induced degradation or stains become an important concern [91]. Thus an all in one real time water quality testing portable system is sparce in contemporary literature that can identify presence of any kind of suspended scatterer, harmful chemicals having emission and dissolved contaminants or bio-markers degrading the water quality. In a study under this thesis work, we have developed a prototype for the estimation of water quality using spectroscopic techniques. This proposed device can simultaneously measure the absorbance of water sample to give the information of dissolved colours, scattering parameters to estimate the suspended particulate matter and fluorescence to quantify the harmful chemicals contaminating the water and degradation of the water quality. Detection of benzopyrene, a harmful carcinogenic common water pollutant [92], mainly contaminating water resources from industry effluents is a global concern of immense importance. In this study, the credentials of the developed proto-type have been established in identifying benzopyrene contamination in water samples. The limit of detection (LOD) of the device in terms of emission of benzopyrene contaminated water is found to be 0.503 ppb, much lower than the drinkable limit of 0.7 ppb [93] as per WHO guidelines which proves the efficacy of the device. Similarly, Crystal Violet (CV) is another dangerous and common mutagenic and teratogenic contaminant of water which enters into the aquatic systems from the effluents of textile or paint industry and also from medical and biotechnology industry and is well known for its mutagenic, teratogenic and mitotic poisoning nature [94]. The developed system is also capable of detecting the presence of such dissolved dyes in water by measuring absorbance. The designed device is found to have LOD 23.9 ppb whereas the safe limit of CV in drinking water is 100 ppb [95]. Simultaneously, the potential of the device in determining suspended particulate matters (SPM) in water is established by detecting Titanium di-oxide (TiO_2) as a model scatterer pollutant in water. The instrument yielded an LOD of 23.25 ppb (0.291 μM) in this case. The bacterial growth indication performance of the device in water was also studied using MRSA (Methicillin-resistant Staphylococcus Aureus) bacteria. Thus, this instrument, has the potential to replace the existing instruments for water quality measurement and has immense applications in the field of environmental research.

Arsenic is a naturally occurring toxic metalloid and is abundant in 'Earth's crust. Importantly, this is classified as a group I carcinogen in humans [96, 97]. Primary sources of ingested arsenic for humans are water and air, apart from some contribution from food. Contaminated groundwater with geogenic arsenic is the major source in various parts of the world, including a large part in the Ganga basin, and pose a major health risk to a large population worldwide [98, 99]. AsO_3^{3-} and AsO_4^{3-} are two primary arsenic species that occur in aqueous environments and contaminated water bodies with AsO_3^{3-} being more soluble than AsO_4^{3-} [100]. Considering the acute and the high level of toxicity induced by iAs^{III} contamination, the World Health Organization (WHO) and U.S. Environmental Protection Agency (EPA) have set the maximum allowed contaminant level for arsenic in drinking water as ≤ 10 ppb [101, 102]. According to a survey, it is estimated that more than150 million people around the globe are at risk because of arsenic contamination [102, 103]. To date, various conventional analytical techniques are commonly used for the detection of inorganic arsenic (iAs^{III}), those include inductively coupled plasma mass spectrometry, atomic absorption spectroscopy, high-performance liquid chromatography with optical spectrometric detection, atomic fluorescence spectrometry and voltammetry [104-111]. Although these techniques allow sensitive and accurate quantification of iAs^{III}, these methods require cumbersome sample processing, time, and highly trained personnel, which limit their applications for routine on-sight measurements [111, 112]. Considering such limitations, there is a conscious and focused effort for developing molecular sensors that could be integrated into an inexpensive optical device for specific, sensitive and instantaneous in-filed detection of the iAs^{III} with an associated optical read-out signal. Notably, such methodology with an associated switch ON optical response helps in achieving a favorable signal-to-noise ratio and a trace level quantification. These criteria are ideally suited for the real-time on-sight application. To the best of our knowledge, examples of any molecular sensors that fulfil all these norms are scarce in contemporary literature. To integrate all the requirements in the optical response of a single fluorescence-based molecular receptor, a new Ir(III)-based luminescent molecule is designed that shows specificity towards inorganic arsenic III (iAs^{III}). To

further improve the solubility of the Ir(III)-based luminescent molecule in the aqueous medium, as well as the improved membrane binding-efficacy with a cationic biomimetic cetyltrimethylammonium bromide (CTAB) micelle and cell-membrane permeability with mitochondrial specificity [113, 114]. The work has also utilized the switch ON luminescence response at ~ 466 nm for developing a hand-held micro-spectrometer-based prototype with an option for remote signal read-out using a smart mobile phone. The proposed device could be used for quantifying iAs^{III} at the sub 10ppb level in drinking water. The delicate balance between the lability of the NO-donor derivative (HPBT) in Ir(III)-based luminescent molecule and the demonstrated affinity of As(III)-centre towards S-donor receptors is effectively utilized for developing a ratiometric luminescence-based chemodosimetric receptor that is specifically localized in mitochondria of the live breast cancer cell lines (MCF-7). The newly developed chemodosimetric receptor, its specificity towards iAs^{III} for generating a ratiometric luminescence response, and integration for developing a hand-held device could be a solution for the population that is impacted with chronic As^{3+} toxicity.

The thesis also highlights scopes of application of optical spectroscopy in food quality control. Tea *(Camellia Sinensis)*, the most widely consumed aromatic, non-alcoholic stimulating beverage in the world [115] is a native plant of southwestern China and eastern India. Tea finds its importance not only for its medicinal values, but also for its substantial export revenue generation. India being the home to world's premium tea, is responsible for 20% of global tea production and has earned INR 5500 crore or 700 million US Dollar through tea export per year [116]. Amongst all the tea variants in India, Darjeeling tea, a special variety of tea grown and produced in the defined area of the Darjeeling District of India, is famous for its distinct aroma and premium quality. To implement and protect the Geographical Indications (GI) of the Darjeeling Tea under Trade-Related Aspects of Intellectual Property Rights (TRIPS Agreement, WTO) [117], a robust identification validity technique of this variety of tea is highly sought after. Though the modern era has witnessed gigantic progress in smart technologies and IoT enabled devices, the tea testing technique continues to be a person specific subjective task. Despite GI validation, the quality assessment of

Darjeeling tea has remained in the primitive stage, with no available automated instrumental validation technique. The existing method for tea identification by tea testers depends solely on a person's sensory skill, and hence it is associated with a higher risk of human errors. It also lacks evidence-based measurement techniques, which could assure the accuracy of tea identification. Furthermore, the economically motivated adulteration (EMA) [118] has become a growing concern all over the world, not only for its economic impact, but primarily because of associated health hazards. It has been predicted that the negative impact of global food-fraud would cost the food industry about $10-$15 billion a year [118]. The tea industry, being no exception, faces severe damage due to such types of fraudulent activities. Some point of care remedies that are being available nowadays for tea quality testing lack in sensitivity, accuracy and field deployability. In this thesis work, spectroscopic studies on a natural biomarker 'quercetin' for the identification of origin and quality of tea extracts for the development of a portable and field deployable prototype have been performed. The performance of the developed device was found promising and reliable in identifying geographical origin, adulteration (specifically mixing of high-quality Darjeeling tea with low grade tea and other adulterants), different flushes and shelf life. Incorporation of machine learning algorithms and statistical analysis methods have increased the device efficacy manyfold.

Other than tea, a detailed interaction of Chlorophyll with the harmful dyes, viz, copper sulphate, malachite green and sudan red III are also studied in the thesis using absorption and emission spectroscopy along with Time-Correlated Single Photon Counting (TCSPC) technique. Chlorophyll is an essential component of vegetables and fruits which are vital dietary requirements to maintain a healthy lifestyle and many of them have anticarcinogenic properties. However, they are frequently adulterated by unscrupulous business practices with toxic illegal dyes for making their appearance fresh and vibrant. The dyes may directly interact with the chlorophyll of fruits and vegetables, either by unethical fraudulent practices of adulteration to keep them fresh, or through intake of dye contaminated soils with industrial or agricultural effluents through the root of plants. In plants, chlorophylls are not freely available, they are encapsulated in granum. To create the similar

restrictive nanoscopic environment in our study, Sodium Dodecyl Sulfate (SDS) micelles was used, which, like granum, confine the chlorophyll. To establish the harmful effects of these dangerous dyes at the molecular level, detailed computational biology technique was also employed in the study for a vivid insight.

1.6. SUMMARY OF THE WORK DONE:

1.6.1. Studies on Interaction Optical Radiation with Human Tissue Using Optical Diffuse Reflectance Spectroscopy for Potential Development of Healthcare Devices and Development of Nano-medicine:

1.6.1.1. Non-invasive Estimation of Hemoglobin and Bilirubin of Neonates Simultaneously Using Whole Optical Spectrum Analysis at Point of Care [119]:

The study was aimed to evaluate the performance of a newly developed spectroscopy-based non-invasive and noncontact device (SAMIRA) for the simultaneous measurement of hemoglobin and bilirubin as an alternative to the invasive biochemical method of blood sampling. The accuracy of the device was assessed in 4318 neonates having incidences of either anemia, jaundice, or hypoxia. Transcutaneous bilirubin and hemoglobin values were obtained by the newly developed instrument which was corroborated with the biochemical blood tests by expert clinicians. The instrument is trained using Artificial Neural Network Analysis to increase the acceptability of the data. The artificial intelligence incorporated within the instrument determines the disease condition of the neonate. The Pearson's correlation coefficient, 'r' was found to be 0.987 for hemoglobin estimation and 0.988 for bilirubin measurement respectively. The bias and the limits of agreement for the measurement of all the three parameters were within the clinically acceptance limit.

1.6.1.2. Molecular Co-localization of Multiple Drugs in a Nanoscopic Delivery Vehicle for Potential Synergistic Remediation of Multi-drug Resistant Bacteria [120]:

Anti-microbial resistant infection is predicted to be alarming in upcoming years. In the present study, we proposed co-localization of two model drugs viz., rifampicin and benzothiazole used in anti-tuberculosis and anti-fungal agents

respectively in a nanoscopic cationic micelle CTAB (cetyl triethyl ammonium bromide) with hydrodynamic diameter of 2.69 nm. Sterilization effect of the co-localized micellar formulation against a model multi-drug resistant bacterial strain viz., Methicillin resistant Staphylococcus aureus was also investigated. 99.88% decrease of bacterial growth in terms of colony forming unit was observed using the developed formulation. While Dynamic Light Scattering and Forster's Resonance Energy Transfer between benzothiazole and rifampicin show co-localization of the drugs in the nanoscopic micellar environment, analysis of time-resolved fluorescence decays by Infelta-Tachiya model and the probability distribution of the donor–acceptor distance fluctuations for 5 μM, 10 μM and 15 μM acceptor concentrations confirm efficacy of the co-localization. Energy transfer efficiency and the donor acceptor distance are found to be 46% and 20.9 Å respectively. We have also used a detailed computational biology framework to rationalize the sterilization effect of our indigenous formulation. It has to be noted that the drugs used in our studies are not being used for their conventional indication. Rather the co-localization of the drugs in the micellar environment shows a completely different indication of their use in the remediation of multi-drug resistant bacteria revealing the re-purposing of the drugs for potential use in hospital-born multi-drug resistant bacterial infection.

1.6.1.3. Development of Nanomedicine from Copper Mine Tailing Waste: A Pavement towards Circular Economy with Advanced Redox Nanotechnology [121]:

Copper, the essential element required for the human body is well-known for its profound antibacterial properties, yet salts and oxides of copper metals in the copper mine tailings are reported to be a big burden in the modern era. Among other copper oxides, CuO, in particular, is known to have beneficial effects on humans, while its slight nanoengineering viz., surface functionalization of the nanometer-sized oxide is shown to make some paradigm shift using its inherent redox property. Here, we have synthesized nanometer-sized CuO nanoparticles and functionalized it with a citrate ligand for an enhanced redox property and better solubility in water. For structural analysis of the nanohybrid, standard analytical tools, such as electron microscopy, dynamic light scattering, and X-ray diffraction studies were conducted.

Moreover, FTIR and UV-VIS spectroscopy studies were performed to confirm its functionalization. The antibacterial study results, against a model bacteria (*S. hominis*), show that CuO nanohybrids provide favourable outcomes on antibiotic-resistant organisms. The suitability of the nanohybrid for use in photodynamic therapy was also confirmed, as under light its activity increased substantially. The use of CuO nanoparticles as antibiotics was further supported by the use of computational biology, which reconfirmed the outcome of our experimental studies. We have also extracted CuO nanogranules (top-down technique) from copper mine tailings of two places, each with different geographical locations, and functionalized them with citrate ligands in order to characterize similar structural and functional properties obtained from synthesized CuO nanoparticles, using the bottom-up technique. We have observed that the extracted functionalized CuO from copper tailings offers similar properties compared to those of the synthesized CuO, which provides an avenue for the circular economy for the utilization of copper waste into nanomedicine, which is known to be best for mankind.

1.6.1.4. "Nano-Copper": A Potential Remediation of Antibiotic-Resistant Infections [122]:

Use of copper to cater various needs of human civilization started immediately after the neolithic age. However, the nano-formulation of copper containing copper or one of its compounds including oxides in order to combat some of the societal challenges are quite recent. Here we have synthesized copper oxide nano particles and functionalized with acetate ligands to form a nano-hybrid which is shown to have medicinal properties. We have used electron microscopy, X-ray diffraction and dynamic light scattering tools for the structural characterization of the nano-hybrid. Functionalization of the copper oxide nanoparticles has been confirmed by FTIR and UV-Vis spectroscopy studies. A detailed study on the functionality of the nano-hybrid is shown to be very promising for antibiotic resistant bacterial infection remediation which is the need of the hour. Light activation enhances the antibacterial efficacy manifold making the nano-hybrid suitable for applications like photo-dynamic therapy. We have also used computational biology strategy in order to rationalize the

antibiotic resistant bacterial remediation (particularly MRSA strains) found in our experimental studies.

1.6.2. Studies on Optical Multi-parameter for Environmental Pollution Monitoring:

1.6.2.1. A Portable Spectroscopic Instrument for Multiplexed Monitoring of Acute Water Toxicity: Design, Testing, and Evaluation [123]:

The deteriorating water environment worldwide, mainly due to population explosion and uncontrolled direct disposal of harmful industrial and farming wastes, earnestly demands new approaches and accurate technologies to monitor water quality before consumption overcoming the shortcomings of the current methodologies. A spectroscopic water quality monitoring and early-warning instrument for evaluating acute water toxicity are the need of the hour. In this study, we have developed a prototype capable of the quantification of dissolved organic matter, dissolved chemicals, and suspended particulate matter in trace amounts dissolved in the water. The prototype estimates the water quality of the samples by measuring the absorbance, fluorescence, and scattering of the impurities simultaneously. The performance of the instrument was evaluated by detecting common water pollutants such as Benzopyrene, Crystal Violet, and Titanium di-oxide. The limit of detection values was found to be 0.50, 23.9, and 23.2 ppb (0.29 µM), respectively.

1.6.2.2. Ultrasensitive Reagent for Ratiometric Detection and Detoxification of iAs^{III} in Water and Mitochondria [124]:

Toxicity induced by inorganic arsenic as AsO_3^{3-} (iAs^{III}) is of global concern. Reliable detection of the maximum allowed contaminant level for arsenic in drinking water and in the cellular system remains a challenge for the water quality management and assessment of toxicity in the cellular milieu, respectively. A new Ir(III)-based phosphorescent molecule (AS-I; λ_{Ext} = 415 nm and λ_{Ems} = 600 nm, Φ = 0.3) is synthesized for the selective detection of iAs^{III} in an aqueous solution with a ratiometric luminescence response even in the presence of iAs^{V} and all other common inorganic cations and anions. The relatively higher affinity of the thioimidazole ligand

(HPBT) toward iAs^{III} led to the formation of a fluorescent molecule iAs^{V}−HPBT (λ_{Ext} = 415 nm and λ_{Ems} = 466 nm, Φ = 0.28) for the reaction of iAs^{III} and the Ir(III)-based luminescent molecule. An improved limit of quantitation (LOQ) down to 0.2 ppb is achieved when the Ir(III)-based luminescent molecule is used in the CTAB micellar system. Presumably, the cationic surfactants favor the localization of Ir(III)-based luminescent molecule in mitochondria of MCF7 cells, and this is confirmed from the images of the confocal laser fluorescence scanning microscopic studies. Importantly, cell viability assay studies confirm that Ir(III)-based luminescent molecule in CTAB micelles induces dose-dependent detoxification of iAs^{III} in live cells. Further, luminescence responses at 466 nm could be utilized for developing a hand-held device for the in-field application. Such a reagent that allows for ratiometric detection of iAs^{III} with LOQ of 2.6 nM (0.5 ppb) in water, as well as helps in visualizing its distribution in mitochondria with a detoxifying effect, is rather unique in contemporary literature.

1.6.3. Development of Optical Spectroscopy-based techniques for the detection of Food-quality assessment:

1.6.3.1. Spectroscopic Studies on a Natural Biomarker for the Identification of Origin and Quality of Tea Extracts for the Development of a Portable and Field Deployable Prototype [125]:

Even in the era of smart technologies and IoT enabled devices, tea testing technique continues to be a person specific subjective task. In this study, we have employed optical spectroscopy-based detection technique for the quantitative validation of tea quality. In this regard, we have employed the external quantum yield of quercetin at 450 nm (λex = 360 nm), which is an enzymatic product generated by the activity of β-glucosidase on rutin, a naturally occurring metabolite responsible for tea-flavour (quality). We have found that a specific point in a graph representing Optical Density and external Quantum Yield as independent and dependent variables respectively of an aqueous tea extract objectively indicates a specific variety of the tea. A variety of tea samples from various geographical origin have been analysed with the developed technique and found to be useful for the tea quality assessment. The principal component analysis distinctly showed the tea samples originated from

Nepal and Darjeeling having similar external quantum yield, while the tea samples from Assam region had a lower external quantum yield. Furthermore, we have employed experimental and computational biology techniques for the detection of adulteration and health benefit of the tea extracts. In order to assure the portability/ field use, we have also developed a prototype which confirms the results obtained in the laboratory. We are of the opinion that the simple user interface and almost zero maintenance cost of the device will make it useful and attractive with minimally trained manpower at low resource setting.

1.6.3.2. Interaction of Chlorophyll with Artificial Colorants in Restricted Nanoscopic Environment: Key Insights on the Toxicity from Electronic Spectroscopy [126]:

Chlorophyll is a vital component of vegetables and fruits which are essential dietary requirements to maintain a healthy lifestyle and many of them have anticancer properties. However, they are frequently adulterated by unscrupulous business practices with toxic illegal dyes for making their appearance fresh and vibrant. On the other hand, chlorophyll may interact with harmful dyes and heavy metals by virtue of its strong tendency of complex formation by the porphyrin ring when root of plants starts consumption from dye contaminated soils with industry or agricultural effluents. Our experimental findings vividly reveal the interaction of chlorophyll with three commonly used illegal dyes, namely copper sulfate, malachite green, and sudan red in a restricted nanoscopic environment of an anionic micelle (SDS). The hypsochromic shift of around 10 nm in the chlorophyll absorbance band supports the copper metal binding and fluorescence quenching and Time Correlated Single Photon Counting (TCSPC) investigations confirmed the nature of dynamic quenching of the chlorophyll emission. The increase of the absorbance peak in the presence of the dye malachite green indicates that dimers of the dye are likely to develop. The absorption peak at the blue end is most pronounced at the maximum concentration of the malachite green dye, at the expense of a weakening of the absorption band at 470 nm. The static quenching mechanism is supported by further considerable fluorescence quenching of chlorophyll after inner filter effect correction and picosecond time

resolved analysis with malachite green addition. The likelihood of Forster Resonance Energy Transfer (FRET) between chlorophyll-SDS and sudan red dye due to their overlapping emission and absorption spectral signatures was investigated and an energy transfer efficiency of roughly 15% was obtained between the doner and acceptor, establishing a modest interaction. The hazardous effects of the dyes on human are also thoroughly investigated using predictive computational biology technique.

1.7. PLAN OF THE THESIS:

Chapter 1: This chapter gives a brief introduction to the different types of spectroscopic methods used in various kinds of biomedical applications, environmental pollution monitoring and food quality monitoring applications. The scope and brief summary of the work done has also been included in this chapter.

Chapter 2: This chapter provides an overview of spectroscopic techniques, both the dynamical and steady-state, the structural aspects of biologically important systems, fluorescent probes and nanomaterials used in the experiments.

Chapter 3: Details of instrumentation, data analysis and experimental procedures have been discussed in this chapter.

Chapter 4: This chapter demonstrates the development and validation of a noncontact spectroscopic device for bilirubin and hemoglobin estimation in neonates without using any blood samples or chemical reagents at point-of-care in human subjects with high precision and accuracy. This chapter also demonstrates that the developed device is equipped with machine learning algorithms and can also generate and instantaneously transmit the report to a medical expert through e-mail, text messaging, or mobile apps. The chapter also discusses of a nano-formulation prepared by molecular co-localization of multiple drugs in a nanoscopic delivery vehicle for potential synergistic remediation of multi drug resistant bacteria. Development of nanomedicine from copper mine tailing waste as a pavement towards circular economy with advanced redox nanotechnology is another topic of discussion of this chapter.

Chapter 5: In this chapter, studies on optical multi-parameter for environmental pollution monitoring have been highlighted. An efficient and portable spectroscopic instrument for multiplexed monitoring of acute water toxicity has been developed. The Design, testing, and evaluation are discussed in details. Arsenic is listed as one of the most harmful pollutants in drinking water. In this chapter, An ultrasensitive reagent for ratiometric detection and detoxification of iAs^{iii} in water and mitochondria has been formulated and its promising performance has been evaluated.

Chapter 6: Spectroscopic studies on a natural biomarker for the identification of origin and quality of tea extracts for the development of a portable and field deployable prototype is discussed in this chapter. Simultaneously, interaction of chlorophyll with artificial colorants like malachite green, copper sulphate and sudan red in restricted nanoscopic environment is elaborately studied in this chapter to explore the key insights on the toxicity from electronic spectroscopy.

REFERENCES

[1] V. Kumar, N. Coluccelli, D. Polli, Coherent optical spectroscopy/microscopy and applications, Molecular and LASER spectroscopy: Advances and applications, *Elsevier Science*, BV, 2018, pp. 87.

[2] D. Berger, A brief history of medical diagnosis and the birth of the clinical laboratory. Part 1-Ancient times through the 19th century, *MLO Med Lab Obs*, 31 (1999) 28.

[3] C. Kinnear, T.L. Moore, L. Rodriguez-Lorenzo, B. Rothen-Rutishauser, A. Petri-Fink, Form follows function: Nanoparticle shape and its implications for nanomedicine, *Chemical Reviews*, 117 (2017) 11476.

[4] B. Pelaz, C. Alexiou, R. Alvarez-Puebla, F. Alves, A. Andrews, S. Ashraf, *et al.*, 732 Bestetti, A, *Brendel, C., et al.,* Diverse Applications of Nanomedicine, *ACS Nano*, 11 (2017) 2313.

[5] S. Bayda, M. Adeel, T. Tuccinardi, M. Cordani, F. Rizzolio, The history of nanoscience and nanotechnology: From chemical–physical applications to nanomedicine, *Molecules*, 25 (2019) 112.

[6] C.M. Dawidczyk, C. Kim, J.H. Park, L.M. Russell, K.H. Lee, M.G. Pomper, *et al.*, State-of-the-art in design rules for drug delivery platforms: Lessons learned from FDA-approved nanomedicines, *Journal of Controlled Release*, 187 (2014) 133.

[7] M.L. Etheridge, S.A. Campbell, A.G. Erdman, C.L. Haynes, S.M. Wolf, J. McCullough, The big picture on nanomedicine: The state of investigational and approved nanomedicine products, *Nanomedicine: Nanotechnology, Biology and Medicine*, 9 (2013) 1.

[8] S.R. D'Mello, C.N. Cruz, M.-L. Chen, M. Kapoor, S.L. Lee, K.M. Tyner, The evolving landscape of drug products containing nanomaterials in the United States, *Nature Nanotechnology*, 12 (2017) 523.

[9] H. Hoover, L.H. Hoover, De re metallica, *Courier Corporation*, 1950.

[10] B. Valeur, M.N. Berberan-Santos, A brief history of fluorescence and phosphorescence before the emergence of quantum theory, *Journal of Chemical Education*, 88 (2011) 731.

[11] T.H. Maiman, Stimulated optical radiation in ruby, *Nature*, 187 (1960) 493.

[12] L. Manning, J.M. Soon, Developing systems to control food adulteration, *Food Policy*, 49 (2014) 23.

[13] M. Mallya, R. Shenoy, G. Kodyalamoole, M. Biswas, J. Karumathil, S. Kamath, Absorption spectroscopy for the estimation of glycated hemoglobin (HbA1c) for the diagnosis and management of diabetes mellitus: A pilot study, *Photomedicine and Laser Surgery*, 31 (2013) 219.

[14] J.E. Sinex, Pulse oximetry: Principles and limitations, *The American Journal of Emergency Medicine*, 17 (1999) 59.

[15] T.G. Papazoglou, Malignancies and atherosclerotic plaque diagnosis—is laser induced fluorescence spectroscopy the ultimate solution?, *Journal of Photochemistry and Photobiology*, 28 (1995) 3.

[16] A. Shahzad, M. Knapp, M. Edetsberger, M. Puchinger, E. Gaubitzer, G. Köhler, Diagnostic application of fluorescence spectroscopy in oncology field: Hopes and challenges, *Applied Spectroscopy Reviews*, 45 (2010) 92.

[17] R.R. Alfano, Advances in ultrafast time resolved fluorescence physics for cancer detection in optical biopsy, *AIP Advances*, 2 (2012) 011103.

[18] M.F. Mitchell, S.B. Cantor, N. Ramanujam, G. Tortolero-Luna, R. Richards-Kortum, Fluorescence spectroscopy for diagnosis of squamous intraepithelial lesions of the cervix, *Obstetrics & Gynecology*, 93 (1999) 462.

[19] G. Yahav, A. Hirshberg, O. Salomon, N. Amariglio, L. Trakhtenbrot, D. Fixler, Fluorescence lifetime imaging of DAPI-stained nuclei as a novel diagnostic tool for the detection and classification of B-cell chronic lymphocytic leukemia, *Cytometry Part A*, 89 (2016) 644.

[20] B.H. Ye, S.J. Lee, Y.W. Choi, S.Y. Park, C.D. Kim, Preventive effect of gomisin J from Schisandra chinensis on angiotensin II-induced hypertension via an increased nitric oxide bioavailability, *Hypertension Research*, 38 (2015) 169.

[21] K. Kong, C. Kendall, N. Stone, I. Notingher, Raman spectroscopy for medical diagnostics: From in-vitro biofluid assays to in-vivo cancer detection, *Advanced Drug Delivery Reviews*, 89 (2015) 121.

[22] K.D. Weltmann, E. Kindel, R. Brandenburg, C. Meyer, R. Bussiahn, C. Wilke, *et al.*, Atmospheric pressure plasma jet for medical therapy: Plasma parameters and risk estimation, *Contributions to Plasma Physics*, 49 (2009) 631.

[23] L. Di Marzo, A. Miccheli, P. Sapienza, M. Tedesco, A. Mingoli, G. Capuani, *et al.*, 31Phosphorus magnetic resonance spectroscopy to evaluate medical therapy efficacy in peripheral arterial disease. A pilot study, *Panminerva Medica*, 41 (1999) 283.

[24] J.W. Bulte, D.L. Kraitchman, Iron oxide MR contrast agents for molecular and cellular imaging, *NMR in Biomedicine*, 17 (2004) 484.

[25] J. Kim, J.E. Lee, S.H. Lee, J.H. Yu, J.H. Lee, T.G. Park, *et al.*, Designed fabrication of a multifunctional polymer nanomedical platform for simultaneous cancer-targeted imaging and magnetically guided drug delivery, *Advance Materials*, 20 (2008) 478.

[26] J. Shin, R.M. Anisur, M.K. Ko, G.H. Im, J.H. Lee, I.S. Lee, Hollow manganese oxide nanoparticles as multifunctional agents for magnetic resonance imaging and drug delivery, *Angewandte Chemie*, 121 (2009) 327.

[27] H. Einaga, S. Futamura, Catalytic oxidation of benzene with ozone over alumina-supported manganese oxides, *Journal of Catalysis*, 227 (2004) 304.

[28] Y.F. Shen, R.P. Zerger, R.N. DeGuzman, S.L. Suib, L. McCurdy, D.I. Potter, *et al.*, Manganese oxide octahedral molecular sieves: Preparation, characterization, and applications, *Science*, 260 (1993) 511.

[29] Y. Lvov, B. Munge, O. Giraldo, I. Ichinose, S.L. Suib, J.F. Rusling, Films of manganese oxide nanoparticles with polycations or myoglobin from alternate-layer adsorption, *Langmuir*, 16 (2000) 8850.

[30] O. Giraldo, S.L. Brock, W.S. Willis, M. Marquez, S.L. Suib, S. Ching, Manganese oxide thin films with fast ion-exchange properties, *Journal of the American Chemical Society*, 122 (2000) 9330.

[31] M. Toupin, T. Brousse, D. Bélanger, Charge storage mechanism of MnO_2 electrode used in aqueous electrochemical capacitor, *Chemistry of Materials*, 16 (2004) 3184.

[32] A.R. Armstrong, P.G. Bruce, Synthesis of layered $LiMnO_2$ as an electrode for rechargeable lithium batteries, *Nature*, 381 (1996) 499.

[33] E.R. Stobbe, B.A. de Boer, J.W. Geus, The reduction and oxidation behaviour of manganese oxides, *Catalysis Today*, 47 (1999) 161.

[34] E.J. Grootendorst, Y. Verbeek, V. Ponec, The role of the mars and van krevelen mechanism in the selective oxidation of nitrosobenzene and the deoxygenation of nitrobenzene on oxidic catalysts, *Journal of Catalysis*, 157 (1995) 706.
[35] J. Shin, R.M. Anisur, M.K. Ko, G.H. Im, J.H. Lee, I.S. Lee, Hollow manganese oxide nanoparticles as multifunctional agents for magnetic resonance imaging and drug delivery, *Angewandte Chemie*, 48 (2009) 321.
[36] T.-L. Ha, H.J. Kim, J. Shin, G.H. Im, J.W. Lee, H. Heo, *et al.*, Development of target-specific multimodality imaging agent by using hollow manganese oxide nanoparticles as a platform, *Chemical Communications*, 47 (2011) 9176.
[37] N.V. Tkachenko, Optical spectroscopy: Methods and instrumentations, *Elsevier*, Amsterdam, 2006.
[38] J. Das, P. Sarkar, A new dipstick colorimetric sensor for detection of arsenate in drinking water, *Environmental Science: Water Research & Technology*, 2 (2016) 693.
[39] Y. Li, L. Sun, X. Hu, T. Sun, Application and prospect of infrared spectroscopy in environmental science, *Guang pu xue yu Guang pu fen xi= Guang pu*, 28 (2008) 2325.
[40] L. Di Marzo, A. Miccheli, P. Sapienza, M. Tedesco, A. Mingoli, G. Capuani, *et al.*, 31Phosphorus magnetic resonance spectroscopy to evaluate medical therapy efficacy in peripheral arterial disease. A pilot study, *Panminerva Medica*, 41 (1999) 283.
[41] C.V. Di Anibal, I. Ruisánchez, M. Fernández, R. Forteza, V. Cerdà, M. Pilar Callao, Standardization of UV–visible data in a food adulteration classification problem, *Food Chemistry*, 134 (2012) 2326.
[42] R. Ullah, S. Khan, H. Ali, M. Bilal, M. Saleem, Identification of cow and buffalo milk based on Beta carotene and vitamin-A concentration using fluorescence spectroscopy, *PLOS ONE*, 12 (2017) e0178055.
[43] K. Ruoff, W. Luginbühl, R. Künzli, S. Bogdanov, J.O. Bosset, K. von der Ohe, *et al.*, Authentication of the Botanical and Geographical Origin of Honey by Front-Face Fluorescence Spectroscopy, *Journal of Agricultural and Food Chemistry*, 54 (2006) 6858.
[44] M.S. Mortz, System for pulse oximetry SpO_2 determination, *Google Patents*, 1999.
[45] I. Yamanouchi, Y. Yamauchi, I. Igarashi, Transcutaneous bilirubinometry: Preliminary studies of noninvasive transcutaneous bilirubin meter in the Okayama National Hospital, *Pediatrics*, 65 (1980) 195.

[46] Z. Huang, A. McWilliams, H. Lui, D.I. McLean, S. Lam, H. Zeng, Near-infrared Raman spectroscopy for optical diagnosis of lung cancer, *International Journal of Cancer*, 107 (2003) 1047.

[47] H. Brits, J. Adendorff, D. Huisamen, D. Beukes, K. Botha, H. Herbst, *et al.*, The prevalence of neonatal jaundice and risk factors in healthy term neonates at National District Hospital in Bloemfontein, *African Journal of Primary Health Care and Family Medicine*, 10 (2018) 1.

[48] N.G. Onyeneho, B.C. Ozumba, S. Subramanian, Determinants of childhood anemia in India, *Scientific Reports*, 9 (2019) 1.

[49] R. Subhi, M. Adamson, H. Campbell, M. Weber, K. Smith, T. Duke, *et al.*, The prevalence of hypoxaemia among ill children in developing countries: A systematic review, *The Lancet Infectious Diseases*, 9 (2009) 219.

[50] J. Brown, L. Theis, L. Kerr, N. Zakhidova, K. O'Connor, M. Uthman, *et al.*, A hand-powered, portable, low-cost centrifuge for diagnosing anemia in low-resource settings, *The American Journal of Tropical Medicine and Hygiene*, 85 (2011) 327.

[51] S. Yap, I. Mohammad, C. Ryan, Avoiding painful blood sampling in neonates by transcutaneous bilirubinometry, *Irish Journal of Medical Science*, 171 (2002) 188.

[52] S. Meites, Skin-puncture and blood-collecting technique for infants: Update and problems, *Clinical Chemistry*, 34 (1988) 1890.

[53] L. Wang, J.M. Cochran, T. Ko, W.B. Baker, K. Abramson, L. He, *et al.*, Non-invasive monitoring of blood oxygenation in human placentas via concurrent diffuse optical spectroscopy and ultrasound imaging, *Nature Biomedical Engineering*, (2022) 1.

[54] S.H. Yun, S.J. Kwok, Light in diagnosis, therapy and surgery, *Nature Biomedical Engineering*, 1 (2017) 1.

[55] L.D. Lilien, V.J. Harris, R.S. Ramamurthy, R.S. Pildes, Neonatal osteomyelitis of the calcaneus: Complication of heel puncture, *The Journal of Pediatrics*, 88 (1976) 478.

[56] H. Lemont, J. Brady, Infant heel nodules: Calcification of epidermal cysts, *Journal of the American Podiatric Medical Association*, 92 (2002) 112.

[57] K. Jangaard, H. Curtis, R. Goldbloom, Estimation of bilirubin using biliChek™, a transcutaneous bilirubin measurement device: Effects of gestational age and use of phototherapy, *Paediatrics & Child Health*, 11 (2006) 79.

[58] W.D. Engle, G.L. Jackson, N.G. Engle, Transcutaneous bilirubinometry, Seminars in perinatology, *Elsevier*, Edinburgh, 2014, pp. 438.
[59] N.B. Hampson, E.D. Ecker, K.L. Scott, Use of a noninvasive pulse CO-oximeter to measure blood carboxyhemoglobin levels in bingo players, *Respiratory Care*, 51 (2006) 758.
[60] L. Lamhaut, R. Apriotesei, X. Combes, M. Lejay, P. Carli, B. Vivien, Comparison of the accuracy of noninvasive hemoglobin monitoring by spectrophotometry (SpHb) and HemoCue® with automated laboratory hemoglobin measurement, *The Journal of the American Society of Anesthesiologists*, 115 (2011) 548.
[61] M.J. Maisels, Transcutaneous bilirubin measurement: Does it work in the real world?, *Pediatrics*, 135 (2015) 364.
[62] M.J. Maisels, E. Kring, Transcutaneous bilirubinometry decreases the need for serum bilirubin measurements and saves money, *Pediatrics*, 99 (1997) 599.
[63] M.J. Maisels, Noninvasive measurements of bilirubin, *Pediatrics*, 129 (2012) 779.
[64] N. Bosschaart, J.H. Kok, A.M. Newsum, D.M. Ouweneel, R. Mentink, T.G. van Leeuwen, *et al.*, Limitations and opportunities of transcutaneous bilirubin measurements, *Pediatrics*, 129 (2012) 689.
[65] S. Wainer, Y. Rabi, S.M. Parmar, D. Allegro, M. Lyon, Impact of skin tone on the performance of a transcutaneous jaundice meter, *Acta paediatrica*, 98 (2009) 1909.
[66] Who, Antimicrobial resistance, in, 2021.
[67] C.J.L. Murray, K.S. Ikuta, F. Sharara, L. Swetschinski, G.R. Aguilar, A. Gray, *et al.*, Global burden of bacterial antimicrobial resistance in 2019: A systematic analysis, *The Lancet*, 399 (2022) 629.
[68] J.M. Munita, C.A. Arias, Mechanisms of Antibiotic Resistance, *Microbiology Spectrum*, 4 (2016).
[69] A. Cassini, L.D. Högberg, D. Plachouras, A. Quattrocchi, A. Hoxha, G.S. Simonsen, *et al.*, Attributable deaths and disability-adjusted life-years caused by infections with antibiotic-resistant bacteria in the EU and the European Economic Area in 2015: A population-level modelling analysis, *The Lancet Infectious Diseases*, 19 (2019) 56.

[70] S. Kannan, A. Solomon, G. Krishnamoorthy, M. Marudhamuthu, Liposome encapsulated surfactant abetted copper nanoparticles alleviates biofilm mediated virulence in pathogenic Pseudomonas aeruginosa and MRSA, *Scientific Reports*, 11 (2021) 1102.

[71] S. Hemaiswarya, A.K. Kruthiventi, M. Doble, Synergism between natural products and antibiotics against infectious diseases, *Phytomedicine*, 15 (2008) 639.

[72] A. Nawaz, S. Goudarzi, M.A. Asghari, S. Pichiah, G.S. Selopal, F. Rosei, *et al.*, Review of hybrid 1D/2D photocatalysts for light-harvesting applications, *ACS Applied Nano Materials*, 4 (2021) 11323.

[73] S.A. Ahmed, M. Nur Hasan, D. Bagchi, H.M. Altass, M. Morad, I.I. Althagafi, *et al.*, Nano-MOFs as targeted drug delivery agents to combat antibiotic-resistant bacterial infections, *Royal Society Open Science*, 7 (2020) 200959.

[74] E. Tinajero-Díaz, D. Salado-Leza, C. Gonzalez, M. Martínez Velázquez, Z. López, J. Bravo-Madrigal, *et al.*, Green metallic nanoparticles for cancer therapy: Evaluation models and cancer applications, *Pharmaceutics*, 13 (2021) 1719.

[75] N.A. Cloete, R. Malekian, L. Nair, Design of smart sensors for real-time water quality monitoring, *IEEE Access*, 4 (2016) 3975.

[76] E.W. Kimani-Murage, A.M. Ngindu, Quality of water the slum dwellers use: The case of a Kenyan slum, *Journal of Urban Health*, 84 (2007) 829.

[77] R.H. Dwight, L.M. Fernandez, D.B. Baker, J.C. Semenza, B.H. Olson, Estimating the economic burden from illnesses associated with recreational coastal water pollution: A case study in Orange County, California, *Journal of Environmental Management*, 76 (2005) 95.

[78] R. Li, M. Dong, Y. Zhao, L. Zhang, Q. Cui, W. He, Assessment of water quality and identification of pollution sources of plateau lakes in Yunnan (China), *Journal of Environmental Quality*, 36 (2007) 291.

[79] E. Lawson, Physico-chemical parameters and heavy metal contents of water from the Mangrove Swamps of Lagos Lagoon, Lagos, Nigeria, *Advances in Biological Research*, 5 (2011) 8.

[80] R. Ramalho, J. Cunha, P. Teixeira, P.A. Gibbs, Improved methods for the enumeration of heterotrophic bacteria in bottled mineral waters, *Journal of Microbiological Methods*, 44 (2001) 97.

[81] G. Sadeghi, M. Mohammadian, M. Nourani, M. Peyda, A. Eslami, Microbiological quality assessment of rural drinking water supplies in Iran, *Journal of Agriculture & Social Sciences*, 3 (2007) 31.

[82] M. Farré, D. Barceló, Toxicity testing of wastewater and sewage sludge by biosensors, bioassays and chemical analysis, *TrAC Trends in Analytical Chemistry*, 22 (2003) 299.

[83] T.H.Y. Tebbutt, Principles of water quality control, *Elsevier*, 2013.

[84] D.R. Lenat, Water quality assessment of streams using a qualitative collection method for benthic macroinvertebrates, *Journal of the North American Benthological Society*, 7 (1988) 222.

[85] B. O'Flynn, R. Martínez-Català, S. Harte, C. O'Mathuna, J. Cleary, C. Slater*, et al.*, SmartCoast: A wireless sensor network for water quality monitoring, 3*2nd IEEE Conference on Local Computer Networks (LCN 2007), IEEE*, 2007, pp. 815.

[86] N.C. Munksgaard, D.L. Parry, Monitoring of labile metals in turbid coastal seawater using diffusive gradients in thin-films, *Journal of Environmental Monitoring*, 5 (2003) 145.

[87] S. Zhou, Z. Yuan, Q. Cheng, Z. Zhang, J. Yang, Rapid in situ determination of heavy metal concentrations in polluted water via portable XRF: Using Cu and Pb as example, *Environmental Pollution*, 243 (2018) 1325.

[88] M.D. Johnston, A simple and rapid test for quality control of liquid media, using the bioscreen microbiological growth analyser, *Journal of Microbiological Methods*, 32 (1998) 37.

[89] B. Ouyang, F.R. Dalgleish, F.M. Caimi, T.E. Giddings, J. Shirron, A.K. Vuorenkoski*, et al.*, Compressive sensing underwater laser serial imaging system, *Journal of Electronic Imaging*, 22 (2013) 021010.

[90] D. Selmo, F. Sturt, J. Miles, P. Basford, T. Malzbender, K. Martinez*, et al.*, Underwater reflectance transformation imaging: A technology for in situ underwater cultural heritage object-level recording, *Journal of Electronic Imaging*, 26 (2017) 011029.

[91] T.P. Lambrou, C.C. Anastasiou, C.G. Panayiotou, M.M. Polycarpou, A low-cost sensor network for real-time monitoring and contamination detection in drinking water distribution systems, *IEEE Sensors Journal*, 14 (2014) 2765.

[92] G. Lux, A. Langer, M. Pschenitza, X. Karsunke, R. Strasser, R. Niessner, *et al.*, Detection of the carcinogenic water pollutant benzo[a]pyrene with an electro-switchable biosurface, *Analytical Chemistry*, 87 (2015) 4538.

[93] F. Edition, Guidelines for drinking-water quality, *WHO Chronicle*, 38 (2011) 104.

[94] M.R. Kulkarni, T. Revanth, A. Acharya, P. Bhat, Removal of Crystal Violet dye from aqueous solution using water hyacinth: Equilibrium, kinetics and thermodynamics study, *Resource-Efficient Technologies*, 3 (2017) 71.

[95] I. Šafařík, M. Šafaříková, Detection of low concentrations of malachite green and crystal violet in water, *Water Research*, 36 (2002) 196.

[96] S. Wei, H. Zhang, S. Tao, A review of arsenic exposure and lung cancer, *Toxicology Research*, 8 (2019) 319.

[97] V.D. Martinez, E.A. Vucic, D.D. Becker-Santos, L. Gil, W.L. Lam, Arsenic exposure and the induction of human cancers, *Journal of Toxicology*, 2011 (2011) 431287.

[98] W.G. Burgess, M.A. Hoque, H.A. Michael, C.I. Voss, G.N. Breit, K.M. Ahmed, Vulnerability of deep groundwater in the Bengal Aquifer system to contamination by arsenic, *Nature Geoscience*, 3 (2010) 83.

[99] M. Amini, K.C. Abbaspour, M. Berg, L. Winkel, S.J. Hug, E. Hoehn, *et al.*, Statistical Modeling of global geogenic Arsenic contamination in groundwater, *Environmental Science & Technology*, 42 (2008) 3669.

[100] K. Henke, Arsenic: Environmental chemistry, health threats and waste treatment, *Wiley*, New Jersey, 2009.

[101] J. Li, C. Packianathan, T.G. Rossman, B.P. Rosen, Nonsynonymous polymorphisms in the human AS3MT arsenic methylation gene: Implications for arsenic toxicity, *Chemical Research in Toxicology*, 30 (2017) 1481.

[102] L. Ramsay, M.M. Petersen, B. Hansen, J. Schullehner, P. van der Wens, D. Voutchkova, *et al.*, Drinking water criteria for arsenic in high-income, low-dose countries: The effect of legislation on public health, *Environmental Science & Technology*, 55 (2021) 3483.

[103] C.M. Steinmaus, C.M. George, D.A. Kalman, A.H. Smith, Evaluation of two new arsenic field test kits capable of detecting arsenic water concentrations close to 10 µg/L, *Environmental Science & Technology*, 40 (2006) 3362.
[104] X. Ge, Y. Ma, X. Song, G. Wang, H. Zhang, Y. Zhang, *et al.*, β-FeOOH nanorods/carbon foam-based hierarchically porous monolith for highly effective arsenic removal, *ACS Applied Materials & Interfaces*, 9 (2017) 13480.
[105] M.-K. Ke, G.-X. Huang, S.-C. Mei, Z.-H. Wang, Y.-J. Zhang, T.-W. Hua, *et al.*, Interface promoted direct oxidation of p-arsanilic acid and removal of total arsenic by the coupling of peroxymonosulfate and Mn-Fe mixed oxide, *Environmental Science & Technology*, 55 (2021) 7063.
[106] T. Gupte, S.K. Jana, J.S. Mohanty, P. Srikrishnarka, S. Mukherjee, T. Ahuja, *et al.*, Highly sensitive As3+ detection using electrodeposited nanostructured MnOx and phase evolution of the active material during sensing, *ACS Applied Materials & Interfaces*, 11 (2019) 28154.
[107] N.-U.-A. Babar, K.S. Joya, M.A. Tayyab, M.N. Ashiq, M. Sohail, Highly sensitive and selective detection of arsenic using electrogenerated nanotextured gold assemblage, *ACS Omega*, 4 (2019) 13645.
[108] T. Wang, R.D. Milton, S. Abdellaoui, D.P. Hickey, S.D. Minteer, Laccase inhibition by arsenite/arsenate: Determination of inhibition mechanism and preliminary application to a self-powered biosensor, *Analytical Chemistry*, 88 (2016) 3243.
[109] S. Deshmukh, D. Banerjee, G. Bhattacharya, S.J. Fishlock, A. Barman, J. McLaughlin, *et al.*, Red mud reduced graphene oxide nanocomposites for the electrochemical sensing of arsenic, *ACS Applied Nano Materials*, 3 (2020) 4084.
[110] N. Priyadarshni, P. Nath, Nagahanumaiah, N. Chanda, DMSA-functionalized gold nanorod on paper for colorimetric detection and estimation of arsenic (III and V) contamination in groundwater, *ACS Sustainable Chemistry & Engineering*, 6 (2018) 6264.
[111] L. Zeng, D. Zhou, J. Gong, C. Liu, J. Chen, Highly sensitive aptasensor for trace arsenic(III) detection using DNAzyme as the biocatalytic amplifier, *Analytical Chemistry*, 91 (2019) 1724.

[112] B.M. Sonkoue, P.M.S. Tchekwagep, C.P. Nanseu-Njiki, E. Ngameni, Electrochemical determination of arsenic using silver nanoparticles, *Electroanalysis*, 30 (2018) 2738.
[113] S.A. Durazo, U.B. Kompella, Functionalized nanosystems for targeted mitochondrial delivery, *Mitochondrion*, 12 (2012) 190.
[114] T.A. Trendeleva, E.I. Sukhanova, A.G. Rogov, R.A. Zvyagilskaya, I.I. Seveina, T.M. Ilyasova, *et al.*, Role of charge screening and delocalization for lipophilic cation permeability of model and mitochondrial membranes, *Mitochondrion*, 13 (2013) 500.
[115] J.A. Novotny, D.J. Baer, Tea, Encyclopedia of human nutrition, *Elsevier*, Edinburgh, 2013.
[116] statistica.com, Main export countries for tea worldwide 2021, in: Statista.
[117] K. Das, International protection of India's geographical indications with special reference to "Darjeeling" tea, *The Journal of World Intellectual Property*, 9 (2006) 459.
[118] Economically Motivated Adulteration (Food Fraud), *FDA*, 2021.
[119] A. Banerjee, N. Bhattacharyya, R. Ghosh, S. Singh, A. Adhikari, S. Mondal, *et al.*, Non-invasive estimation of hemoglobin, bilirubin and oxygen saturation of neonates simultaneously using whole optical spectrum analysis at point of care, *Scientific Reports*, 13 (2023) 2370.
[120] A. Banerjee, D. Mukherjee, A. Bera, R. Ghosh, S. Mondal, S. Mukhopadhyay, *et al.*, Molecular co-localization of multiple drugs in a nanoscopic delivery vehicle for potential synergistic remediation of multi-drug resistant bacteria, *Scientific Reports*, 12 (2022) 18881.
[121] A. Banerjee, R. Ghosh, T. Adhikari, S. Mukhopadhyay, A. Chattopadhyay, S.K. Pal, Development of nanomedicine from copper mine tailing waste: A pavement towards circular economy with advanced redox nanotechnology, *Catalysts*, 13 (2023) 369.
[122] A. Banerjee, R. Ghosh, A. Bera, S. Mukhopadhyay, M.M. Al-Rooqi, I.I. Althagafi, *et al.*, "Nano-Copper": A potential remediation of antibiotic-resistant infections, *Journal of Nanomedicine*, 6 (2023) 1058.

[123] A. Banerjee, S. Singh, R. Ghosh, M.N. Hasan, A. Bera, L. Roy, *et al.*, A portable spectroscopic instrument for multiplexed monitoring of acute water toxicity: Design, testing, and evaluation, *Review of Scientific Instruments*, 93 (2022) 115105.
[124] S.S. Pasha, A. Banerjee, S. Sreedharan, S. Singh, N. Kandoth, K.A. Vallis, *et al.*, Ultrasensitive reagent for ratiometric detection and detoxification of iAs III in water and Mitochondria, *Inorganic Chemistry*, 61 (2022) 13115.
[125] A. Banerjee, R. Ghosh, S. Singh, A. Adhikari, S. Mondal, L. Roy, *et al.*, Spectroscopic studies on a natural biomarker for the identification of origin and quality of tea extracts for the development of a portable and field deployable prototype, *Spectrochimica Acta Part A: Molecular and Biomolecular Spectroscopy*, 299 (2023) 122842.
[126] A. Banerjee, D. Mukherjee, M.N. Hasan, S. Mukhopadhyay, D. Karmakar, R. Das, *et al.*, Interaction of chlorophyll with artificial colorants in restricted nanoscopic environment: Key insights on the toxicity from electronic spectroscopy, *Nanoscience and Nanotechnology Open Access*, 2 (2023) 1012.

CHAPTER 2

Overview of Experimental Techniques and Systems

The use of various optical spectroscopy-based methods to extract underlying information from biological, food and environmental samples is well known. In this chapter, a few spectroscopic techniques and experimental tools are discussed briefly that can help to gain a better understanding of various molecular level interactions enriching knowledge in the fields mentioned above.

2.1. MEASUREMENT AND ANALYSIS TOOLS:

2.1.1. Absorption Spectroscopy:

The absorbance spectroscopy is the measurement of relative change of transmittance of light while passing through a solution. The total amount of light passed through the sample is well expressed by Lambert Beer's law [1, 2] in terms of the light intensity as described in the following Equation 2.1.

$$A = log_{10}(\frac{I_0}{I}) = \varepsilon lc \quad (2.1)$$

Where the term '*A*' is the absorbance, *Io* and *I* are the initial and final intensities of light, 'ε' is the molar extinction coefficient of the solution with unit $M^{-1}cm^{-1}$ when the optical path length is '*l*' and 'c' is the concentration of the solution expressed in cm and molarity(M) respectively. Recent advances in spectrometer technologies including CCD and CMOS array have made the detection easy, accurate and cost effective [3]. Such progress in detector domain has made spectroscopy much popular than colour and image analysis. RGB analysis is one of the examples of image analysis which also has found many applications in real world [4]. Often air/water quality has been determined using airborne cameras and subsequent image analysis [5].

2.1.2. Diffuse Reflectance Spectroscopy:

Light incidence on biological targets and interacts with the skin and other targets and the retro reflected beam carries meaningful information back to the

receiver. The Ultra Violet (UV) and visible spectrum contributes in exciting electrons to valence band and the spectrum receiver analyses the contribution of each wavelength. Optical scattering in biological targets in random trajectory, or diffusion, of incident photons experiences multiple elastic scattering from cells, extracellular matrix, blood vessels, and other tissue components [6]. Optically scattered signals from skin, brain tissues, and vessel walls have helped development of new technologies and hence have attracted the attention of scientist all over the world [7].

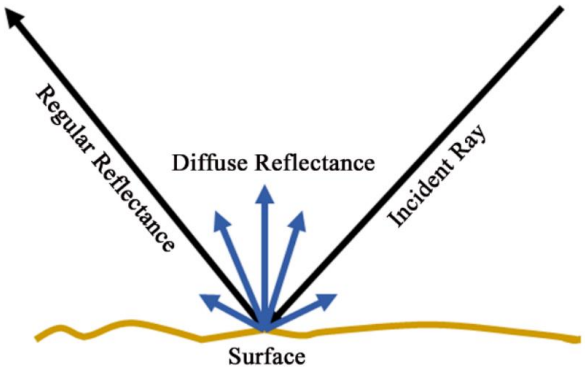

Figure 2.1. *Schematic representation of the diffuse reflection from a solid sample. The diffuse light can be collected for spectroscopic studies.*

Similarly, optical scattering method finds interesting applications in meteorological field. Optical propagation in aerosols may mathematically be predicted with acceptable precision by single-scattering methods. Nevertheless, multiple scattering effect needs to be considered for denser targets like clouds [8]. Several optical instruments have been designed based on this principle. Lidar is a classic example of such instrument.

The difference between specular spectroscopy and diffuse reflection spectroscopy [9] is, the former measures the direct change in the light intensity, whereas the later measures the relative change in the amount of reflected light from a surface. Light scattering spectroscopy [10] is another form of reflectance spectroscopy. It determines the tissue structures by observing the intrinsic elastic scattering properties. The rate of the electrons jumping from the valence band to the conduction band due to optical excitation depends upon the absorbance of the light at given bandgap (E_g) independent of the transmittance. In the diffuse reflectance spectroscopy, the Kubelka-Munk theory [11] determines from the diffused reflectance

spectra. For an object under test, with a particle diameter which is comparable to the wavelength of incident light then diffuse reflectance no longer permits the secondary contributions of reflection, refraction, and diffraction, the absorption coefficient can be given by equation 2.2.

$$\frac{K}{S} = \frac{(1-R_\alpha)^2}{2R_\alpha} \equiv F(R_\alpha) \tag{2.2}$$

R_α is the diffuse reflectance and $F(R_\alpha)$ is called the Kubelka-Munk function. *K* and *S* are the absorption coefficient and scattering coefficient respectively. The absorption coefficient becomes equal to twice of absorption coefficient when the incident light scatters in a perfectly diffuse manner. In this case, considering the scattering coefficient as constant with respect to wavelength, Kubelka-Munk equation [12, 13] is used to determine the E_g as in equation 2.3,

$$[F(R_\alpha)h\nu]^2 = C(h\nu - E_g) \tag{2.3}$$

where α is linear absorption coefficient, ν is light frequency, h is the Plank's constant and *C* is the proportionality constant.

2.1.3. Fluorescence Spectroscopy:

Fluorescence detection is a powerful and effective tool for the sensitive and selective monitoring of the physical and chemical performance of compounds under study. The Jablonski diagram [14] offers a convenient representation of electrons in ground state with the relevant transitions. The excitation procedure to the excited state (S_1) from the ground state (S_0) is very fast. After excitation, the fluorophore quickly relaxed from the singlet electronic state to an allowable vibrational level in the electronic ground state and fluorescence emission occurs. With increasing absorption, the fluorescence intensity of fluorophores decreases owing to increased internal conversion. In this regard, both fluorescence quantum yield is one among the most important selection criteria for fluorophores in single-molecule fluorescence spectroscopy. The fluorescence quantum yield(ϕ_f) gives the efficiency of the

fluorescence process and given by the ratio of photons emitted to photons absorbed as given in the equation 2.4

$$\phi_f = \frac{k_r}{k_r + k_{nr}} \tag{2.4}$$

the quantum yield can be described by two rate constants, the radiative rate constant, k_r, and the nonradiative rate constant, k_{nr}, comprising all possible competing deactivation pathways, such as phosphorescence, intersystem crossing, internal conversion etc. The fluorescence intensity, I_f is given by he amount of light absorbed and the fluorescence quantum yield, ϕ as expressed in equation 2.5.

$$I_f = kI_0\phi[1 - 10^{-\varepsilon bc}] \tag{2.5}$$

By simplifying the equation 2.5 can be rewritten as,

$$I_f = kI_0\phi[\varepsilon bc] \tag{2.6}$$

k is a proportionality constant attributed to the instrument, I_0 is the incident light intensity ε is the molar absorptivity, b is the path length, and c is the concentration of the substrate. This simplified relationship shows that fluorescence intensity is proportional to concentration.

2.1.4. Förster Resonance Energy Transfer (FRET):

Förster Resonance Energy Transfer [15] is an electrodynamic phenomenon involving the non-radiative transfer of the excited state energy from the donor dipole (D) to an acceptor dipole (A) (Figure 2.2a). FRET has got wide uses in all fluorescence applications including medical diagnostics, DNA analysis and optical imaging. Since FRET can measure the size of a protein molecule or the thickness of a membrane, it is also known as "spectroscopic ruler" [16]. FRET is very often used to measure the distance between two sites on a macromolecule. Basically, FRET is of two types: (a) Homo-molecular FRET and (b) Hetero-molecular FRET. In the former case same fluorophore acts both as energy donor and acceptor, while in the latter case two different molecules act as donor and acceptor.

Each donor-acceptor (D-A) pair participating in FRET is characterized by a distance known as Förster distance (R_0) i.e., the D-A separation at which energy transfer is 50% efficient. The R_0 value ranges from 20 to 60 Å. The rate of resonance energy transfer (k_T) from donor to an acceptor is given by [17],

$$k_T = \frac{1}{\tau_D}\left(\frac{R_0}{r}\right)^6 \tag{2.7}$$

where, τ_D is the lifetime of the donor in the absence of acceptor, R_0 is the Förster distance and r is the donor to acceptor (D-A) distance. The rate of transfer of donor energy depends upon the extent of overlap of the emission spectrum of the donor with the absorption spectrum of the acceptor ($J(\lambda)$), the quantum yield of the donor (Q_D), the relative orientation of the donor and acceptor transition dipoles (κ^2) and the distance between the donor and acceptor molecules (r) (Figure 2.2b). In order to estimate FRET efficiency of the donor and hence to determine distances of donor-acceptor pairs, the methodology described below is followed [17]. The Förster distance (R_0) is given by,

$$R_0 = 0.211[\kappa^2 n^{-4} Q_D J(\lambda)]^{1/6} \text{ (in Å)} \tag{2.8}$$

where, n is the refractive index of the medium, Q_D is the quantum yield of the donor and $J(\lambda)$ is the overlap integral. κ^2 is defined as,

$$\kappa^2 = (cos\,\theta_T - 3\,cos\,\theta_D\,cos\,\theta_A)^2 = (sin\theta_D sin\theta_A cos\varphi - 2cos\theta_D cos\theta_A)^2 \tag{2.9}$$

where, θ_T is the angle between the emission transition dipole of the donor and the absorption transition dipole of the acceptor, θ_D and θ_A are the angles between these dipoles and the vector joining the donor and acceptor and φ is angle between the planes of the donor and acceptor (Figure 2.2b). κ^2 value can vary from 0 to 4. For collinear and parallel transition dipoles, $\kappa^2 = 4$; for parallel dipoles, $\kappa^2 = 1$; and for perpendicularly oriented dipoles, $\kappa^2 = 0$. For donor and acceptors that randomize by rotational diffusion prior to energy transfer, the magnitude of κ^2 is assumed to be 2/3. $J(\lambda)$, the overlap integral, which expresses the degree of spectral overlap between the donor emission and the acceptor absorption, is given by,

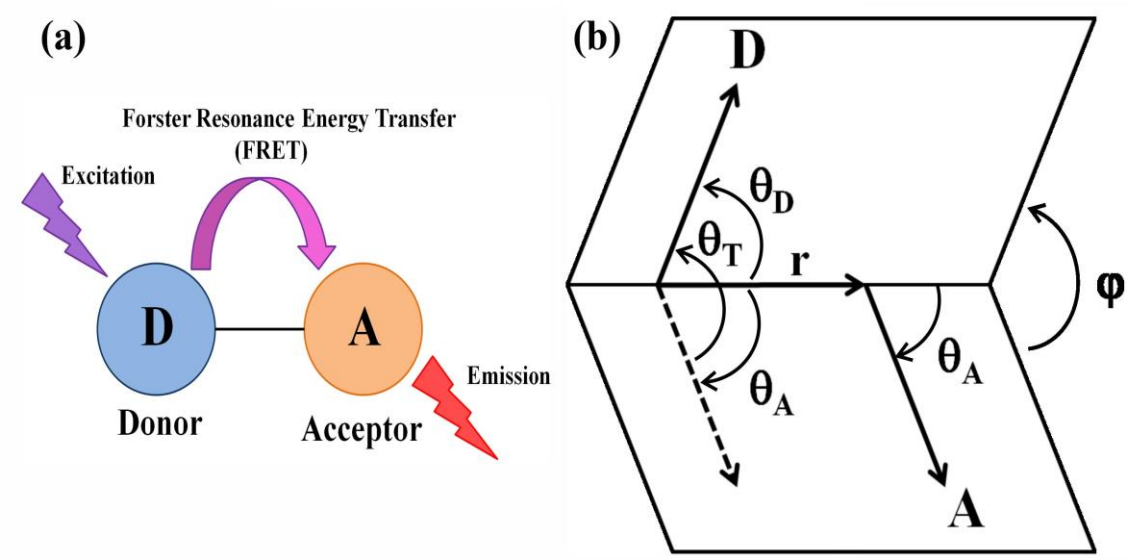

Figure 2.2. *(a) Schematic illustration of the Förster Resonance Energy Transfer (FRET) process. (b) Dependence of the orientation factor κ^2 on the directions of the emission and absorption dipoles of the donor and acceptor, respectively.*

$$J(\lambda) = \frac{\int_0^\infty F_D(\lambda)\varepsilon_A(\lambda)\lambda^4 d\lambda}{\int_0^\infty F_D(\lambda)d\lambda} \tag{2.10}$$

where, $F_D(\lambda)$ is the fluorescence intensity of the donor in the wavelength range of λ to λ +d λ and is dimensionless. $\varepsilon_A(\lambda)$ is the extinction coefficient (in $M^{-1}cm^{-1}$) of the acceptor at λ. If λ is in nm, then J(λ) is in units of M^{-1} cm^{-1} nm^4.

Once the value of R_0 is known, the efficiency of energy transfer can be calculated. The efficiency of energy transfer (E) is the fraction of photons absorbed by the donor which are transferred to the acceptor and is defined as,

$$E = \frac{k_T(r)}{\tau_D^{-1} + k_T(r)} \tag{2.11}$$

$$E = \frac{R_0^6}{r^6 + R_0^6} \tag{2.12}$$

The transfer efficiency is measured using the relative fluorescence intensity of the donor, in absence (F_D) and presence (F_{DA}) of the acceptor as,

$$E = 1 - \frac{F_{DA}}{F_D} \tag{2.13}$$

For D-A systems decaying with multiexponential lifetimes, E is calculated from the amplitude weighted lifetimes $\langle\tau\rangle = \sum_i \alpha_i \tau_i$ [17] of the donor in absence (τ_D) and presence (τ_{DA}) of the acceptor as,

$$E = 1 - \frac{\tau_{DA}}{\tau_D}. \quad (2.14).$$

The D-A distances can be measured using equations (2.12), (2.13) and (2.14). The distances measured using equation 2.13 and 2.14 are revealed as R^S (steady state measurement) and R^{TR} (time-resolved measurement), respectively. In one of recent studies from our group [18], we have reported the potential danger of using equation 2.13 to conclude the nature of energy transfer as Förster type. The study shows that the energy transfer efficiency E, calculated from steady state experiment (equation 2.13) might be due to re-absorption of donor emission, but not due to dipole-dipole interaction (FRET).

2.1.4.1. Distance Distribution between Donor and Acceptor:

Distance distribution between donor and acceptor was estimated according to the procedure described in the literature [19, 20]. The observed fluorescence transients of the donor molecules in absence of acceptor were fitted using a nonlinear least-squares fitting procedure (software SCIENTIST) to the following function;

$$I_D(t) = \int_0^t E(t')p(t'-t)dt' \quad (2.15)$$

which comprises the convolution of the instrument response function (IRF) ((E(t)) with exponential ($p(t) = \sum_i \alpha_{Di}\, exp(-t/\tau_{Di})$). The convolution of the distance distribution function P(r) in the fluorescence transients of donor in presence of acceptor in the system under studies is estimated using the same software (SCIENTIST) in the following way.

The intensity decay of D-A pair, spaced at a distance r, is given by;

$$I_{DA}(r,t) = \sum_i \alpha_{Di}\, exp\left[-\frac{t}{\tau_{Di}} - \frac{t}{\tau_{Di}}\left(\frac{R_0}{r}\right)^6\right] \quad (2.16)$$

and the intensity decay of the sample considering distance distribution probability function, P(r) is given by;

$$I_{DA}(t) = \int_{r=0}^{\infty} P(r) I_{DA}(r,t) dr \tag{2.17}$$

where P(r) consist of the following terms;

$$P(r) = \frac{1}{\sigma\sqrt{2\pi}} exp\left[-\frac{1}{2}\left(\frac{\bar{r}-r}{\sigma}\right)^2\right] \tag{2.18}$$

In this equation r̄ is the mean of the Gaussian with a standard deviation of σ. Usually distance distributions are described by the full width at half maxima (hw). This half width is given by hw = 2.354 σ.

2.1.5. Data Analysis of Time-resolved Fluorescence Transients:

Curve fitting of the time-resolved fluorescence transients was carried out using a nonlinear least square fitting procedure to a function (2.19) comprised of convolution of the IRF,

$$X(t) = \int_0^t E(t') R(t-t') dt' \tag{2.19}$$

($E(t)$) with a sum of exponentials (2.20) with pre-exponential factors (B_i),

$$R(t) = A + \sum_{i=1}^{N} B_i exp(-\frac{t}{\tau_i}) \tag{2.20}$$

characteristic lifetimes (τ_i) and a background (A). Relative concentration in a multiexponential decay is expressed as equation (2.21),

$$c_n = \frac{B_n}{\sum_{i=1}^{N} B_i} \times 100 \tag{2.21}$$

Average lifetime (amplitude-weighted) of a multiexponential decay is expressed as,

$$\tau_{av} = \sum_{i=1}^{N} c_i \tau_i \tag{2.22}$$

2.1.6. 'Infelta-Tachiya' Model (Kinetic Model):

In some of our studies [21, 22] we have employed a kinetic model developed by Infelta and Tachiya for better understanding of the distribution of energy acceptors

(quenchers) around the micelles. The decay of excited probes in a micelle may be described by the following kinetic model [21]:

$$P_n^* \xrightarrow{K_0} P_n \tag{2.23}$$

$$P_n^* \xrightarrow{nk_q} P_n \tag{2.24}$$

where P_n* and P_n stand for a micelle containing n quencher molecules with and without an excited probe, respectively. k_0 is the total decay constant of the excited state in absence of a quencher. k_q is the rate constant for quenching of an excited probe in a micelle containing one quencher molecule. In this kinetic model, it is assumed that the distribution of the number of quenchers attached to one micelle follows a Poisson distribution, [23] namely,

$$p(n) = \frac{m^n}{n!} \times exp(-m) \tag{2.25}$$

where m is the mean number of quenchers in a micelle. Mathematically m can be expressed as,

$$m = \frac{k_+[A]}{k_-} \tag{2.26}$$

where k_+ is the rate constant for entry of a quencher molecule into a micelle, while k_- is the rate constant for exit of a quencher molecule from a micelle containing one quencher molecule. "A" stands for a quencher molecule in the aqueous phase. Based upon the above model, the equation for the total concentration $P^*(t)$ of excited probes at time t is given by [21]:

$$P^*(t) = P^*(0)exp\left[-\left(k_0 + \frac{k_0 k_+[A]}{k_- + k_q}\right) \times t + \frac{k_q^2 k_+[A]}{k_- \times (k_- + k_q)^2} \times \{1 - exp[-(k_- + k_q) \times t]\}\right. \tag{2.27}$$

For the case $k_- << k_q$, the above equation reduces to,

$$P^*(t) = P^*(0)exp\{-k_0 t - m \times [1 - exp(-k_q t)] \tag{2.28}$$

The observed fluorescence transients can be fitted using a nonlinear least square fitting procedure (software SCIENTIST™) to a function $X(t) = \int_0^t E(t') \times P(t - t')dt'$ comprising of the convolution of the instrument response function (IRF) ($E(t)$) with exponential $P^*(t) = P^*(0)\exp\{-k_0 t - m \times [1 - exp(-k_q t)]\}$. The purpose of

this fitting is to obtain the decays in an analytic form suitable for further data analysis. In case of quantum dots (QDs), along with the quencher/acceptor (in case of energy transfer process), there exist some unidentified traps that further cause quenching of the lifetime of excited QD probe, which are also taken into account. If the distribution of the number of unidentified traps around the donor QDs follows a Poisson distribution with the average number (m_t), the decay curves of the excited state of QDs in solvent in absence and presence of acceptor are described by [24]:

$$P^*(t,0) = P^*(0)exp\{-k_0t - m_t \times \left[1 - exp\left(-k_{qt}t\right)\right]\} \quad (2.29)$$

$$P^*(t,m) = P^*(0)exp\{-k_0t - m_t \times \left[1 - exp\left(-k_{qt}t\right)\right] - m[1 - exp\left(-k_{qt}t\right)]\} \quad (2.30)$$

where the quenching rate constant (k_{qt}) by unidentified traps may be different from that (k_q) by acceptor. The extended Infelta-Tachiya kinetic model can be described by the following equation [25],

$$P^*(t) = P^*(0)\ exp\ [-\gamma t + \mu(\exp^{-\beta t} - 1) \quad (2.31)$$

Where γ, μ, and β are functions of the rate constants of probe migration (k), quenching (kq), and quencher exchange either by micelle collision (k_e) or via the aqueous phase (k-) and are explicitly defined as,

$$\gamma = k_0 + k + ma_2k_q / \beta \quad (2.32)$$

$$\mu = m\ k_q^2 / \beta^2 \quad (2.33)$$

$$\beta = k_q + a_2 \quad (2.34)$$

$$a_2 = k_e[M] + k_- \quad (2.35)$$

In the expressions (2.32) to (2.35), k_0, m and [M] stand for the deactivation rate constant of the excited probe in absence of quencher, the average number of quenchers per micelle, and the micelle concentration, respectively.

2.1.7. Transmission of Light through Optical Fiber:

An optical fiber is a cylindrical dielectric waveguide (nonconducting waveguide) that transmits light along its axis, by the process of total internal

reflection. The fiber consists of a core surrounded by a cladding layer, both of which are made of dielectric materials. To confine the optical signal in the core, the refractive index of the core must be greater than that of the cladding. The boundary between the core and cladding may either be abrupt, in step-index fiber, or gradual, in graded-index fiber. When the light (electromagnetic wave) travels to the boundary between the core and the clad (with an angle greater than the critical angle) a localized attenuating electromagnetic field is generated which is called the evanescent field.

Evanescent wave is a near-field wave with an intensity that exhibits exponential decay without absorption as a function of the distance from the core-clad boundary of the optical fiber as shown in Figure 2.3. The standard practice for the estimation of penetration depth (d_p) of the evanescent field in a "

non-absorbing" medium can be illustrated in the following way [26]. In a fiber optic cable the optical signal is transmitted by total internal reflection of the light. The light from the silica core with refractive index n_1 is incident on the clad with refractive index n_2, where $n_1 > n_2$. As a result the light is internally reflected totally, depending upon the incident angle θi, where $\theta i > \theta_c$ (θ_c is the critical angle). In practice the light does not reflect back from the exact plane of separation between core and clad, rather it has certain penetration depth in the clad region. The penetration depth or depth of penetration (d_p) is defined as [26],

$$d_p = \frac{\lambda}{2\pi\sqrt{(n_1{}^2 \sin^2\theta - n_2{}^2)}} \tag{2.36}$$

The estimated penetration depth for our case is in the range of few hundreds of nm. However, if any portion of clad is removed or etched (as in our case) the depth of penetration would change. It is also worth mentioning that evanescent field strongly interacts with the environment outside the fiber and carry spectroscopic information, and is the key of all the waveguide-based sensors [26]. The scenario would change in the case of an environment, which offers strong optical absorption to the light responsible for the evanescent field.[27, 28] This can be conveniently taken into account by defining a complex refractive index [27],

$$\tilde{n} = n + i\kappa \tag{2.37}$$

where, the real part of the refractive index n indicates the phase speed, while imaginary part κ indicates the amount of absorption loss when electromagnetic wave propagates through the medium. Both the real and imaginary parts of the refractive index are the functions of wavelength of the light propagating through the optical fiber. One way to incorporate attenuation of the evanescent field in the absorbing medium is via an absorption coefficient (α_{abs}) [27, 28] in the following way,

$$I(z) = I_0 exp(-\alpha_{abs} z) \tag{2.38}$$

where, I(z) is the intensity of the evanescent field at a distance of z from the interface having field intensity of I_0. a_{abs} denotes absorption coefficient of the medium and equal to twice the magnitude of the imaginary component of the refractive index (2xκ) [27]. In this formulation the penetration depth, d_p would be just inverse of the absorption coefficient ($1/a_{abs}$) [27]. From the above formulation it is clear that the penetration depth of the evanescent field in an absorbing medium very much depends on the concentration of the analyte in the medium.

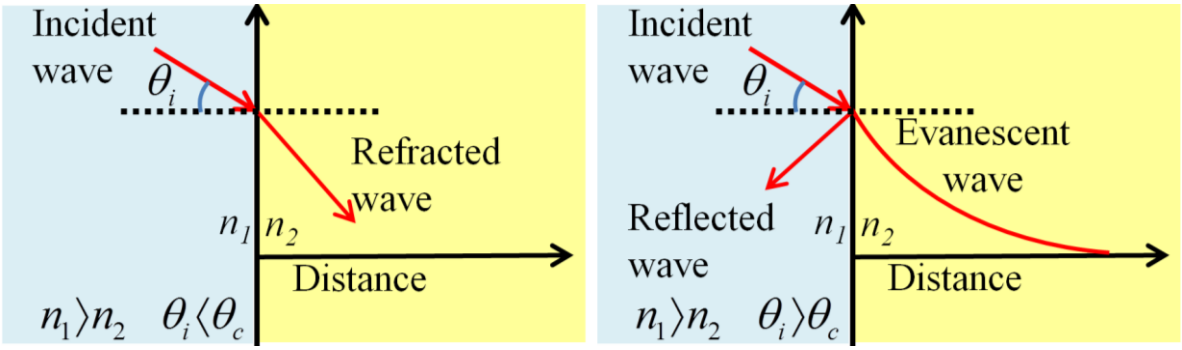

Figure 2.3. *Schematic representation of light refraction from medium with higher to lower refractive index and the evanescent wave in the medium with lower refractive index when* $\theta i > \theta_c$ *(right).*

2.2. SYSTEMS:

2.2.1. Molecular Probes:

In this section, we have discussed about the different molecular probes that have been used in the course of study.

2.2.1.1. Crystal Violet (CV):

CV has a positively charged ammonium ion and three aromatic rings (Figure 2.4.a), used as a staining material. It can bind to the negatively charged phosphate

backbone of DNA and negatively charged amino acids of proteins. It is highly soluble in water and other polar solvents. Its concentration is determined using extinction coefficient, 1,12,000 M^{-1} cm^{-1} at 509 nm [29]. The interaction of CV probe molecules on SDS micelle has been investigated previously and concluded to reside at the surface of the micelle [30].

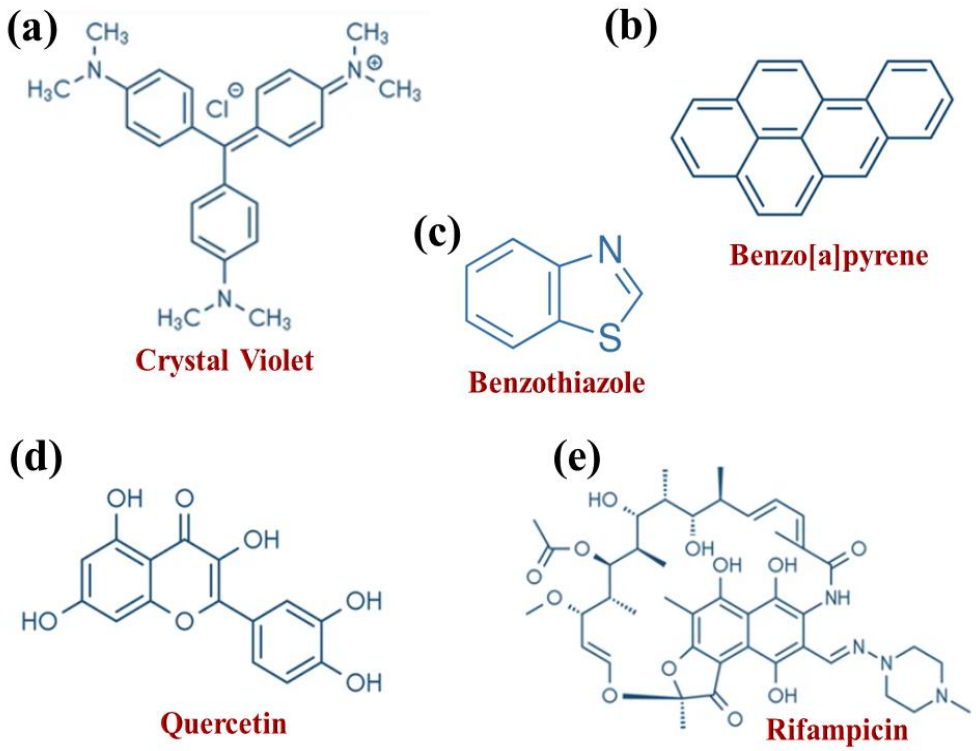

Figure 2.4. *Schematic representation of the molecular probes used in the course of study.*

2.2.1.2. Benzo[a]pyrene (BP):

It is a potent environmental carcinogen which can bind to DNA, extremely hydrophobic and belongs to the class of polyaromatic hydrocarbons (PAHs) [31]. Being a pyrene derivative (Figure 2.4.b), it is characterized by a high quantum yield near unity in micellar solutions [22] along with multiple vibronic bands in its emission spectrum [31].

2.2.1.3. Benzothiazole (BT):

Benzothiazole is a colourless, slightly viscous aromatic heterocyclic compound consisting of a 5-membered 1,3-thiazole ring fused to a benzene ring as shown in Figure 2.4.c. The heterocyclic core of the molecule is readily substituted at the unique

methyne centre in the thiazole ring. It is a thermally stable electron-withdrawing moiety with numerous applications in dyes such as thioflavin [32] and as antifungal agents [33].

2.2.1.4. Quercetin:

Quercetin (Figure 2.4.d) is a well-known plant pigment, a potent antioxidant flavonoid and more specifically a flavonol, found mostly in tea leaves, onions, grapes, and citrus fruits. It is a versatile antioxidant known to possess protective abilities against tissue injury induced by various drug toxicities. its anti-inflammatory, antihypertensive, vasodilator effects, antiobesity, antihypercholesterolemic and antiatherosclerotic activities [34, 35]. It is a naturally occurring polar auxin transport inhibitor [36].

2.2.1.5. Rifampicin (RF):

Rifampicin (also known as rifampin) is an antibiotic medication that belongs to a class of drugs known as rifamycins as shown in Figure 2.4.e. It is primarily used in the treatment of bacterial infections caused by organisms susceptible to rifampin. Rifampin is a key component of standard TB treatment regimens. RF is a first line anti-tuberculosis drug which is highly active against *Mycobacterium tuberculosis* as well as few other Mycobacterial species [37].

Rifampicin is also used to treat infections caused by other mycobacterial species, such as Mycobacterium leprae (the causative agent of leprosy) and certain nontuberculous mycobacteria. It can be used alone or in combination with other drugs like, isoniazid and pyrazinamide for the treatment of tuberculosis. It is a potent inhibitor of DNA dependent RNA synthesis from bacteria [38]. It is sometimes used in combination with other antibiotics to treat serious infections caused by MRSA, particularly in cases where the bacteria are resistant to other antibiotics. Rifampicin works by inhibiting the activity of an enzyme called RNA polymerase, which is essential for bacterial RNA synthesis. By blocking this enzyme, rifampin effectively stops the bacteria from producing essential proteins, ultimately leading to their death. RF absorbs light at 228 nm, 333 nm and 473 nm. Its solubility in water is 1.3 mg/ml at pH 4.3. The molar extinction coefficient of RF at 473 nm is 15,286 M^{-1} cm^{-1}.

2.2.1.6. Micelles:

Micelles are spherical or nearly spherical aggregates of amphiphilic surfactant molecules formed in aqueous solution above a concentration known as critical micellar concentration (CMC). Micelles are formed above a critical temperature called "Kraft point" which is different for different surfactants. Micellar aggregates have diameter varying within 10 nm and the aggregation number, i.e., the number of surfactant molecules per micelle, ranges from 20 to 200. Israelachvili et al. [39] have proposed that surfactant molecular packing considerations are determinant in the formation of large surfactant aggregates. In particular, it is considered that the surfactant packing parameter θ ($\theta=\nu/\sigma l$, where ν is the surfactant molecular volume, σ is the area per polar head, and l is the length of hydrophobic part) gives a good idea of the shape of aggregates which will form spontaneously [39]. It is considered that normal or direct rod-like micelles are formed when $2<\theta<3$ [40]. Micelles can be both neutral (triton X-100) and ionic (sodium dodecyl sulfate, SDS (anionic) and hexadecyltrimethylammonium bromide, CTAB (cationic)). The structure of a typical micelle is schematically shown in Figure 2.5. The core of a micelle is essentially "dry" and consists of the hydrocarbon chains with the polar and charged head groups projecting outward toward the bulk water. The stern layer, surrounding the core, comprises of the ionic or polar head groups, bound counter ions and water molecules. Between the stern layer and the bulk water there is a diffused Guoy-Chapman (GC) layer, which contains the free counter ions and water molecules. In non-ionic polyoxyethylated surfactants e.g. triton X-100 (TX-100), the hydrocarbon core is surrounded by a palisade layer, which consists of the polyoxyethylene groups hydrogen-bonded to water molecules [41]. Small angle X-ray and neutron scattering have provided detailed information on the structure of the CTAB micelles [42, 43]. According to these studies, CMC and aggregation number of CTAB micelle are 0.8 mM and 52 respectively and the thickness of the stern layer is 6-9 Å [42-45]. The overall radius of CTAB micelle is about 50 Å. For TX-100 micelle, the CMC, thickness of the palisade layer and overall radius of the hydrophobic core are reported to be 0.1 mM, 51 Å and 25-27 Å, respectively and that of SDS micelles are 8.6 mM [46], 33 Å [47] and 5 Å, respectively [48].

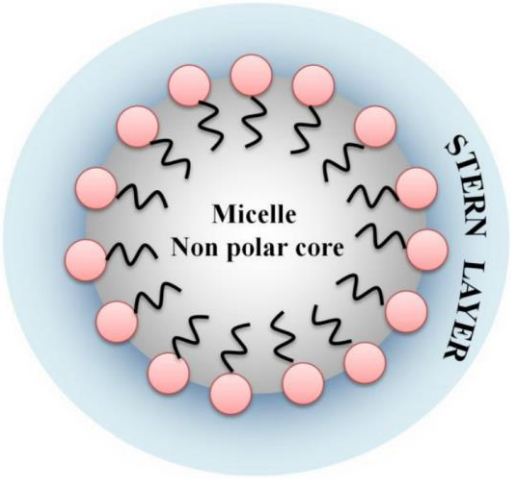

***Figure* 2.5.** *Schematic representation of the structure of a micelle.*

2.2.1.7. Dichlorofluorescein (DCFH):

Dichlorofluorescin (DCFH) is a probe (Figure 2.6.) that is trapped within cells and is easily oxidized to fluorescent dichlorofluorescein (DCF) [49]. Dichlorofluorescin (DCFH) is non-fluorescent and converts to fluorescent DCF upon oxidation through reacting with reactive oxygen species (ROS). This quantifies the amount of ROS as well as cellular oxidative stress.

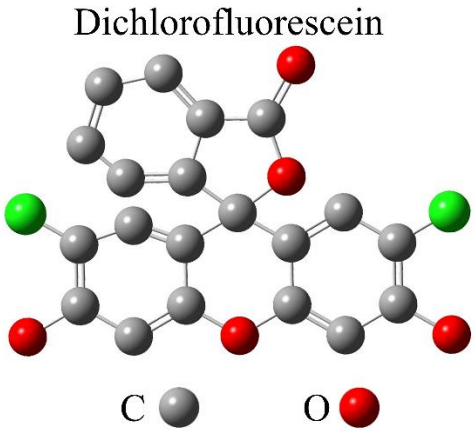

***Figure* 2.6:** *Chemical structure of dichlorofluorescein (DCFH).*

2.2.1.8. 2,2-Diphenyl-1-picrylhydrazyl (DPPH):

DPPH (Figure 2.7.) is a well-known radical and a trap ("scavenger") for other radicals. Therefore, the reduction rate of a chemical reaction upon the addition of DPPH is used as an indicator of the radical nature of that reaction [50].

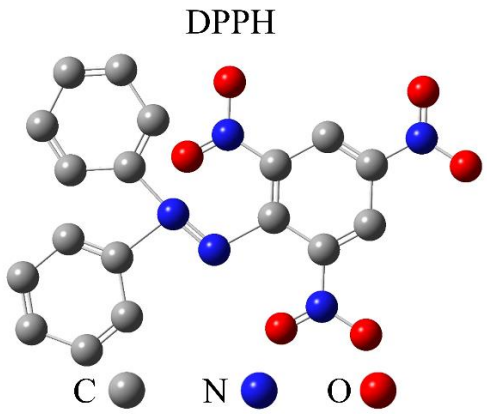

Figure 2.7. *The chemical structure of 2,2-Diphenyl-1-picrylhydrazyl (DPPH).*

Because of a strong absorption band centered at about 520 nm, the DPPH radical has a deep violet color in the solution, and it becomes colorless or pale yellow when neutralized. This property allows visual monitoring of the reaction, and the number of initial radicals can be counted from the change in the optical absorption at 520 nm.

2.2.1.9. 4',6-Diamidino-2-phenylindole (DAPI):

The dye DAPI (Figure 2.8.) is a commercially available fluorescent cytological stain for DNA [51]. Studies on the DAPI-DNA complexes show that the probe exhibits a wide variety of interactions of different strength and specificity with DNA [52]. The dye exhibits intramolecular proton transfer as an important mode of excited state relaxation at physiological pH [53], which takes place from the amidino to the indole moiety.

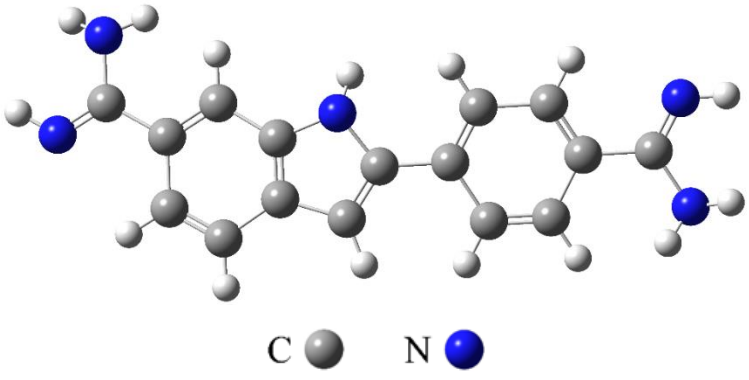

Figure 2.8. *Chemical structure of the molecule DAPI.*

REFERENCES

[1] M. Bhatt, K.R. Ayyalasomayajula, P.K. Yalavarthy, Generalized Beer–Lambert model for near-infrared light propagation in thick biological tissues, *Journal of Biomedical Optics*, 21 (2016) 076012.

[2] G. Wypych, Handbook of material weathering, *Elsevier*, Edinburgh, 2018.

[3] T.S. Yeh, S.S. Tseng, A low cost LED based spectrometer, *Journal of the Chinese Chemical Society*, 53 (2006) 1067.

[4] Y.-C. Chang, J.F. Reid, RGB calibration for color image analysis in machine vision, *IEEE Transactions on Image Processing*, 5 (1996) 1414.

[5] L. Goddijn, M. White, Using a digital camera for water quality measurements in Galway Bay, *Estuarine, Coastal and Shelf Science*, 66 (2006) 429.

[6] A. Moy, J. Tunnell, Diffuse Reflectance Spectroscopy and Imaging, *Imaging in Dermatology*, *Elsevier*, Edinburgh, 2016.

[7] V.V. Tuchin, Light scattering study of tissues, *Physics-Uspekhi*, 40 (1997) 495.

[8] L.R. Bissonnette, P. Bruscaglioni, A. Ismaelli, G. Zaccanti, A. Cohen, Y. Benayahu, *et al.*, LIDAR multiple scattering from clouds, *Applied Physics B*, 60 (1995) 355.

[9] B. van Ginneken, M. Stavridi, J.J. Koenderink, Diffuse and specular reflectance from rough surfaces, *Applied Optics*, 37 (1998) 130.

[10] I. Georgakoudi, B.C. Jacobson, J. Van Dam, V. Backman, M.B. Wallace, M.G. Müller, *et al.*, Fluorescence, reflectance, and light-scattering spectroscopy for evaluating dysplasia in patients with Barrett's esophagus, *Gastroenterology*, 120 (2001) 1620.

[11] W.E. Vargas, G.A. Niklasson, Applicability conditions of the Kubelka–Munk theory, *Applied Optics*, 36 (1997) 5580.

[12] R. López, R. Gómez, Band-gap energy estimation from diffuse reflectance measurements on sol–gel and commercial TiO 2: a comparative study, *Journal of Sol-gel Science and Technology*, 61 (2012) 1.

[13] L. Yang, B. Kruse, Revised Kubelka–Munk theory. I. Theory and application, *Journal of the Optical Society of America A*, 21 (2004) 1933.

[14] P.T. So, C.Y. Dong, Fluorescence spectrophotometry, *Encyclopedia of Life Sciences*, *Wiley,* New Jersey, 2001.

[15] T. Förster, Intramolecular energy migration and fluorescence, *Annals of Physics.*, 2 (1948) 55.

[16] L. Stryer, Fluorescence energy transfer as a spectroscopic ruler, *Annual Review of Biochemistry*, 47 (1978) 819.

[17] J.R. Lakowicz, Principles of fluorescence spectroscopy, 3rd ed., *Springer*, New York, 2006.

[18] P. Majumder, R. Sarkar, A.K. Shaw, A. Chakraborty, S.K. Pal, Ultrafast dynamics in a nanocage of enzymes: Solvation and fluorescence resonance energy transfer in reverse micelles, *Journal of Colloid and Interface Science*, 290 (2005) 462.

[19] S. Batabyal, T. Mondol, S.K. Pal, Picosecond-resolved solvent reorganization and energy transfer in biological and model cavities, *Biochimie*, 95 (2013) 1135.

[20] A. Rodger, B. Nordén, Circular dichroism and linear dichroism, *Oxford University Press*, USA, 1997.

[21] S. Banerjee, M. Tachiya, S.K. Pal, Caffeine-mediated detachment of mutagenic ethidium from various nanoscopic micelles: An ultrafast förster resonance energy transfer study, *The Journal of Physical Chemistry B*, 116 (2012) 7841.

[22] S. Banerjee, N. Goswami, S.K. Pal, A potential carcinogenic pyrene derivative under förster resonance energy transfer to various energy acceptors in nanoscopic environments, *ChemPhysChem*, 14 (2013) 3581.

[23] M. Tachiya, Application of a generating function to reaction kinetics in micelles. Kinetics of quenching of luminescent probes in micelles, *Chemical Physics Letters*, 33 (1975) 289.

[24] S. Sadhu, M. Tachiya, A. Patra, A stochastic model for energy transfer from CdS quantum dots/rods (donors) to nile red dye (acceptors), *The Journal of Physical Chemistry C*, 113 (2009) 19488.

[25] M.H. Gehlen, M. Van der Auweraer, F. De Schryver, Fluorescence quenching in micellar microdomains: Analysis of an approximate solution to the fluorescence decay including exchange of probe and quencher, *Langmuir*, 8 (1992) 64.

[26] A. Leung, P.M. Shankar, R. Mutharasan, A review of fiber-optic biosensors, *Sensors and Actuators B-Chemical*, 125 (2007) 688.

[27] D.J. Griffiths, Introduction to electrodynamics, *Prentice Hall*, India, 1999.

[28] J.D. Jackson, Classical electrodynamics, *Wiley*, New Jersey, 1975.
[29] H. Langhals, Color chemistry. synthesis, properties and applications of organic dyes and pigments, By Heinrich Zollinger, *Wiley Online Library*, New Jersey, 2004.
[30] G. Revillod, I. Russier-Antoine, E. Benichou, C. Jonin, P.-F. Brevet, Investigating the interaction of crystal violet probe molecules on sodium dodecyl sulfate micelles with hyper-Rayleigh scattering, *The Journal of Physical Chemistry B*, 109 (2005) 5383.
[31] S.C. Beck, D.T. Cramb, Condensed phase dispersive interactions of benzo[a]pyrene with various solvents and with DNA: A twist on solvatochromism, *The Journal of Physical Chemistry B*, 104 (2000) 2767.
[32] R.K. Gill, R.K. Rawal, J. Bariwal, Recent advances in the chemistry and biology of benzothiazoles, *Archiv der Pharmazie*, 348 (2015) 155.
[33] S. Maddila, S. Gorle, N. Seshadri, P. Lavanya, S.B. Jonnalagadda, Synthesis, antibacterial and antifungal activity of novel benzothiazole pyrimidine derivatives, *Arabian Journal of Chemistry*, 9 (2016) 681.
[34] S. Salvamani, B. Gunasekaran, N.A. Shaharuddin, S.A. Ahmad, M.Y. Shukor, Antiartherosclerotic effects of plant flavonoids, *BioMed Research International*, 2014.
[35] B. Sultana, F. Anwar, Flavonols (kaempeferol, quercetin, myricetin) contents of selected fruits, vegetables and medicinal plants, *Food Chemistry*, 108 (2008) 879.
[36] C. Fischer, V. Speth, S. Fleig-Eberenz, G. Neuhaus, Induction of zygotic polyembryos in wheat: influence of auxin polar transport, *The Plant Cell*, 9 (1997) 1767.
[37] D. Mitchison, The Garrod Lecture: Understanding the chemotherapy of tuberculosis-current problems, *Journal of Antimicrobial Chemotherapy*, 29 (1992) 477.
[38] W. Wehrli, F. Knüsel, K. Schmid, M. Staehelin, Interaction of rifamycin with bacterial RNA polymerase, *Proceedings of the National Academy of Sciences*, 61 (1968) 667.
[39] J.N. Israelachvili, D.J. Mitchell, B.W. Ninham, Theory of self-assembly of hydrocarbon amphiphiles into micelles and bilayers, *Journal of the Chemical Society, Faraday Transactions 2: Molecular and Chemical Physics*, 72 (1976) 1525.
[40] D.J. Mitchell, B.W. Ninham, Micelles, vesicles and microemulsions, *Journal of the Chemical Society, Faraday Transactions 2: Molecular and Chemical Physics*, 77 (1981) 601.
[41] H.H. Paradies, Shape and size of a nonionic surfactant micelle. Triton X-100 in aqueous solution, *The Journal of Physical Chemistry*, 84 (1980) 599.

[42] S. Berr, Solvent isotope effects on alkytrimethylammonium bromide micelles as a function of alkyl chain length, *Journal of Physical Chemistry*, 91 (1987) 4760.

[43] S.S. Berr, E. Caponetti, J.S. Johnson Jr, R.R. Jones, L.J. Magid, Small-angle neutron scattering from hexadecyltrimethylammonium bromide micelles in aqueous solutions, *The Journal of Physical Chemistry*, 90 (1986) 5766.

[44] X. Lei, G. Zhao, Y. Liu, N.J. Turro, Influence of binding strength of added electrolytes on the properties of micelles and of micellized radical pairs, *Langmuir*, 8 (1992) 475.

[45] H. Tavernier, F. Laine, M. Fayer, Photoinduced intermolecular electron transfer in micelles: dielectric and structural properties of micelle headgroup regions, *The Journal of Physical Chemistry A*, 105 (2001) 8944.

[46] N.J. Turro, X.-G. Lei, K. Ananthapadmanabhan, M. Aronson, Spectroscopic probe analysis of protein-surfactant interactions: the BSA/SDS system, *Langmuir*, 11 (1995) 2525.

[47] P. Hassan, S.R. Raghavan, E.W. Kaler, Microstructural changes in SDS micelles induced by hydrotropic salt, *Langmuir*, 18 (2002) 2543.

[48] A.K. Shaw, S.K. Pal, Activity of subtilisin Carlsberg in macromolecular crowding, *Journal of Photochemistry and Photobiology B: Biology*, 86 (2007) 199.

[49] S. Sardar, S. Chaudhuri, P. Kar, S. Sarkar, P. Lemmens, S.K. Pal, Direct observation of key photoinduced dynamics in a potential nano-delivery vehicle of cancer drugs, *Physical Chemistry Chemical Physics*, 17 (2015) 166.

[50] M. Szabo, D. Radu, S. Gavrilas, D. Chambre, C. Iditoiu, Antioxidant and antimicrobial properties of selected spice extracts, *International Journal of Food Properties*, 13 (2010) 535.

[51] J. Kapuscinski, DAPI: A DNA-specific fluorescent probe, *Biotechnic & Histochemistry*, 70 (1995) 220.

[52] W.D. Wilson, F.A. Tanious, H.J. Barton, R.L. Jones, K. Fox, R.L. Wydra, *et al.*, DNA sequence dependent binding modes of 4', 6-diamidino-2-phenylindole (DAPI), *Biochemistry*, 29 (1990) 8452.

[53] M. Barcellona, E. Gratton, A molecular approach to 4′, 6-diamidine-2-phenylindole (DAPI) photophysical behaviour at different pH values, *Biophysical chemistry*, 40 (1991) 223.

CHAPTER 3

Instrumentation and Sample Preparation

This chapter focusses on the instrumental setup and sample preparation techniques used in the thesis work in comprehensive details. The testing, calibration and validation of various biological, food and environmental samples were performed using developed instruments which were designed at certain times particularly for the development. However, calibration and validation were performed using conventional equipment available in various laboratories. The details of the sample preparation mechanism and sensor development have also been discussed in this chapter.

3.1. INSTRUMENTAL SET-UP:

3.1.1. Steady-state UV-Vis Absorption and Fluorescence Spectroscopy:

Steady-state UV-Vis absorption and emission spectra of samples were recorded using Shimadzu Model UV-2600 spectrophotometer (Shimadzu Corporation, Kyoto,

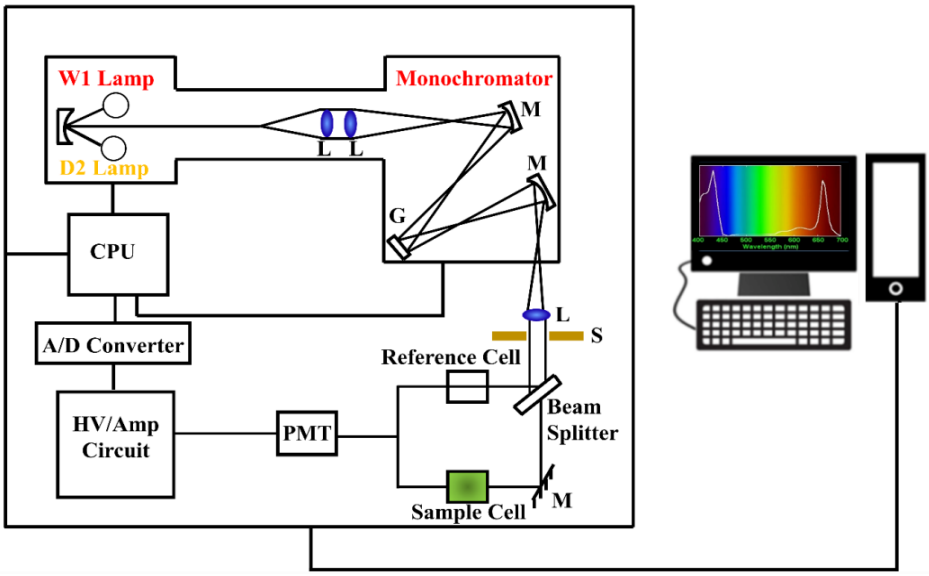

Figure 3.1. *Schematic ray diagram of an absorption spectrophotometer. Tungsten halogen (W1) and deuterium lamps (D2) are used as light sources in the visible and UV regions, respectively. M, G, L, S, PMT designate mirror, grating, lens, shutter and photomultiplier tube, respectively. CPU, A/D converter and HV/amp indicate central processing unit, analog to digital converter and high-voltage/amplifier circuit, respectively.*

Japan) and Jobin Yvon Fluoromax-3® spectrofluorometer (Horiba, Kyoto, Japan), respectively. Schematic ray diagrams of these two instruments are shown in Figures 3.1 and 3.2.

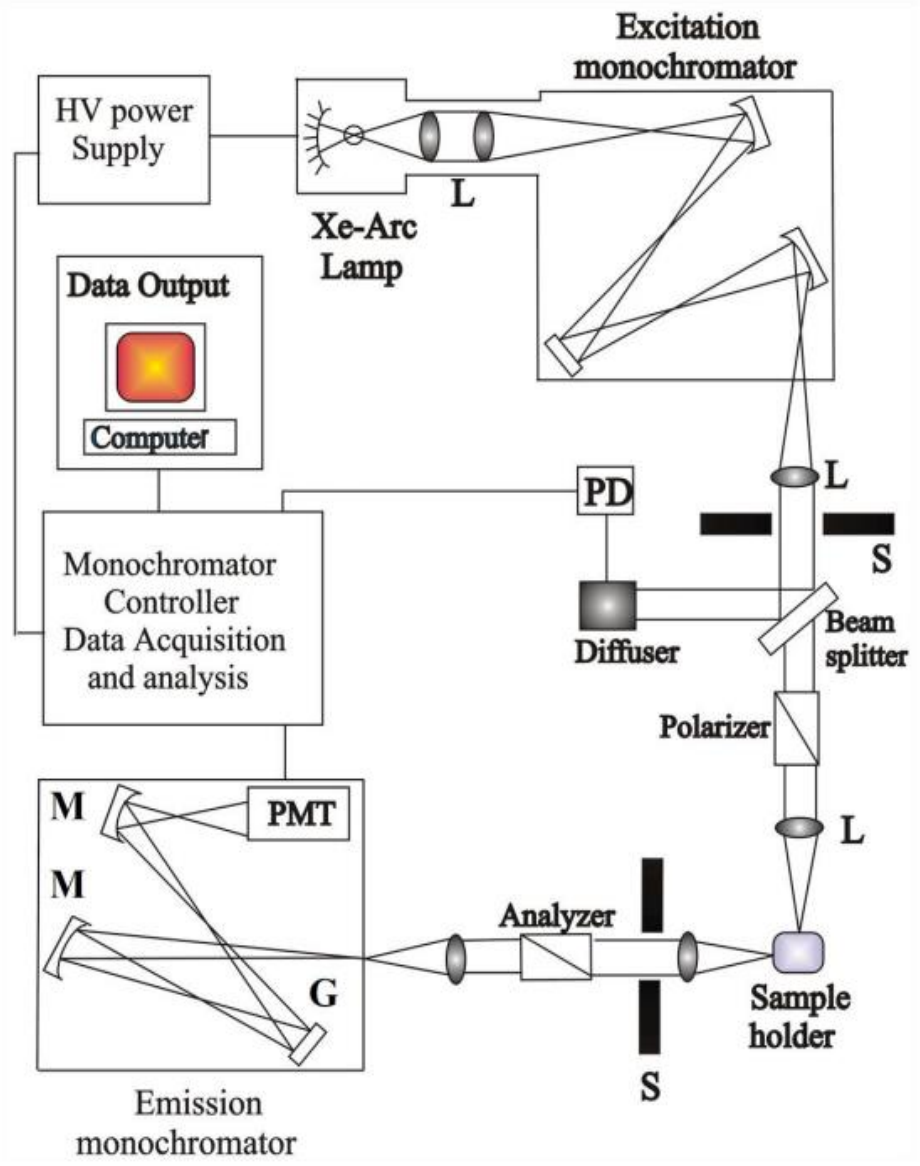

Figure 3.2. *Schematic ray diagram of an emission spectrofluorometer. M, G, L, S, PMT and PD represent mirror, grating, lens, shutter, and photomultiplier tube and reference photodiode, respectively.*

3.1.2. Dynamic Light Scattering (DLS):

Dynamic light scattering (DLS), also known as photon correlation spectroscopy (PCS) or quasi-elastic light scattering (QELS), is one of the most popular techniques used to determine the hydrodynamic size of the particles.

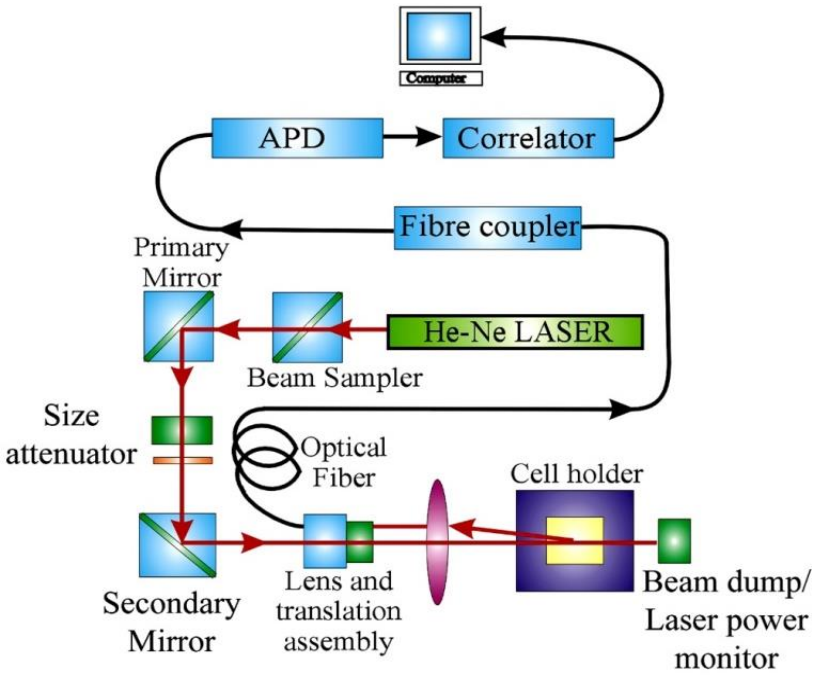

Figure 3.3. *Schematic ray diagram of dynamic light scattering (DLS) instrument. The avalanche photodiode (APD) is connected to the preamplifier/amplifier assembly and finally to the correlator. It has to be noted that lens and translational assembly, laser power monitor, size attenuator and laser are controlled by the computer.*

DLS measurements were performed on a Zetasizer Nano S from Malvern Panalytical, United Kingdom, employing a 4 mW He-Ne laser (λ= 632.8 nm) and equipped with a thermostatic sample chamber. The Zetasizer Nano S provides the highest sensitivity for size diameter measurement ranging from 0.3nm to 10 microns. The instrument allows DLS measurements in which all the scattered photons are collected at 173° scattering angle. The instrument measures the time-dependent fluctuation in intensity of light scattered from the particles in solution at a fixed scattering angle. The ray diagram of the DLS setup is shown in Figure 3.3. It has been seen that particles in dispersion are in a random Brownian motion and this causes the intensity of scattered light to fluctuate as a function of time. The correlator used in a DLS instrument constructs the intensity autocorrelation function G(τ) of the scattered intensity,

$$G(\tau) = \langle I(t)I(t+\tau)\rangle \tag{3.1}$$

where τ is the time difference (the sample time) of the correlator. For a large number of monodisperse particles in Brownian motion, the correlation function (given the symbol G) is an exponential decay function of the correlator time delay τ,

$$G(\tau) = A[1 + B\ exp(-2\Gamma\tau)] \quad (3.2)$$

where A is the baseline of the correlation function, and B is the intercept of the correlation function. Γ is the first cumulant which is related to the translational diffusion coefficient as, $\Gamma = Dq^2$, where q is the scattering vector and its magnitude is defined as,

$$q = \left(\frac{4\pi n}{\lambda_0} sin\left(\frac{\theta}{2}\right)\right) \quad (3.3)$$

where n is the refractive index of dispersion, λ_0 is the wavelength of the laser, and θ is the scattering angle. For polydisperse samples, the equation can be written as,

$$G(\tau) = A\left[1 + B\left|g^{(1)}(\tau)\right|^2\right] \quad (3.4)$$

where the correlation function $g^{(1)}(\tau)$ is no longer a single exponential decay and can be written as the Laplace transform of a continuous distribution G(Γ) of decay times,

$$g^{(1)}(\tau) = \int_0^\infty G(\Gamma)\, exp(-\Gamma\tau)\, d\Gamma \quad (3.5)$$

The scattering intensity data in DLS are processed using instrumental software to obtain the hydrodynamic diameter (d_H) and the size distribution of the scatterer in each sample. In a typical size distribution graph from the DLS measurement, *X*-axis shows a distribution of size classes in nm, while the *Y*-axis shows the relative intensity of the scattered light. The diffusion coefficient (D) can be calculated using the d_H of the particle from the Stoke-Einstein relation,

$$D = \frac{k_B T}{3\pi\eta d_H} \quad (3.6)$$

where k_B, T, d_H, η are Boltzmann constant, the temperature in Kelvin, hydrodynamic diameter and viscosity, respectively.

3.1.3. X-ray Diffraction (XRD) Measurement:

XRD is a popular and powerful technique for determining the crystal structure of crystalline materials. By examining the diffraction pattern, one can identify the crystalline phase of the material. Small-angle scattering is useful for evaluating the average interparticle distance while wide-angle diffraction is useful for refining the

atomic structure of nanoclusters. The widths of the diffraction lines are closely related to strain and defect size and distribution in nanocrystals. As the size of the nanocrystals decreases, the line width is broadened due to the loss of long-range order relative to the bulk. This XRD line widths can be used to estimate the size of the particle by using the Debye-Scherrer formula 3.7. XRD measurements were performed on a PANalytical XPERT-PRO diffractometer (Figure 3.4) equipped with CuK_{α} radiation (λ = 1.5418 Å at 40 mA, 40 kV). XRD patterns were obtained by employing a scanning rate of 0.02° s^{-1} in the 2θ range from 10° to 80°.

$$D = \frac{0.9\lambda}{\beta \cos\theta} \tag{3.7}$$

where, D is the nanocrystal diameter, λ is the wavelength of light, β is the full-width half-maximum (FWHM) of the peak in radians, and θ is the Bragg angle.

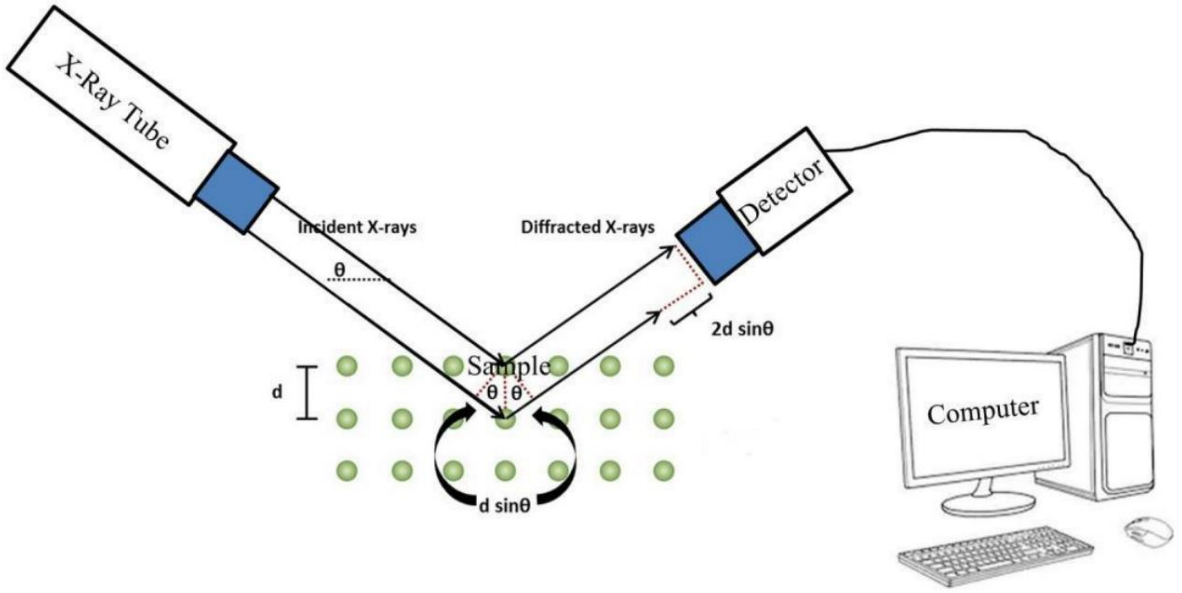

Figure 3.4: *Schematic diagram of an X-ray diffraction (XRD) instrument. By varying the angle θ, the Bragg's law conditions, 2dsinθ = nλ are satisfied by different d-spacings in polycrystalline materials. Plotting the angular positions and intensities of the resultant diffracted peaks of radiation produces a pattern, which is characteristic of the sample.*

3.1.4. Fourier Transform Infrared (FTIR) Spectroscopy:

FTIR spectroscopy is a technique that can provide very useful information about functional groups in a sample. An infrared spectrum represents the fingerprint of a sample with absorption peaks which correspond to the frequencies of vibrations between the bonds of the atoms making up the material. Because each different

material is a unique combination of atoms, no two compounds produce the same infrared spectrum. Therefore, infrared spectroscopy can result in an identification (qualitative analysis) of different kinds of material. Also, the size of the peaks in the spectrum is a direct indication of the amount of material present.

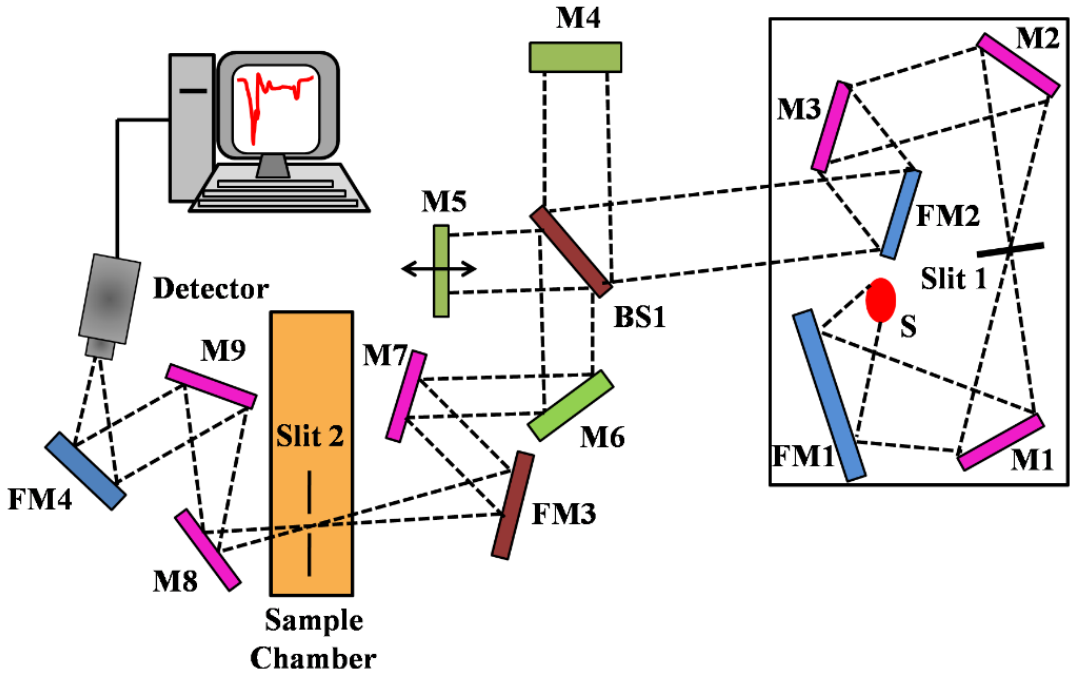

Figure 3.5: *Schematic representation of fourier transform infrared (FTIR) spectrometer. It is a Michelson interferometer in which one of the two fully-reflecting mirrors is movable, allowing a variable delay (in the travel time of the light) to be included in one of the beams. M, FM, and BS1 represent the mirror, focusing mirror and beam splitter, respectively. M5 is a moving mirror.*

The two-beam Michelson interferometer is at the heart of the FTIR spectrometer. It consists of a fixed mirror (M4), a moving mirror (M5), and a beam-splitter (BS1), as illustrated in Figure 3.5. The beam-splitter is a laminate material that reflects and transmits light equally. The collimated IR beam from the source is partially transmitted to the moving mirrors and partially reflected in the fixed mirror by the beam-splitter. The two IR beams are then reflected in the beam-splitter by the mirrors. The detector then detects the transmitted beam from the fixed mirror and the reflected beam from the moving mirror, simultaneously. The two combined beams interfere constructively or destructively depending on the wavelength of the light (or frequency in wavenumbers) and the optical path difference introduced by the moving mirror. The resulting signal is called an interferogram which has the unique property that each data point (a function of the moving mirror position) which makes up the signal

that has information about every infrared frequency which comes from the source. Because the analyst requires a frequency spectrum (a plot of the intensity at each frequency) to make an identification, the measured interferogram signal cannot be interpreted directly.

A means of "decoding" the individual frequencies is required, which can be accomplished *via* a well-known mathematical technique called the Fourier transformation. This transformation is performed by the computer which then presents the user with the desired spectral information for analysis. FTIR measurements were performed on a JASCO FTIR-6300 spectrometer (transmission mode). For the FTIR measurements, powdered samples were mixed with KBr powder and pelletized. The background correction was made using a reference blank KBr pellet. Sometime Fourier transform infrared spectroscopy (FTIR) of the powder samples are also performed with the attenuated total reflectance (ATR) method using a Vertex 70 V instrument (Bruker, Germany). Each spectrum consists of 100 scans (0−4000 cm^{-1}) acquired at 0.5 cm^{-1} resolution.

3.1.5. Transmission Electron Microscope (TEM):

A FEI TecnaiTF-20 field-emission high-resolution TEM (Figure 3.6) equipped with an

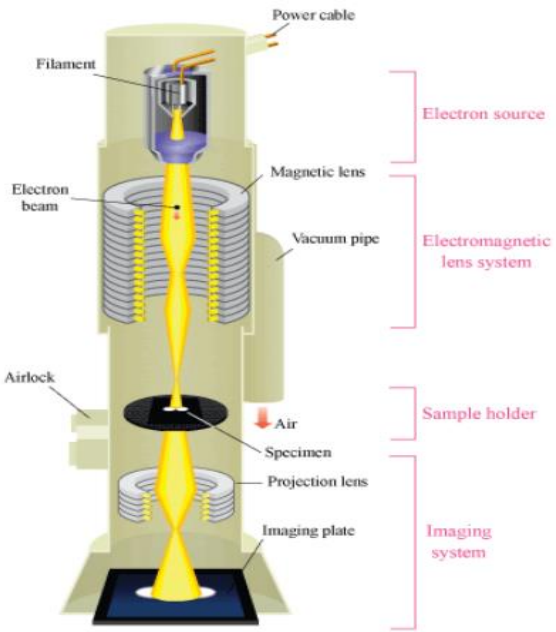

Figure 3.6. *Schematic diagram of a typical transmission electron microscope (TEM). After the transmission of electron beam through a specimen, the magnified image is formed either in the fluorescent screen or can be detected by a CCD camera.*

energy dispersive X-ray (EDAX) spectrometer was used to characterize the microscopic structures of samples and to analyze their elemental composition. The sizes of the nanoparticles were determined from the TEM images obtained at 200 kV acceleration voltage of the microscope. Samples for TEM were prepared by placing a drop of the nanoparticle solution on a 300-mesh carbon-coated copper grid and allowing the film to evaporate overnight at room-temperature.

3.1.6. Scanning Electron Microscope (SEM):

Characterization of mice red blood corpuscles (RBC) after treatment with nanoparticles were performed by field emission scanning electron microscopy (FESEM, QuantaTM 250 FEG, FEI Company, Oregon, USA). An electron-gun is attached to SEM and the electrons from filament triggered by 0 KV to 30 KV voltages. These electrons go first through a condenser lens and then through an objective lens, then through an aperture and finally reach to the specimen. The high energy electrons go a bit in the sample and back again give secondary electrons. The signal from secondary electrons are detected by detector and amplified. The ray diagram of the SEM setup is shown in Figure 3.7.

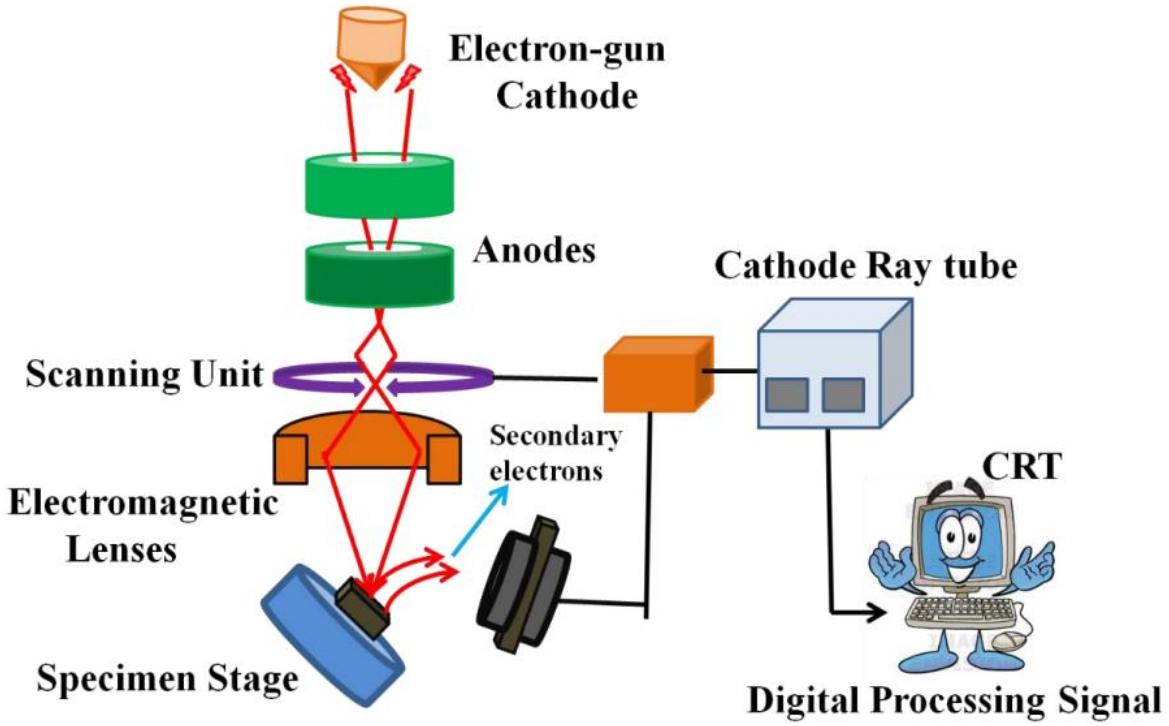

Figure 3.7. *Schematic diagram of typical scanning electron microscope (SEM).*

3.1.7. Fluorescence Microscope:

Commercially available fluorescence microscope (BX-51, Olympus America, Inc.) was used in our study. The light source is usually a mercury-vapor lamp. For bright field, Tungsten-halogen lamp was used. In particular, an inverted setup with a mercury-vapor lamp as light source is shown. The dichroic mirror, excitation and emission filter are joined together within the filter cube (Figure 3.8). Since mercury-vapor lamps emit light over the whole optical spectrum as well as in the ultraviolet range, an optical excitation filter is used to isolate one specific wavelength. Due to the Stokes shift, it is possible to separate excitation and emission light in the same light path optically via a dichroic mirror. This way, only the emission light is collected by the objective. An emission filter helps to suppress unwanted background light.

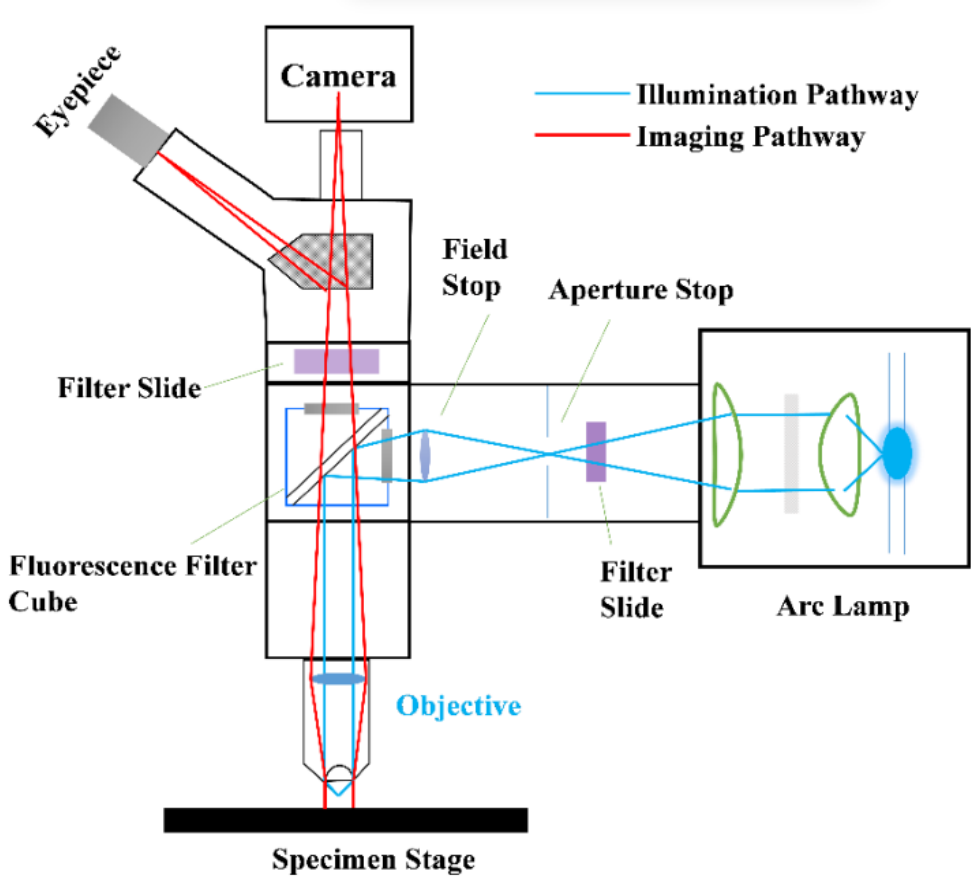

Figure 3.8. *Schematic presentation of the fluorescence microscope.*

3.1.8. Time-correlated Single Photon Counting (TCSPC) Technique:

Time-correlated single photon counting (TCSPC) is a powerful technique used to measure the arrival times of individual photons with high precision. It enables the

investigation of fluorescence lifetimes, fluorescence decay kinetics, and photon emission dynamics. TCSPC is widely employed in fields such as biophysics, chemistry, and materials science for studying dynamic processes at the molecular level. The principle behind TCSPC involves the measurement of the time interval between the excitation of a sample and the detection of a single photon emitted from the sample. It relies on the use of ultrafast detectors and timing electronics to achieve accurate time resolution in the picosecond or even sub-picosecond range. A pulsed laser is used as the excitation source. It generates short-duration pulses of light to excite the sample. The sample under investigation contains fluorescent molecules or materials that emit photons upon excitation. These fluorophores may have different fluorescence lifetimes or decay characteristics. A single-photon detector, such as a photomultiplier tube (PMT) or an avalanche photodiode (APD), is used to detect the emitted photons. These detectors can measure the arrival time of individual photons with high sensitivity. The timing electronics provide precise timing signals to measure the time intervals between the excitation pulse and the detected photon. They include a time-to-amplitude converter (TAC), a time-to-digital converter (TDC), and a clock source. The TAC converts the time interval into an analog voltage, while the TDC converts it into a digital time value. The data acquisition system collects the time-stamped detection events from the TDC and stores them for further analysis. It records the arrival times of the photons and constructs a fluorescence decay curve or histogram. All the picosecond-resolved fluorescence decays were collected using the TCSPC technique. The schematic block diagram of a TCSPC system is shown in Figure 3.9.

A commercial TCSPC setup from Edinburgh instruments (U.K.) was used during fluorescence decay acquisitions. The instrument response functions (IRFs) of the laser sources at different excitation wavelengths varied between 70 ps to 90 ps. The fluorescence from the sample was detected by a photomultiplier after dispersion through a grating monochromator [1]. For all excited state lifetime measurement experiments, the polarizer in the emission side was adjusted to be at 54.7° (magic angle) to the polarization axis of the excitation beam.

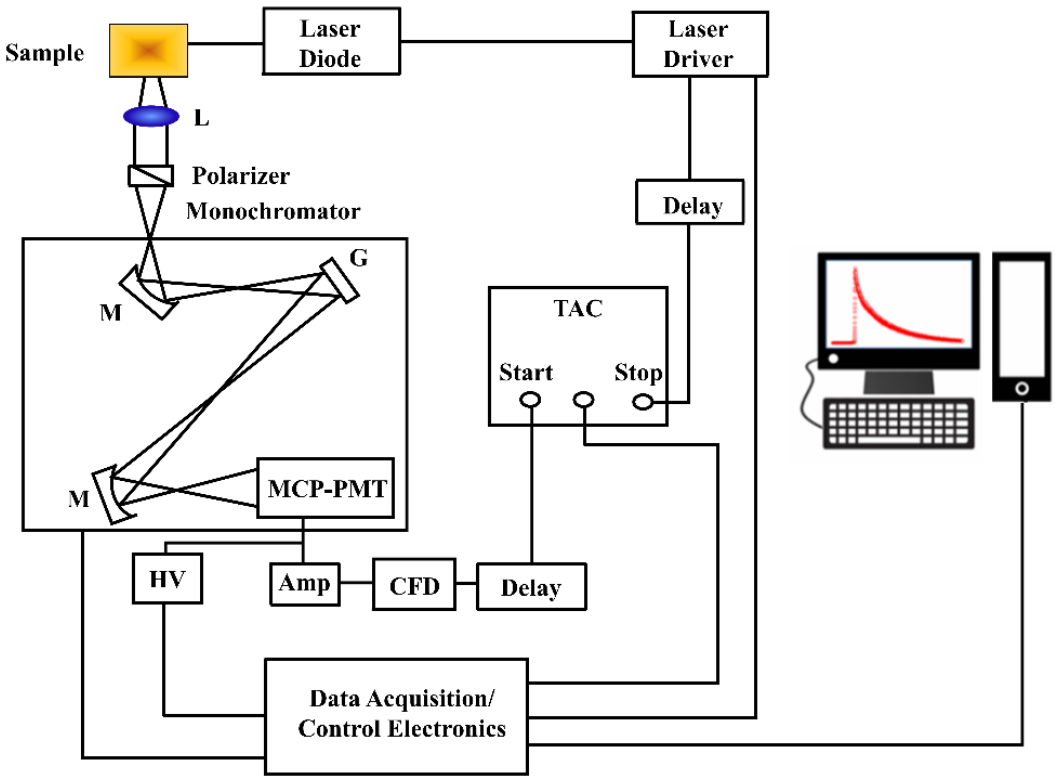

Figure 3.9: *Schematic ray diagram of time-correlated single photon counting (TCSPC). A signal from a microchannel plate photomultiplier tube (MCP-PMT) is amplified (Amp) and connected to the start channel of time to amplitude converter (TAC) via constant fraction discriminator (CFD) and delay. The stop channel of the TAC is connected to the laser driver via a delay line. L, M, G and HV represent lens, mirror, grating and a high voltage source, respectively.*

3.1.9. Nuclear Magnetic Resonance (NMR) Spectroscopy:

NMR spectra were recorded by using a Bruker AX 500 spectrometer (500 MHz) NMR spectroscope.

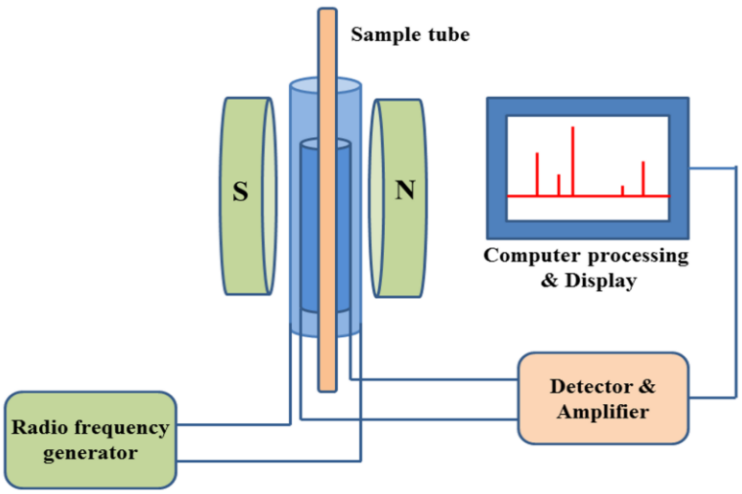

Figure 3.10. *Schematic diagram of a Nuclear Magnetic Resonance (NMR) spectrometer is shown.*

NMR spectroscopy is a powerful tool to study the chemical bonding of a molecule. The basic arrangement of an NMR spectrometer is displayed in Figure 3.10. A sample (in a small glass tube) is placed between the poles of a strong magnetic. A radio frequency generator pulses the sample and excites the nuclei causing a spin flip. The spin flip is detected by the detector and the signal sent to a computer where it is processed.

3.1.10. Light Sources and Optical Components:

Light sources are the most important component for the development of an optical device. In the present work, light-emitting diodes (LED) of different wavelengths and LASER sources have been used. For the studies on development of a non-invasive estimation of hemoglobin, and bilirubin of neonates simultaneously using whole optical spectrum analysis at point of care [2] we have used a white light source (3 W,400-700nm, 700LUX, 4.78 mW optical power). Whereas, for the projects on water and food quality assessment [3], in addition to the previous light source, an additional 375 nm 3W UV LED was used. All the optical parts used in our studies including optical fiber, collimator, fiber couplers etc. are from Ocean Optics. Whereas, the basic components like front surface reflecting mirrors, dichroic mirrors, parabolic mirrors and optical stands are from Thorlabs. A lab grade 6:1 diffuse reflectance fiber optic probe manufactured by Ocean Optics, Florida was used to transmit the light from source to subject nail by the 6 peripheral excitation fibers of the probe and receive the response signal by the central collection fiber by holding the probe tip at perpendicular position with the nail.

For the development of a non-invasive and non-contact device used in detection of neonatal jaundice and anemia, STS-VIS Spectrometers (Figure 3.11) from Ocean Optics, USA was used with wavelength resolution of 0.47 nm. For multiplexed monitoring of water quality and spectroscopic investigation of the origin and quality of tea extracts for the development of a portable and field deployable prototype, a microspectrometer (Model: C12880MA) manufactured by Hamamatsu, Japan has

been used and the results have been validated with conventional spectrophotometer discussed in section 3.1.1.

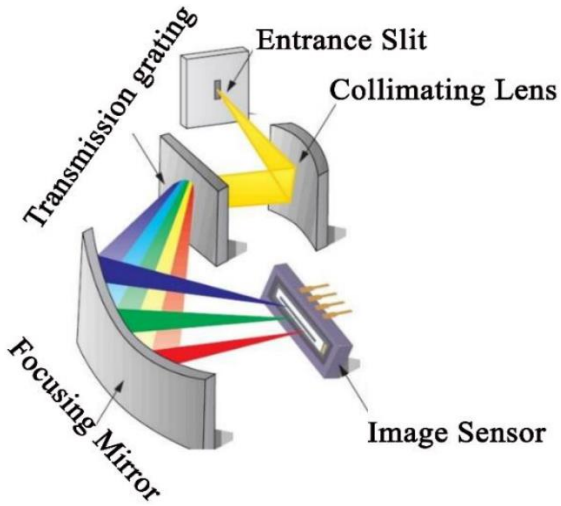

Figure 3.11: *Basic internal ray diagram of CCD array detector-based STS-VIS spectrographs.*

3.1.11. Calculation of Accuracy, Limit of Detection (LOD) and Limit of Quantification (LOQ) of the Device:

The accuracy of a developed device for this thesis work is defined by the following equation (3.8),

$$\text{Accuracy} = 100\% - \text{Error Rate} \tag{3.8}$$

Where, Error Rate = (|Observed Value - Actual Value|/Actual Value × 100).

The formulae used for the calculations of Limit of Detection (LOD), Limit of Quantification (LOQ) [4] in this study are as follows:

$$\text{LOD} = (3.3 \text{ X S.D.}/S) \tag{3.9}$$

$$\text{LOQ} = (10 \text{ X S.D.}/S) \tag{3.10}$$

Where 'S.D' and 'S' are standard deviation and slope of calibration curve respectively.

3.1.12. Bacterial Strain and Culture Conditions:

The antibacterial action of the nano-formulation using colocalized rifampicin and benzothiazole in CTAB micelles has been studied against a strain of MRSA bacteria. Methicillin-resistant Staphylococcus aureus (MRSA) strain (ATCC 25923) was procured from ATCC. For antibacterial assay, fresh MRSA bacteria have been cultured using Luria–Bertani (LB) medium in a shaker incubator at a temperature of 37 °C for 24 hrs. The freshly grown MRSA culture was further diluted 10^6 times and

samples were added. The treatment of bacteria was performed on LB agar plates by the colony-forming unit (CFU) assays method under dark condition. The cells were incubated with 1 mM of CTAB, RF (80 μM), BT (80 μM), RF-BT in 1 mM CTAB (The concentration of BT and RF is 80 μM), RF (80 μM) in 1 mM of CTAB and BT (80 μM) in 1 mM of CTAB separately for 3 h without any photo-activation. Then the cultures were uniformly spread on LB agar plates and the plates were incubated at 37°C for 24 h to get the CFUs. To quantify the antibacterial activity, the CFU numbers were manually counted and presented as a bar diagram.

The antibacterial activity of the synthesized and extracted citrate functionalized CuO samples have been investigated against a strain of Staphylococcus hominis bacteria. The gram-positive *S. hominis* strain was procured from ATCC. For antibacterial assay, fresh *S. hominis* bacteria have been cultured using sterilized Luria–Bertani (LB) medium in a shaker incubator at a temperature of 37 °C for 24 hrs. All used glass wares, suction nozzle and culture medium were sterilized in an autoclave at a high pressure of 0.1 MPa and a temperature of 120°C for 30 minutes prior to experiments. The treatment of bacteria was performed on LB agar plates by the colony-forming unit (CFU) assay method under dark and light illumination conditions. The freshly grown original *S. hominis* bacterial suspension was firstly washed twice with phosphate-buffered saline (PBS; pH 7.4) solution. and further diluted 10^6 times and test samples were added. Then, they were incubated with respective nanoparticles for 1 hour. The resulting bacterial PBS suspensions (200 μL) were uniformly spread over gelatinous LB agar plates, culturing at 37°C for 24 hours to obtain the CFUs. To quantify the antibacterial activity, the number of survival colonies was manually counted and presented as a bar diagram.

Detection of microbial growth was also performed in cuvette system for different citrate CuO NPs under various conditions. For this bacterial mortality study, bacterial solution of 10^8 CFU/ml was considered and incubated with test solutions of 1 mM concentration initially for 3 hrs with photo-activation. For the cuvette-based detection of microbial growth, the cells were cultured in a Luria Broth (LB) medium under an incubator shaker at 37°C for 24 h. The optical density of freshly grown overnight culture was fixed to 0.1 in LB medium initially. The culture was then put in

a cuvette, mixed with test samples and incubated at 37°C with shaking for 9 hours under dark and illumination condition. The absorbance is taken at every hour interval and plotted against time with baseline correction for studying the growth curves.
For microscopic studies, the bacteria cells after proper incubation with the nanoparticles were stained with DAPI and PI. The DAPI stains all cells while PI only stains the membrane disrupted cells. The (1-Red/Blue) ratio was obtained to assess the viability of *S. hominis*. The tests were repeated three times. The samples (15 µL) were observed under a fluorescence microscope (Leica digital inverted microscopes DMI8).

The antibacterial action of the synthesized actetate CuO samples has been studied against a strain of Methicillin-resistant Staphylococcus aureus (MRSA) bacteria. The MRSA strain (ATCC 25923) was procured from ATCC. For antibacterial assay, fresh MRSA bacteria have been cultured using Luria–Bertani (LB) medium in a shaker incubator at a temperature of 37 °C for 28 hrs. The freshly grown MRSA culture was further diluted 10^6 times and test samples were added. The treatment of bacteria was performed on LB agar plates by the colony-forming unit (CFU) assay method under dark and white light illumination conditions. The cells were incubated with 1 mM of acetate CuO NP solution for 3 hrs with photo-activation. Then the cultures were uniformly spread on LB agar plates and the plates were incubated at 37°C for 24 hrs to get the CFUs. To quantify the antibacterial activity, the CFU numbers were manually counted and presented as a bar diagram.

3.2. CHEMICALS USED:

The chemicals and spectroscopic probes for the thesis work were procured from the different sources as discussed below. Analytical-grade chemicals were used for synthesis without further purification. Deionized (DI) water of resistivity value ≥ 18 MΩ cm, from the Milli-Q system (Millipore GmbH, Germany), was used to prepare all aqueous solutions. Different solvents including Methanol, Ethanol, Acetonitrile (ACN) and Dimethyl sulfoxide (DMSO) were purchased from Sigma-Aldrich (St. Louis, MO, USA, California). 2-(2-Hydroxyphenyl) benzothiazole (BT), rifampicin (RF), Cetyltrimethylammonium bromide (CTAB), Ethanol, were purchased from

Sigma Aldrich, California. Luria broth (LB) and LB top agar medium for bacterial studies were bought from HIMEDIA. Copper acetate, citric acid, glacial acetic acid, sodium hydroxide and sodium citrate were also purchased from Sigma Aldrich (St. Louis, MO, USA), California. 2,7-dichlorodihydrofluorescein diacetate (DCFH-DA) was bought from Calbiochem to estimate the production of reactive oxygen species (ROS). 2,2-diphenyl-1-picrylhydrazyl (DPPH) was also obtained from Sigma (St. Louis, MO, USA) for monitoring antioxidant activity of samples. The Gram-positive bacteria Staphylococcus hominis (*S. hominis*) strain and Gram-negative bacteria Methicillin-resistant Staphylococcus aureus (MRSA) strain (ATCC 25923) were procured from ATCC. For the drinkability study Benzo[a]pyrene ($C_{20}H_{12}$), Crystal violet ($C_{25}N_3H_{30}C_l$) and Titanium di-Oxide (TiO_2) were purchased from Sigma-Aldrich. Salicylaldehyde, 2-aminothiophenol, iridium (III) chloride, benzo(h)quinolone, SDS(Sodium dodecyl sulfate) and Triton X-100 were purchased from TCI, Japan. The sodium arsenite was procured from Merck. Analytical thin-layer chromatography (TLC) was performed on glass-backed silica-coated plates (Merck TLC Silicagel 60 F254, 250 µm). Milk used in the DPPH assay was bought from Mother Dairy Kolkata and diluted with double distilled water before use. Sugars used were purchased from local super-markets of Kolkata, India. ZnO NPs (30 nm) was purchased from Sigma Aldrich. Malachite Green (MG), Copper Sulphate pentahydrate ($CuSO_4,5H_2O$) and Sudan Red (SR) were purchased from Sigma Aldrich, California and used with no further purification. All other chemicals were obtained from Merck (NJ, USA) unless otherwise stated.

3.3. SAMPLE PREPARATION & DATA COLLECTION:

In this section the different sample preparation and data collection methods have been discussed.

3.3.1. Synthesis of Functionalized CuO Nanoparticles:

3.3.1.1. Synthesis of Citrate Capped CuO:

In this study, the CuO NPs were synthesized following the reported procedure of precipitation method by Zhu et al. [5]. The citrate ligands generated in the process

provided satisfactory passivation against aggregation and sufficient stability to the NPs in colloidal suspension. Briefly, 150 ml of deionized water were used to dissolve 0.54 g of copper acetate. Next, 0.52g of citric acid was added, and the mixture was vigorously stirred while being heated to boiling at 100°C. Once the mixture's pH attained the value 6-7, 0.7 gm or 0.015 mol of sodium hydroxide (NaOH) was added quickly, causing a significant amount of dark brown precipitate to form at the same time. The blue colour solution was converted to brown right away, indicating the production of CuO NPs. The liquid was cooled to room temperature while being stirred after 5 additional minutes of reflux. The CuO-NPs were subsequently separated by centrifugation (4000 rpm, 10 minutes), and washed two times with water and next two times with ethanol. The supernatant which contains citrate capped CuO NPs then separated.

Using the citric acid grafting procedure, the CuO NPs were further functionalized. In a water to ethanol ratio of 8:2, suspensions of 200 mM acetic acid and 65 mM CuO were made. The produced citric acid solution was combined with the CuO suspension, and the pH of the resulting combination was raised to 12 by the addition of 6 M NaOH. Next, the mixture was refluxed for three hours. The product was then centrifuged and properly cleaned three times to get rid of extra citric acid. For obtaining citrate capped CuO (C-CuO) from the two copper tailings from the mines of Peru and Bhopal (India), exactly similar procedure was followed. Only 160mg of each stone dust was mixed initially with 150ml of de-ionized water before addition of citric acid and boiling.

3.3.1.2. Synthesis of Acetate Capped CuO:

The synthesis was carried out following previously described methodology in Zhu et. Al (2004) [5] The acetate ligands generated during the synthesis process, provided satisfactory passivation against aggregation yielding high colloidal stability. In brief, 0.54 gm copper acetate was dissolved in 150 ml of deionized water. 0.52 gm glacial acetic acid was then added and the mixture was brought to boiling at 100°C under vigorous stirring. Subsequently, 0.7 gm sodium hydroxide (0.015 mol) was

quickly added until the pH value of the mixture reached 6–7, where a large amount of dark brown precipitate was simultaneously produced (Figure 1a inset). The blue-coloured mixture was observed to turn brown immediately indicating the formation of CuO NPs. After 5 more minutes of reflux, the mixture was cooled to room temperature under stirring. The CuO-NPs were then isolated by centrifugation (4000rpm, 10 minutes) and washed twice with water and twice with ethanol, respectively. The supernatant containing acetate capped CuO NPs was separated. Precipitated CuO-NPs were redispersed in deionized water for further use.

For further functionalization of the CuO NPs, acetic acid grafting method was followed. 65 mM CuO and 200 mM acetic acid suspensions were prepared in a 8:2 v/v ratio of water to ethanol. The CuO suspension was mixed with the prepared acetic acid solution and the pH of the mixture was adjusted to pH 12 by adding 6 M NaOH. The mixture was then refluxed for 3 hrs. Afterward, the product was centrifuged and washed thoroughly three times to remove excess acetic acid.

3.3.2. Data Collection for Noninvasive Hemoglobin and Bilirubin Measurement of Neonatal Subjects:

3.3.2.1. Experimental Protocol:

The experimental protocol consisted of the data collection using the in-house device (SAMIRA), parameters were calculated from the data. The measurements using the device was recorded at the same time blood was collected from neonate. The blood was sent for analysis to estimate the TSB and Hb, which was corroborated by a statistician blinded to the entire study. A single measurement was taken from the neonate's thumb nail bed to estimate two blood parameters simultaneously.

3.3.2.2. Study Settings:

This was a prospective observational study conducted over 25 months starting from January 2017 at the Department of Pediatric Medicine, Nil Ratan Sircar Medical College and Hospitals (NRSMH, a Govt. aided tertiary hospital), Kolkata, India.

3.3.2.3. Sample Size Estimation:

The sample size was estimated using the Everald's equation for power calculation in diagnostics tests [6]. Assuming the expected lowest sensitivity (SN) to

be 95%, lowest expected specificity (SP) to be 80%, confidence interval (W) for both sensitivity and specificity to be 5% and prevalence of neonatal jaundice, anemia and hypoxia to be 15% [7-9] the minimal sample size required to achieve the targeted sensitivity and specificity were found to be 487 and 290 each respectively. Hence, the effective population size is 2331. However, we decided to include a much higher number (N = 4318) of subjects in our study to reach a more robust statistical outcome. Out of this, 3427 subjects were analyzed using our developed algorithm. The remaining 891 subjects were excluded on the basis of our proposed algorithm.

3.3.2.4. Study Design and Subjects:

The study included 4668 neonates with gestational age from 28 to 40 weeks. Among them, 70 subjects failed the recruitment criteria, of which 47 subjects had cannula on either of the hands and 9 patients had other complications (e.g., inaccessible thumbnail, uneven nail bed, or other physical problems with the thumb), and were thus excluded. Based on deteriorated blood samples (hemolysed blood samples, delayed blood processing, inadequate blood volume, and ambiguous blood information), 223 patients were further ruled out from the analysis. Hence, the effective population size of 4319 neonates was considered for the study. Comprehensive details of the subjects are provided in Table 3.1. Out of this, 3689 subjects were analyzed using our developed algorithm. The remaining 630 subjects were excluded on the basis of our proposed algorithm. Particulars about inclusion and exclusion criteria are described in Table 3.2. Out of the 3689 neonates, measurements from 1784 subjects were used for the training or calibration of the device. The rest of the 1935 neonatal subjects were selected for the validation of the instrument.

Table 3.1. *Demographic details of the neonates participated in the study*

Description		**Number of Subjects**
Neonates (N)		4318
Trans cutaneous measurement (n)		4318
Mode of delivery	Spontaneous vaginal	1295
	Assistive vaginal	1727

	Elective C-section	864
	Emergency C-section	432
Gestational Age (wk)	<35	950
	35-37	1252
	38-39	1080
	40	172
	Unknown	864
Birth Weight	Low birthweight (LBW)	600
	Very low birthweight (VLBW)	384
	Extremely low birthweight (ELBW)	179
Gender	Male	2706
	Female	1929
	Ambiguous	32
Race	Asian	3475
Feeding	Breast (%)	3022
	Formula (%)	431
	Both (%)	863
	Unknown (%)	2
Post-natal age	≤24 hrs	472
	24-47.9 hrs	579
	48-71.9 hrs	836
	≥72 hrs	3105
Disorders	Congenital heart disease	278
	Respiratory Distress Syndrome	398
	Pneumonia	123

	Rh incompatibility	143
	Birth asphyxia	509
	ABO Incompatibility	362
	Others*	2505

*Other disorders include hypoglycemia, sepsis, infant of diabetic mother, jitteriness, premature rupture of the membranes (PROM), apnoea of prematurity, maternal varicella, intra uterine growth retarded (IUGR), hepatosplenomegaly, torch (+ve, HSV, CMV), congenital rubella (IgM +ve), hypothyroid, osteogenesis imperfect, meningitis, Pierre Robin Syndrome and chrorioamnionitis.

Table 3.2. *Inclusion and exclusion criteria for the study*

Inclusion criteria	Inclusion criteria comprised of all the neonates irrespective of the gestational age admitted to the Department of Paediatric Medicine, NRSMH with or without jaundice or anaemia or hypoxia and whose parents were willing to provide written informed consent after getting detailed information about the study.
Exclusion criteria	A. Neonates having cannula in either of the hands. B. Neonates who are extremely sick and from whom blood samples cannot be drawn. C. Babies having major congenital malformation. D. Neonates having lower peripheral circulation, etc.
Jaundiced Subjects	Neonates having bilirubin level above the Bhutani nomogram and is undergoing phototherapy.
Anemic Subjects	Neonates with hemoglobin level less than 11 gm/dL

It is worth mentioning that the recruitment of neonates was not consecutive as not all physicians practicing in the department were involved in the study. The neonates getting treatment under the physicians associated with the study were inducted. The appearance of possible selection bias was avoided following the approach described by Hammer et al [10]. Random assignment of doctors (a general policy for the public

hospitals in India), large time frame of the study (15 months), sufficiently large sample size, collection of data throughout 24 hours window, and enough number of subjects in each subcategory (i.e., stratification of samples) helped in avoidance of the sampling bias.

3.3.2.5. Quality Assurance in Data Collection:

Care was taken that a similar clinical protocol i.e., study, reference, and sample collection methods, and patient enrolment strategies were prospectively maintained throughout the experimental period. To avoid bias in measurements, particular care was taken to keep the technicians, clinicians, investigators, and data analysts at data collection sites blinded to the SAMIRA and the hematological data. Data of each neonate on pre-defined variables like the date, identification number, sex, gestational age, maternal history, whether having any risk factors, treatment details, etc. was collected from clinical charts on a tablet having required database with the in-built proforma by one laboratory technician hired for the study purpose. Blood collection, serum isolation, and measurements by SAMIRA were performed by trained nurses of the Department of Pediatric Medicine, NRSMH. They were responsible for uploading the SAMIRA readings to the database. The hematological parameters were measured by expert clinical biochemists at Central Laboratory, NRSMH who were completely unaware of the study. The TSB and Hb readings with proper identification numbers of the selected subjects were uploaded by another laboratory technician hired for the study purpose. The readings of both the methods (SAMIRA and the conventional) were matched based on the identification number by one research staff, to ensure complete blindness of the study. Complete blinding was maintained to keep the two sets of readings separate.

3.3.2.6. Hematological Measurement:

For simultaneous measurement, about 2 mL of blood was collected for the conventional TSB and Hb measurement test within 30 minutes of the data collected from SAMIRA. The TSB of the subjects was quantitatively determined by the 2,5-dichlorophenyldiazonium tetrafuoroborate (DPD) diazo method described by Jendrassik & Groff [11], using the commercially available test kit (Autospan Liquid

Gold, Span Diagnostics, India) within 1 h of blood collection in the Central Laboratory, NRSMH. For the test, serum was first isolated from the collected blood and then examined with the test kit. To prevent the photoreduction of bilirubin the serum samples were carefully kept in the dark at 4°C before analysis. For hemoglobin and arterial blood gas measurement the collected blood samples were subjected to an automated hematology analyzer (Sysmex KX-21) [12] for complete blood count (CBC) analysis and GEM premier 3000 system [13] (Instrumentation Laboratory. Bedford, MA), respectively. All the guidelines provided by the National Accreditation Board for Testing and Calibration Laboratories (NABL) [14] were followed to maintain the accuracy and precision of the techniques. The coefficient of variation for the hospital laboratory was targeted for < 6%. During the study period, each of the actual variance values, assessed every 3 months, ranged from 3 to 5%.

3.3.2.7. Statistical Analysis:

Analysis of the data was done using descriptive statistical analysis, simple linear regression analysis, and the Bland & Altman method [15-18]. For the correlation between the values obtained from the device and the gold standard, linear regression and Bland Altman was used. The mean (n) of the measurements was calculate according to the formula:

$$n = \frac{Sum\ of\ the\ data\ points}{Number\ of\ data\ points} \tag{3.11}$$

The Standard deviation between the successive measurements was measured using the formula

$$SD = \sqrt{\frac{\sum_{i=0}^{N}(x_i - \mu)}{N}} \tag{3.12}$$

Where, 'N' refers to the number of experimental outcomes, 'μ' is the mean of the individual outcomes and 'x_i' is each outcome of the experiment. GraphPad Prism 5.0 (GraphPad Sofware, USA) and SigmaPlot 12.5 (Systat Sofware, USA) were utilized for the analysis of the data.

3.3.2.8. Ethical Considerations:

For the present work, all necessary ethical permissions were taken from the Institutional Medical Ethics Committee, NRSMH, Kolkata (Ref. No. - No/NMC/439,

dated January 27, 2020). All studies involving human subjects were performed following the Declaration of Helsinki [19] and guidelines provided by the Indian Council for Medical Research (ICMR), Govt. of India. Written informed consent was obtained from parents or legal guardians who agreed to participate in the study after understanding the details of the study and its consequences. All data and information about the subjects were anonymized kept confidential and used only for this study.

3.3.3. DPPH Assay for *In Vitro* Antioxidant Activity Study:

UV-vis assisted DPPH assay was performed to study the antioxidant activity of the samples using the reported methodology [20]. The degradation kinetics of 1,1-Diphenyl-2-picrylhydrazyl (DPPH) was observed and monitored by measuring the decrease in this characteristic absorption peak of DPPH at 535 nm as a function of time. The free-radical scavenging capability of the samples of interest was determined using the DPPH assay method. 0.15 mM DPPH solution was prepared in methanol and 0.5 ml citrate CuO nanoparticles of various concentrations were added in 2.5ml of the freshly prepared DPPH solution. The characteristic absorption maxima of DPPH at 535 nm was selected to monitor the degradation process with DPPH in the presence and absence of light at room temperature. In the interval of 2 seconds for an hour, the absorption spectra of DPPH were recorded using SPECTRA SUITE software provided by Ocean Optics. For the tea quality evaluation, a 2ml sample solution of appropriate concentration was mixed with 40 mM DPPH in ethanol and kinetics was performed for 30 mins by measuring absorbance at 535 nm at 1 min interval and the DPPH free radical scavenging activity was measured with the following equation (3.13):

$$\textit{Radical scavenging activity} = (A_1 - A_2) / A_1 \qquad (3.13)$$

where A_1 is the absorbance of the sample at time zero immediately after mixing DPPH to the reaction mixture and A_2 is the absorbance after 30 minutes.

Along with the DPPH assay of tea extracts, the assay was also done with freshly brewed Nepal and Darjeeling tea extract with additives such as milk, sugar, milk and sugar both and with zinc oxide to see the effect of antioxidant activity with addition of different additives to tea samples.

3.3.4. Quantification and Characterization of ROS:

For the purpose of quantification of the generated ROS we used 2′,7′-Dichlorofluorescein (DCFH) which is a well-known reagent. The DCFH was prepared via a de-esterification reaction from DCFH-DA at room temperature following a standardized protocol described in the previous studies [21, 22]. The oxidation of DCFH, in the presence of light leads to the production of DCF giving fluorescence [23, 24]. In this study, the ROS generated in the aquous citrate functionalized CuO NPs convert DCFH in DCF which has a characteristic emission maximum at 522 nm upon excitation at 488 nm. The DCF emissions were recorded in the Fluorolog Model LFI-3751 (Horiba-Jobin Yvon, Edison, NJ) spectrofluorometer. The ROS experiments were performed in the dark as well as in light for 30 mins. The ROS experiments for the acetate capped CuO samples were performed in the dark for 10 mins followed by under irradiation of a white light of 400−700 nm wavelength for 30 mins.

3.3.5. General Synthesis of Ir(III)-based Luminescent Molecule (AS-1):

A flame-dried flask was charged with $IrCl_3.3H_2O$ and benzo(h)quinoline (1 : 2.5 equivalent), sealed with a septum, and evacuated and backfilled with N_2 three times. Anhydrous ethanol was added via syringe and the reaction was refluxed for 24h. After 24 hours a yellow precipitation of Chloro-bridge iridium complex formed. This complex is filtered by using G3 sintered crucible and washed with water and cold methanol three times. To this freshly prepared Chloro-bridge iridium complex (1 equiv.), HPBT (2.1 equiv.) and aqueous sodium carbonate (3 equiv.) added and refluxed for 1 hour. A red precipitation of AS-1 was formed. AS-1 was further purified by recrystallization in ethanol.

3.3.5.1. Method of preparation of the solution of AS-1 for As^{III} sensing:

50 mL of 10 mM stock solution of CTAB in water, 2mL of a 1000 ppm of AS-1 in PBS buffer. 5 mL glass tubes were taken and labelled as Blank, Na^+, K^+, Ag^+, Zn^{2+}, Fe^{2+}, Pb^{2+}, Cd^{2+}, Co^{2+}, Cu^{2+}, Ni^{2+}, Hg^{2+}, Mn^{2+}, Ca^{2+}, Mg^{2+}, Fe^{3+}, Cr^{3+}, Al^{3+}, As^{3+}, As^{5+}, F^-, Cl^-, Br^-, I^-, NO_3^-, PO_4^{3-}, OAc^-, SO_4^{2-} , $Cr_2O_7^{2-}$, OH^-, ClO_4^- and CO_3^{2-}. 100 microliters of

stock solution of AS-1 and 2mL of the CTAB solution and 10 equivalents of the corresponding metal salt (10^{-3}M) were then added to each labeled glass tube. The concentration of phosphate buffer saline used was 0.1 M.

3.3.6. Statistical Analysis:

All quantitative data are expressed as Mean ± Standard Deviation (SD), unless otherwise stated. One-way analysis of variance (ANOVA) followed by Tukey's post hoc multiple comparison test was performed for comparison. GraphPad Prism v8.0 (GraphPad Software), and Sigmaplot v14.0 (Systat Software, Inc.) were used for statistical analysis. Unpaired 2-tailed T-Test was used to calculate differences between groups. For all comparisons, a P value <0.05 was considered statistically significant.

3.3.7. Computational Study:

3.3.7.1. Density Functional Theory (DFT):

The first principles density functional theoretical calculations have been performed to investigate the electronic structure of Chl and Chl–Cu(II) using Vienna ab initio simulation package (VASP). The spin-polarised plane-wave methods were employed within Generalized Gradient Approximation and Perdew-Burke-Ernzerhof exchange correlation functional and projector augmented wave pseudopotentials. The ionic relaxations were achieved with a conjugate gradient algorithm till the Hellmann–Feynmann force are lower than 0.001 eV/Å on each ion. The k-meshes are prepared by using Monkhorst–Pack grid, plane-wave cut-off energy was chosen to be 500 eV and convergence was set to 10^{-6} eV. The ionically relaxed structures were used to calculate the electronic density of states by using Gaussian smearing.

3.3.7.1. Computational Biology Study of Compound Protein Interaction:

To predict Chemical-Protein (CP) Interaction Networks of the drugs on bacteria, the web-resource STITCH (version 5.0) provided by STITCH Consortium2016 (http://stitch.embl.de/) was used. STITCH database can predict about 430,000 chemicals and 960,0000 proteins curated from 2031 eukaryotic and prokaryotic genome [25, 26]. The association for a chemical-protein interaction can be

predicted by the confidence score, where higher score corresponds to a stronger interaction. In this database, the predictive value of a particular chemical-protein interaction can be controlled by the confidence score and for the present study the value was kept at 0.4. Eight different sources, i.e. experiments, text mining, neighborhood, gene fusion, databases, co-expression, co-occurrence and predictions are used to populate the active interactions.

3.3.8. Chemometric Analysis:

In the current study, principal component analysis (PCA) is performed using the 'Orange' tool (https://orangedatamining.com/) [27]. Different geographical indices were ascertained as a variable and analyzed statistically as 'D', 'N' and 'A' quadrants. The integration of feed-forward artificial neural network (ANN) were created using Anaconda distribution [28]. The confusion matrix and the area under the receiver operating characteristic (ROC) curve (AUC) were used as performance metrics for the development of machine learning algorithms.

REFERENCES

[1] D.V. O'Conner, D. Philips, Time correlated single photon counting, *Academic Press*, London, 1984.

[2] A. Banerjee, D. Mukherjee, M.N. Hasan, S. Mukhopadhyay, D. Karmakar, R. Das, *et al.*, Interaction of chlorophyll with artificial colorants in restricted nanoscopic environment: Key insights on the toxicity from electronic spectroscopy, *Nanoscience and Nanotechnology Open Access*, 2 (2023) 1012.

[3] N. Polley, S. Singh, A. Giri, S.K. Pal, Evanescent field: A potential light-tool for theranostics application, *Review of Scientific Instruments*, 85 (2014) 033108.

[4] D.A. Armbruster, T. Pry, Limit of blank, limit of detection and limit of quantitation, *The Clinical Biochemist Reviews*, 29 (2008) S49.

[5] J. Zhu, D. Li, H. Chen, X. Yang, L. Lu, X. Wang, Highly dispersed CuO nanoparticles prepared by a novel quick-precipitation method, *Materials Letters*, 58 (2004) 3324.

[6] S. Jones, S. Carley, M. Harrison, An introduction to power and sample size estimation, *Emergency Medicine Journal: EMJ*, 20 (2003) 453.

[7] N.G. Onyeneho, B.C. Ozumba, S. Subramanian, Determinants of childhood anemia in India, *Scientific Reports*, 9 (2019) 1.

[8] D. Dutta, M. Bhattacharya, S. Bhattacharya, A. Chaudhuri, M. Lahiri, U. Mitra, *et al.*, Influence of admission weight on neonatal mortality amongst hospitalised neonates in Calcutta, *Journal of the Indian Medical Association*, 90 (1992) 308.

[9] R. Subhi, M. Adamson, H. Campbell, M. Weber, K. Smith, T. Duke, *et al.*, The prevalence of hypoxaemia among ill children in developing countries: A systematic review, *The Lancet Infectious Diseases*, 9 (2009) 219.

[10] G.P. Hammer, J.-B. du Prel, M. Blettner, Avoiding bias in observational studies: Part 8 in a series of articles on evaluation of scientific publications, *Deutsches Ärzteblatt International*, 106 (2009) 664.

[11] C.C. Garber, Jendrassik--Grof analysis for total and direct bilirubin in serum with a centrifugal analyzer, *Clinical Chemistry*, 27 (1981) 1410.

[12] A.K. Fares, Performance evaluation of two haematology analysers: The Sysmex KX-21 and the Beckman Coulter AC. T diff, *Sysmex Journal International*, 11 (2001) 27.

[13] B. Bénéteau-Burnat, M.-C. Bocque, A. Lorin, C. Martin, M. Vaubourdolle, Evaluation of the blood gas analyzer GEM (r) PREMIER (tm) 3000, *Clinical Chemistry and Laboratory Medicine (CCLM)*, 42 (2004) 96.

[14] A. Kanagasabapathy, P. Rao, Laboratory accreditation-procedural guidelines, *Indian Journal of Clinical Biochemistry*, 20 (2005) 186.

[15] N. Polley, S. Saha, S. Singh, A. Adhikari, S. Das, B.R. Choudhury*, et al.*, Development and optimization of a noncontact optical device for online monitoring of jaundice in human subjects, *Journal of Biomedical Optics*, 20 (2015) 067001.

[16] J.M. Bland, D. Altman, Statistical methods for assessing agreement between two methods of clinical measurement, *The Lancet*, 327 (1986) 307.

[17] J.M. Bland, D.G. Altman, Correlation, regression, and repeated data, *BMJ: British Medical Journal*, 308 (1994) 896.

[18] A. Halder, A. Adhikari, R. Ghosh, S. Singh, A. Banerjee, N. Ghosh*, et al.*, Large scale validation of a new non-invasive and non-contact bilirubinometer in neonates with risk factors, *Scientific Reports*, 10 (2020) 1.

[19] G.A.o.t.W.M. Association, World Medical Association Declaration of Helsinki: Ethical principles for medical research involving human subjects, *The Journal of the American College of Dentists*, 81 (2014) 14.

[20] D. Bagchi, S. Chaudhuri, S. Sardar, S. Choudhury, N. Polley, P. Lemmens*, et al.*, Modulation of stability and functionality of a phyto-antioxidant by weakly interacting metal ions: Curcumin in aqueous solution, *RSC Advances*, 5 (2015) 102516.

[21] S. Mondal, A. Adhikari, R. Ghosh, M. Singh, M. Das, S. Darbar*, et al.*, Synthesis and spectroscopic characterization of a target-specific nanohybrid for redox buffering in cellular milieu, *MRS Advances*, 6 (2021) 427.

[22] N. Polley, S. Saha, A. Adhikari, S. Banerjee, S. Darbar, S. Das*, et al.*, Safe and symptomatic medicinal use of surface-functionalized Mn_3O_4 nanoparticles for hyperbilirubinemia treatment in mice, *Nanomedicine*, 10 (2015) 2349.

[23] A. Bera, M.N. Hasan, U. Pal, D. Bagchi, T.K. Maji, T. Saha-Dasgupta*, et al.*, Fabrication of nanohybrids toward improving therapeutic potential of a NIR photo-sensitizer: An optical spectroscopic and computational study, *Journal of Photochemistry and Photobiology A: Chemistry*, 424 (2022) 113610.

[24] M.N. Hasan, A. Bera, T.K. Maji, D. Mukherjee, N. Pan, D. Karmakar, *et al.*, Functionalized nano-MOF for NIR induced bacterial remediation: A combined spectroscopic and computational study, *Inorganica Chimica Acta*, 532 (2022) 120733.

[25] D. Szklarczyk, A. Santos, C. Von Mering, L.J. Jensen, P. Bork, M. Kuhn, STITCH 5: Augmenting protein–chemical interaction networks with tissue and affinity data, *Nucleic Acids Research*, 44 (2016) D380.

[26] M. Kuhn, D. Szklarczyk, S. Pletscher-Frankild, T.H. Blicher, C. Von Mering, L.J. Jensen, *et al.*, STITCH 4: Integration of protein–chemical interactions with user data, *Nucleic Acids Research*, 42 (2014) D401.

[27] J. Demšar, T. Curk, A. Erjavec, Č. Gorup, T. Hočevar, M. Milutinovič, *et al.*, Orange: Data mining toolbox in Python, *the Journal of Machine Learning Research*, 14 (2013) 2349.

[28] A. Banerjee, R. Ghosh, S. Singh, A. Adhikari, S. Mondal, L. Roy, *et al.*, Spectroscopic studies on a natural biomarker for the identification of origin and quality of tea extracts for the development of a portable and field deployable prototype, *Spectrochimica Acta Part A: Molecular and Biomolecular Spectroscopy*, 299 (2023) 122842.

CHAPTER 4

Studies on Interaction of Optical Radiation and Indigenous Nanomaterials with Biomedical Subjects using Electronic Spectroscopy for Potential Application in Healthcare

4.1. INTRODUCTION:

Neonatal jaundice and anemia are the most common health issues encountered by newborns globally and constitute a major percentage of infant mortality. The prevalence of neonatal jaundice and anemia is quoted to be between 50% and 60% among healthy term neonates [1-3]. According to the recent reports of World Health Organization, neonatal jaundice effects one in every two infants globally. One of the major reasons for pathologic hyperbilirubinemia is the excessive production of bilirubin, a byproduct of hemoglobin breakdown, and the impaired ability of the newborn to excrete it [4]. Among the reported cases of neonatal hyperbilirubinemia, about 15% of the neonates suffer from persistent jaundice that lasts for about 14 to 21 days [5]. All these infants suffering from persistent jaundice have significantly decreased hemoglobin levels [6] and elevated bilirubin concentration in blood due to the increased bilirubin production from hemolysis resulting in a simultaneous pathologic condition of jaundice and anemia among neonates [4, 6]. According to the American Academy of Pediatrics (AAP), the incidence of neonatal hyperbilirubinemia is increased among infants having risk factors like, ABO incompatibility, Rh incompatibility, birth asphyxia, etc [7]. It has been reported that the occurrence of neonatal jaundice is more likely among neonates suffering from birth asphyxia, than neonates without birth asphyxia [8-11] due to the lack of oxygen supply to the liver which results in hypoxic damage followed by the bilirubin conjugation ability of the liver, which ultimately results into jaundice [8]. Additionally, perinatal asphyxia and hypoxic-ischemic encephalopathy can lead to the disruption of the blood-brain

barrier, allowing the free entry of unconjugated bilirubin to the neurons resulting in acute bilirubin encephalopathy [8]. In addition to this, dysregulation of blood flow to the lungs due to hemolysis can also cause an imbalance in the ventilation and perfusion ratio thereby, resulting in a hypoxic condition [12] in the neonates [13]. Thus, simultaneous monitoring of bilirubin, and hemoglobin levels in newborns is essential to ensure appropriate management. The contemporary method of measurement of serum bilirubin concentrations (TSB) and hemoglobin levels (Hb) involves painful blood sampling [14-17] which suffers from multiple long term consequences like infection at the sampling site, osteomyelitis (though in rare cases), blood loss, etc.[15, 18, 19]. Although, non-invasive methods (BiliCheck™ [20], JM-105™ [21], Rad 57™ [22] NBM-200, etc) [23] have been established as alternatives to repeated blood samplings for TSB and Hb measurement [24, 25] however, they suffer from certain inherent limitations that restrict their usage in widespread hospital settings [24, 26, 27]. Particularly, the accuracy of these non-invasive devices vary across races and have been found to be less accurate in Asian, Hispanic and African populations (having dark skin tone) [28]. Therefore, monitoring of bilirubin and hemoglobin values is needed at the bedside of the neonate suffering from either jaundice, anemia or hypoxia for the proper management. In a study under this thesis work, we aim to develop a non-invasive point of care device (i.e. SAMIRA, Spectrum Assisted Medical Inoffensive Radiation Application) for the simultaneous determination of hemoglobin and bilirubin in neonates. The newly developed instrument utilizes an algorithm to quantify two blood parameters from a single discrete measurement. The simultaneous measurement of bilirubin and hemoglobin from neonates in a non-invasive manner from a single measurement for their proper management is the current motivation of the current work. As the device collects data from the blood vessels of the distal subungual arcade and the superficial arcade area discarding the influence of melanin or skin colour, it is hypothesized to give accurate transcutaneous measurement values of TSB and Hb. Additional incorporation of machine learning and artificial intelligence has improved the data accuracy of the proposed device stronger. By virtue of the machine learning algorithm the developed device is capable of locking a data which is 98% accurate. Studies on a huge number

of neonatal populations helped in exact incident light dosage determination, data acquisition time optimization etc., making the device highly precise and accurate for point of care settings. Till date, to the best of our knowledge no device has been developed that can monitor these two blood parameters at the same time in a non-invasive way.

In another study, molecular co-localization of multiple drugs in a nanoscopic delivery vehicle for potential synergistic remediation of multi-drug resistant bacteria has been explored. World Health Organization (WHO) has declared antimicrobial-resistant (AMR) infections as one of the top 10 global public health threats [29]. It was reported that in 2019 alone, the AMR organisms were the primary cause of 1.27 million deaths worldwide [30]. If corrective mechanisms are not put into place, it is likely to skyrocket. In an alarming report, commissioned by the UK government, it was predicted that antimicrobial resistance may cause up to 10 million deaths annually by 2050 [31]. Amongst antimicrobial-resistant bacteria, the emergence of multidrug-resistant (MDR) bacteria species is of great concern, primarily because of their ability to mutate genes and to reduce drug action. Poor drug binding capacity and low cell penetration [32] make multidrug-resistant bacteria responsible for almost 65% infections which are linked with HealthCare-Associated disease [33]. The inappropriate use of antibiotics is responsible for rise in bacterial resistance, which makes the clinical management of infections hard to manage with conventional antibiotics [34]. Numerous bacteria, especially MDR, can grow and survive on the contaminated damp surfaces [35], for a longer time, mainly in healthcare facility. The dirt and organic element from human or animal origin can work as substrates for the growth of the bacteria and facilitates the spread of micro-organism induced infection from individual to the community. Hence, the rapid and effective disinfection of surfaces and environmental cleanliness is one of the primary measures to control the spread of MDR bacteria. Amongst all multidrug-resistant bacteria, Methicillin-resistant *Staphylococcus aureus* (MRSA) has been categorized as a high priority multidrug-resistant pathogen by WHO [36]. It can cause a mild skin infections to fatal infections [34]. MRSA and is resistant to penicillin, methicillin, oxacillin and amoxicillin [37]. MRSA, being one of the most critical human organism and colonizing

bacteria, is responsible for one of the leading causes of infections worldwide [38]. Infections induced by MRSA carry significant clinical load for the patient and medical practitioner [39]. Prolonged hospital stay, increased hospital cost as well as higher hospital mortality [40] also impart a huge economic burden to the patient-family, healthcare systems and to the society [41, 42]. Emerging MDR strains of MRSA are clinically notorious because of their lack of response to conventional antimicrobial therapy. It is known that biofilm formation is one of the main causes behind antibiotic resistance. Biofilm, an organized colony of microorganisms, forms an extracellular polymeric matrix of substance and shows adhesion with the neighbouring living and non-living surfaces [43]. It facilitates microorganism interaction and protect tolerant cells from the change in living environment for a long period of time [44]. The biofilm matrix strengthen the tolerance to disinfectants by wrapping the underlying cells [45] [46] and by restricting diffusion of disinfectants into the biofilm matrix [47]. Hence, regulating biofilm formation has become an alternative approach to limit persistent infections [48]. Regular use of disinfectants on potential-contaminated surfaces have become an important routine practice for sterilization [49, 50] as it reduces biofilm formation and reduces transmission of infectious pathogens, in turn. Currently, bleach (sodium hypochlorite) - derivative solutions are used in healthcare facilities [51] as disinfectant spray. Although, it has significant adverse effect on bacterial contaminants, due to its oxidizing capacity and toxicity, the bleach-derivative products are not suitable for long-term use [52]. Despite the presence of significant environmental threat, chlorine (Cl_2) and its derivative sodium hypochlorite (NaOCl) are still the most widely used disinfectants. Organic chloride compounds released by these chloride-based sterilising agents in the wastewater are toxic for aquatic organisms and possess a significant threat as environmental contaminants [53]. Hence, new avenues are required to be examined to control the huge adverse impact of the MRSA infections [54]. Previously it was pointed out that the combination of two different drugs linked through a selectively chosen drug carrier, improves the efficacy of the system against AMR activities [55, 56]. The present study explores the co-localization of an antituberculosis drug rifampicin (RF) with another drug benzothiazole (BT) in an organized assembly of Cetyl Triethyl Ammonium Bromide

(CTAB) micelles, and their prospect as an antibacterial spray against MRSA. RF is a popular drug with a proven safety profile for treatment of tuberculosis for its sterilizing activity and ability to shorten treatment [57, 58]. BT is an important class of medicine possessing antibacterial [59], antiviral [60], anticancer [61], antifungal [62] and antitumor [63] properties. On the other hand, CTAB solution which works as a nanoscopic vehicle by bringing BT and RF together, too is safe and familiar for their antimicrobial properties [64]. In this context it is worth mentioning that some studies already investigated the development and design of novel drug delivery systems using density functional theory calculations and molecular dynamics simulations [65], [66]. For our study, to obtain precise location of the drugs RF and BT in the organized assembly of CTAB, FRET between BT (energy donor) and RF (energy acceptor) was employed because the fluorescence spectrum of BT overlaps reasonably well with the absorption spectrum of RF. Time-resolved studies on FRET [67-69] were employed to obtain precise information on localization of the drugs (RF and BT) in CTAB micelles. In addition, dynamic light scattering (DLS) technique was used to investigate the integrity of the nanoscopic organized assembly of CTAB micelles. Furthermore, we have applied a kinetic model developed by Tachiya to analyze the fluorescence decay of BT in presence of RF in CTAB micelles [70, 71] and compared them with the experimental data. These findings are finally extended to MRSA bacteria and the promising potential of the RF-BT encapsulated in CTAB micelles as a strong antibacterial spraying agent has been established. It was observed that separately these compounds, i.e., RF, BT and CTAB show low to moderate level effectivity against the MRSA colonies. Whereas their combined effect has shown impressive results by successfully eliminating almost all the colonies of MRSA. Singular and doublet combinations of these chemicals were also studied to comprehensively explore sterilising possibilities. Computational biology study on the formulation shows that the drugs rifampicin and benzothiazole, although conventionally used as tuberculosis and antifungal agents, can be repurposed for remediation of the MDR micro-bacteria including MRSA.

In another work, development of a nanomedicine was attempted from copper mine tailing wastes as a pavement towards circular economy using advanced redox

nanotechnology. Copper was the first metal discovered in the history of human civilization during the chalcolithic or copper age, around 6000 years ago. This marvel metal was well known in ancient times, not only for its ability to enhance the strengths of the tools, but also for its impressive healing capacity. The ancient Indians, Greeks and Egyptians used copper containers for water purification, treatment of wounds and lung ailments. Copper cooking utensils were employed throughout the Roman empire to stop the spread of disease [72]. In recent times, the US Environmental Protection agency (EPA) has classified copper and its derivatives as antibacterial materials [73]. On the other hand, the essentiality of copper in human body for healthy development, cardiovascular and lung functionality, neovascularization, neuroendocrine function and iron metabolism is well reported in the literature [74].

Metallic copper, cupric oxide (CuO) and cuprous oxide (Cu_2O) nanoparticles are attracting considerable research interests nowadays due to their widespread applications in catalysts and therapeutic domains [75-81] compared to their bulk counterparts by virtue of their nano-dimensional higher surface area to volume ratio. Specifically, copper oxide nanoparticles (CuO NPs) display broad-spectrum antibacterial and photocatalytic properties [82] and have the potential to be used as the alternative to antibiotics. The design and development of new compounds as antibiotics possess an emergent need, as the overuse and misuse of the existing antibiotics is responsible for the growing episodes of antibiotic resistance infections and deaths globally [83]. The antibacterial activity of CuO NPs against Gram-positive bacteria, such as *S. aureus* and *B. subtilis* as well as Gram-negative bacteria such as *E. coli* and *P. aeruginosa* are reported in various studies [84-88]. Metallic Cu and CuO NPs are also found to exhibit multi-toxicity on multi-drug resistant bacterial species such as the methicillin-resistant *S. aureus* (MRSA) [89]. In case of CuO NPs, it is suggested that its antibacterial effect might be associated with the cell membrane dissociation and reactive oxygen species (ROS) production [90]. Various simultaneous mechanisms of action of CuO nanoparticles against bacteria make it almost impossible for the microbes to develop resistance, as the bacterial cell would be required to generate multiple simultaneous gene mutations to develop this resistance [91]. The copper oxide nanoparticles are obtaining growing attention for their cheaper price and

abundance in comparison with other noble and expensive metals like silver or gold and their competent potential application as microbial agents [86, 92, 93]. The size, morphology and solubility play a significant role on the antibacterial activities of Cu, CuO and Cu_2O [94-96]. However, the major limitation of metallic CuO NPs in the nano-size range is the lack of significant stability in dispersions due to their strong tendencies of aggregation and formation of larger clusters to reduce the energy associated with their high surface area [97-99]. The formation of clusters results in sedimentation leading to loss of reactivity and antimicrobial performance in which a nanometric size is essential [99]. Further surface modifications of CuO NPs by post-functionalization approach not only enhances their colloidal stability but also introduces unique physical and chemical properties including possible enhancement of their antimicrobial activities. Functionalization or capping of an inorganic nanoparticle with an organic ligand like citrate or folate are evidenced to produce nanohybrids that have unique therapeutic potentials [100]. In the current study, we have explored the effect of citrate capped CuO NPs on a Gram-positive *Staphylococcus hominis* (SH) bacterial strain. *S. hominis* is one of the commensal bacteria that reside on human skin [101]. Although it is apparently harmless, it has been reported that one of its subspecies novobiosepticus, is multidrug resistant and causes nosocomial infections, like sepsis and bloodstream infections in neonates and immunocompromised patients [102] and various opportunistic infections of humans [103]. S. Hominis is also well known for its ability to generate pungent body odour in human [104]. In the present study, we have reported the synthesis or extraction, characterization and antimicrobial activity of citrate functionalized CuO NPs on Staphylococcus hominis bacterial strain. CuO NPs were synthesized and capped by precipitation technique [105] and grafting method [106] respectively in a bottom-up approach. Similarly in a top-down way, CuO NPs were extracted and citrate functionalized from two types of copper containing stones from copper mines. Structural properties of both synthesized and extracted CuO NPs were examined by X-ray diffraction (XRD), field emission scanning electron microscopy (FESEM) equipped with energy dispersive X-ray spectroscopy (EDS) and found to be similar. Dynamic Light Scattering (DLS) and zeta potential studies were also employed for

estimating the hydrodynamic diameter and solubility assessment of the synthesized nano hybrid. The surface functionalization of CuO NPs by citrate ligands were confirmed by FTIR and UV-Vis spectroscopy. Antimicrobial activity of citrate-CuO NPs was examined on S. Hominis bacteria strain. The citrate functionalized NPs were found to generate reactive oxygen species (ROS) upon photo-excitation, which is responsible for their anti-microbial action as ROS has the ability to destroy the active substances in the bacterial inner and outer membrane [107-109]. This phenomenon establishes the credentials of citrate CuO NPs for applications like antibacterial photo dynamic therapy (PDT) with enhanced efficacy. We have also used computational biology strategy in order to rationalize the antibiotic resistant bacterial remediation found in our experimental studies. Immediately after the establishment of the CuO nano-hybrid to be a potential antibacterial agent, we have also explored the use of copper mine tailings as a source of raw materials for the nano-hybrid synthesis in order to cater low-cost antibiotics to wider population across the globe and to remediate the burden from the copper mines simultaneously. We have also developed a prototype FMCG product (talcum powder) for remediation of bacteria S. Hominis which are responsible for generation of several human disorders.

Simultaneously, as an extension of the above work, acetate functionalized CuO nanoparticles were studied for a potential remediation of antibiotic-resistant infections. As already discussed, copper oxide nanoparticles (CuO NPs) have attracted high degree of research interests over other metallic nanoparticles by virtue of their tremendous potential applications in diverse fields like chemo and biosensing, medicinal therapeutics, particularly as anti-microbial, anti-bacterial and anticarcinogenic agents, drug delivery systems, energy saving devices, optics and optoelectronics, electrochemistry and catalysis [110-118]. However, CuO, the semiconducting compound with a monoclinic structure is mainly considered most for its well reported antimicrobial properties [119]. It is used widely as an antifungal, antibiotic and antimicrobial agent when introduced into textiles and coatings [120] but limited information on the antimicrobial activity of surface functionalized CuO is available. Further surface modifications of CuO NPs by post-functionalization approach introduces unique physical and chemical properties [121, 122] including

possible enhancement of their antimicrobial activities. Antimicrobial-resistant (AMR) infections are declared as one of the top ten global public health threats by World Health Organization (WHO) and it was reported that in the year 2019 only, the AMR organisms were the primary cause of 1.27 million deaths worldwide [123]. Amongst AMR bacteria, multi drug resistant (MDR) species are of greater concern because of their capability to mutate genes and developing resistance towards antibiotics. Methicillin-resistant *Staphylococcus aureus* (MRSA) is such a notorious MDR bacteria that has been categorized as a high priority multidrug-resistant pathogen by WHO [123]. Improper and uncontrolled use of antibiotics is the root cause of rise in bacterial resistance, making the clinical management of infections harder to manage using conventional antibiotics. MRSA is resistant to many antibiotics like penicillin, methicillin, oxacillin and amoxicillin [124]. The sustained emergence and rapid spread of MRSA infections along with the scarcity of new antibiotics provoke urgent interest in alternative and novel antimicrobial agents such as small antibiotics, metal NPs, cationic polymers and antimicrobial peptides [96, 125-128]. In the current study, we reported synthesis, characterization and antimicrobial activity of acetate functionalized CuO NPs on MRSA bacterial strain. CuO NPs were synthesized and capped by precipitation technique [105] and grafting method respectively [106]. Structural properties of CuO NPs were examined by X-ray diffraction (XRD), field emission scanning electron microscopy (FESEM) equipped with energy dispersive X-ray spectroscopy (EDS). Dynamic Light Scattering (DLS) and zeta potential studies were also employed for estimating the hydrodynamic diameter and solubility assessment of the synthesized nano hybrid. Functionalization of CuO NPs by acetate ligands were confirmed by FTIR and UV-Vis spectroscopy. Antimicrobial activity of acetate-CuO NPs was examined on MRSA bacteria strain. The acetate functionalized NPs were found to produce reactive oxygen species (ROS) upon photo-excitation, which is responsible for their anti-microbial action as ROS has the ability to destroy the active substances in the bacterial inner and outer membrane [107, 108, 129]. This phenomenon establishes the credentials of acetate CuO NPs for applications like antibacterial photo dynamic therapy (PDT) with enhanced efficacy. We have also used

computational biology strategy in order to rationalize the antibiotic resistant bacterial remediation found in our experimental studies.

4.2. RESULTS AND DISCUSSIONS:

4.2.1. Non-invasive Estimation of Hemoglobin and Bilirubin of Neonates Simultaneously Using Whole Optical Spectrum Analysis at Point of Care [130]:

4.2.1.1. Development of the Hardware:

The instrumental set up as shown in Figure 4.1.a has been designed based on the principle of diffused reflectance spectroscopy. The proposed device utilizes the principles of diffused reflectance spectroscopy (DRS) for the quantification of the blood parameters. The DRS technique is based on the amount of light collected from the tissue layers after penetration of the incident light [131-133]. The retro-reflected light thus contains information about the tissue microstructure and the biomolecular content. The thumb nail plate of neonatal subjects is illuminated with light from a white Light Emitting Diode (LED) source (3 W,400-700nm, 700LUX, 4.78 mW optical power) and the diffused optical signal in the visible range was collected in a CCD based spectrograph (STS-VIS, manufactured by Ocean Optics, Florida) with wavelength resolution of 0.47 nm. A lab grade 6:1 diffuse reflectance fiber optic probe manufactured by Ocean Optics, Florida was used to transmit the light from source to subject nail by the 6 peripheral excitation fibers of the probe and receive the response signal by the central collection fiber by holding the probe tip at perpendicular position with the nail. The obtained spectral response in the spectrometer is then transferred to a computer through USB connection for processing in our developed graphical user interface in LabVIEW (National Instruments) platform. Subsequent data acquisition, analysis and result generation are taken care of by the custom-made software. Proper cooling arrangements (5V DC fans, 0.2 Amp) for dissipation of excess heat generated by components have also been incorporated in the instrument by virtue of which the device performance remain unaltered under varying temperature conditions. In the customized power supply module driven device, artificial intelligence is also implemented by the software automatically to filter out reliable spectrum after data

acquisition by guiding the user to take more data unless appropriate accuracy level is achieved.

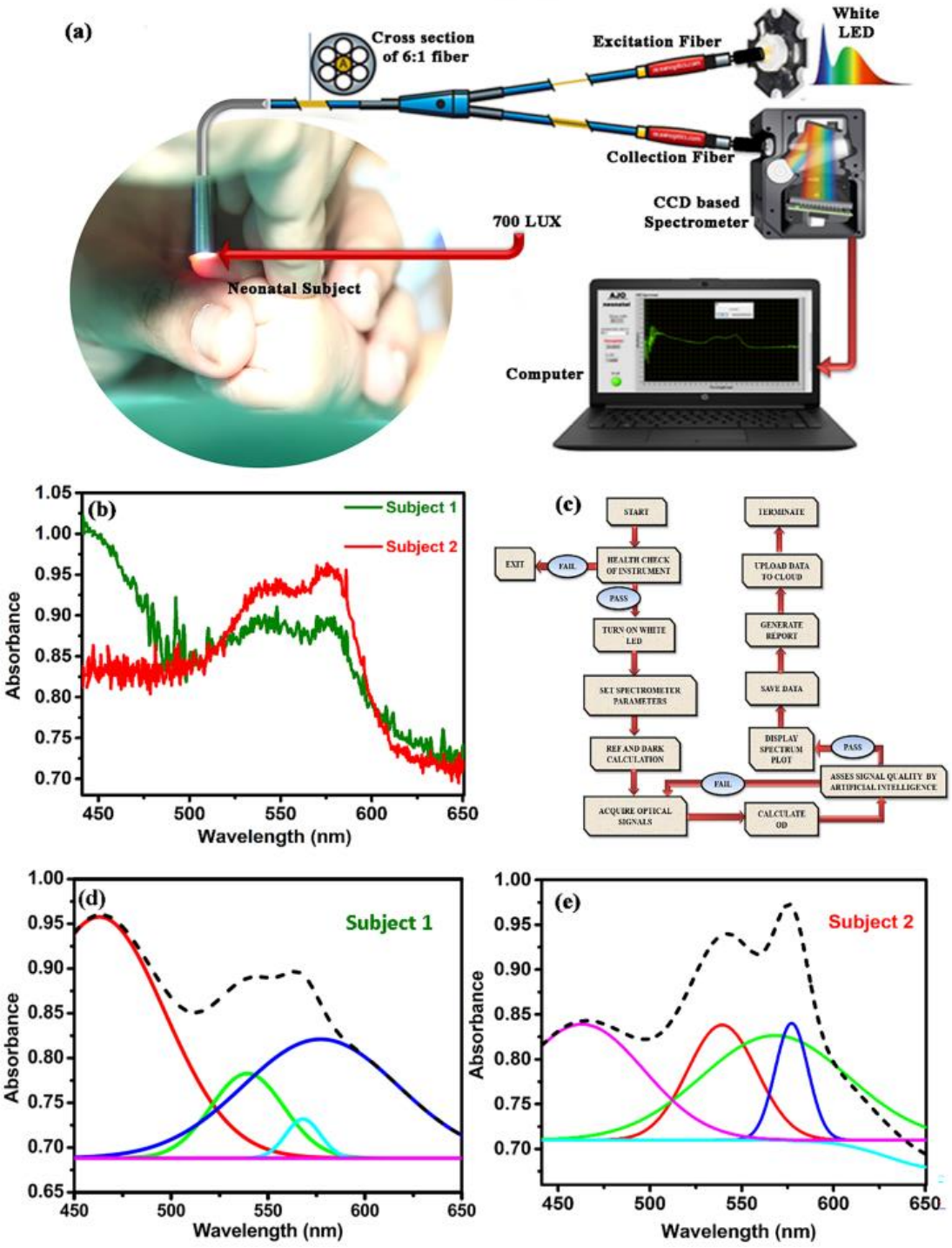

Figure 4.1. *Design of the developed prototype with the acquired data and the de-convoluted spectrum (a) The instrument consists of a LED source, a 6:1 optical fibre, a CCD based spectrophotometer and an integrated electronic module (See text for details). (b) The acquired spectra from two subjects. Subject 1 is diseased with TSB value 29.8 mg/dL and Hb value 10.2 gm/dL. Subject 2 is from a normal infant with TSB value 2.4 mg/dL and Hb value 19.1 gm/dL. (c) Work flow of the instrument (d) De-convoluted peaks from subject 1 along with the cumulative fit (e) De-convoluted peaks from subject 2 along with the cumulative fit (see text).*

Figure 4.1.b reveals the distinct difference in the spectral signature of blood for a control neonate (TSB of 2.4 mg/dL and Hb of 19.1 gm/dL) in comparison to a sick neonate (TSB of 29.8 mg/dL and Hb of 10.2 gm/dL). A graphic user interface was developed using LABVIEW software (National Instruments) for data acquisition, data analysis and generation of subsequent results [134, 135]. The algorithm for the work flow of the device is shown in Figure 4.1.c. The whole blood spectrum obtained from the neonate's nail bed was de-convoluted to obtain five independent signals at five wavelengths (462.92 nm, 539.34 nm, 568.09 nm, 577.2 nm and 620 nm). A comparative spectral response between a jaundiced and anemic infant (Subject 1) and a normal (Subject 2) and their de-convoluted spectra is shown in Figure 4.1.d and 4.1.e.

4.2.1.2. Development of the Machine Learning Algorithm:

The present study uses a sophisticated machine learning (ML) algorithm known as Artificial Neural Networks (ANN) to analyze the vast amount of data-set collected during the study. The main objective is to introduce artificial intelligence (AI) framework through machine learning (ML) techniques, which are dedicated algorithms to train the software to learn from data [136].

The ANN algorithm tries to imitate the network of a human brain by learning tasks and solving problems [137]. The input layers and output layers of the network are connected by single or multiple hidden layers and interconnecting nodes with variable 'weight factor' [138]. Utmost care was taken for spectrum data acquisition through the developed prototype. Figure 4.1.c illustrates the simple sequential program flow diagram of the software for accurate assessment of blood hemoglobin and bilirubin levels in neonates. After getting powered up, health check-up and initialization of the instrument takes place. If there is any discrepancy, the device auto-corrects different conditions and restarts automatically, followed by a pop-up window asking for patient details including name, age, sex, medical conditions etc. to be saved along with data in individual folders. The software next guides to store 'reference' and 'dark' spectra one time for a particular ambient condition. The dark spectrum was acquired in the presence of ambient light by turning off the source LED. The effect of light scattering from the nail bed was taken into account by recording the reference

spectrum. The reference spectrum was collected using a standard scatterer (WS-1 Reflectance Standards, Ocean Optics) with a spot size of 0.7 cm in diameter. The distance between the probe tip and the scatterer was maintained perpendicularly at a distance of ~1.5 cm, such that the maximum light was scattered. The pre-acquired dark spectrum and reference spectrum, (which were acquired each day before starting the data collection) were read from the preloaded file location for spectrum processing. It is to be noted that the dark and reference spectra were acquired each day before starting the data collection to avoid the potential effects of variation in ambient light. In case of a change in the measurement location both spectra were re-acquired. The integration time of the spectrometer was kept fixed at 3000 milliseconds and the boxcar width (Smoothening factor/running average) at 2 in this entire study for maintaining a proper signal to noise ratio (S/N) of the spectra. The average time to acquire reliable data using the device is approximately 30 seconds, whereas the time required to communicate the acquired data to the cloud is nearly 1 minute.

For data processing mechanism, the following structure describes the various layers of ANN used for the present study (Figure 4.2.).

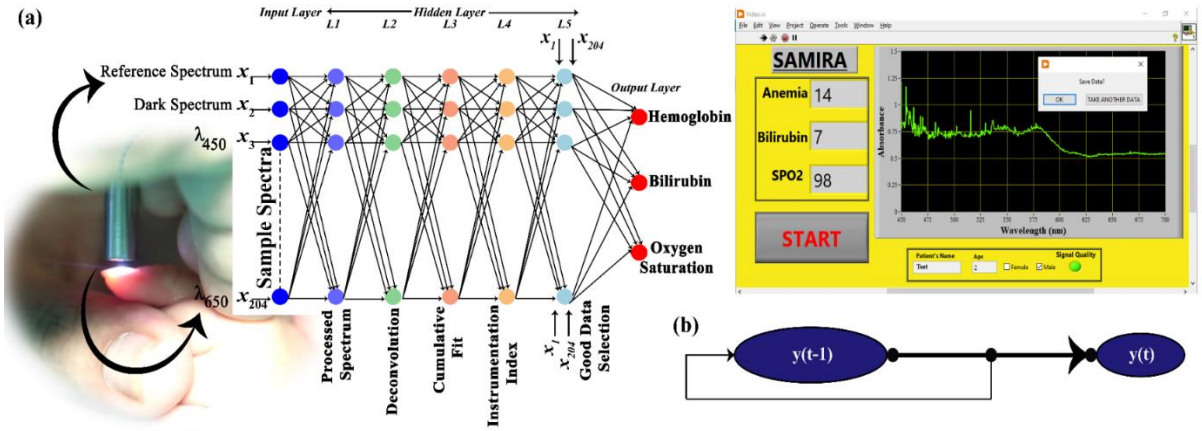

Figure 4.2. *Machine Learning Algorithm (a) Schematic representation of ANN used in the proposed device for the detection of Hemoglobin and Bilirubin (b) Time dependent continuous series flow diagram to estimate the blood parameters in regular time intervals (see text).*

4.2.1.2.1. Input Layer: The dark, reference and sample spectra containing the absorbance values from 450nm to 650nm are the primary elements used by the input layer.

4.2.1.2.1.1. Hidden Layer L1:

This layer generates the processed spectrum data using the following equation

$$Processed\ spectrum = -log_{10}\left(\frac{Sample\ Spectrum - Dark\ Spectrum}{Reference\ Spectrum - Dark\ Spectrum}\right) \quad (4.1)$$

The recording of the dark and reference spectrum and the processing of the acquired signal in accordance to equation (4.1), compensates the impact of light scattering from the neonate's nail bed. A training statement was also introduced in this layer which limits the amplitude of the absorbance range within 0.5 and 0.6 at 620 nm. This was maintained by the following instruction: $0.5 \leq Abs_{620\ nm} \geq 0.6$. This condition was given in order to maintain the spot size to be 0.7 cm and the distance between the probe tip and nail bed to be 0.6 cm.

4.2.1.2.1.2. Hidden Layer L2:

Layer for de-convolution of the processed spectrum (raw signals) and assessing the residuals (amount of scattered data from the fitted line) of the fit parameters to be acceptable by the system. The whole blood spectrum collected from the neonates' nail bed was de-convoluted into five Gaussian functions (Figure 4.1.d and Figure 4.1.e). The equation for each Gaussian function (y) is as follows:

$$y = y_0 + A\ exp\ (-0.5\ ((x-x_c)/w)^2) \quad (4.2)$$

where y_0 is the offset, A is the amplitude of the Gaussian curve, w is the full width by half maxima (FWHM) and x_c is the peak wavelength of the Gaussian curve. Each of the five Gaussian curves has a fixed peak wavelengths at 462.92 nm, 539.34 nm, 568.09 nm, 577.2 nm and 620 nm. The peak wavelengths were chosen on the basis of the pattern of absorption of oxygenated hemoglobin, de-oxygenated hemoglobin and of bilirubin. This layer is also responsible for generation of membership functions, where the peak wavelength of 462.92 nm corresponds to the absorption of bilirubin, 539.34 nm and 577.2 nm corresponds to the Q bands of oxy-hemoglobin and that of 568.09 nm corresponds to the de-oxygenated peak of hemoglobin. The additional peak at 620 nm has been considered to correct the baseline and scattering contributions from the acquired spectrum.

4.2.1.2.1.3. Hidden Layer L3:

In this layer a cumulative fit of the data was procured by adding each of the independent five Gaussian curves as follows.

$$y = y_0 + A_1 \exp(-0.5((x-x_{c1})/w_1)^2) + A_2 \exp(-0.5((x-x_{c2})/w_2)^2) + A_3 \exp(-0.5((x-x_{c3})/w_3)^2) + A_4 \exp(-0.5((x-x_{c4})/w_4)^2) + A_5 \exp(-0.5((x-x_{c5})/w_5)^2) \quad (4.3)$$

where A_1 A_2, A_3, A_4 and A_5 is the amplitude of the Gaussian curves with peak wavelengths at 462.92 nm, 539.34 nm, 577.2 nm, 568.09 nm, and 620 nm respectively, as mentioned earlier. In this layer, the area under each of the Gaussian curves is calculated using the Trapezoidal Rule, using the cumulative fitted equation. Assuming f(x) to be continuous over [a,b], the area under each of the Gaussian curve has been calculated using,

$$\lim_{n\to\infty} T_n = \int_a^b f(x)\,dx \quad (4.4)$$

4.2.1.2.1.4. Hidden Layer L4:

The instrumentation indices for the parameters were identified in this layer using the area under the five Gaussian curves and appropriate weightage was given to each one of them. It was noted that, summation of the area under the curves (AUC) corresponding to the wavelength of 539.34 nm and 577.2 nm ($AUC_{539.34}$+$AUC_{577.2}$) provide an estimation of haemoglobin as the absorption band at 539 nm and 577 nm of the blood spectrum corresponds to the absorption of oxygenated hemoglobin and the trough at 568 nm corresponds to the de-oxygenated hemoglobin [139, 140]. Similarly, bilirubin level was calculated by measuring the $AUC_{462.92}$ (as 462nm is the characteristic peak of bilirubin [141]). The amplitude of the Gaussians changed in relation to the amount of the biomolecule (bilirubin and hemoglobin) present. The change in the AUCs was mapped with the gold standard to obtain the calibration curve.

4.2.1.2.1.5. Hidden Layer L5:

In this layer the residual number of points of the fitted data from the acquired spectrum was analysed. The amount of the scattered data from the acquired signal with respect to the pre specified parameters given in hidden layer L3 is analysed in this layer. For the acceptability of the data, 98% of the residual data points necessarily must be within the range of $\pm$ 0.02% from the cumulative fitted curve. On the contrary, the scattered data points beyond $\pm$ 0.02% will be rejected. A comparison between the accepted data and the rejected data is shown in Figure 4.3.a to 4.3.d.

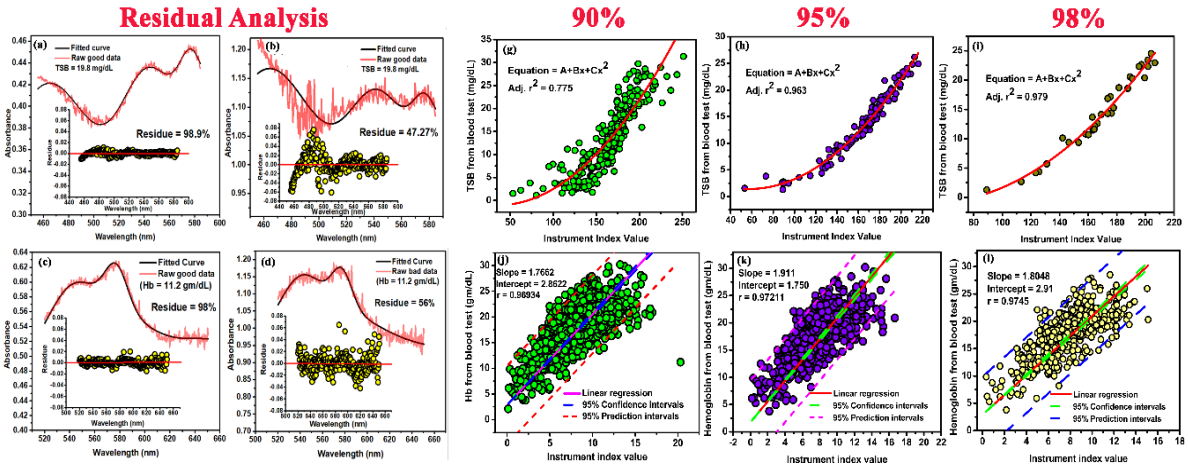

Figure 4.3. *Training sets of the device using the self-devised algorithm (a), (c): Raw and fitted data with the scattered residual points between ±0.02% from the cumulative fitted data, used for the estimation of TSB (19.8mg/dL) and Hb (11.2 gm/dL). (b), (d): Raw and fitted data with the scattered residual points beyond ±0.02% from the cumulative fitted data, discarded by the algorithm for the estimation of TSB (19.8mg/dL) and Hb (11.2 gm/dL). (g), (h), (i) The calibration curve between the instrument index values acquired from the device with the obtained TSB values from blood test at the three partitions (see text) in 229 neonates respectively. The calibration curve shows a polynomial nature with the TSB values and the instrument index function. (j), (k), (l) The calibration curve between the instrument index values acquired from the device with the obtained Hb values from blood test at the three partitions (see text) in 1072 neonates respectively. The calibration curve shows a linear dependency with the Hb values and the instrument index function.*

Initially, the machine was trained to accept the spectra, when 90% of the residual data points of the fitted data were within the range of ± 0.02%. The Adjusted r^2 for quantification of hemoglobin and bilirubin (Table 4.1) was found to be 0.77, 0.96 and 0.95 respectively for this training data set (Figure 4.3.g). Thus, a library containing the hemoglobin and bilirubin values of neonates were prepared. The prototype-specific instrument indices were clinically validated using a regression analysis (Figure 4.3.) [142, 143]. The minimization problem was utilized to minimize the error between the predicted value and the actual value using the following equations

$$Minimize \frac{1}{n} \sum_{i=0}^{n} (predi_i - y_i)^2 \tag{4.5}$$

$$J = \frac{1}{n} \sum_{i=0}^{n} (predi_i - y_i)^2 \tag{4.6}$$

where, J is the minimization function. The difference between the predicted values and the acquired values measures the error difference. The Mean Squared Error (MSE) function over all the data points, has been computed by squaring the error difference and summed over all data points and divided that value by the total number of data

points. To reduce the error the machine was trained to accept the spectra, when 95% of the residual data points of the fitted data were within the range of $\pm$ 0.02%. The Adjusted r^2 for quantification of hemoglobin and bilirubin was found to be 0.96 and 0.97 respectively for this training data set (Figure 4.3.). However, the standard deviation was $\pm$5.4 for the estimation of the two blood parameters. Finally, the machine was trained to accept the spectra, when 98% of the residual data points of the fitted data were within the range of $\pm$ 0.02%. The Adjusted r^2 for quantification of hemoglobin, and bilirubin was found to be 0.96 and 0.97 respectively for this training data set (Figure 4.3.). The hidden layer L5 basically identifies good data and bad data, through the error calculation. Figure 4.3.a-4.3.d shows clearly, how the good data is remarkably different from bad data in terms of the amount of scattered data from the cumulative fitted line. The processed data in a data library and deposited locally as well as in the cloud-storage. Provision of a dynamic calibration library strengthens the overall algorithm of the device by iterative method. This layer is responsible for decision making protocol as well. Identification of a good data leads to output layer, where blood report would be generated, whereas, for bad data, back-propagation technique would be adopted.

4.2.1.2.2. Output Layer:

Output layer estimated the hemoglobin and bilirubin of the neonates and displayed them. Consequently, it also displayed whether the neonate is suffering from, either anemia or jaundice. The IOT enabled device enables its user to send blood reports via email and SMS. If anemia is detected, the online report may be dispatched to the doctor or patient party to expedite the treatment procedure. Finally, a dialog box appears to ensure that whether the job is to be terminated or repeated. The easy and user- friendly operating software interface makes the device to be handled by any layman without any prior medical or instrumentation knowledge.

The developed prototype can detect the blood parameters in equal time intervals and is suitable for time series monitoring governed by the following equation:

$$y\,(t) = f\,(y(t\text{-}1)\ldots\ldots y(t\text{-}d)) \tag{4.7}$$

For the neonates undergoing phototherapy, the equal interval time series analysis would be compared with the Bhutani nomogram [7], to detect the risk level associated with infant's hours of age and serum bilirubin concentration. For haemolytic anaemic patients, time dependent data monitoring of haemoglobin will be crucial for treatment management and to determine the future courses of therapeutic action.

4.2.1.3. Calibration, Validation and Repeatability of the Instrument:

In order to, acquire the optimum condition for data acquisition, we performed data analysis using the self-devised algorithm in 3 different partitions on the calibration dataset. The dataset was divided into 3 partitions depending on the amount of scattered data points from the cumulative fitted curve. The three partitions are 90% (when 90% of the data points are within the range of $\pm$0.02); 95% (when 95% of the data points are within the range of $\pm$0.02) and 98% (when 98% of the data points are within the range of $\pm$0.02).

The correlation plot of the instrument at the three partitions with the two blood parameters calculated from the standard biochemical test on 1784 neonatal subjects shows three patterns of dependency on the blood parameters (Figure 4.3.g-4.3.l). Figure 4.3.g-4.3.i shows the second order polynomial dependency of the instrument index values with serum TSB levels for all the three partitions. The Adjusted r^2 was found to be as follows: when 90% of the data points are within the range of $\pm$0.02, 0.77. When 95% of the data points are within the range of $\pm$0.02, the adjusted r^2 is 0.96 and when 98% of the data points are within the range of $\pm$0.02, the adjusted r^2 is 0.97. The instrument index values maintain a linear relationship with the Hb values obtained from blood tests for all the partitions (Figure 4.3.j-4.3.l). The Pearson's correlation coefficient, r was found to be 0.969 (slope=1.7622; intercept=2.862) when 90% of the data points are within the range of $\pm$0.02. When 95% of the data points are within the range of $\pm$0.02, correlation coefficient, r was found to be 0.972 (slope=1.911; intercept=1.75) and when 98% of the data points are within the range of $\pm$0.02, the correlation coefficient, r was 0.9745 (slope=1.8; intercept=2.91). The Adjusted r^2 was found to be as follows: when 90% of the data points are within the range of $\pm$0.1. 0.953;

When 95% of the data points are within the range of ±0.05, the adjusted r^2 is 0.974 and when 98% of the data points are within the range of ±0.02, the adjusted r^2 is 0.989.

A total number of 1935 neonates were selected for validation of the instrument (Figure 4.4.). The instrument was validated in 409 subjects suffering from neonatal jaundice. 65 anemic subjects, and 223 subjects suffering from hypoxia. The remaining 1238 subjects were taken as control population for the purpose of validation of the device. All the datasets were divided into three partitions and the analyzed using the developed algorithm. Linear regression and Bland-Altman analysis was performed to evaluate the correlation between the obtained data produced by the instrument with the gold standard clinical laboratory tests.

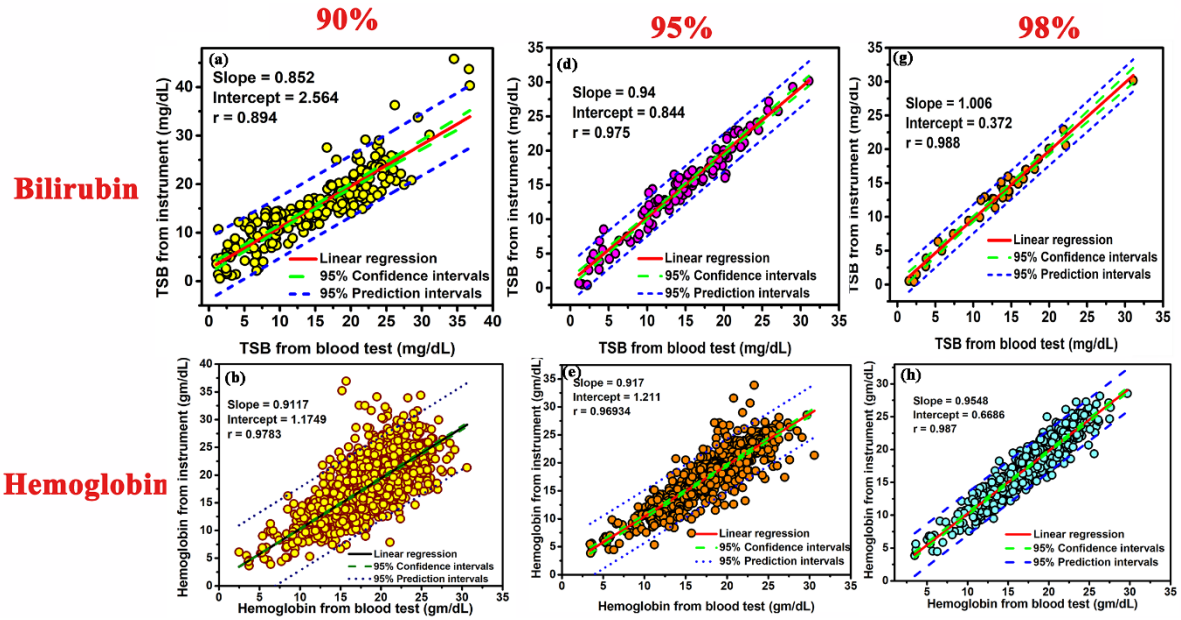

Figure 4.4. *Validation of the instrument in different partitions of the dataset. Linear regression plot of the developed device verses TSB on 230 neonates, when (a) 90% of the acquired data points are scattered within ± 0.02% from the cumulative fitted curve in the residual plot. (d) 95% of the acquired data points are scattered within ± 0.02% from the cumulative fitted curve in the residual plot. (g) 98% of the acquired data points are scattered within ± 0.02% from the cumulative fitted curve in the residual plot. Linear regression plot of the developed device verses Hb on 1073 neonates, when (b) 90% of the acquired data points are scattered within ± 0.02% from the cumulative fitted curve in the residual plot. (e) 95% of the acquired data points are scattered within ± 0.02% from the cumulative fitted curve in the residual plot. (h) 98% of the acquired data points are scattered within ± 0.02% from the cumulative fitted curve in the residual plot.*

Linear regression analysis between the values obtained from the instrument at the three partitions with the blood tests show a more correlation when 98% of the data points are within the range of ±0.02 (for TSB estimation, r =0.988; slope=1.006;

intercept=0.372; for Hb estimation, r = 0.987; slope=0.954; intercept=0.668, Figure 4.4.g-4.4.h) in comparison when 95% of the data points are within the range of ±0.02 (for TSB estimation, r =0.975; slope=0.94; intercept=0.844; for Hb estimation, r =0.969 slope=0.917; intercept=1.211, Figure 4.4.d-4.4.e). On the contrary, when 90% of the data points are within the range of ±0.02 the correlation was reduced (for TSB estimation, r =0.894; slope=0.852; intercept=2.564; for Hb estimation, r = 0.9783; slope=0.911; intercept=1.1749, Figure 4.4.a- 4.4.b). Bland-Altman analysis (Figure 4.5.) also corroborated the highest correlation between the when 98% of the data points are within the range of ±0.02 and the obtained blood parameter values of TSB and Hb for both normal and diseased neonatal subjects in comparison to the other two partitions. The statistical parameters when 98% of the data points are scattered within a range of ±0.02 are as follows: with the TSB values obtained from the biochemical test, (bias for normal=-0.491 mg/dL, jaundiced subjects=0.099 mg/dL ; 95% limits of agreement for normal=-2.37 mg/dL to 1.3 mg/dL and jaundiced subjects=-1.98 mg/dL to 1.71 mg/dL, Figure 4.5.c and 4.5.l) and with Hb values obtained from the blood tests (bias for normal; -0.08 gm/dL, anemic; 0.19 gm/dL; 95% limits of agreement for normal; -3.43 gm/dL to 3.10 gm/dL, anemic; -2.04 gm/dL to 2.07 gm/dL and -0.93 gm/dL to 1.23 gm/dL, Figure 4.5.f and 4.5.o). The statistical parameters when 95% of the data points are within the range of ±0.02 are as follows: with the TSB values obtained from the biochemical test, (bias for normal=0.25 mg/dL, jaundiced subjects=-0.11 mg/dL; 95% limits of agreement for Normal= -2.56 mg/d to 3.13 mg/dL, Jaundice subjects= -2.7 mg/dL to 2.62 mg/dL Figure 4.5.b and 4.5.k) and with Hb values obtained from the blood tests (bias for normal=-0.3104 gm/dL anemic=0.4952 gm/dL; 95% limits of agreement for Normal=-5.17 gm/dL to 4.55 gm/dL, Anemic= -2.36 gm/dL to 3.35 gm/dL Figure 4.5.e and 4.5.n). However, when the 90% of the data points are within the range of ±0.02 , the statistical parameters are as follows: with the TSB values obtained from the biochemical test, (bias for normal=0.37 mg/dL, jaundiced subjects=0.153 mg/dL; 95% limits of agreement for normal= -2.85 mg/dL to 4.2 mg/dL and jaundiced subjects=-6.39 mg/dL to 6.56 mg/dL, Figure 4.5.a and 4.5.j) and with Hb values obtained from the blood tests (bias for Normal=-0.43 gm/dL, Anemic= 0.91 gm/dL; 95% limits of agreement for Normal=-8.14 gm/dL to 7.26 gm/dL,

Anemic= -3.71 gm/dL to 5.54 gm/dL, Figure 4.5.d and 4.5.m). 95% limits of agreement means that 95% of the differences are assumed to lie within these limits and how far apart the measurements obtained using the two methods are likely to be for most individuals. Bias refers to the difference between the expected value obtained from the device and the true value of the parameter being estimated obtained from the haematological tests. Detailed results of comprehensive statistical analysis are presented in Table 4.2.

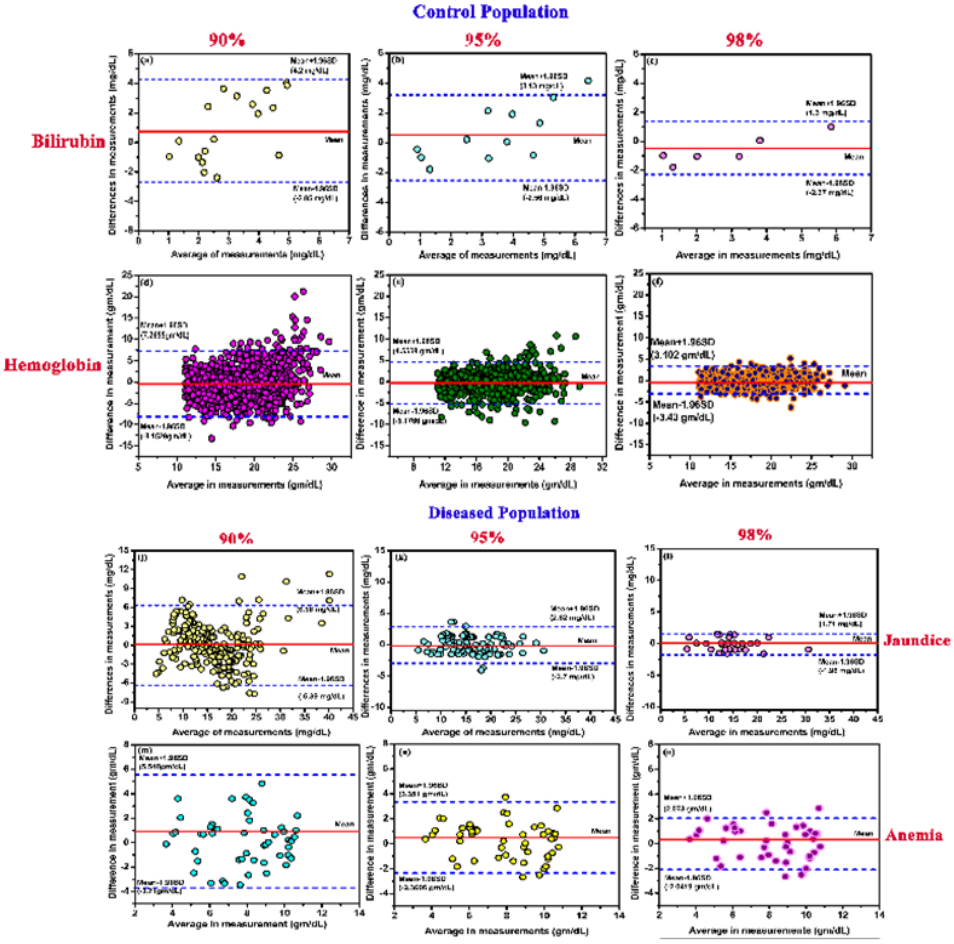

Figure 4.5. *Relationship between the developed device and the blood parameters obtained from blood sampling in normal neonates (Control population) and diseased neonates. Bland-Altman plots (mean and 95% limits of agreement) between the developed device and TSB values in control and jaundiced subjects respectively when, (a),(j) 90% of the acquired data points are scattered within ± 0.02% from the cumulative fitted curve in the residual plot. (b), (k) 95% of the acquired data points are scattered within ± 0.02% from the cumulative fitted curve in the residual plot. (c), (l) 98% of the acquired data points are scattered within ± 0.02% from the cumulative fitted curve in the residual plot. Bland-Altman plots (mean and 95% limits of agreement) between the developed device and Hb values in control and anemic subjects respectively when, (d),(m) 90% of the acquired data points are scattered within ± 0.02% from the cumulative fitted curve in the residual plot. (e), (n) 95% of the acquired data points are scattered within ± 0.02% from the cumulative fitted curve in the residual plot. (f), (o) 98% of the acquired data points are scattered within ± 0.02% from the cumulative fitted curve in the residual plot.*

In order to check the repeatability of the device, measurement was taken from the neonate's nail bed 5 times by the same observer. The repeatability of the device to parameterize the hemoglobin and bilirubin values was performed in 135 neonates (Figure 4.6).

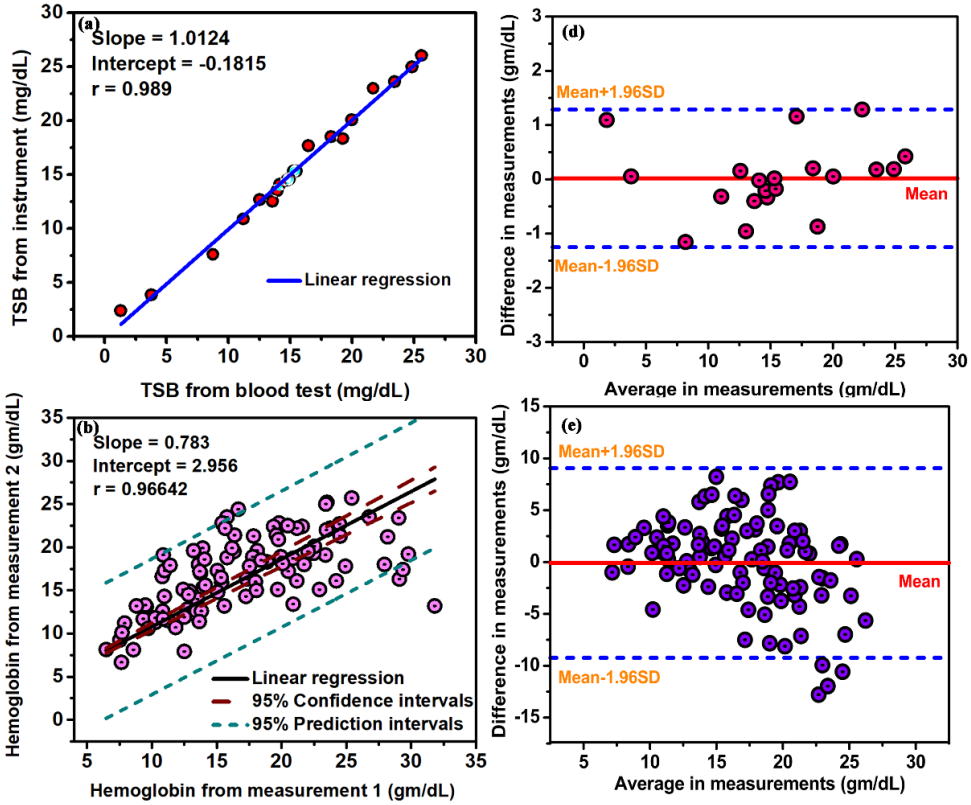

Figure 4.6. *Repeatability of the data acquired using the developed device. Linear Regression analysis for five successive values of (a) Bilirubin and (b) Hemoglobin measurement on the same subject by the same observer. Bland-Altman analysis for five successive values of (d) Bilirubin and (e) Hemoglobin measurement on the same subject by the same observer.*

We found a standard deviation of 3.2mg/dL between back-to-back measurements in the same subject by the same observer in the estimation of bilirubin. For the estimation of hemoglobin, the standard deviation was found to be 4.6 gm/dL. The calculated SD and mean were almost the same in both the measurements, for both the two blood parameters. The linear regression analysis between the two measurements further confirmed the accuracy of the two measurements. For the repeatability analysis, the correlation between the measurements are as follows: for TSB measurement, ($r=0.989$; slope=1.0124; intercept=0.1815, $P < 0.001$) and for the estimation of Hb ($r=0.96642$; slope=0.783; intercept=2.95, $P < 0.001$). Bland Altman analysis was performed to confirm the correlation between successive measurements.

For TSB measurement (bias = 0.183 mg/dL, 95% limits of agreement =-1.25 to 1.287 mg/dL) and for Hb estimation (bias = -0.85gm/dL 95% limits of agreement = -9.2 gm/dL to 9.05 gm/dL).

The conventional non-invasive trans cutaneous methods are yet to replace the invasive method of blood sampling due to certain shortcomings of the transcutaneous devices. The TcB (trans cutaneous bilirubin) measured by these non-invasive devices consists of a major contribution from the extravascular bilirubin, which is a completely a different physiological parameter in comparison to the TSB. The unpredictable process that regulated the dynamics of bilirubin in the extravascular space makes a 1 to 1 comparison of TSB and TcB impossible [26, 27]. Confinement of the measurement volume only to the intravascular space could help in overcoming the problem [27]. Whereas, the Hb values acquired by the available transcutaneous hemoglobin meters have a significant positive bias [144, 145]. This in turn, causes improper management particularly to the diseased population that tend to get their Hb and blood saturation values over estimated. The SAMIRA device is based on such spectroscopy based approach where the information is collected from the vascular bed underneath the nail plate [146]. Thus, we hypothesize that SAMIRA will be able overcome the limitations of the conventional trans cutaneous devices for the simultaneous measurement of two blood parameters from a single optical spectrum. Our results suggests that the bilirubin and hemoglobin values obtained from SAMIRA has a positive linear correlation with both the two blood parameters (for Hb measurement, r = 0.96; for bilirubin measurement, r = 0.98). Using the self-devised algorithm and multivariate regression analysis, we observed that when 95% of the acquired data points are within the range of $\pm$0.02, the optimum condition for acquiring reliable data from the neonates was achieved. Furthermore, the demographic analysis (Table 3.1, Chapter 3) showed that postnatal age, exclusive breastfeeding, gestational age or any other risk factor are not associated with any variation in the performance of the device. No bias of birth weight and/or gestational age was found to observe on the non-invasive blood parameter measurements in the intensive study on 4318 neonatal subjects. Moreover, as the study was conducted on a subgroup of Indian population, the interference of dark skin colour (or variation within the Indian subpopulation) can

also be ruled out, as Indian population consists of mixed races with varied skin tones. Skin tone was not found to be a confounding factor for the estimation of Hb or TSB. However, the device slightly overestimated the bilirubin values by 5mg/dL when the TSB exceeded 15 mg/dL. Otherwise, it marginally overestimated the bilirubin values by less than 2 mg/dL. Although this may result in unnecessarily prolonged hospitalization, it eliminates the chances of serious clinical errors like mismanagement of a diseased infant and hence decreases infant morbidity and mortality.

Table 4.1. *Statistical parameters defining the correlation of the three partitions of the calibration dataset (see text for details) with the two blood parameters*

Amount of scattered data from the cumulative fitted curve	**Statistical Test**	**Parameter**	**Hb measurement**	**TSB measurement**
90%	Linear Regression Analysis	Regression Coefficient (r)	0.77	0.74
		P value	<0.0001	<0.0001
		Slope	0.9117	0.852
		Intercept	1.1749	2.564
95%	Linear Regression Analysis	Regression Coefficient (r)	0.87	0.84
		P value	<0.0001	<0.0001
		Slope	0.917	0.94
		Intercept	1.211	0.844
98%	Linear Regression Analysis	Regression Coefficient (r)	0.98	0.98
		P value	<0.0001	<0.0001
		Slope	0.9548	1.006
		Intercept	0.6686	0.372

Table 4.2. *Statistical parameters defining the correlation between the developed device and the blood test in a diseased population*

Category	**Statistical Test**	**Parameters**	**Values**
Anemic Subjects (Hb < 11 gm/dL)	Bland Altman Analysis	Bias (95% CI)	0.19 gm/dL
		Standard Deviation	1.401
		Limits Of Agreement	-2.0419 gm/dL to 2.073 gm/dL
Jaundiced Subjects	Bland Altman Analysis	Bias (95% CI)	0.099 mg/dL
		Standard Deviation	0.9451 mg/dL
		Limits Of Agreement	-1.98 mg/dL to 1.71 mg/dL
Subjects with heart diseases	Bland Altman Analysis	Bias (95% CI)	-1.05%
		Standard Deviation	1.93
		Limits Of Agreement	-3.45 to 1.6

The correlation coefficient between the developed device and the TSB values was found to be 0.88, which was better than the correlation shown other non-invasive devices which was of the order of 0.7-0.8 [147, 148]. It has to be noted that these studies were conducted on white population in which the conventional TcB meters generally show good efficacy. Several studies have reported that TcB meters overestimate bilirubin values in dark skin populations like Hispanic, Asian, African, etc. [24, 28, 149].In our study values of overestimation by ≥ 2 mg/dL, ≥ 3 mg/dL and ≥ 4 mg/dL were found to be 25%, 4.2% and 0.9% respectively. To the best of our knowledge, no TcB device has been developed to address bilirubin overestimation in the black population, and a low-cost, non-invasive, point of care device for these ethnic groups holds promise for low and middle income countries [150]. The correlation of the device in the anemic region (Hb < 11 gm/dl) was found to be 0.99, which was highly comparable with the commercially available devices with a correlation coefficient of 0.95 [22, 23]. It has to be noted that these available instruments estimated the hemoglobin values in adults. Due to the different architecture and thickness of the skin, adult hemoglobin meters are not a suitable comparison to the neonatal trans

cutaneous hemoglobin meters. The Bland-Altman analysis confirmed that SAMIRA was highly sensitive in the anemic region, which suggests that even the mildest form of anemia can be detected by the device.

This is one of the few studies that extensively assessed the performance of a non-invasive device in neonates suffering either from hyperbilirubinemia and anemia or hypoxia. We think that the strength of the study lies in the prospective design, a large number of sample in each category, the intra-racial variation in the dark skin color, the parallel measurement of two blood parameters (bilirubin and hemoglobin) by two methods (SAMIRA and the biochemical tests), and the collection of the blood for the routine biochemical tests by regular nurses for clinical use rather than specifically for the study purpose in which conditions might be optimized. The conventional measurements were performed by the experienced clinical biochemists and laboratory technicians of a tertiary care hospital, reducing the possibility of operator error. Overall, we believe that our results provide a robust estimation of the accuracy of non-invasive hemoglobin and bilirubin measurement by a new device and the sources of error are applicable to routine clinical settings.

Our study had few limitations over the other trans-cutaneous devices. The available trans cutaneous instruments did not perform well on subjects having a bilirubin report of more than 15 mg/dL. [151, 152]. In subjects where the bilirubin crossed more than 15 mg/dL, it was associated with severe complications like exchange transfusion and was avoided for complications. Another confounding factor of the study was that measurements on neonates with less than 500 grams of body weight was not considered for the study due to their added complications. Studying the population having high TSB values and also associated with the risk factors for hyperbilirubinemia, anemia and hypoxia, and manipulation of the intensity of illumination can further increased the accuracy of the device. Lastly, the results obtained from the non-invasive measurements (SAMIRA) were used for clinical management. A real-time clinical management using these readings have helped to assess the actual accuracy of this device to reduce painful blood sampling in day-to day clinical practice.

4.2.2. Molecular Co-localization of Multiple Drugs in a Nanoscopic Delivery Vehicle for Potential Synergistic Remediation of Multi-drug Resistant Bacteria [153]:

The drug rifampicin is reported to be hydrophobic [154-156], as it is less soluble in aqueous solution. However, in aqueous medium (pH = 7) RF can be amphiphilic or amphoteric [157, 158] considering its charge distribution.

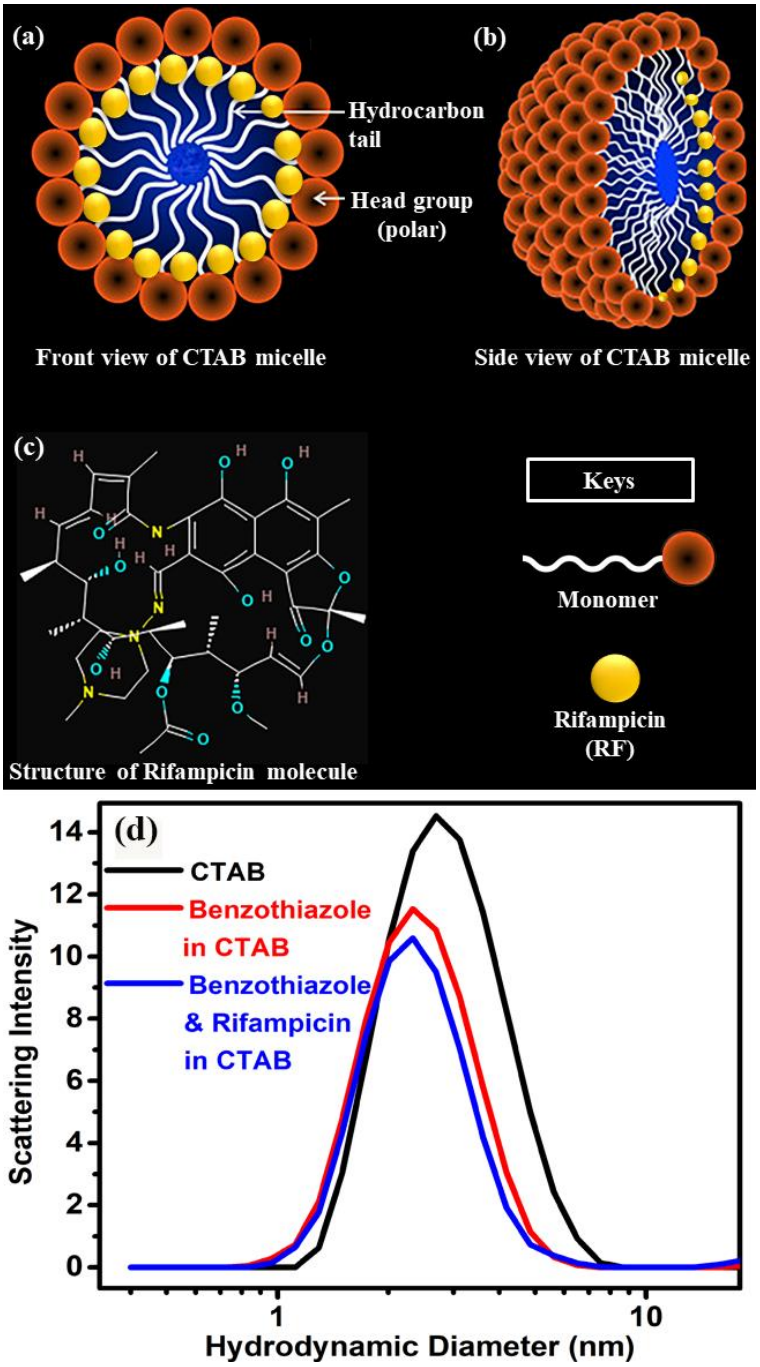

Figure 4.7. *(a) Front view of CTAB micelle (b) Side view of CTAB micelle (c) Structure of rifampicin molecule (d) Scattering Intensity of 50 mM CTAB micelle, BT added to CTAB and BT and RF added together to CTAB as obtained from the Dynamic Light Scattering study.*

Thus, RF is expected to interact superficially with the cationic CTAB micelle or bind to the outer surface of CTAB micelle which is also amphiphilic [159]. Considering that RF at pH 7 remains in the Zwitterionic form [157], it can interact electrostatically with the head group of the CTAB micelle and is therefore most likely to stay in the micelle–water interface [154] as portrayed in Figure 4.7.a and Figure 4.7.b. Dynamic light scattering (DLS) studies (Figure 4.7.d) indicate that the CTAB micelles form mono-dispersed spheres, in aqueous buffer, of hydrodynamic diameter (d_H) of 2.69 nm. After addition of the energy donor (BT) and the energy acceptor (RF) in 50 mM micellar solution, the hydrodynamic diameter peaks were observed to remain almost in the same position confirming our conjecture of binding of RF (Figure 4.7.c) inside the periphery of the cationic micelle. Except Dynamic Light Scattering (DLS), another technique is the HRTEM (High-Resolution Transmission Electron Microscopy) by which one can characterize the monodispersity of the micellar solution. Bahadur et. al. has already performed cryo-TEM at ~ 150 mM CTAB micellar solution and found it to be completely monodispersed which further discard the possibility of micellar aggregation in our study [160, 161] Another proof of the monodispersity is the UV-visible absorption of the drug loaded micelle where the existence of the aggregation can be ruled out by the higher absorption value of the drug at the absorption tail. Furthermore, our prepared micellar solution is completely transparent which further supports the monodispersity of the micellar solution at the particular concentration used in our study. The angstrom (Å) sized drugs should not bring any effect on the micellar size after encapsulation. The hydrodynamic diameter is calculated automatically by the instrument from the fitting parameter of the autocorrelation function. It is an average phenomenon and accuracy depends on the number of runs performed by an experimentalist during the experiment. Standard deviation of the Malvern DLS instrument in terms of hydrodynamic diameter lies within the range of ± 0.7 nm. In our study, the size reduction obtained as ~ ±0.4 nm as shown in Figure 4.7.d, and to the best of our understanding it is inconclusive as it lies within fluctuation range of the measurement. 50 mM, 3 mM and 4 mM stock solutions of CTAB in DI water (Milli-Q), RF in ethanol and BT in acetonitrile were prepared for the current work. The solutions were diluted according to the experimental study.

4.2.2.1. Forster Resonance Energy Transfer (FRET):

FRET is an energy transfer process between a pair of fluorophores, where the donor fluorophore, initially in its electronic excited state, transfers energy to an acceptor fluorophore [68, 162]. In our study, RF, a well-known anti tuberculosis drug, is chosen as an acceptor for studying FRET in CTAB because of two reasons. Firstly, RF, being a neutral dye, localizes in the interfacial region of the micellar headgroup and hydrophobic hydrocarbon chains [163].

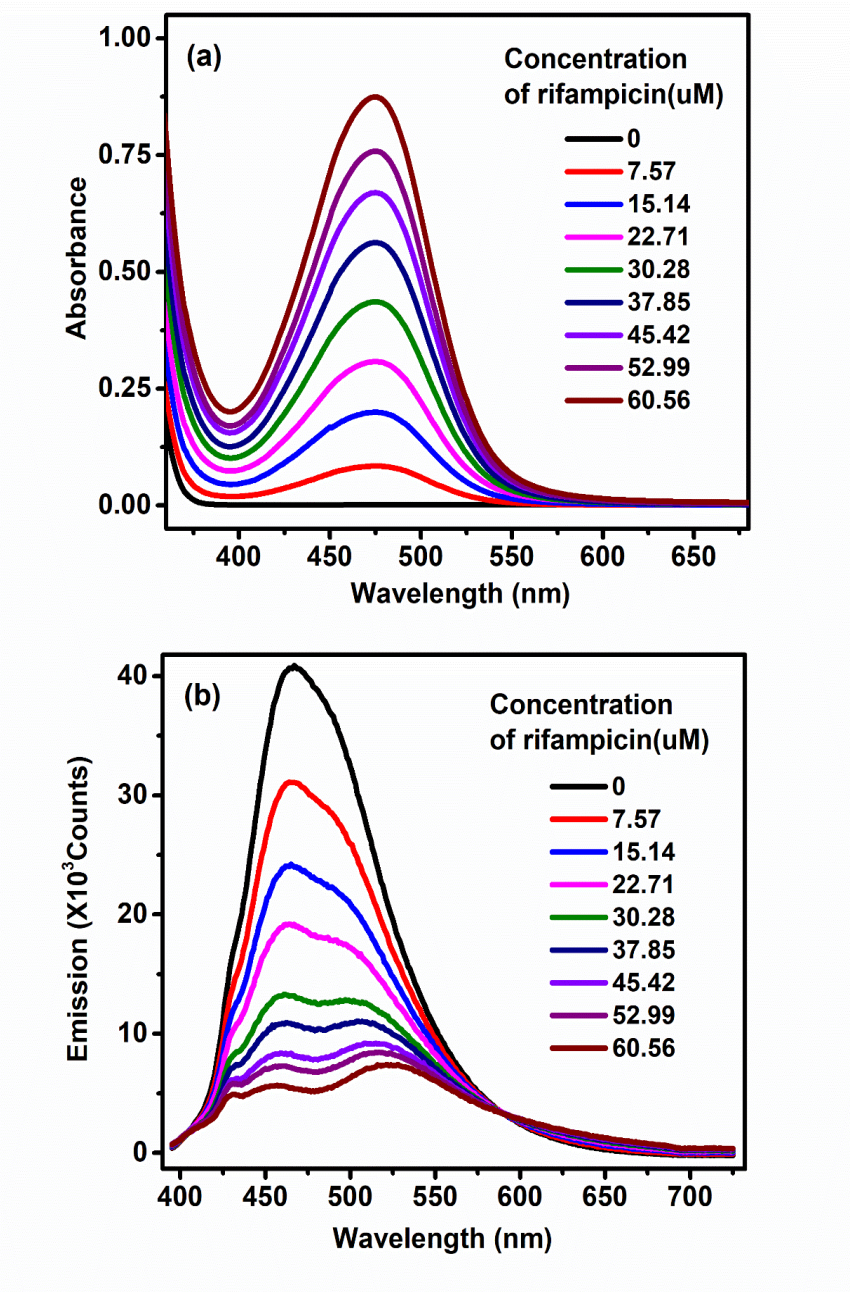

Figure 4.8. *(a) Absorbance spectra of Rifampicin (RF) in 50 mM CTAB micelles for concentrations 0μM to 60.56 μM (b) Emission spectra of benzothiazole in 50 mM CTAB without and with varying concentrations of RF from 0μM to 60.56 μM*

Secondly, the fluorescence spectra of BT as donor overlaps excellently (Figure 4.9.a) with the absorption spectra of RF (Figure 4.8.a). The drugs RF and BT were thus chosen due to their efficacy of forming FRET-pair. In order to study the co-localization of the two model drugs, FRET is found to be very efficient tool as indicated in our study. Figure 4.8.b and Figure 4.9.b show significant decrease in fluorescence intensity of BT in 50 mM CTAB solution upon addition of increasing amount of RF indicating to an efficient energy transfer from BT to RF. Time-resolved fluorescence decay of BT becomes distinctly faster (Figure 4.9.c) in presence of RF consistent with significant quenching of the fluorescence transients of BT in CTAB micelle. The average fluorescence lifetime of BT decreases remarkably (Table 4.3.) from 2.56 ns to 1.37 ns in presence of 10 μM of RF in 50 mM CTAB micelle confirming an efficient energy transfer from BT to RF which is consistent with a donor acceptor distance of 20.9 Å (Table 4.4.). This highly efficient (E = 46%, Table 4.4.) energy transfer from BT to RF is consistent with co-localization of both the drugs within the CTAB micelle.

Table 4.3. *Time-resolved decay parameters of BT in CTAB in absence and in presence of RF at two different concentrations*

System	τ1/ ns (%)	τ2/ ns (%)	τ3/ ns (%)	τavg/ ns (%)
BT in CTAB	0.302 (30%)	1.263 (14%)	4.11 (56%)	2.56
BT in CTAB+5 μM RF	0.209 (36%)	0.973 (18%)	4.07 (46%)	2.12
BT in CTAB+ 10 μM RF	0.042 (54%)	0.550 (21%)	4.00 (25%)	1.37

Table 4.4. *FRET parameters of BT (donor) and RF (acceptor) in CTAB micelle*

System	τD/ ns	τDA/ ns	E(%)	J (λ)/ M(-1) cm(-1) nm(4)	rDA in Å	hw in Å
BT in CTAB+5 μM RF	2.56	2.12	17	$5.16X10^{14}$	26.6	2.23
BT in CTAB+ 10 μM RF	2.56	1.37	46	$5.16X10^{14}$	20.9	3.29

Table 4.5. *Values of quenching parameters obtained from simplified Infelta Tachiya model*

System	k_0 (ns^{-1})	m	k_q (ns^{-1})
BT in CTAB+ 0 μM RF	0.17		
BT in CTAB+ 5 μM RF	0.17	0.21	0.74
BT in CTAB+ 10 μM RF	0.17	0.37	1.03

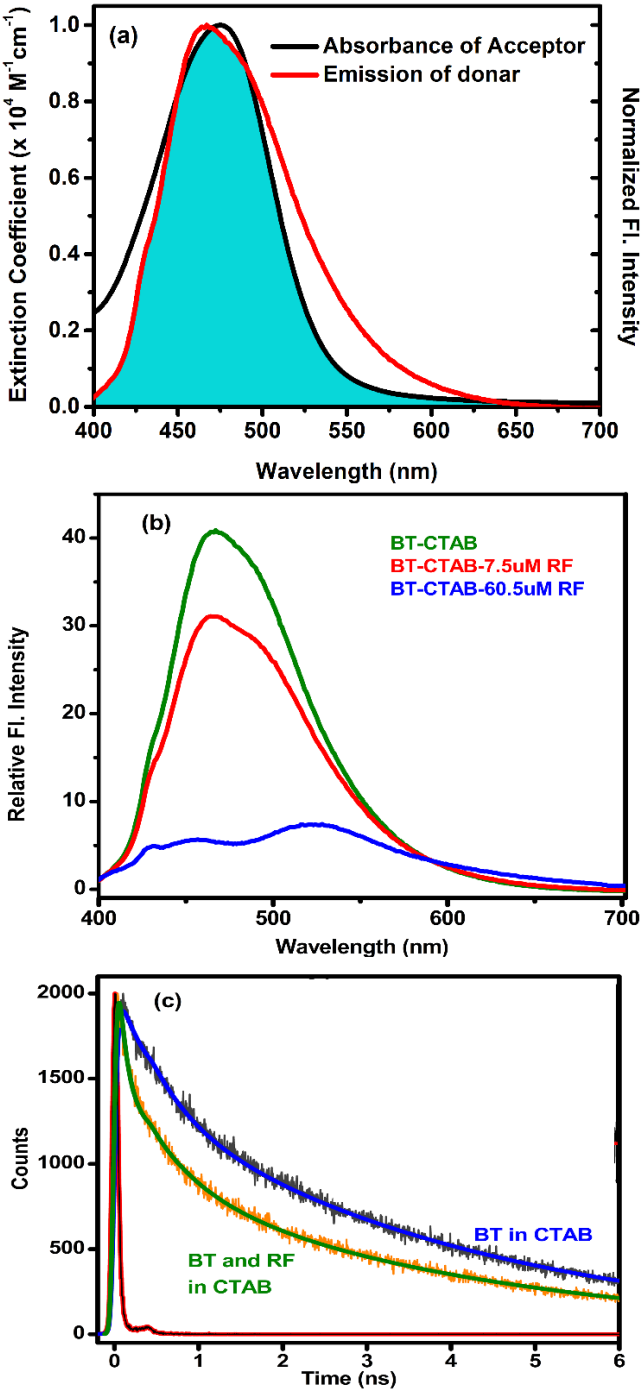

Figure 4.9. *(a) Spectral overlap of BT fluorescence (Red) and RF absorbance (black) when both are incorporated in CTAB micelle. (b) Forster Resonance Energy Transfer (FRET) process is of BT ligand to RF within the CTAB micelle is evident from the quenching of the steady-state fluorescence intensity. (c) Picosecond-resolved fluorescence transients of the BT ligand as donor in CTAB micelle in absence and in presence of RF as an acceptor.*

We have further employed the probability distribution (P(r)) of donor-acceptor distances to characterize the nature of the interaction of both the donor/acceptor at three different acceptor concentrations upon incorporation into the micellar cavity

(Figure 4.10.). The distribution function becomes broader at higher acceptor concentration relative to that of the lower concentration, which corresponds to the higher average amplitude in fluctuation of the donor-acceptor distance during energy transfer process for the former than the later.

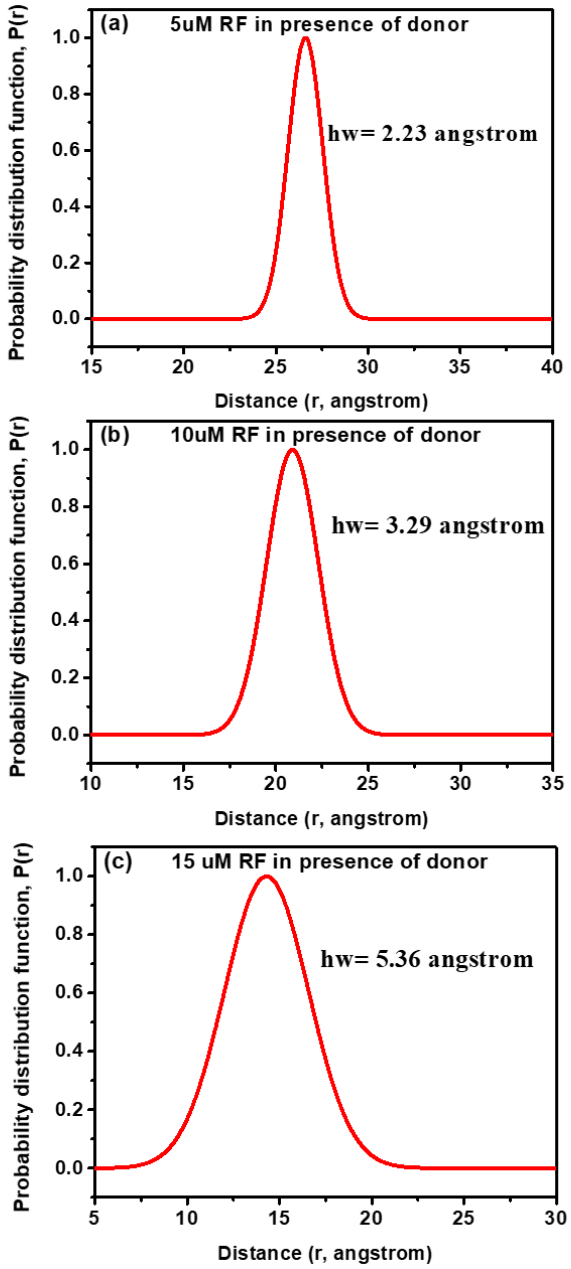

Figure 4.10. *Probability distribution of donor–acceptor distances between Rifampicin and 2-(2-hydroxyphenyl)-benzothiazole in CTAB micelles for different concentrations of acceptor (a) 5 μM (b) 10μM (c) 15μM.*

This is further reflected in increasing value (Table 4.4. and Figure 4.10.) of the 'hw' parameter (full width at half maxima) of the P(r) upon increasing concentrations of the acceptor concentrations (RF). The increase in the amplitude of the donor/acceptor

distance fluctuation is consistent with the progressive increase of the FRET efficiency and decrease in the donor/acceptor distance. Thus, the CTAB micelle turns out to be an efficient nanoscopic vehicle for co-encapsulation of both BT and RF, giving rise to a formulation with better antimicrobial activity than that based on only BT or RF.

4.2.2.2. Infelta-Tachiya Model for the Quantitative Estimation of the Donor/Acceptor Distribution in the Micellar cavity:

For better assessment of the association between RF and BT in CTAB micelle, it is important to estimate the distribution of RF molecules, because, the energy transfer efficiency solely depends on the availability of the acceptor molecules in the vicinity of the donor molecules. Fluorescence transients of the fluorophores in CTAB micelle in the excited state can be considered by the Infelta−Tachiya kinetic model [70].

$$P_n^* \xrightarrow{K_0} P_n \tag{4.8}$$

$$P_n^* \xrightarrow{nk_q} P_n \tag{4.9}$$

Herein P_n^* signifies the CTAB micelle containing excited BT fluorophores, and n is number of the acceptor RF molecules. In contrast, P_n denotes the micelle which contains n number of quencher molecules in absence of any excited BT fluorophore. k_0 is considered to be the total decay constant of the excited state donor fluorophore in absence of any acceptor molecules and k_q is the decay constant of the same fluorophore in CTAB micelle in presence of one quencher molecule. Subsequently the rate constant at which a donor molecule in micelle decays from an excited state in presence of 'n' number of quencher molecules can be expressed as k_0+nk_q and nk_q is the total energy transfer rate constant. In this particular kinetic model, it is postulated that the distribution of the quencher molecules around the vicinity of donor molecules follow the Poisson distribution [70] which can be defined as

$$p(n) = \frac{m^n}{n!} \times exp(-m) \tag{4.10}$$

where m is the total average number of quencher molecules in micelles available to quench the BZ fluorescence. Mathematically m can be expressed as

$$m = \frac{k_+[A]}{k_-} \tag{4.11}$$

where, k_+ and k_- are the associated rate constants by which an acceptor molecule enters the micellar cavity and exits from the cavity respectively. [A] is the concentration of the acceptor molecules in aqueous phase. By considering the above model, probability of finding the fluorophore molecules in its excited state at a particular time t can be expressed as

$$P^*(t) = P^*(0)exp\left[-\left(k_0 + \frac{k_0 k_+[A]}{k_- + k_q}\right) \times t + \frac{k_q^2 k_+[A]}{k_- \times (k_- + k_q)^2} \times \{1 - exp[-(k_- + k_q) \times t]\}\right] \quad (4.12)$$

For the case $k_- << k_q$, the above equation reduces to,

$$P^*(t) = P^*(0)exp\{-k_0 t - m \times [1 - exp(-k_q t)]\} \quad (4.13)$$

Figure 4.11. displays the fluorescence transients of BT in CTAB micelle in absence and in presence of various concentrations of RF (acceptor). The transients are fitted by using equation (4.13) based on the Infelta-Tachiya model of the excited state decay of the fluorophore. Those transients are well fitted to an exponential function ($X(t) = \int_0^t E(t') \times P(t - t')dt'$) where it is deconvoluted during the fitting procedure with respect to instrument response function (IRF) (by using Micromath Scientist). It is evident that the transients are fitted reasonably well (Figure 4.11.) by the Infelta-Tachiya model with reduced χ^2 value between 1.0-1.2. From the fitting parameters (Table 4.5.) it becomes evident that availability (m) of the RF molecules in the vicinity of the energy donor drug BT increases in CTAB micelle at increased concentration of RF. The energy transfer rate constant (k_q) of BT in CTAB micelle also increases with increasing concentration of acceptor (RF) indicating to closer association between BT and RF, which is consistent with the results obtained from FRET. However, conventional FRET analysis fails to provide overview of the distribution of the acceptor molecules in the donor vicinity in a nanoscopic micellar system quantitatively. The average number of acceptor (RF) molecules to quench the fluorescence of a single BT molecule is found to be < 1 (m = 0.3, Table 4.5.) even when excess concentration of RF is used, which discards the possibility of quenching of the donor (BT) fluorescence thorough the association of multiple acceptor molecules in the micellar cavity. Our observation is quite similar to that of [164] where the fluorescence of CDS QDs has been quenched by Ox170. The average number of attracted acceptor towards the trap state of QDs is more or less 1, which indicates that

the energy transfer process in the particular event occurs at a single molecule level of both donors/acceptors. Banerjee et. al. has further studied acceptor association induced quenching of donor transients in nanoscopic micellar surface by a potential carcinogen benzo[a]pyrene (BP) as donor in presence of various acceptors [165] which shows the available number of acceptor molecule in micellar surface to quench donor fluorescence is ~ 1 for a FRET efficiency of ~ 86%.

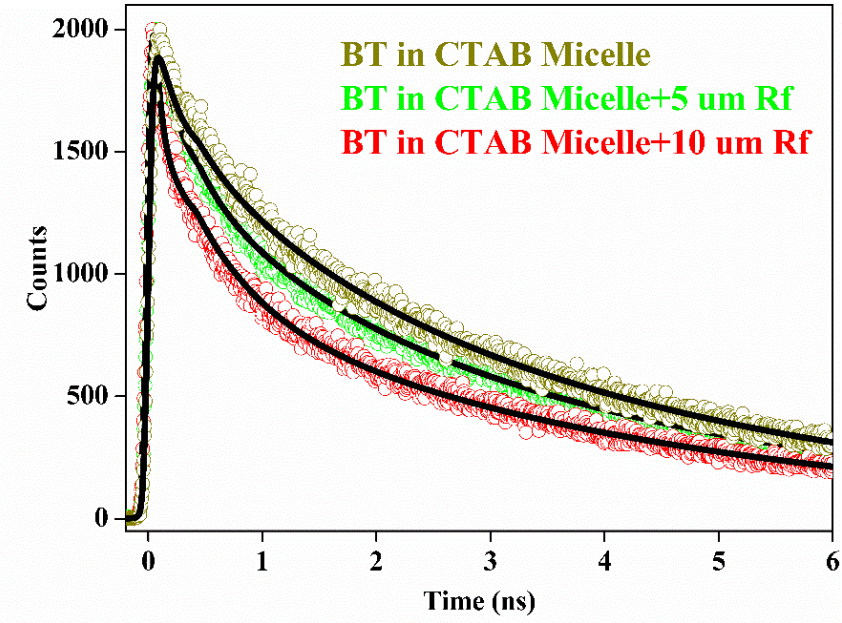

Figure 4.11. *Time-resolved fluorescence transients of BT in CTAB in absence and in presence of two different concentration of RF. The bold line represents the fitting line of the curves by considering simplified infelta tachiya kinetic model of donor acceptor association in CTAB micelle.*

4.2.2.3. Antibacterial Studies:

The antimicrobial activity of co-localized rifampicin-benzothiazole (RF-BT) in the nanoscopic system of a CTAB micelle was investigated against the MRSA growth to explore the sanitization potential against bacterial infections. To probe the antibacterial action of RF-BT in CTAB, RF in CTAB, BT in CTAB and CTAB only were used for incubating the culture for 3 h. As shown in Figure 4.12., almost no colonies were observed (the bacterial growth is found to have decreased by 99.88 % in CFU) for the RF-BT complex in CTAB. The bacterial growth is found to be decreased by 37.33 % in CFU for CTAB only. In case of RF and BT, the bacterial growth is found to be decreased by 69.46 % and 36.55 % in CFU respectively. On the other hand, a huge decrement of the bacterial growth is observed for RF in CTAB (decreased by 89.38 %

in CFU) and BT in CTAB (decreased by 96.46 % in CFU) separately. The anti-bacterial study of RF-BT in aqueous medium has not been performed as both the drugs show instability in aqueous solution and result in precipitation. The individual effects of RF in DMSO and BT in acetonitrile are explored along with the combined effect of RF and BT in CTAB. From these results it is evident that CTAB itself is an antibacterial agent and is efficient as a drug delivery vehicle for BT and RF which triggers an overall huge antibacterial effect.

For studying the drugs loading level, the drug solution (RF and BT) was prepared in PBS buffer, separately. Then the solution was dropwise added to the CTAB solution and incubated at room temperature followed by vigorous stirring for ~6 hrs. Free drug solution was removed by centrifuging the CTAB micelle encapsulated drug at 14000 rpm for ~50 mins. The absorbance of encapsulated drug ($A_{encapsulated}$) was obtained by using UV-visible spectrophotometer after dissolving the pellets obtained after centrifugation in PBS buffer at respective absorption maxima of the drugs. The encapsulation efficiency (EE) was found to be 70 % calculated by following equation [166]:

$$EE\ (\%) = \frac{A_{encapsulated}}{A_{total}} \times 100 \tag{4.14}$$

Where A_{total} was the absorbance of drug added to the solution before centrifugation. However, in the present work, our intension is to establish the synergistic effect of two co-localized drugs in a nanoscopic delivery vehicle for potential remediation of a multi-drug resistant bacteria. The details of the ratiometry of the drugs on the anti-bacterial effect including MED (Minimum Effective Dose) will be the subject of our future publication.

There are other methods to test bacterial viability like fluorescence microscopy-based assay by PI (Propidium Iodide) staining [167] or FACS (fluorescence-activated single cell sorting, a flow cytometry technique) [168]. However, in the present work, our aim is to establish the synergistic effect of two co-localized drugs in a nanoscopic delivery vehicle for potential remediation of a multi-drug resistant bacteria. Thus, we did not focus on multiple methods and followed a single standard method which is well reported in the literature to study the viability of bacteria [169, 170].

To study the effect of the drugs rifampicin and benzothiazole in CTAB micelle, bacterial cultures were performed 5 times for each group (control, RF in DMSO, RF in CTAB, BT in ACN, CTAB, BT in CTAB, RF+BT in CTAB etc.) and their difference was calculated to identify their significance level. The sample size for each of the groups were 5. The p-value was calculated using unpaired 2-tailed T-Test and $p<0.05$ was considered to be significant. The '*' represent p-value<0.1 and '****' represent p-value<0.0001[171].

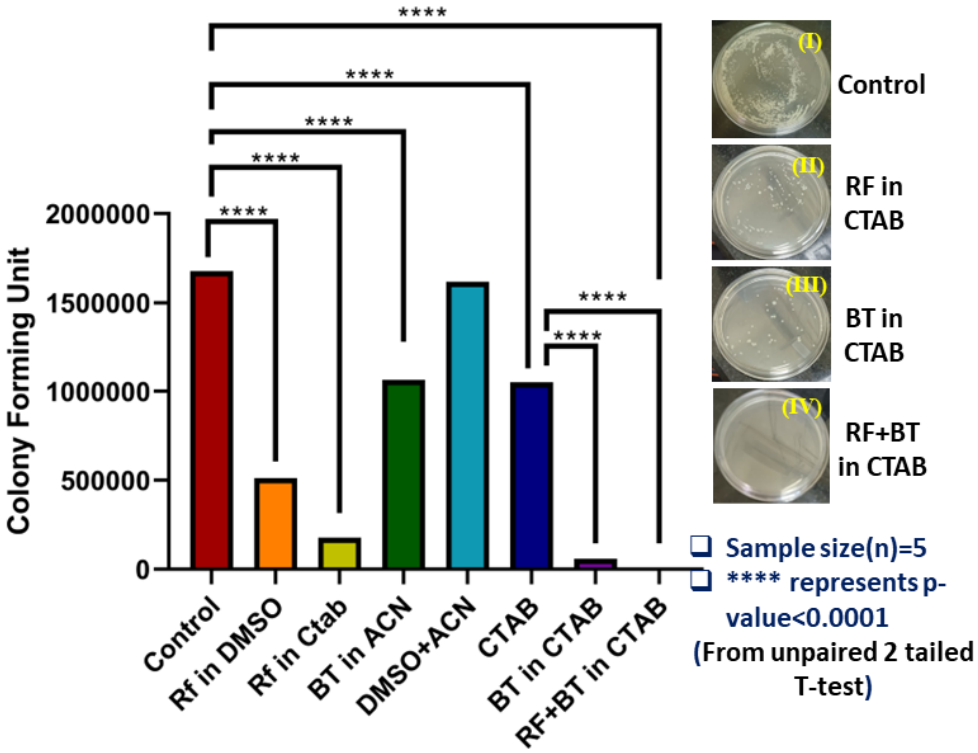

Figure 4.12. *Bacterial viability studies after treatment with RF-BT complex in CTAB (2 units), RF in CTAB (178 units), BT in CTAB (59 units), BT in ACN (1064 units) and RF in DMSO (512 units) where the control is 1677 units. The inset shows images of MRSA culture plates for (I) Control, (II) Treated with RF in CTAB, (III) Treated with BT in CTAB and (IV) Treated with RF-BT in CTAB. The sample size is 5(n) for each group. P-value for each group is <0.0001 as indicated by '****' obtained from unpaired two-tailed T-test (see text); p<0.05 was considered to be significant.*

4.2.2.4. Computational rationalization of anti-microbial effect (Synergism amongst CTAB, RF and BZ):

We have observed during the study that separately the compounds, RF, BT and CTAB show low to moderate level effectivity against the MRSA colonies whereas their combined effect has shown impressive results by successfully eliminating almost all (99.88%) the colonies of MRSA. The extraordinary effect of RF, BT and CTAB together may be hypothesized using predictive biological interactions. Figure 4.13. (a, b and c)

depicts compound-protein (CP) interactions for all three compounds, viz, CTAB, RF and BT separately using STITCH 5.0. Primary as well as secondary interactions were considered for CP network analysis.

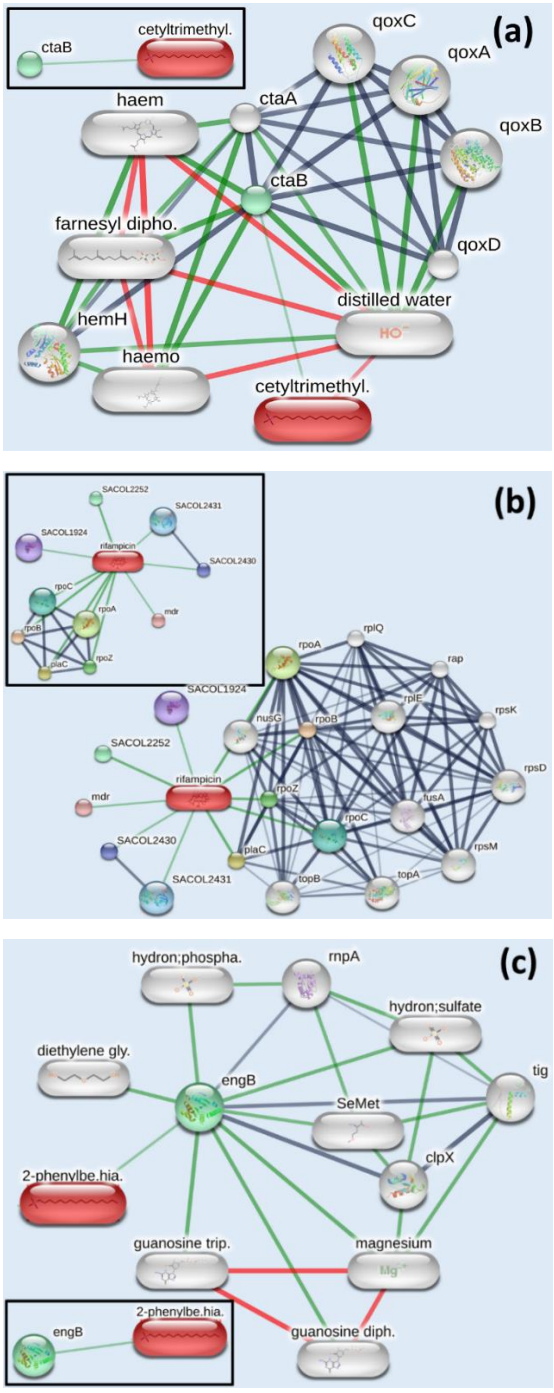

Figure 4.13. *Direct and indirect compound protein interactions of (a) CTAB (b) Rifampicin (RF) and (c) Benzothiazole (BT) on MRSA. The inset for each shows the direct interactions only.*

To grasp the mechanism of action of CTAB, rifampicin and benzothiazole on MRSA, three separate comprehensive tables (Table 4.6, 4.7 and 4.8) of target proteins/compounds and their biological activities are listed below.

Table 4.6. *Effect of Cetyltrimethyl Ammonium Bromide (CTAB) on MRSA*

Name of protein/compound	Mode of action	Biological function
ctaB	Direct	Protoheme IX Farnesyltransferase (ctaB) controls the hemolytic activity in MRSA [172] which in turn responsible for virulence of *S. aureus* [173]. CTAB decreases virulence activity, as well as enhanced pigment production and persister survival of MRSA [172] which justifies the low effectiveness of CTAB against MRSA.
ctaA	Indirect	CTAB alters the production of enzyme ctaB, which also affects the generation of cytochrome oxidase assembly protein ctaA. ctaA is a key enzyme which controls not only its starvation survival, but also, recovery, and Cytochrome Biosynthesis in *S. aureus* [174].
qoxA, qoxB, qoxC, qoxD	Indirect	Quinol oxidase subunits, qoxA, qoxB, qoxC, qoxD genes [175] play an important role in respiration and folding of membrane proteins [176]. Although presence of persister cells favored by the terminal oxidases may lead to chronic infection [177].
hemH	Indirect	Heme synthesis is directly related to iron metabolism. hemH gene catalyzes the heme biosynthesis, which influences the addition of ferrous iron (Fe2+) into protoporphyrin IX. Both porphyrins and iron facilitate the generation of highly reactive oxygen species,

		which is toxic to the cells and may lead to damage of most biomolecules [178]
farnesyl diphosphate	Indirect	High concentrations of farnesyl diphosphate, slows down the production of the protein heptaprenyl diphosphate synthase, which is responsible for menaquinone formation, a key electron transporter in many bacteria [179]

Table 4.7. *Effect of antituberculosis drug Rifampicin (RF) on MRSA*

Compound	Mode	Activity
SACOL1924	Direct	Potential multi-drug exporting ABC transporter permease/ATP-binding protein [180]
SACOL2252	Direct	AcrB/AcrD/AcrF family protein and part of multidrug resistance pumps [181]
Mdr-SACOL0700, SACOL2430, SACOL2431	Direct	ABC transporter ATP-binding protein/permease
plaC, SACOL1618	Direct	RNA polymerase sigma factor which facilitates the binding of RNA polymerase to specific initiation sites. It was observed that dispute in the plaC gene cause fatal effect on *S. Aureus* [182]
rpoZ, SACOL1222	Direct	DNA-directed RNA polymerase subunit omega which facilitates RNA polymerase assembly. Mutation in rpoZ gene leads to stress resistance and to fully form a biofilm. [183]

rpoA, SACOL2213, rpoB, SACOL0588 rpoC, SACOL0589	Direct	The RNA polymerase (RNAP) core enzyme of *S. aureus* comprises of four different subunits, which are encoded by the rpoA, rpoB, and rpoC genes, respectively. This DNA-dependent RNAP activates the transcription of DNA into RNA. Rifampin prohibits the production of RNAP and attaches to the β-subunit of RNAP within the DNA/RNA channel and hampers the elongation of RNA [184]
rplQ, SACOL2212,	Indirect	The rplQ gene encodes the ribosomal protein L17 of the 50S subunit. [185]
nusG, SACOL0582	Indirect	nusG is a transcription regulation protein which controls transcription elongation, termination and antitermination [186]
topB, SACOL2243	Indirect	DNA topoisomerase III, encoded by the topB gene, releases the supercoiling and torsional tension of DNA. It may have a pivotal role in bacterial genome stabilization. Mutants with topB deletion have a higher rate of spontaneous deletions [187].
topA, SACOL1267	Indirect	DNA topoisomerase I, encoded by the topA gene, releases the supercoiling and torsional tension of DNA, which is important for DNA repair [188]
rpsM, SACOL2215,	Indirect	*rpsM gene regulates* translation/ribosome structure. Its mutations may prompt the stress response and develop enhanced homogeneous resistance [189]

fusA, SACOL0593,	Indirect	mutations in fusA leads to high proportion of *S. aureus* colonizing skin and nares and are resistant to fusidic acid [190]
rpsD, SACOL1769	Indirect	30S ribosomal protein S4, one of the major rRNA binding proteins is also known as ribosomal protein small-subunit D (rpsD). It may be useful as a target [191]
rpsK, SACOL2214	Indirect	30S ribosomal protein S11, necessary for growth and reproduction [192]
rplE, SACOL2227	Indirect	50S ribosomal protein L5 which binds the 5S RNA into the large ribosomal subunit, and forms part of the central protuberance.
rap, SACOL2236,	Indirect	50S ribosomal protein L2 and one of the primary rRNA binding proteins. Clinical isolates of *S. aureus* are responsive to RAP (RNAIII-activating peptide), which facilitates biofilm formation capacity and virulence [193]

Table 4.8. *Effect of Benzothiazole (BT) on MRSA*

Compound	Mode	Activity
engB, SACOL1720,	Direct	ribosome biogenesis GTP-binding protein YsxC is necessary for regular cell division and for the maintenance of normal septation. It may also be involved in ribosome biogenesis [194]
rnpA, SACOL2739,	Indirect	The protein component of ribonuclease P (RNase P), rnpA is responsible for mRNA decay and may also have a role in bulk mRNA

		turnover. This makes it a suitable target for antimicrobial drug discovery [195]
clpX, SACOL1721,	Indirect	ATP-dependent protease ATP-binding subunit ClpX. In MRSA, clpX is an essential element which governs virulence [196]
tig, SACOL1722	Indirect	trigger factor involves in protein export in a mouse model of infection. tig gene mutation led to reduced biofilm development but no substantial decrease in virulence [197]
diethylene glycol	Indirect	Poly(ethylene glycol) coatings are familiar for reduction in microbial adhesion by numbers and binding strength [198]
guanosine diphosphate guanosine triphosphate	Indirect	They help bacteria to adjust according to different environmental stresses [199]
Magnesium	Indirect	Mg2+ metal ions rupture *S. aureus* membranes and kill stationary-phase *S. aureus* cells, which denotes membrane-activity [200]
SeMet	Indirect	SeMet may inhibit bacterial growth and is protective on macrophages [201]

From the above-mentioned protein descriptions, it is quite evident that the combined application of CTAB, RF and BT creates a synergistic effect, as the pathway of action of these three compounds are totally different. The results from antibacterial study are also consistent with computational observations.

4.2.3. Development of Nanomedicine Out of Copper Mine Tailing Waste: A Pavement Towards Circular Economy with Advanced Redox Nanotechnology [202]:

X-ray diffraction (XRD) characterization of the synthesized and extracted CuO NPs was carried out for estimating the precise elemental composition, particle size and superficial morphology as depicted in Figure 4.14.a.

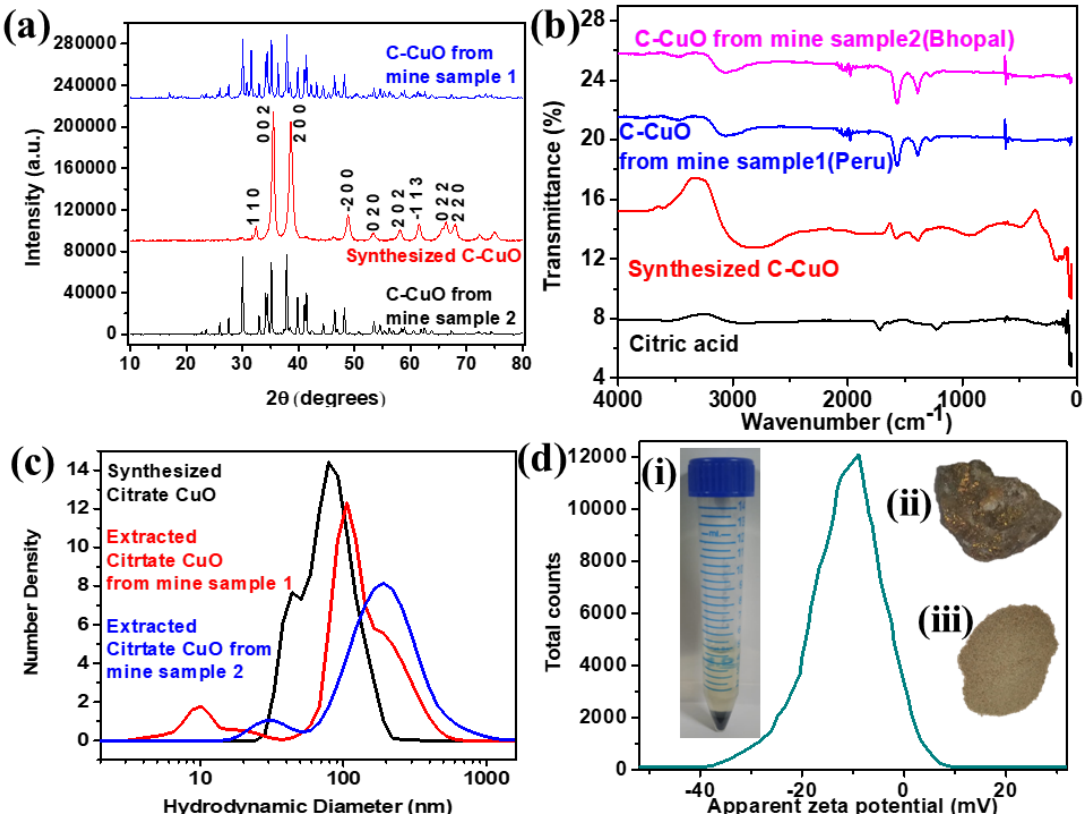

Figure 4.14. *XRD of the synthesized and extracted (from Peru and Bhopal samples) CuO nanoparticles. (b) FTIR spectra of different citrate capped CuO samples and citric acid in the range 0 to 4000 cm^{-1} (c) DLS of the citrate capped CuO from supernatants of C-CuO samples (d) Zeta potential distribution of the synthesized citrate functionalized CuO NP. The inset (i), (ii) and (iii) of Figure 4.14.d are the synthesized C-CuO, the Peru mine tailing and Bhopal mine sludge respectively.*

It was determined that all CuO NPs were in a monoclinic geometry with a space group of C2/C. No characteristic peaks of any other impurities were detected, suggesting the preparation of high quality CuO NPs. Moreover, the obtained χ^2 value of 1.82 for the Le Bail fitting indicates excellent agreement with the previously reported literature [203, 204]. The crystallite size is estimated from the XRD pattern using the Debye Scherrer's equation (4.15) [205]:

$$D = K\lambda/\beta \cos\theta \qquad (4.15)$$

where K = 0.94 is the shape factor, λ is the X-ray wavelength of Cu Kα radiation (1.541 Å), θ is the Bragg diffraction angle and β is the full width at half maxima (FWHM) of the respective diffraction peak. The crystallite size corresponding to the highest peak observed in XRD was found to be 34.4 nm. The presence of sharp structural peaks in XRD patterns and crystallite size less than 100 nm corresponds to the nanocrystalline nature of synthesized CuO NPs. The peaks at 32.5, 35.4, 35.5, 38.7, 38.9,46.2, 48.8, 51.3, 53.4, and 56.7 in 2θ correspond to the different CuO planes, respectively [206]. Similarly, as shown in Figure 4.14.a, the CuO obtained from Peru and Bhopal mine samples exhibited peaks corresponding to the synthesized CuO NPs.

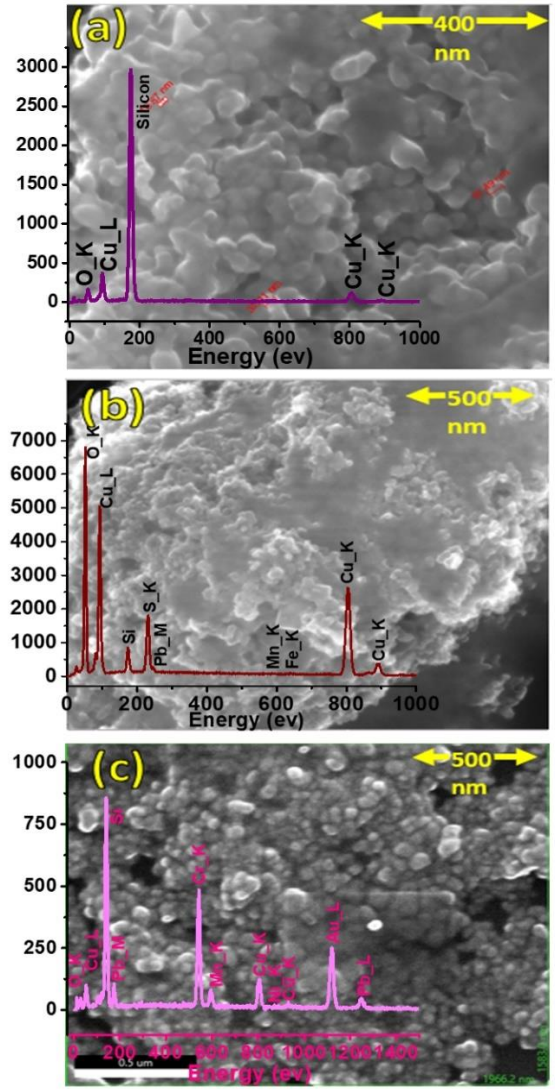

***Figure 4.15**. FESEM images of (a) Synthesized citrate capped CuO NPs. The inset shows the EDAX parameters of the nanoparticles. (b) Extracted and citrate capped CuO from Peru mine stone sample. The inset shows the EDAX parameters of the nanoparticles. (c) Extracted and citrate capped CuO from Bhopal mine stone sample. The inset shows the EDAX parameters of the nanoparticles.*

The peaks at the same 2θ positions for the extracted CuO nanoparticles from both Peru and Bhopal mine samples are referred here which confirm the extraction of CuO from the mine samples. The additional peaks are appearing due to the attribution of the elements like Au, Cr etc. present in the mine samples as revealed from the SEM EDAX analysis (Figure 4.15.).

For ensuring the surface functionalization of the synthesized and extracted CuO NPs by citrate, FTIR analysis was performed on citric acid and the nanoparticles (Figure 4.14.b). The absorption band around 620.9 cm^{-1} in synthesized citrate CuO (C-CuO), C-CuO from mine sample 1 (Peru) and C-CuO from mine sample 2 (Bhopal) can be attributed to the vibrations of the Cu−O group [207, 208]. Furthermore, the absence of other molecular vibrations due to calcination of the synthesized C-CuO, confirms the formation of a pristine surface. The citric acid was found to exhibit an absorption band occurring around 1718 cm^{-1} which is attributed to the C=O stretching and the band occurring at 1394 cm^{-1} is attributed to the C−O stretching [209]. Moreover, the signature of the O−H stretching from the tertiary alcohol of citric acid can be witnessed at around 1099 cm^{-1}, and the bending of the O−H group from the carboxylic acid portion can be observed at 1383 cm^{-1}. Finally, the absorption band at 3299 cm^{-1} comes due to the presence of O−H bond from the citric acid. In the CuO FTIR spectrum, the C−O and C=O stretching can be seen at 1370 cm^{-1} and around 1600 cm^{-1}, while the tertiary alcohol band is at 1080 cm^{-1}.The shift in C=O and C−O indicates that the CA bonded to the CuO via chemisorption of the carboxylate group. Therefore, the weakening of C=O causes a shift in frequency from 1700 to 1600 cm^{-1}. This characterization confirmed the success of surface modification of CuO with citric acid. All the FTIR spectra shown in Figure 4.14.b are baseline corrected, however, the apparent baseline shift may be due to the excess concentration of the synthesized citrate CuO nanoparticles in comparison with the extracted CuO NPs from the copper mine tailings.

The hydrodynamic diameter of the synthesized CuO nanohybrid, C-CuO mine sample 1 (Peru) and 2 (Bhopal) were estimated to be 78.8nm,106nm and190 nm respectively from the dynamic light scattering (DLS) studies (Figure 4.14.c) which are close enough to each other. The results of DLS corroborates with the size obtained

from XRD (34.4nm) and FESEM analysis (38.1nm). The Dynamic Light Scattering (DLS) accounts the hydrodynamic diameter of the functionalized nano-material comprising of core CuO and citrate ligands at the surface along with associated water molecules and some possible aggregation of the functionalized nanoparticles in the aqueous solution. The electron micrograph of the nanoparticles shows the inorganic nanomaterial as a whole containing crystalline and amorphous inorganic core substrate. On the other hand, the size from the XRD accounts only the crystalline materials in the core inorganic particles. Thus, it is obvious that DLS overestimates the size, while XRD reveals the crystalline nanoparticles in the core [210]. Additionally, the citrate CuO NPs exhibited a ζ-potential of magnitude -10.38mV assuring moderate solubility of the NPs (Figure 4.14.d). The ζ-potential for the Peru and Bhopal samples were obtained to be -11.2mV and -8mV respectively. These results lower the possibility of instability and particle agglomeration or precipitate tendencies of the CuO NPs out of the solutions. The full curve for a sample is only provided by the instrument software while titration experiment is performed as we obtained in case of synthesized pure Citrate capped CuO nanohybrid. However, for the extracted Citrate CuO nanoparticles from Peru and Bhopal mine samples only zeta potential measurements were carried out for which only values in mV unit are provided as mentioned previously, no full curves were available from the instrument. The insets i, ii and iii of Figure 4.14.d are the synthesized C-CuO, the Peru mine tailing and Bhopal mine sludge respectively.

Figure 4.15.a, b and c show the FESEM images of the C-CuO NPs. The inset of Figure 4.15.a depicts the EDAX spectrum of synthesized CuO NPs. The EDAX analysis of the extracted citrate CuO from the Peru and Bhopal mine tailings are shown in the insets of Figure 4.15.b and 4.15.c. The EDAX result shows that there are no other elemental impurities present in the prepared CuO NPs. However, trace amount of Au, Cr etc. were found in the extracted CuO NPs in EDAX method. The peak of Silicon appearing in the EDAX graphs of Figure 4.15. is attributed from the substrate. For EDAX analysis, the test sample was drop casted on Si wafer substrate and the thickness of the drop casted layer may not be uniform throughout the substrate. In the FESEM images of C-CuO the synthesized nano-hybrids are seen to be consisting of

clustered spherical particulates of approximate diameter 38-46 nm. The average diameter of CuO NPs was calculated from measuring over 100 particles in random field of FESEM view. The SEM-EDAX analysis demonstrated that the atomic composition of the Cu and O elements were 38.41% and 61.59%, respectively. The mean ratio of Cu and O was therefore 38.41:61.5 and an accurate compound formula based on this atomic ratio of Cu and O can thus be given as Cu1.2O or CuO0.8. Therefore, it can be ensured that most of the synthesized nanoparticulate sample was indeed CuO.

The UV-Vis spectra of the citrate capped CuO samples (Figure 4.16.a) exhibited a broad absorbance peak at 285 nm characteristic of surface plasmon resonance of the CuO nanoparticles [211]. A less stronger peak at around 350 nm, signifies the d-d transition of CuO nanoparticles due to citrate functionalization and quantum confinement effect of CuO NPs on citrate functionalization [212]. Similarly, the peaks observed at 285 nm and 350 nm after the capping of the Peru and the Bhopal samples signified the presence of citrate capped CuO NPs within the system.

Dark and photoinduced ROS generation capability of the Citrate CuO NPs is illustrated using a well-known non-fluorescent probe, DCFH (Figure 4.16.b). DCFH is oxidized to fluorescent dichlorofluorescein (DCF) by ROS, exhibiting an emission near 522 nm upon excitation at 488 nm. Thus, the enhancement of the ROS generation level is indicated by the increase in the emission intensity at 522 nm [108]. The oxidation of only DCFH control and CuO NPs are monitored for 35 mins in the dark and then under irradiation of UV light (365 nm). In the dark, there is considerable enhancement of emission intensity at 522 nm indicating presence of dark ROS generation. However, with the light exposure, a greater increase of emission intensity is observed for the citrate CuO nanohybrid as compared to the control (Figure 4.16.b). This confirms the ROS generation capability of the synthesized nanohybrid under light exposure making it suitable to apply for photodynamic therapy.

The antioxidant activity of the citrate functionalized CuO NPs was evaluated using DPPH assay method (Figure 4.16.c and 4.16.d). Absorbance of DPPH at 535 nm was observed to decrease with time establishing the presence of antioxidant

properties of the CuO NPs under dark condition with a visual transition of the solution from purple to yellow.

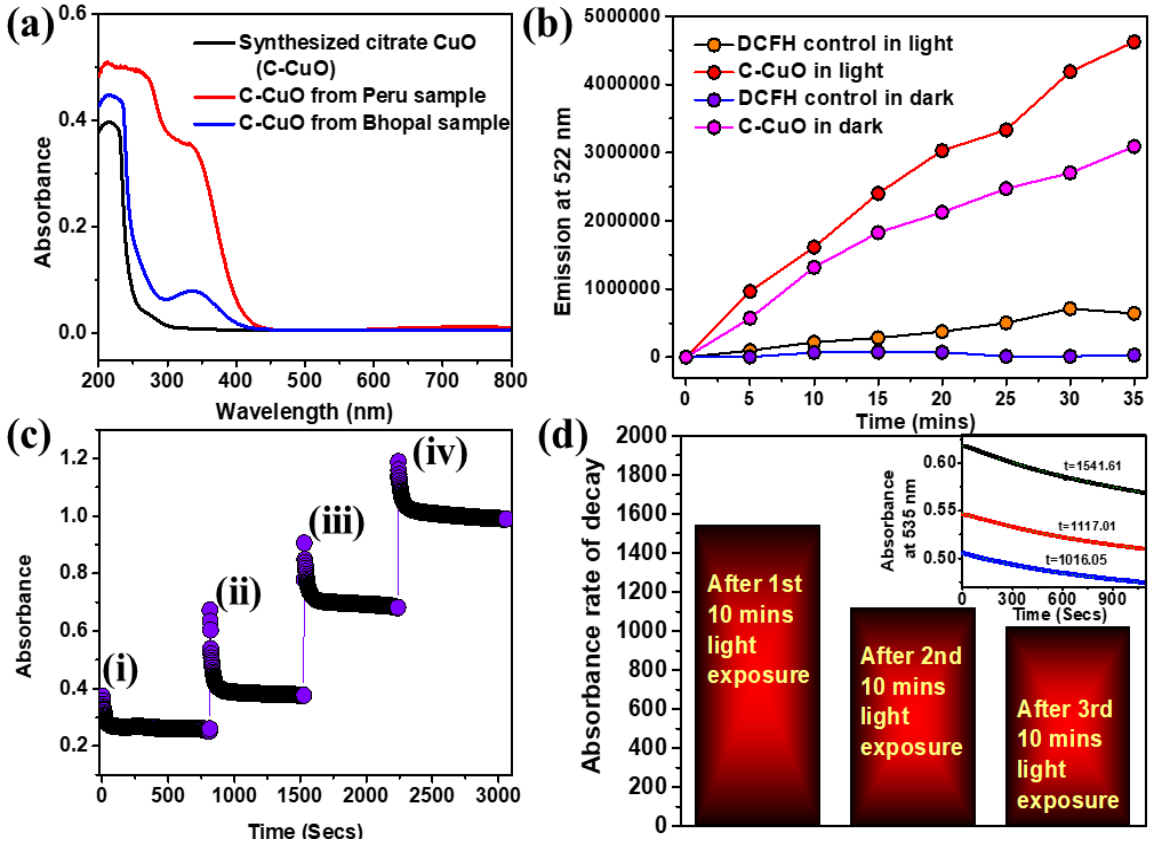

Figure 4.16. *(a) Absorbance spectra of synthesized and extracted citrate-CuO nanohybrids. (b) DCFH oxidation (monitored at 522 nm) with time in the presence and absence of citrate CuO NPs under dark and illumination conditions. (c) The DPPH catalytic activity of the synthesized CuO NPs in dark condition upon addition of DPPH in periodic interval of time (i) (ii) (iii) and (iv). (d) The DPPH assay of the synthesized CuO NPs under UV light illumination condition. Inset shows the decay of absorbance of DPPH radical at 535 nm with multiple light exposure of 10 mins interval.*

Now, upon further addition of 50uM DPPH after a periodic interval of time, it is observed that the free radical scavenging activity remains almost intact in the same sample of 100uM C-CuO. The study of antioxidant activity in presence of UV light (365nm) is a prerequisite to a full understanding of its potential antioxidant property. As depicted in Figure 4.16.d, it is observed that the rate of absorbance decay at 535nm is decreased from 1541.51 to 1117.01 to 1016.05 sec with each 10mins UV exposure to the sample without varying the concentrations of DPPH and C-CuO NPs. The results corroborate the enhancement of anti-oxidant activities with light exposure. The same sample of C-CuO NPs are capable of providing catalytic activities after getting recharged by light exposure.

The antibacterial activities of the C-CuO NPs, synthesized and extracted from mine samples were investigated against gram positive *S. Hominis* bacteria by analyzing their growth curves. Figure 4.17.a reveals the growth pattern of the bacteria in terms of absorbance at 600nm with one hour interval. The synthesized C-CuO, under illumination as well as dark conditions, is observed to almost nullify the growth with respect to the controls where only the bacteria are present in LB media. The C-CuO extratcted from Peru and Bhopal mine samples are observed to exhibit better antimicrobial activity in presence of light.

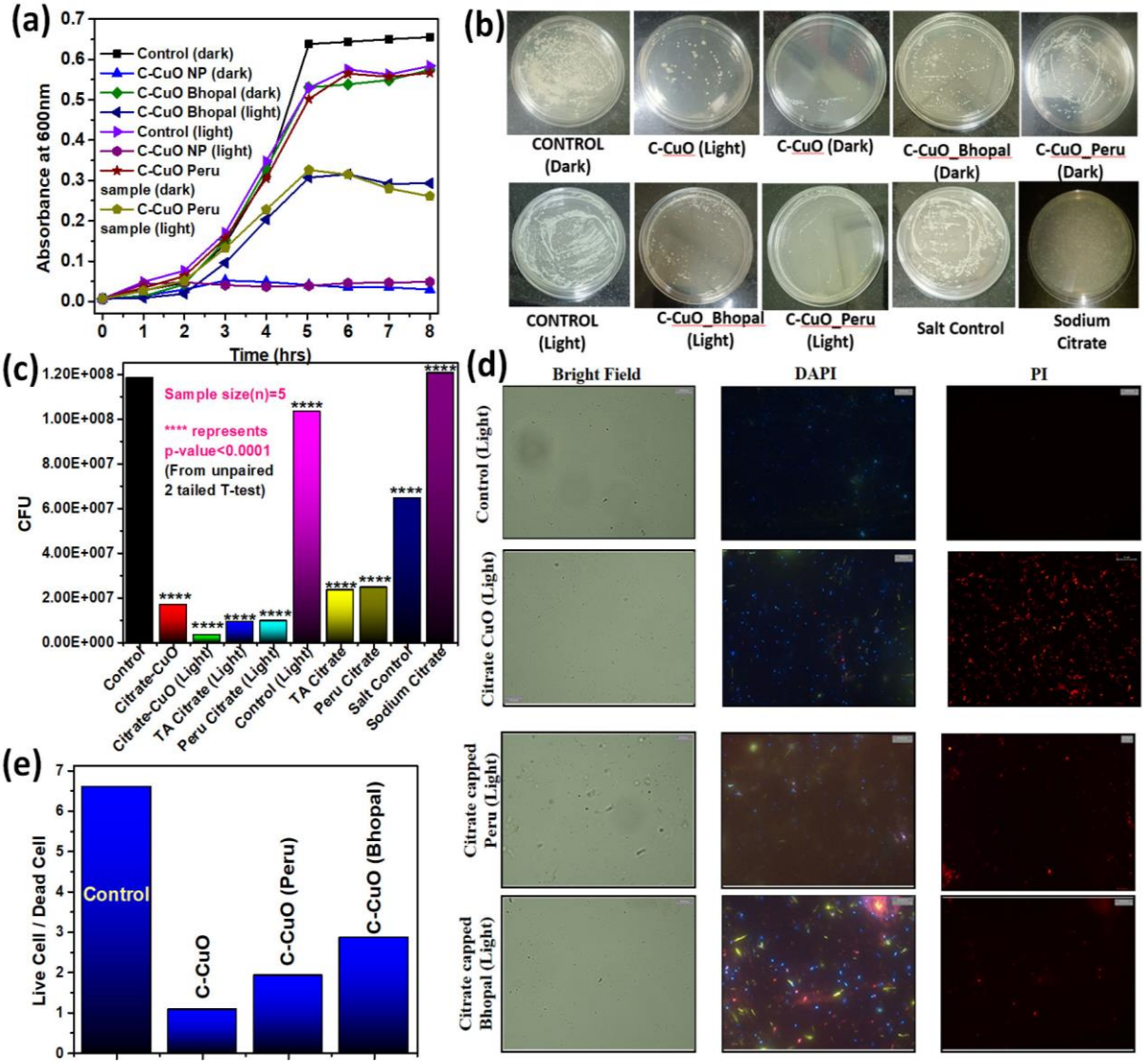

Figure 4.17. *(a) Effect of C-CuO NPs on the growth curves of S. Hominis bacteria under dark and illumination conditions. (b) Bacterial viability after treatment with different citrate CuO NPs in the presence and absence of light irradiation (c) Agar plate colony count assay (d) Bright field microscopic images and fluorescence micrographs of bacteria stained with DAPI and fluorescence micrographs of bacteria stained with PI. (e) Ratio of live and dead cells obtained from microscopy.*

The copper chloride salt used for the synthesis of CuO NPs and sodium citrate used for the capping purpose were found to have almost no effect on bacterial growth establishing the fact that the entire antimicrobial activities are solely generated by the C-CuO NPs.

The antimicrobial activity of the synthesized and extracted CuO NPs after citrate functionalization was investigated against the *S. Hominis* growth to explore the antibiotic potential against bacterial infections in agar plate assay method also. To probe the antibacterial action of the nanoparticles they were used for incubating the culture for 3 h. As shown in Figure 4.17.b and 4.17.c, minimal colonies were observed (the bacterial growth is found to have decreased by 96.9 % in CFU from the control plate) for the nano hybrid under UV light illumination condition. The bacterial growth is found to be decreased by 85% only in CFU for under dark condition. The effect of two different mine extracted copper nanohybrids under dark and light irradiation condition was then studied further upon the growth of *S. Hominis* bacteria (Figure 4.17.b). In case of the Peru and Bhopal samples, the bacterial growth is found to be decreased by 79 % CFU and 80% CFU respectively in dark condition. On the other hand, a huge decrement of the bacterial growth is observed for both Peru and Bhopal samples after citrate capping on UV illumination. The bacterial growth was reduced by 90% and 91% for citrate capped Peru and Bhopal samples respectively on UV illumination. To nullify the effect of the salt and the capping agent (sodium citrate), the antibacterial effect of them were studied. No significant change in the number of colonies in the negative control group was found indicating a low antibacterial effect of these salts on *S. Hominis*. Thus, the antibacterial effect found is solely due to the citrate capped CuO NP. From these results it is evident that the nanohybrid itself is an antibacterial agent and its efficiency enhances manyfold upon white light exposure which triggers an overall huge antibacterial effect.

To study the effect of the citrate CuO nanohybrid, bacterial cultures were performed 5 times for each group (control in dark and light, citrate CuO in dark and light, different concentrations of the nanohybrid etc.) and their difference was calculated to identify their significance level. The sample size for each of the groups were 5. The p-value was calculated using unpaired 2-tailed T-Test and $p<0.05$ was

considered to be significant. Statistical difference in between control and treatment is designated by '*'. The '*' represents p-value<0.1 and '****' represents p-value<0.0001 [213].

Antimicrobial activity of the NPs was further investigated using optical microscopy. We used *S. hominis*, the gram-positive bacteria as the model biological system. *S. hominis*, were incubated with both synthesized and extracted CuO samples for two hours in LB broth and then stained with DAPI and PI. While, DAPI stains all the cells in the medium, PI is specific to the dead cells as it cannot cross the intact cell membrane. So, the ratio of DAPI stained cells to PI stained cells reveals the viability of the cells. Figure 4.17.d and e show the results of the microscopic microbial studies. Figure 4.17.d first row contains the microscopic images of control cells after staining with DAPI and PI. As expected, here the number of viable cells was more than the dead cells (ratio ~6.6). The microscopic images of synthesized C-CuO NPs (Figure 4.17.d, second row) incubated bacteria showed a reduced ratio i. e. dead cells were more in numbers than the live cells (ratio ~2.1) compared to control. Interestingly, the group of bacteria treated with C-CuO NPs extracted from Bhopal and Peru mine samples (Figure 5.4d, row 3 and 4) also showed higher viability as compared to control. The ratio for these C-CuO NP-treated groups were similar to that of synthesized C-CuO treated group as shown in Figure 4.17.e. Therefore, the microscopic studies revealed that the C-CuO NPs exerted toxic effects and effectively killed *S. hominis*. The therapeutic action of the CuO NPs against *S. hominis* bacteria occur primarily via the generation of reactive oxygen species which mainly include formation of hydroxyl radical ($HO.^{*}$) and superoxide radical (O_2^{-*}). Initially an electron-hole (e^-/h^+) pairs are formed when the electromagnetic radiation of energy ($h\upsilon$) is either greater than or equal to the bandgap energy (E_g) of the CuO NPs. This phenomenon excites the electron from the valence band (VB) to the conduction band (CB), leaving holes behind in the VB. These photoexcited electrons reduce the surface adsorbed O_2 to O_2^-., while the holes oxidize H_2O or HO- to OH.[214-216]as described in Figure 4.18.

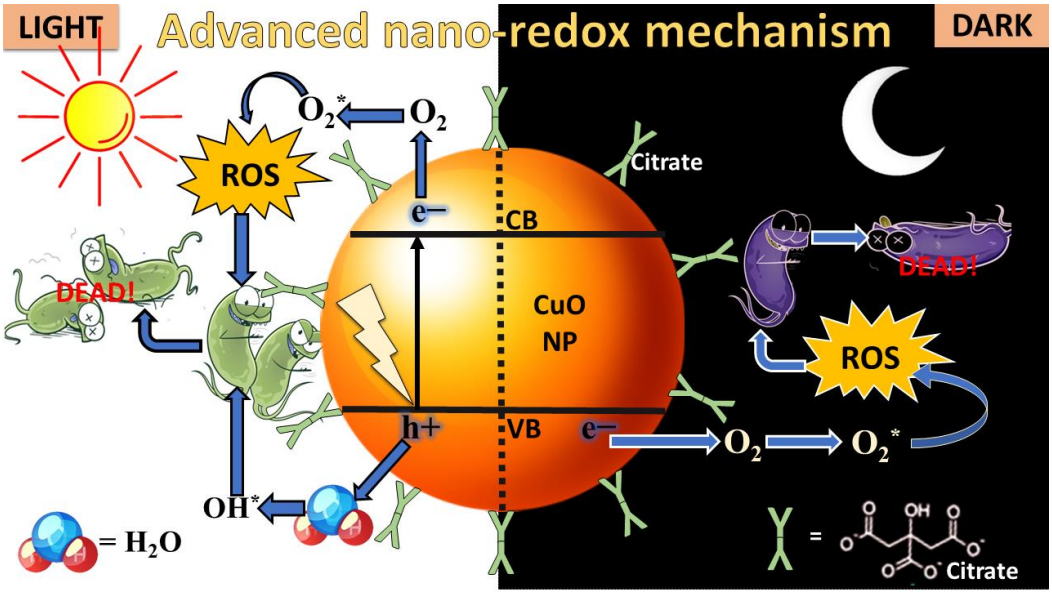

Figure 4.18. *The mechanism of advanced nano-redox technology.*

These in-situ production of reactive radicals starts off attacking the bacterial population and eliminates them by the production of toxic by-products as a result of ROS mediated damage to the cellular system.

$$CuO+h\upsilon = CuO\ (e^{-}+h^{+})$$

$$O_2+e^{-} = O_2^{-*}.$$

$$H_2O+h^{+} = H^{+}+HO^{*}.$$

In absence of an electromagnetic radiation, the anti-microbial activity may be attributed to the ligand to metal charge transfer (LMCT) of the C-CuO NPs. The LMCT bands originate due to the interaction of the $Cu^{1+/2+}$ centres in the NP with the surface bound citrate ligands. In the dark condition the origin of the anti-bacterial activity might be due to the conversion of the Cu^{1+} to Cu^{2+} states at the centre accompanied by the direct injection of the electrons into the CB of the C-CuO NPs followed by the reduction of the surface adsorbed O_2 to O_2-.

$$Cu^{1+}\text{-}O = Cu^{+2}\text{-}O^{*}+ e^{-}$$

$$O_2+e^{-} = O_2^{-}$$

The enhanced efficacy of the citrate functionalized CuO NPs in presence of light for more bacterial remediation establishes its credentials for the application of APDT (Antibacterial Photo-dynamic Therapy).

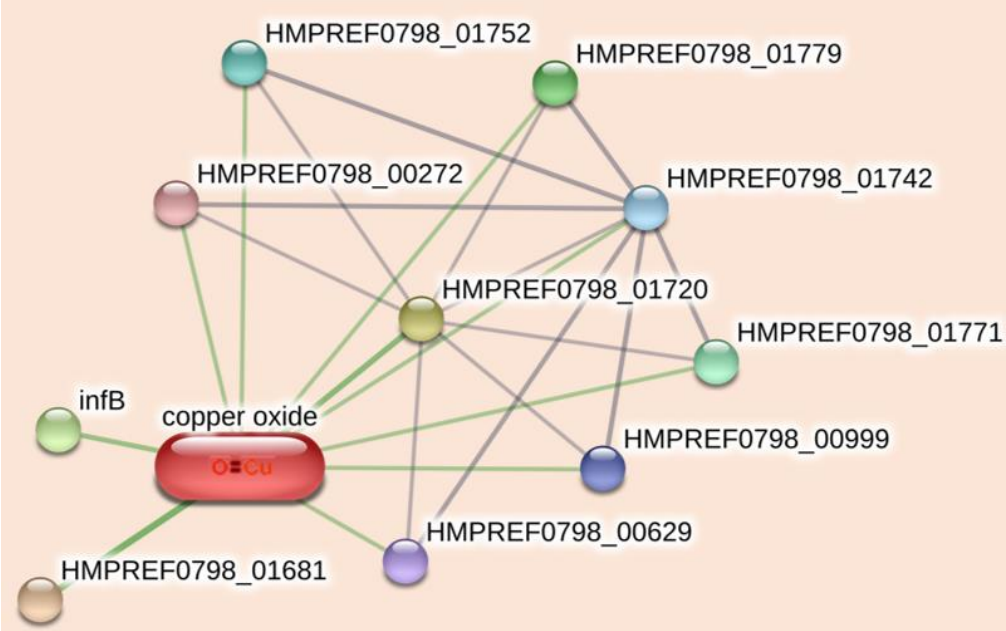

Figure 4.19. *Compound protein interactions network of citrate-CuO nanohybrid on S. Hominis bacterial strain.*

The extraordinary effect of the synthesized copper nanohybrid may be hypothesized using predictive biological interactions. To compare our findings with the existing research works, and related predictive models, the previously mentioned STITCH database was used. It generated an interaction network (Figure 4.19.) between the ligand CuO and its effect on various proteins of *S. Hominis*. To understand how CuO affects the survival of the bacteria, a comprehensive table (Table 4.9.) was populated with the protein names and their respective activities. The table suggests the negative impact of CuO on key-proteins of *S. Hominis*, which help the organism to deal with the environmental stress, energy metabolism, GTP binding, translation regulation etc.

Table 4.9. *Effect of citrate functionalized CuO NPs on S. Hominis bacterial strain*

Identifier	**Corresponding Protein Name**	**Activity**
HMPREF0798_01720	Catalase	Catalase, an antioxidant enzyme found in all aerobic organisms, facilitates the transformation of H_2O_2

		into water and oxygen under environmental stress [217].
HMPREF0798_01742	Pyridine nucleotide-disulfide oxidoreductase family protein	Controls mitochondrial function [218].
HMPREF0798_00999	Pyridine nucleotide-disulfide oxidoreductase	
HMPREF0798_01779	Dihydrolipoyl dehydrogenase	This oxidoreductase is a key factor in bacterial pathogenesis and is responsible for energy metabolism [219].
HMPREF0798_01752	Dihydrolipoyl dehydrogenase	
HMPREF0798_00272	Dihydrolipoyl dehydrogenase	
HMPREF0798_00629	Dihydrolipoyl dehydrogenase	
HMPREF0798_00484, infB	Translation initiation factor, IF-2	IF2 is a crucial protein which binds GTP and increases the rate of translation [220].
HMPREF0798_01681	Cell division protein SufI	SufI is a protein responsible for cell division and also considered as bacterial twin arginine translocation protein [221].
HMPREF0798_01771	Mercury(II) reductase	This protein helps the organism to withstand the toxic Hg concentrations [222].

4.2.3. "Nano-Copper": A Potential Remediation of Antibiotic-Resistant Infections [223]:

The identification of precise elemental composition, particle size range and surface morphology of the acetate functionalized nanoparticulate CuO is a prerequisite to a full understanding of its potential application capabilities. The XRD pattern of the synthesized CuO NPs are depicted in Figure 4.20.a. It was determined that all CuO NPs were in a monoclinic geometry with a space group of C2/C. No characteristic peaks of any impurities were detected, suggesting that high quality of CuO NPs was prepared. Moreover, the obtained χ^2 value of 1.85 for the Le Bail fitting indicates excellent agreement with the previously reported literature [203, 204]. The crystallite size has been estimated from the XRD pattern using the Debye Scherrer's equation (4.15) [205]:

$$D = K\lambda/\beta \cos\theta \quad (4.15)$$

where K = 0.94 is the shape factor, λ is the X-ray wavelength of Cu Kα radiation (1.541 Å), θ is the Bragg diffraction angle and β is the full width at half maxima (FWHM) of the respective diffraction peak. The crystallite size corresponding to the highest peak observed in XRD was found to be 24.31 nm. The presence of sharp structural peaks in XRD patterns and crystallite size less than 100 nm corresponds to the nanocrystalline nature of synthesized CuO NPs. The peaks at 32.5, 35.4, 35.5, 38.7, 38.9,46.2, 48.8, 51.3, 53.4, and 56.7 in 2θ correspond to the different CuO planes, respectively [206].

Figure 4.20.b depicts the EDAX spectrum of synthesized CuO NPs. The EDAX result shows that there are no other elemental impurities present in the prepared CuO NPs. FESEM image of acetate-CuO is shown in inset of Figure 4.20.b. The synthesized nano-hybrid is seen to be consisting of clustered spherical particles of approximate diameter 38 nm. The average diameter of CuO NPs was calculated from measuring over 100 particles in random field of FESEM view. The SEM-EDAX analysis demonstrated that the atomic composition of the Cu and O elements were 54.1% and 45.2%, respectively. The mean ratio of Cu and O was therefore 54.1:45.2 and an accurate compound formula based on this atomic ratio of Cu and O can thus be given as $Cu_{1.2}O$ or $CuO_{0.8}$. Therefore, it can be ensured that most of the synthesized nanoparticulate sample was indeed CuO.

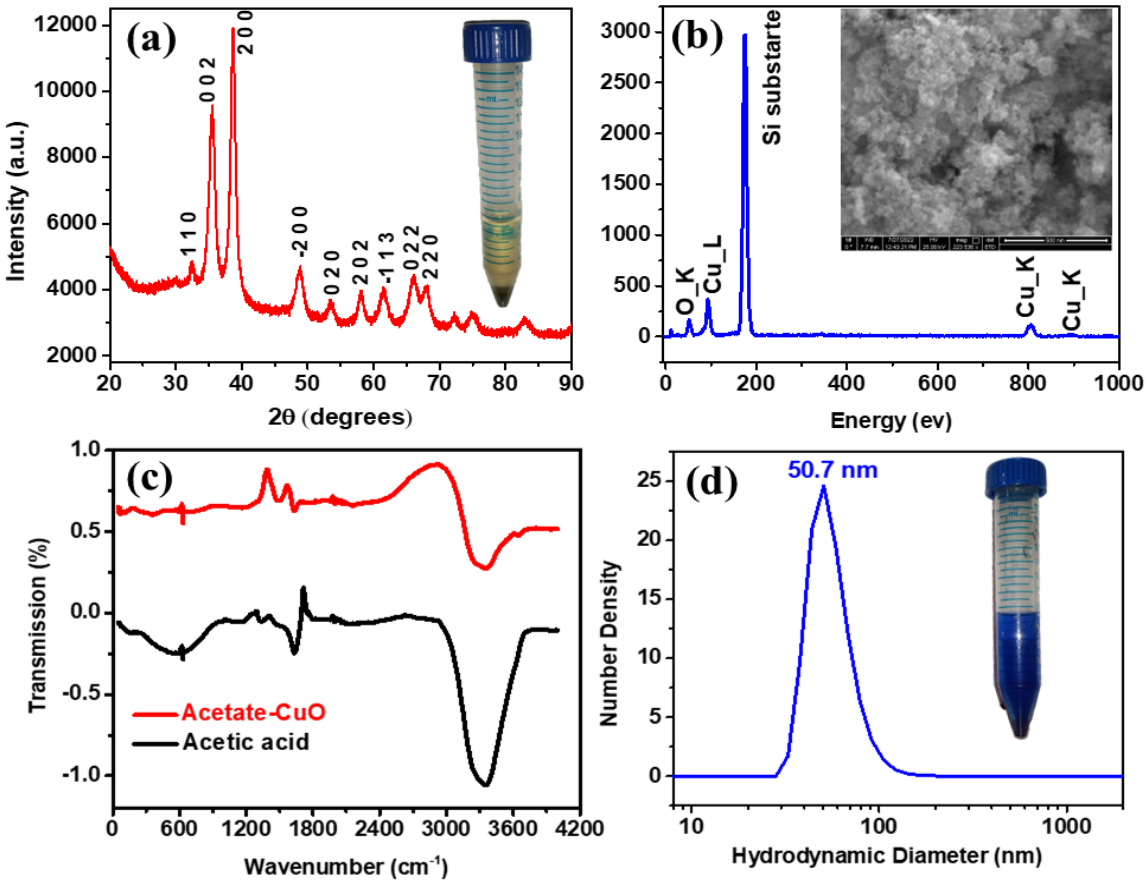

Figure 4.20. *(a) XRD of the synthesized CuO nanoparticles. Inset shows the CuO nanoparticles precipitated after centrifugation during synthesis process. (b) FESEM image and EDAX of CuO NPs (c) FTIR spectra of acetate capped CuO and acetic acid in therange 0 to 4000 cm-1 (d) DLS of the acetate capped CuO from supernatant (inset).*

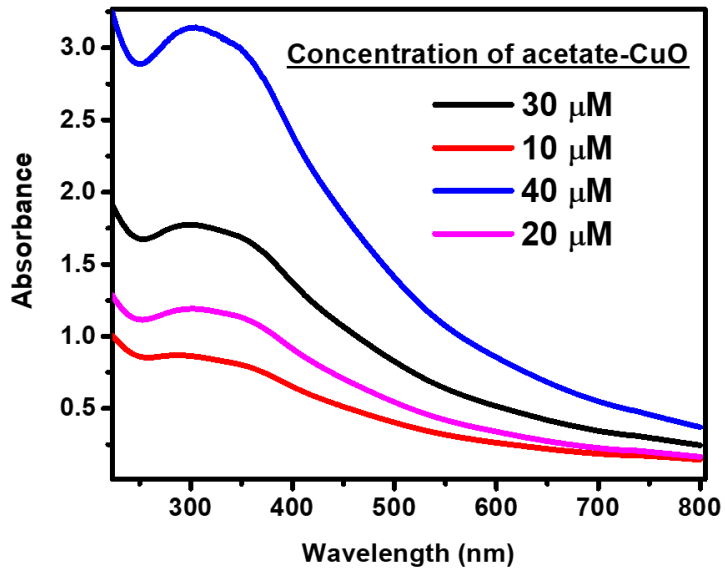

Figure 4.21. *Absorbance spectra of synthesized acetate-CuO nanohybrid for different concentrations.*

The attachment of acetate on the surface of the CuO nanoparticles was ensured by FTIR of the functionalized CuO nanoparticle along with acetic acid (Figure 4.20.c). The acetic acid showed an absorption band at 1700cm^{-1}, which can be attributed due to the C=O stretching of the carboxylate group of acetic acid [209]. In addition, the absorption peak occurring at 1300 cm^{-1} may be attributed to the bending of the O-H group of the C-OH bond of the carboxylic acid portion [224]. Moreover, the absorption band at ~3500 cm^{-1} is due to the –OH of the acetic acid [224]. In the IR spectrum of the acetate capped CuO nanoparticle, the stretching frequency of C-O and C=O has been found at ~1360cm^{-1} and ~1780cm^{-1}. This shift in the C-O and C=O indicates that the CuO nanoparticles are functionalised by the adsorption of the carboxylate group of acetic acid on the nanoparticle surface [225, 226]. Moreover, the weakening of the –OH bond in the acetate capped CuO nanoparticle, further confirms the surface functionalization of CuO with acetic acid.

The hydrodynamic diameter of the synthesized CuO nanohybrid was estimated to be 50.7 nm from the dynamic light scattering (DLS) studies (Figure 4.20.d). The results of DLS corroborates with the size obtained from XRD and FESEM analysis. Additionally, the Acetate CuO NPs exhibited a ζ-potential of magnitude -18.3mV assuring moderate solubility of the NPs. This result lowers the possibility of instability and particle agglomeration or precipitate tendencies of the CuO NPs out of the solutions.

The UV-Vis spectra in Figure 4.21. of the acetate capped CuO exhibited a broad absorbance peak at 285 nm characteristic of surface plasmon resonance of the CuO nanparticles [211]. A less strong peak at around 350 nm, signifies the d-d transition of CuO nanoparticles due to acetate functionalization [227].

Photoinduced ROS generation capability of the Acetate CuO NP is illustrated using a well-known non-fluorescent probe, DCFH (Figure 4.22.). DCFH is oxidized to fluorescent dichlorofluorescein (DCF) by ROS, exhibiting an emission near 522 nm upon excitation at 488 nm. Thus, the enhancement of the ROS generation level is indicated by the increase in the emission intensity at 522 nm [108]. The oxidation of only DCFH control and CuO NPs are monitored for 10 mins in the dark and then under irradiation of white light (400-700nm) for 30 mins. In the dark, there is no

considerable enhancement of emission intensity at 522 nm indicating absence of dark ROS generation. However, with the increase in the light exposure time, a greater increase of emission intensity is observed for the actetate CuO nanohybrid as compared to the control (Figure 4.22.). This confirms the ROS generation capability of the synthesized nanohybrid under light exposure making it suitable to apply for photodynamic therapy.

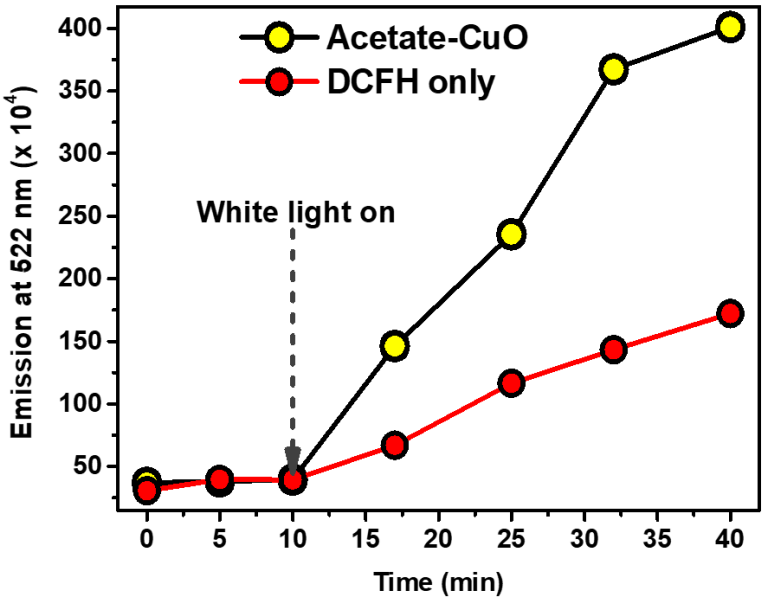

Figure 4.22. *DCFH oxidation (monitored at 522 nm) with time in the presence and absence of acetate CuO NPs under dark (initial 10 mins) and white light (30 mins) illumination condition.*

The antimicrobial activity of the synthesized acetate-CuO NPs was investigated against the MRSA growth to explore the antibiotic potential against bacterial infections. To probe the antibacterial action of the nanoparticles they were used for incubating the culture for 3 h. As shown in Figure 4.23.a, minimal colonies were observed (the bacterial growth is found to have decreased by 78.88 % in CFU from the control plate) for the nano hybrid under white light illumination condition. The bacterial growth is found to be decreased by 8% only in CFU for under dark condition. The effect of two different concentrations of copper nanohybrid under white light irradiation condition was then studied further upon the growth of MRSA bacteria (Figure 4.23.b). In case of 10uM concentration, the bacterial growth is found to be decreased by 46 % CFU. On the other hand, a huge decrement of the bacterial growth is observed for 50uM concentration of acetate CuO, 92% reduction in terms of CFU

with respect to the control. From these results it is evident that the nanohybrid itself is an antibacterial agent and its efficiency enhances manyfold upon white light exposure which triggers an overall huge antibacterial effect.

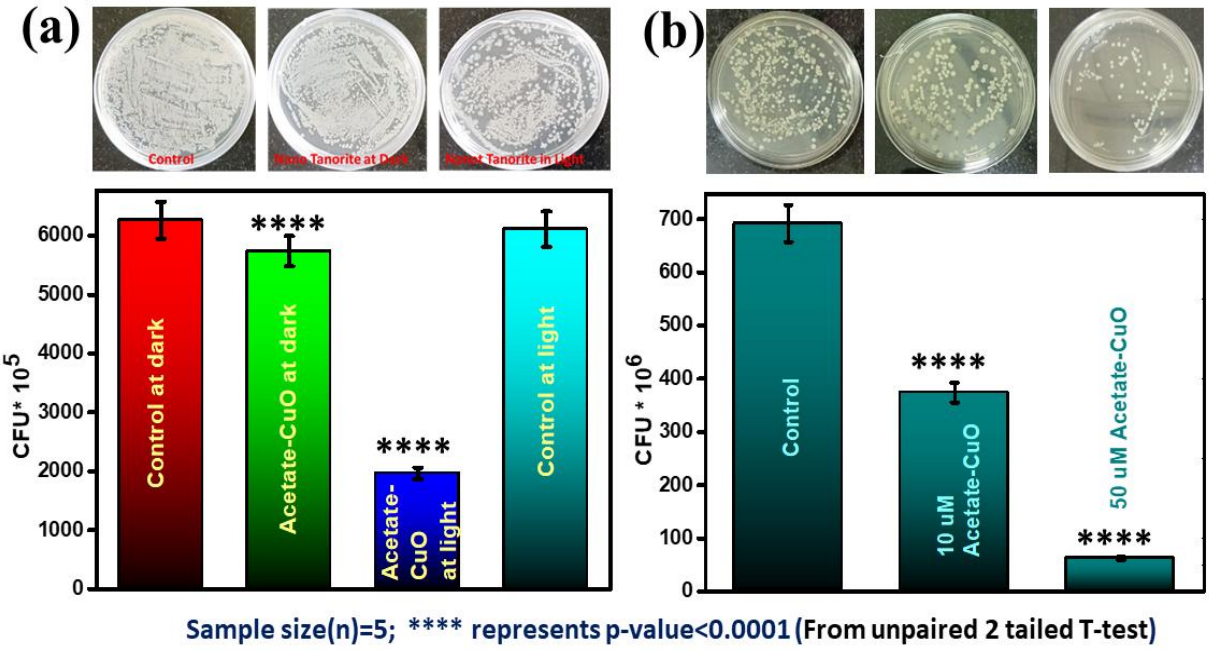

Figure 4.23. *(a) Bacterial viability after treatment with acetate CuO NPs in the presence and absence of white-light irradiation (30 mins). (b) Dose-dependent antibacterial effect of the nanohybrid at concentrations 10uM and 50uM on MRSA under white light irradiation condition. The insets show images of MRSA plates treated with acetate CuO under different conditions.*

To study the effect of the acetate CuO nanohybrid, bacterial cultures were performed 5 times for each group (control in dark and light, acetate CuO in dark and light, different concentrations of the nanohybrid etc.) and their difference was calculated to identify their significance level. The sample size for each of the groups were 5. The p-value was calculated using unpaired 2-tailed T-Test and $p<0.05$ was considered to be significant. Statistical difference in between control and treatment is designated by '*'. The '*' represents p-value<0.1 and '****' represents p-value<0.0001 [213]

The extraordinary effect of the synthesized copper nanohybrid may be hypothesized using predictive biological interactions (Figure 4.24.). To grasp the mechanism of action of acetate CuO NPs on MRSA, a separate comprehensive table (Table 4.10.) of target proteins/compounds and their biological activities are listed below.

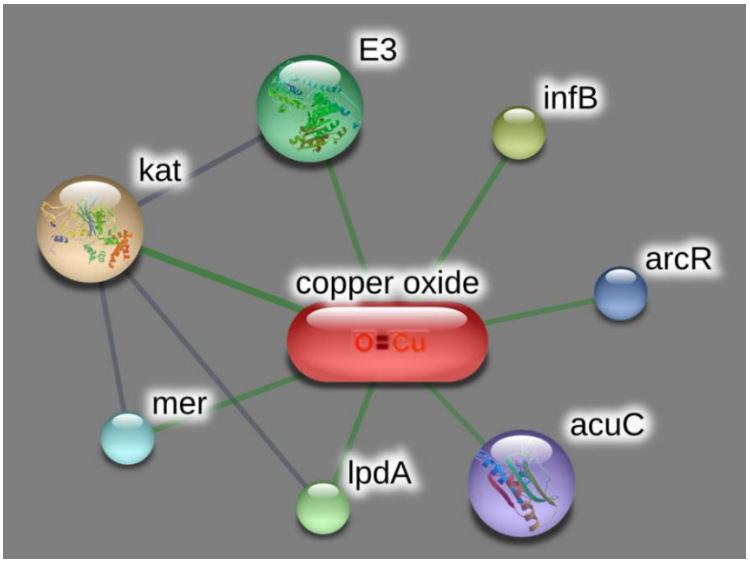

Figure 4.24. *Compound protein interactions network of acetate-CuO nanohybrid on MRSA bacterial strain.*

Table 4.10. *Effect of acetate functionalized CuO NPs on MRSA*

Protein	Activity
auk	Acetoin utilization protein AcuC; Bacterial growth on acetoin and butanediol is inhibited when acuC expression is disrupted. In the absence of additional carbon sources, the bacterial fermentation product acetoin can be converted to acetate via the butanediol cycle; its decomposition is thought to be triggered by deacetylation mediated by acuC [228].
E3	Dihydrolipoamide dehydrogenase; There is a strong probability that a relationship between the DLDH (E3) enzyme and its effects on virulence exists [229].
kat	Catalase; Catalases are common group of enzymes that efficiently protect cells from the toxic effects of hydrogen peroxide, by decomposing it into water and oxygen to prevent cell oxidative damage [230].
mer	Pyridine nucleotide-disulfide oxidoreductase.
lpdA	Dihydrolipoamide dehydrogenase; They have been classified according to their presence in various bacteria and eukaryotes and the properties of the enzymes are similar among the members of these domains.

	Additionally, it has been suggested that IpdA acts in the binding protein-dependent transport of galactose and maltose and in protecting biological membranes from oxidative degradation [231].
infB	Translation initiation factor IF-2; One of the essential components for the initiation of protein synthesis. Protects formylmethionyl-tRNA from spontaneous hydrolysis and promotes its binding to the 30S ribosomal subunits. Also involved in the hydrolysis of GTP during the formation of the 70S ribosomal complex.
arcR	Crp/FNR family transcriptional regulator; The Crp-Fnr regulators, the DNA-binding proteins, positively regulates the expression of the transcription factors [232].

4.3. CONCLUSION:

The new non-invasive non-contact device (SAMIRA) can accurately measure hemoglobin and bilirubin levels simultaneously from a single optical spectrum. It could also measure TSB > 20 mg/dL, which was eliminated by the modification in the illumination intensity of the source. Interestingly, in this study we also found that the device gave accurate results to predict the onset of heart diseases in neonates by measuring their blood saturation levels. This will help clinicians to better monitor the neonates and reduce the frequency of blood sampling. Moreover, the device collects the data from the neonate's nail bed which contains less melanin interference irrespective of the skin tone of the neonate. Overall, our results suggests that our device can be accurately used in hospital settings for the accurate measurement of hemoglobin and bilirubin for the screening of hyperbilirubinemia and anemia in neonates.

In the next study, a highly potential antibacterial agent is developed by embedding a well-known antituberculosis drug rifampicin with a common antifungal drug benzothiazole inside a cationic CTAB micelle as delivery vehicle. Dynamic light scattering (DLS) studies have been utilized to characterize the integrity of a CTAB micelle and to confirm the encapsulation of RF and BT within the micelle. FRET

measurements along with probability distribution of donor-acceptor distances were employed to locate the binding of the drug RF with respect to BT in the micellar surface. The distance between the donor (BT)–acceptor (RF) pair is found to be 20.9 Å in the micellar surface. Infelta-Tachiya model has been further employed to understand the kinetics of energy transfer from BT to RF molecules with increasing quencher (RF) concentration, The results obtained it are consistent with the FRET data. The credence of this antibacterial agent has been finally established by anti-bacterial studies on MRSA bacteria. Predictive biological models also support the MRSA eradication mechanism. These studies demonstrate the high potential of a new antibacterial sanitizing spray for use in healthcare facilities against multi drug resistant MRSA bacteria, responsible for numerous health hazards.

Further, a pure grade citrate capped CuO NP was synthesized by simple precipitation and grafting methods. From two types of copper mine tailings, CuO NPs were also extracted and functionalized with citrate. XRD spectrum confirmed the formation of monoclinic crystals of CuO NPs with space group C2/C. FESEM and EDAX revealed the morphology of CuO NPs. The average SEM diameter of CuO NPs was around 38.1nm that agreed fairly well with XRD and DLS data. FTIR and UV Vis spectroscopy confirmed the surface functionalization of the CuO NPs with citrate ligand. The synthesized nanohybrid was found to generate ROS under UV light exposure in DCFH assay and showed excellent antimicrobial activity against *S. Hominis* bacterial strains in a triparted study consisting of growth curve analysis, agar plate assay method and microscopic studies after staining using DAPI and PI. The C-CuO NPs were also found to possess anti-oxidant properties in DPPH assay. Consequently, citrate functionalized CuO NPs can therefore be used as an antibacterial agent in surface coatings on a variety of substrates to stop microbes from adhering to them, colonising and growing on them, and producing biofilms, such as in habitational medical equipment. This study suggests that mechanisms of antimicrobial response of citrate-CuO nanohybrid in different species of bacteria should be further explored. The use of copper mine tailings as a source of raw materials for the nano-hybrid synthesis in order to cater low-cost antibiotics to wider

population across the globe and to remediate the burden from the copper mines simultaneously was also explored.

In the extedned study, a pure grade acetate capped CuO NP was synthesized by simple precipitation and grafting methods. XRD spectrum confirmed the formation of monoclinic crystals of CuO NPs with space group C2/C. FESEM and EDAX revealed the morphology of CuO NPs. The average SEM diameter of CuO NPs was around 38 nm that agreed fairly well with XRD and DLS data. FTIR and UV Vis spectroscopy confirmed the surface functionalization of the CuO NPs with acetate ligand. The synthesized nanohybrid was found to generate ROS under white light exposure in DCFH assay and showed excellent antimicrobial activity against MRSA bacterial strains. Consequently, acetate functionalized CuO NPs have potential for external uses as an antibacterial agent in surface coatings on various substrates to prevent microorganisms from attaching, colonizing, growing and forming biofilms for example in dwelling medical devices. This study suggests that mechanisms of antimicrobial response of acetate-CuO nanohybrid in different species of bacteria should be further explored.

REFERENCES

[1] H. Brits, J. Adendorff, D. Huisamen, D. Beukes, K. Botha, H. Herbst, *et al.*, The prevalence of neonatal jaundice and risk factors in healthy term neonates at National District Hospital in Bloemfontein, *African Journal of Primary Health Care and Family Medicine*, 10 (2018) 1.

[2] N.G. Onyeneho, B.C. Ozumba, S. Subramanian, Determinants of childhood anemia in India, *Scientific reports*, 9 (2019) 1.

[3] R. Subhi, M. Adamson, H. Campbell, M. Weber, K. Smith, T. Duke, *et al.*, The prevalence of hypoxaemia among ill children in developing countries: A systematic review, *The Lancet Infectious Diseases*, 9 (2009) 219.

[4] P.A. Dennery, D.S. Seidman, D.K. Stevenson, Neonatal hyperbilirubinemia, *New England Journal of Medicine*, 344 (2001) 581.

[5] S.M. Gilmour, Prolonged neonatal jaundice: When to worry and what to do, *Paediatrics & Child Health*, 9 (2004) 700.

[6] A. Alkhotani, E.E.M.N. Eldin, A. Zaghloul, S. Mujahid, Evaluation of neonatal jaundice in the Makkah region, *Scientific Reports*, 4 (2014) 1.

[7] A.A.O. Pediatrics, Management of hyperbilirubinemia in the newborn infant 35 or more weeks of gestation (Subcommittee on Hyper-bilirubinemia), *Pediatrics*, 114 (2004) 297.

[8] A.D. Bizuneh, B. Alemnew, A. Getie, A. Wondmieneh, G. Gedefaw, Determinants of neonatal jaundice among neonates admitted to five referral hospitals in Amhara region, Northern Ethiopia: An unmatched case-control study, *BMJ Paediatrics Open*, 4 (2020) e000830.

[9] D.S. Devi, B. Vijaykumar, Risk factors for neonatal hyperbilirubinemia: A case control study, *International Journal of Reproduction, Contraception, Obstetrics and Gynecology*, 6 (2017) 198.

[10] D.E. Omekwe, M.D. George, B.T. Kennis, B.N. Fakuma, C. Evdence, E. Destiny, *et al.*, Survey and management outcome of neonatal jaundice from a developing tertiary health centre, Southern Nigeria, *IOSR Journal of Dental and Medical Sciences*, 13 (2014) 35.

[11] S. Kolawole, H. Obueh, O. Okandeji-Barry, Prevalence of neonatal jaundice in Eku Baptist community hospital in delta state Nigeria, *Journal of Public Health and Epidemiology*, 8 (2016) 87.
[12] M. Nouraie, J.S. Lee, Y. Zhang, T. Kanias, X. Zhao, Z. Xiong, *et al.*, The relationship between the severity of hemolysis, clinical manifestations and risk of death in 415 patients with sickle cell anemia in the US and Europe, *Haematologica*, 98 (2013) 464.
[13] H. Quraishi, M. Chee, Pediatric Otolaryngology, An Issue of Pediatric Clinics of North America, E-Book, *Elsevier Health Sciences*, Edinburgh, 2022.
[14] S. Yap, I. Mohammad, C. Ryan, Avoiding painful blood sampling in neonates by transcutaneous bilirubinometry, *Irish Journal of Medical Science*, 171 (2002) 188.
[15] S. Meites, Skin-puncture and blood-collecting technique for infants: Update and problems, *Clinical Chemistry*, 34 (1988) 1890.
[16] L. Wang, J.M. Cochran, T. Ko, W.B. Baker, K. Abramson, L. He, *et al.*, Non-invasive monitoring of blood oxygenation in human placentas via concurrent diffuse optical spectroscopy and ultrasound imaging, *Nature Biomedical Engineering*, 6 (2022) 1017.
[17] S.H. Yun, S.J. Kwok, Light in diagnosis, therapy and surgery, *Nature Biomedical Engineering*, 1 (2017) 1.
[18] L.D. Lilien, V.J. Harris, R.S. Ramamurthy, R.S. Pildes, Neonatal osteomyelitis of the calcaneus: Complication of heel puncture, *The Journal of Pediatrics*, 88 (1976) 478.
[19] H. Lemont, J. Brady, Infant heel nodules: Calcification of epidermal cysts, *Journal of the American Podiatric Medical Association*, 92 (2002) 112.
[20] K. Jangaard, H. Curtis, R. Goldbloom, Estimation of bilirubin using biliChek™, a transcutaneous bilirubin measurement device: Effects of gestational age and use of phototherapy, *Paediatrics & Child Health*, 11 (2006) 79.
[21] W.D. Engle, G.L. Jackson, N.G. Engle, Transcutaneous bilirubinometry, Seminars in perinatology, *Elsevier*, Edinburgh, 2014.
[22] N.B. Hampson, E.D. Ecker, K.L. Scott, Use of a noninvasive pulse CO-oximeter to measure blood carboxyhemoglobin levels in bingo players, *Respiratory Care*, 51 (2006) 758.
[23] L. Lamhaut, R. Apriotesei, X. Combes, M. Lejay, P. Carli, B. Vivien, Comparison of the accuracy of noninvasive hemoglobin monitoring by spectrophotometry (SpHb)

and HemoCue® with automated laboratory hemoglobin measurement, *The Journal of the American Society of Anesthesiologists*, 115 (2011) 548.

[24] M.J. Maisels, Transcutaneous bilirubin measurement: Does it work in the real world?, *Pediatrics*, 135 (2015) 364.

[25] M.J. Maisels, E. Kring, Transcutaneous bilirubinometry decreases the need for serum bilirubin measurements and saves money, *Pediatrics*, 99 (1997) 599.

[26] M.J. Maisels, Noninvasive measurements of bilirubin, *Pediatrics*, 129 (2012) 779.

[27] N. Bosschaart, J.H. Kok, A.M. Newsum, D.M. Ouweneel, R. Mentink, T.G. van Leeuwen, *et al.*, Limitations and opportunities of transcutaneous bilirubin measurements, *Pediatrics*, 129 (2012) 689.

[28] S. Wainer, Y. Rabi, S.M. Parmar, D. Allegro, M. Lyon, Impact of skin tone on the performance of a transcutaneous jaundice meter, *Acta Paediatrica*, 98 (2009) 1909.

[29] WHO, Global antimicrobial resistance and use surveillance system (GLASS) report: 2021.

[30] C.J.L. Murray, K.S. Ikuta, F. Sharara, L. Swetschinski, G.R. Aguilar, A. Gray, *et al.*, Global burden of bacterial antimicrobial resistance in 2019: A systematic analysis, *The Lancet*, 399 (2022) 629.

[31] U.K.G. and T.W.T. commissioned by the, AMR Review, 2016 (https://amr-review.org/).

[32] J.M. Munita, C.A. Arias, Mechanisms of antibiotic resistance, *Microbiology Spectrum*, 4 (2016) 10.1128.

[33] A. Cassini, L.D. Högberg, D. Plachouras, A. Quattrocchi, A. Hoxha, G.S. Simonsen, *et al.*, Attributable deaths and disability-adjusted life-years caused by infections with antibiotic-resistant bacteria in the EU and the European Economic Area in 2015: A population-level modelling analysis, *The Lancet Infectious Diseases*, 19 (2019) 56.

[34] P.-F. Liu, C.-W. Lo, C.-H. Chen, M.-F. Hsieh, C.-M. Huang, Use of nanoparticles as therapy for Methicillin-resistant Staphylococcus aureus infections, *Current Drug Metabolism*, 10 (2009) 875.

[35] J.S. Garner, Guideline for isolation precautions in hospitals: The hospital infection control practices advisory committee, *Infection Control and Hospital Epidemiology*, 17 (1996) 53.

[36] WHO, 2017 (https://www.who.int/data/gho/publications/world-health-statistics).

[37] A.S. Haddadin, Methicillin resistant Staphylococcus aureus (MRSA) in the intensive care unit, *Postgraduate Medical Journal*, 78 (2002) 385.

[38] J. Rolo, M. Miragaia, A. Turlej-Rogacka, J. Empel, O. Bouchami, N.A. Faria, *et al.*, High genetic diversity among community-associated Staphylococcus aureus in Europe: Results from a multicenter study, *PLOS ONE*, 7 (2012) e34768.

[39] Y. Mehta, A. Hegde, R. Pande, K.G. Zirpe, V. Gupta, J. Ahdal, *et al.*, Methicillin-resistant Staphylococcus aureus in intensive care unit setting of India: A Review of clinical burden, patterns of prevalence, preventive measures, and future strategies, *Indian Journal of Critical Care Medicine : Peer-reviewed, Official Publication of Indian Society of Critical Care Medicine*, 24 (2020) 55.

[40] X. Zhen, C.S. Lundborg, M. Zhang, X. Sun, Y. Li, X. Hu, *et al.*, Clinical and economic impact of methicillin-resistant Staphylococcus aureus: A multicentre study in China, *Scientific Reports*, 10 (2020) 3900.

[41] H. Uematsu, K. Yamashita, S. Kunisawa, K. Fushimi, Y. Imanaka, Estimating the disease burden of methicillin-resistant Staphylococcus aureus in Japan: Retrospective database study of Japanese hospitals, *PLOS ONE*, 12 (2017) e0179767.

[42] B.Y. Lee, A. Singh, M.Z. David, S.M. Bartsch, R.B. Slayton, S.S. Huang, *et al.*, The economic burden of community-associated methicillin-resistant Staphylococcus aureus (CA-MRSA), *Clinical Microbiology and Infection: The Official Publication of the European Society of Clinical Microbiology and Infectious Diseases*, 19 (2013) 528.

[43] J.W. Costerton, P.S. Stewart, E.P. Greenberg, Bacterial biofilms: A common cause of persistent infections, *Science (New York, N.Y.)*, 284 (1999) 1318.

[44] J. Wang, Z. Zhang, J. Li, B. Huang, Z. Jiang, Y. Pan, *et al.*, Tranexamic acid protects against implant-associated infection by reducing biofilm formation, *Scientific Reports*, 12 (2022) 4840.

[45] An introduction to the world of microbiology and biofilmology, S. Percival, K. Cutting (Eds.) Microbiology of Wounds, *CRC Press*, Florida, 2010.
[46] M. Abdallah, O. Khelissa, A. Ibrahim, C. Benoliel, L. Héliot, P. Dhulster, *et al.*, Impact of growth temperature and surface type on the resistance of Pseudomonas aeruginosa and Staphylococcus aureus biofilms to disinfectants, *International Journal of Food Microbiology*, 214 (2015) 38.
[47] A. Bridier, R. Briandet, V. Thomas, F. Dubois-Brissonnet, Resistance of bacterial biofilms to disinfectants: A review, *Biofouling*, 27 (2011) 1017.
[48] A. Selvaraj, T. Jayasree, A. Valliammai, S.K. Pandian, Myrtenol attenuates MRSA biofilm and virulence by suppressing sarA expression dynamism, *Frontiers in Microbiology*, 10 (2019).
[49] W.A. Rutala, D.J. Weber, Disinfection, sterilization, and control of hospital waste, *Mandell, Douglas, and Bennett's Principles and Practice of Infectious Diseases*, *Elsevier*, Edinburgh, 2015.
[50] X. Zhao, F. Zhao, J. Wang, N. Zhong, Biofilm formation and control strategies of foodborne pathogens: Food safety perspectives, *RSC Advances*, 7 (2017) 36670.
[51] W.A. Rutala, D.J. Weber, Uses of inorganic hypochlorite (bleach) in health-care facilities, *Clinical Microbiology Reviews*, 10 (1997) 597.
[52] R.J. Slaughter, M. Watts, J.A. Vale, J.R. Grieve, L.J. Schep, The clinical toxicology of sodium hypochlorite, *Clinical Toxicology*, 57 (2019) 303.
[53] E. Emmanuel, G. Keck, J.-M. Blanchard, P. Vermande, Y. Perrodin, Toxicological effects of disinfections using sodium hypochlorite on aquatic organisms and its contribution to AOX formation in hospital wastewater, *Environment International*, 30 (2004) 891.
[54] T.V. Gregory, K. Ellis, R. Valeriani, F. Khan, X. Wu, L. Murin, *et al.*, MoWa: A disinfectant for hospital surfaces contaminated with Methicillin-Resistant Staphylococcus aureus (MRSA) and other nosocomial pathogens, *Frontiers in Cellular and Infection Microbiology*, 11 (2021) 676638.
[55] S. Kannan, A. Solomon, G. Krishnamoorthy, M. Marudhamuthu, Liposome encapsulated surfactant abetted copper nanoparticles alleviates biofilm mediated

virulence in pathogenic Pseudomonas aeruginosa and MRSA, *Scientific Reports*, 11 (2021) 1102.

[56] S. Hemaiswarya, A.K. Kruthiventi, M. Doble, Synergism between natural products and antibiotics against infectious diseases, *Phytomedicine*, 15 (2008) 639.

[57] M. Grobbelaar, G.E. Louw, S.L. Sampson, P.D. van Helden, P.R. Donald, R.M. Warren, Evolution of rifampicin treatment for tuberculosis, *Infection, Genetics and Evolution*, 74 (2019) 103937.

[58] P. O'Hara, A.J. Hickey, Respirable PLGA microspheres containing rifampicin for the treatment of tuberculosis: Manufacture and characterization, *Pharmaceutical Research*, 17 (2000) 955.

[59] M. Gjorgjieva, T. Tomašič, D. Kikelj, L.P. Mašič, Benzothiazole-based compounds in antibacterial drug discovery, *Current Medicinal Chemistry*, 25 (2018) 5218.

[60] Y.I. Asiri, A. Alsayari, A.B. Muhsinah, Y.N. Mabkhot, M.Z. Hassan, Benzothiazoles as potential antiviral agents, *Journal of Pharmacy and Pharmacology*, 72 (2020) 1459.

[61] A. Irfan, F. Batool, S.A. Zahra Naqvi, A. Islam, S.M. Osman, A. Nocentini, *et al.*, Benzothiazole derivatives as anticancer agents, *Journal of Enzyme Inhibition and Medicinal Chemistry*, 35 (2020) 265.

[62] H. Bujdáková, M. Múčková, Antifungal activity of a new benzothiazole derivative against Candida in vitro and in vivo, *International Journal of Antimicrobial Agents*, 4 (1994) 303.

[63] I. Hutchinson, S.A. Jennings, B.R. Vishnuvajjala, A.D. Westwell, M.F.G. Stevens, Antitumor Benzothiazoles, synthesis and pharmaceutical properties of antitumor 2-(4-Aminophenyl)benzothiazole amino acid prodrugs, *Journal of Medicinal Chemistry*, 45 (2002) 744.

[64] K. Nakata, T. Tsuchido, Y. Matsumura, Antimicrobial cationic surfactant, cetyltrimethylammonium bromide, induces superoxide stress in Escherichia coli cells, *Journal of Applied Microbiology*, 110 (2011) 568.

[65] H. Hashemzadeh, H. Raissi, Loading and release of anticancer drug from phosphorene as a template material with high efficient carrier: From vacuum to cell membrane, *Journal of Molecular Liquids*, 291 (2019) 111346.

[66] F. Farzad, H. Hashemzadeh, Probing the effect of polyethene glycol on the adsorption mechanisms of Gem on the hexagonal boron nitride as a highly efficient polymer-based drug delivery system: DFT, classical MD and Well-tempered Metadynamics simulations, *Journal of Molecular Graphics and Modelling*, 98 (2020) 107613.

[67] P. Rajdev, T. Mondol, A. Makhal, S.K. Pal, Simultaneous binding of anti-tuberculosis and anti-thrombosis drugs to a human transporter protein: A FRET study, *Journal of Photochemistry and Photobiology B: Biology*, 103 (2011) 153.

[68] P. Majumder, R. Sarkar, A.K. Shaw, A. Chakraborty, S.K. Pal, Ultrafast dynamics in a nanocage of enzymes: Solvation and fluorescence resonance energy transfer in reverse micelles, *Journal of Colloid and Interface Science*, 290 (2005) 462.

[69] J. Maiti, S. Biswas, A. Chaudhuri, S. Chakraborty, S. Chakraborty, R. Das, Environment sensitive fluorescent analogue of biologically active oxazoles differentially recognizes human serum albumin and bovine serum albumin: Photophysical and molecular modeling studies, *Spectrochimica Acta Part A: Molecular and Biomolecular Spectroscopy*, 175 (2017) 191.

[70] M. Tachiya, Application of a generating function to reaction kinetics in micelles. Kinetics of quenching of luminescent probes in micelles, *Chemical Physics Letters*, 33 (1975) 289.

[71] M. Tachiya, Kinetics of quenching of luminescent probes in micellar systems. II, *The Journal of Chemical Physics*, 76 (1982) 340.

[72] G. Borkow, J. Gabbay, Copper, an ancient remedy returning to fight microbial, fungal and viral infections, *Current Chemical Biology*, 3 (2009) 272.

[73] H. Dollwet, Historic uses of copper compounds in medicine, *Journal of Trace Elements in Medicine*, 2 (1985) 80.

[74] N.R. Council, Copper in drinking water, *National Academies Press (US)*, Washington (DC), 2000.

[75] K. Giannousi, G. Sarafidis, S. Mourdikoudis, A. Pantazaki, C. Dendrinou-Samara, Selective synthesis of Cu2O and Cu/Cu2O NPs: Antifungal activity to yeast Saccharomyces cerevisiae and DNA interaction, *Inorganic Chemistry*, 53 (2014) 9657.

[76] N.V. Gandhare, R.G. Chaudhary, V.P. Meshram, J.A. Tanna, S. Lade, M.P. Gharpure, *et al.*, An efficient and one-pot synthesis of 2, 4, 5-trisubstituted imidazole compounds catalyzed by copper nanoparticles, *Journal of the Chinese Advanced Materials Society*, 3 (2015) 270.

[77] J.A. Tanna, R.G. Chaudhary, V.N. Sonkusare, H.D. Juneja, CuO nanoparticles: Synthesis, characterization and reusable catalyst for polyhydroquinoline derivatives under ultrasonication, *Journal of the Chinese Advanced Materials Society*, 4 (2016) 110.

[78] H. Sun, H. Kim, S. Song, W. Jung, Copper foam-derived electrodes as efficient electrocatalysts for conventional and hybrid water electrolysis, *Materials Reports: Energy*, 2 (2022) 100092.

[79] X. Han, P. Liu, R. Ran, W. Wang, W. Zhou, Z. Shao, Non-metal fluorine doping in Ruddlesden–Popper perovskite oxide enables high-efficiency photocatalytic water splitting for hydrogen production, *Materials Today Energy*, 23 (2022) 100896.

[80] P. Kuang, Z. Ni, J. Yu, J. Low, New progress on MXenes-based nanocomposite photocatalysts, *Materials Reports: Energy*, 2 (2022) 100081.

[81] J. He, P. Liu, R. Ran, W. Wang, W. Zhou, Z. Shao, Single-atom catalysts for high-efficiency photocatalytic and photoelectrochemical water splitting: Distinctive roles, unique fabrication methods and specific design strategies, *Journal of Materials Chemistry A*, 10 (2022) 6835.

[82] K. Ssekatawa, D.K. Byarugaba, M.K. Angwe, E.M. Wampande, F. Ejobi, E. Nxumalo, *et al.*, Phyto-mediated copper oxide nanoparticles for antibacterial, antioxidant and photocatalytic performances, *Frontiers in Bioengineering and Biotechnology*, 10 (2022) 820218.

[83] A.C. Palmer, R. Kishony, Understanding, predicting and manipulating the genotypic evolution of antibiotic resistance, *Nature Reviews Genetics*, 14 (2013) 243.

[84] R.G. Chaudhary, V.N. Sonkusare, G.S. Bhusari, A. Mondal, D.P. Shaik, H.D. Juneja, Microwave-mediated synthesis of spinel $CuAl_2O_4$ nanocomposites for enhanced electrochemical and catalytic performance, *Research on Chemical Intermediates*, 44 (2018) 2039.

[85] C. Kaweeteerawat, C.H. Chang, K.R. Roy, R. Liu, R. Li, D. Toso, *et al.*, Cu nanoparticles have different impacts in Escherichia coli and Lactobacillus brevis than their microsized and ionic analogues, *ACS Nano*, 9 (2015) 7215.

[86] U. Bogdanovic, V. Vodnik, M. Mitric, S. Dimitrijevic, S.D. Skapin, V. Zunic, *et al.*, Nanomaterial with high antimicrobial efficacy copper/polyaniline nanocomposite, *ACS Applied Materials & Interfaces*, 7 (2015) 1955.

[87] Y.-H. Hsueh, P.-H. Tsai, K.-S. Lin, pH-dependent antimicrobial properties of copper oxide nanoparticles in Staphylococcus aureus, *International Journal of Molecular Sciences*, 18 (2017) 793.

[88] F. Nishino, M. Jeem, L. Zhang, K. Okamoto, S. Okabe, S. Watanabe, Formation of CuO nano-flowered surfaces via submerged photo-synthesis of crystallites and their antimicrobial activity, *Scientific Reports*, 7 (2017) 1.

[89] L. Weaver, J. Noyce, H. Michels, C. Keevil, Potential action of copper surfaces on meticillin-resistant Staphylococcus aureus, *Journal of Applied Microbiology*, 109 (2010) 2200.

[90] S. Jadhav, S. Gaikwad, M. Nimse, A. Rajbhoj, Copper oxide nanoparticles: Synthesis, characterization and their antibacterial activity, *Journal of cluster science*, 22 (2011) 121.

[91] R.Y. Pelgrift, A.J. Friedman, Nanotechnology as a therapeutic tool to combat microbial resistance, *Advanced Drug Delivery Reviews*, 65 (2013) 1803.

[92] Z. Zhu, S. Wan, Y. Zhao, Y. Gu, Y. Wang, Y. Qin, *et al.*, Recent advances in bismuth-based multimetal oxide photocatalysts for hydrogen production from water splitting: Competitiveness, challenges, and future perspectives, *Materials Reports: Energy*, 1 (2021) 100019.

[93] H. Xiao, P. Liu, W. Wang, R. Ran, W. Zhou, Z. Shao, Enhancing the photocatalytic activity of Ruddlesden-Popper Sr_2TiO_4 for hydrogen evolution through synergistic silver doping and moderate reducing pretreatment, *Materials Today Energy*, 23 (2022) 100899.

[94] G. McDonnell, A.D. Russell, Antiseptics and disinfectants: Activity, action, and resistance, *Clinical Microbiology Reviews*, 12 (1999) 147.

[95] H. Pang, F. Gao, Q. Lu, Morphology effect on antibacterial activity of cuprous oxide, *Chemical Communications*, 9 (2009) 1076.

[96] G. Ren, D. Hu, E.W. Cheng, M.A. Vargas-Reus, P. Reip, R.P. Allaker, Characterisation of copper oxide nanoparticles for antimicrobial applications, *International Journal of Antimicrobial Agents*, 33 (2009) 587.

[97] M.J. Wozniak-Budych, Ł. Przysiecka, B.M. Maciejewska, D. Wieczorek, K. Staszak, M. Jarek, *et al.*, Facile synthesis of sulfobetaine-stabilized Cu_2O nanoparticles and their biomedical potential, *ACS Biomaterials Science & Engineering*, 3 (2017) 3183.

[98] J. Zhou, H. Xiang, F. Zabihi, S. Yu, B. Sun, M. Zhu, Intriguing anti-superbug Cu_2O@ ZrP hybrid nanosheet with enhanced antibacterial performance and weak cytotoxicity, *Nano Research*, 12 (2019) 1453.

[99] E.M. Hotze, T. Phenrat, G.V. Lowry, Nanoparticle aggregation: Challenges to understanding transport and reactivity in the environment, *Journal of Environmental Quality*, 39 (2010) 1909.

[100] S. Mondal, R. Ghosh, A. Adhikari, U. Pal, D. Mukherjee, P. Biswas, *et al.*, In vitro and microbiological assay of functionalized hybrid nanomaterials to validate their efficacy in nanotheranostics: A combined spectroscopic and computational study, *ChemMedChem*, 16 (2021) 3739.

[101] L. Zhang, J.C. Thomas, M. Miragaia, O. Bouchami, F. Chaves, P.A. d'Azevedo, *et al.*, Multilocus sequence typing and further genetic characterization of the enigmatic pathogen, Staphylococcus hominis, *PLOS One*, 8 (2013) e66496.

[102] S.-D. Kim, L.C. McDonald, W.R. Jarvis, S.K. McAllister, R. Jerris, L.A. Carson, *et al.*, Determining the significance of coagulase-negative staphylococci isolated from blood cultures at a community hospital a role for species and strain identification, *Infection Control & Hospital Epidemiology*, 21 (2000) 213.

[103] M.N. Iyer, W.J. Wirostko, S.H. Kim, K.B. Simons, Staphylococcus hominis endophthalmitis associated with a capsular hypopyon, *American journal of ophthalmology*, 139 (2005) 930.

[104] T.H. Lam, D. Verzotto, P. Brahma, A.H.Q. Ng, P. Hu, D. Schnell, *et al.*, Understanding the microbial basis of body odor in pre-pubescent children and teenagers, *Microbiome*, 6 (2018) 1.

[105] J. Zhu, D. Li, H. Chen, X. Yang, L. Lu, X. Wang, Highly dispersed CuO nanoparticles prepared by a novel quick-precipitation method, *Materials Letters*, 58 (2004) 3324.

[106] S. Mallakpour, M. Dinari, E. Azadi, Grafting of citric acid as a green coupling agent on the surface of CuO nanoparticle and its application for synthesis and characterization of novel nanocomposites based on poly (amide-imide) containing N-trimellitylimido-L-valine linkage, *Polymer-Plastics Technology and Engineering*, 54 (2015) 594.

[107] A. Nawaz, S. Goudarzi, M.A. Asghari, S. Pichiah, G.S. Selopal, F. Rosei, *et al.*, Review of Hybrid 1D/2D Photocatalysts for Light-Harvesting Applications, *ACS Applied Nano Materials*, 4 (2021) 11323.

[108] S.A. Ahmed, M. Nur Hasan, D. Bagchi, H.M. Altass, M. Morad, I.I. Althagafi, *et al.*, Nano-MOFs as targeted drug delivery agents to combat antibiotic-resistant bacterial infections, *Royal Society Open Science*, 7 (2020) 200959.

[109] E. Tinajero-Díaz, D. Salado-Leza, C. Gonzalez, M. Martínez Velázquez, Z. López, J. Bravo-Madrigal, *et al.*, Green metallic nanoparticles for cancer therapy: Evaluation models and cancer applications, *Pharmaceutics*, 13 (2021) 1719.

[110] C.A. Antonyraj, J. Jeong, B. Kim, S. Shin, S. Kim, K.-Y. Lee, *et al.*, Selective oxidation of HMF to DFF using Ru/γ-alumina catalyst in moderate boiling solvents toward industrial production, *Journal of Industrial and Engineering Chemistry*, 19 (2013) 1056.

[111] F. Neville, N.A. Pchelintsev, M.J. Broderick, T. Gibson, P.A. Millner, Novel one-pot synthesis and characterization of bioactive thiol-silicate nanoparticles for biocatalytic and biosensor applications, *Nanotechnology*, 20 (2009) 055612.

[112] S. Menon, S. Rajeshkumar, V. Kumar, A review on biogenic synthesis of gold nanoparticles, characterization, and its applications, *Resource-Efficient Technologies*, 3 (2017) 516.

[113] R. Emmanuel, M. Saravanan, M. Ovais, S. Padmavathy, Z.K. Shinwari, P. Prakash, Antimicrobial efficacy of drug blended biosynthesized colloidal gold nanoparticles from Justicia glauca against oral pathogens: A nanoantibiotic approach, *Microbial Pathogenesis*, 113 (2017) 295.

[114] M. Saravanan, V. Jacob, J. Arockiaraj, P. Prakash, Extracellular biosynthesis, characterization and antibacterial activity of silver nanoparticles synthesized by Bacillus subtilis (NCIM—2266), *Journal of Bionanoscience*, 8 (2014) 21.

[115] M. Saravanan, T. Asmalash, A. Gebrekidan, D. Gebreegziabiher, T. Araya, H. Hilekiros, *et al.*, Nano-medicine as a newly emerging approach to combat human immunodeficiency virus (HIV), *Pharmaceutical Nanotechnology*, 6 (2018) 17.

[116] M. Saravanan, H. Barabadi, B. Ramachandran, G. Venkatraman, K. Ponmurugan, Emerging plant-based anti-cancer green nanomaterials in present scenario, *Comprehensive Analytical Chemistry*, 87 (2019) 291.

[117] H. Barabadi, K. Damavandi Kamali, F. Jazayeri Shoushtari, B. Tajani, M.A. Mahjoub, A. Alizadeh, *et al.*, Emerging theranostic silver and gold nanomaterials to combat prostate cancer: A systematic review, *Journal of Cluster Science*, 30 (2019) 1375.

[118] H. Barabadi, B. Tajani, M. Moradi, K. Damavandi Kamali, R. Meena, S. Honary, *et al.*, Penicillium family as emerging nanofactory for biosynthesis of green nanomaterials: A journey into the world of microorganisms, *Journal of Cluster Science*, 30 (2019) 843.

[119] N. Cioffi, L. Torsi, N. Ditaranto, G. Tantillo, L. Ghibelli, L. Sabbatini, *et al.*, Copper nanoparticle/polymer composites with antifungal and bacteriostatic properties, *Chemistry of Materials*, 17 (2005) 5255.

[120] O. Abramov, A. Gedanken, Y. Koltypin, N. Perkas, I. Perelshtein, E. Joyce, *et al.*, Pilot scale sonochemical coating of nanoparticles onto textiles to produce biocidal fabrics, *Surface and Coatings Technology*, 204 (2009) 718.

[121] Y. Xia, H. Yang, C.T. Campbell, Nanoparticles for catalysis, *Accounts of Chemical Research*, 46 (2013) 1671.

[122] C. Chimeno-Trinchet, A. Fernández-González, J.Á. García Calzón, M.E. Díaz-García, R. Badía Laíño, Alkyl-capped copper oxide nanospheres and nanoprolates for sustainability: Water treatment and improved lubricating performance, *Science and technology of Advanced Materials*, 20 (2019) 657.

[123] A. Banerjee, D. Mukherjee, A. Bera, R. Ghosh, S. Mondal, S. Mukhopadhyay, *et al.*, Molecular co-localization of multiple drugs in a nanoscopic delivery vehicle for

potential synergistic remediation of multi-drug resistant bacteria, *Scientific Reports*, 12 (2022) 1.

[124] A. Haddadin, S. Fappiano, P.A. Lipsett, Methicillin resistant Staphylococcus aureus (MRSA) in the intensive care unit, *Postgraduate Medical Journal*, 78 (2002) 385.

[125] A.S. Al-Thubiani, Y.A. Maher, A. Fathi, M.A. Abourehab, M. Alarjah, M.S. Khan, *et al.*, Identification and characterization of a novel antimicrobial peptide compound produced by Bacillus megaterium strain isolated from oral microflora, *Saudi Pharmaceutical Journal*, 26 (2018) 1089.

[126] R.M. El-Masry, D. Talat, S.A. Hassoubah, N.M. Zabermawi, N.Z. Eleiwa, R.M. Sherif, *et al.*, Evaluation of the antimicrobial activity of ZnO nanoparticles against enterotoxigenic Staphylococcus aureus, *Life*, 12 (2022) 1662.

[127] T. Al-Warhi, D.M. Elimam, Z.M. Elsayed, M.M. Abdel-Aziz, R.M. Maklad, A.A. Al-Karmalawy, *et al.*, Development of novel isatin thiazolyl-pyrazoline hybrids as promising antimicrobials in MDR pathogens, *RSC Advances*, 12 (2022) 31466.

[128] R. Nelson, Antibiotic development pipeline runs dry, *The Lancet*, 362 (2003) 1726.

[129] A. Gomathi, S.X. Rajarathinam, A.M. Sadiq, S. Rajeshkumar, Anticancer activity of silver nanoparticles synthesized using aqueous fruit shell extract of Tamarindus indica on MCF-7 human breast cancer cell line, *Journal of Drug Delivery Science and Technology*, 55 (2020) 101376.

[130] A. Banerjee, N. Bhattacharyya, R. Ghosh, S. Singh, A. Adhikari, S. Mondal, *et al.*, Non-invasive estimation of hemoglobin, bilirubin and oxygen saturation of neonates simultaneously using whole optical spectrum analysis at point of care, *Scientific Reports*, 13 (2023) 2370.

[131] M.S. Nogueira, S. Maryam, M. Amissah, H. Lu, N. Lynch, S. Killeen, *et al.*, Evaluation of wavelength ranges and tissue depth probed by diffuse reflectance spectroscopy for colorectal cancer detection, *Scientific Reports*, 11 (2021) 1.

[132] Z.I. Volynskaya, A.S. Haka, K.L. Bechtel, M. Fitzmaurice, R. Shenk, N. Wang, *et al.*, Diagnosing breast cancer using diffuse reflectance spectroscopy and intrinsic fluorescence spectroscopy, *Journal of Biomedical Optics*, 13 (2008) 024012.

[133] J.J. Soto-Bernal, G.V. Vázquez, R. González-Mota, I. Rosales-Candelas, J.A. Ortiz-Lozano, H.A. De-León-Martínez, Optical method to characterize and assess setting evolution of cement pastes, *Applied Optics*, 59 (2020) D1.

[134] C. Elliott, V. Vijayakumar, W. Zink, R. Hansen, National instruments LabVIEW: A programming environment for laboratory automation and measurement, *JALA: Journal of the Association for Laboratory Automation*, 12 (2007) 17.

[135] I. Kirkman, P. Buksh, Data acquisition and control using National Instruments'''LabVIEW''software, *Review of Scientific Instruments*, 63 (1992) 869.

[136] T.S. Toh, F. Dondelinger, D. Wang, Looking beyond the hype: Applied AI and machine learning in translational medicine, *EBioMedicine*, 47 (2019) 607.

[137] L. Vanneschi, M. Castelli, Multilayer perceptrons, *Encyclopedia of Bioinformatics and Computational Biology*, 1 (2019) 612.

[138] Y. Park, K.H. Cho, J. Park, S.M. Cha, J.H. Kim, Development of early-warning protocol for predicting chlorophyll-a concentration using machine learning models in freshwater and estuarine reservoirs, Korea, *Science of the Total Environment*, 502 (2015) 31.

[139] D.J. Faber, M.C. Aalders, E.G. Mik, B.A. Hooper, M.J. van Gemert, T.G. van Leeuwen, Oxygen saturation-dependent absorption and scattering of blood, *Physical Review Letters*, 93 (2004) 028102.

[140] S. Prahl, Optical absorption of hemoglobin, 1999 (http://omlc. ogi. edu/spectra/hemoglobin).

[141] A.A. Lamola, M. Russo, Fluorescence excitation spectrum of bilirubin in blood: A model for the action spectrum for phototherapy of neonatal jaundice, *Photochemistry and Photobiology*, 90 (2014) 294.

[142] C. Park, C.C. Took, J.-K. Seong, Machine learning in biomedical engineering, *Biomedical Engineering Letters*, 8 (2018) 1.

[143] V. Nasteski, An overview of the supervised machine learning methods, *Horizons. B*, 4 (2017) 51.

[144] Y.H. Jung, J. Lee, H.-S. Kim, S.H. Shin, J.A. Sohn, E.-K. Kim*, et al.*, The efficacy of noninvasive hemoglobin measurement by pulse CO-oximetry in neonates, *Pediatric Critical Care Medicine*, 14 (2013) 70.

[145] E.H. Kim, J.H. Lee, I.K. Song, H.S. Kim, Y.E. Jang, S. Yoo, *et al.*, Accuracy of pulse oximeters at low oxygen saturations in children with congenital cyanotic heart disease: An observational study, *Pediatric Anesthesia*, 29 (2019) 597.
[146] A. Halder, A. Adhikari, R. Ghosh, S. Singh, A. Banerjee, N. Ghosh, *et al.*, Large scale validation of a new non-invasive and non-contact bilirubinometer in neonates with risk factors, *Scientific Reports*, 10 (2020) 1.
[147] C. Nicholas, R. George, S. Sardesai, M. Durand, R. Ramanathan, R. Cayabyab, Validation of noninvasive hemoglobin measurement by pulse co-oximeter in newborn infants, *Journal of Perinatology*, 35 (2015) 617.
[148] H. Kazanasmaz, M. Demir, The Comparison of hemoglobin values measured by blood and continuous non-invasive monitoring (SpHb) in newborn infants, *Journal of Tropical Pediatrics*, 67 (2021) fmaa050.
[149] M.J. Maisels, E.M. Ostrea, S. Touch, S.E. Clune, E. Cepeda, E. Kring, *et al.*, Evaluation of a new transcutaneous bilirubinometer, *Pediatrics*, 113 (2004) 1628.
[150] B.O. Olusanya, T.A. Ogunlesi, P. Kumar, N.-Y. Boo, I.F. Iskander, M.F.B. de Almeida, *et al.*, Management of late-preterm and term infants with hyperbilirubinaemia in resource-constrained settings, *BMC Pediatrics*, 15 (2015) 1.
[151] V.K. Bhutani, G.R. Gourley, S. Adler, B. Kreamer, C. Dalin, L.H. Johnson, Noninvasive measurement of total serum bilirubin in a multiracial predischarge newborn population to assess the risk of severe hyperbilirubinemia, *Pediatrics*, 106 (2000) e17.
[152] S.N. El-Beshbishi, K.E. Shattuck, A.A. Mohammad, J.R. Petersen, Hyperbilirubinemia and transcutaneous bilirubinometry, *Clinical Chemistry*, 55 (2009) 1280.
[153] A. Banerjee, D. Mukherjee, A. Bera, R. Ghosh, S. Mondal, S. Mukhopadhyay, *et al.*, Molecular co-localization of multiple drugs in a nanoscopic delivery vehicle for potential synergistic remediation of multi-drug resistant bacteria, *Scientific Reports*, 12 (2022) 18881.
[154] T. Mondol, P. Rajdev, A. Makhal, S.K. Pal, Interaction of an antituberculosis drug with a nanoscopic macromolecular assembly: Temperature-dependent Förster

resonance energy transfer studies on rifampicin in an anionic sodium dodecyl sulfate micelle, *The Journal of Physical Chemistry. B*, 115 (2011) 2924.
[155] K.J. Williams, L.J. Piddock, Accumulation of rifampicin by Escherichia coli and Staphylococcus aureus, *The Journal of Antimicrobial Chemotherapy*, 42 (1998) 597.
[156] R. Langer, Drug delivery. Drugs on target, *Science (New York, N.Y.)*, 293 (2001) 58.
[157] B.D. Howes, L. Guerrini, S. Sanchez-Cortes, M.P. Marzocchi, J.V. Garcia-Ramos, G. Smulevich, The influence of pH and anions on the adsorption mechanism of rifampicin on silver colloids, *Journal of Raman Spectroscopy*, 38 (2007) 859.
[158] M.A. Moretton, R.J. Glisoni, D.A. Chiappetta, A. Sosnik, Molecular implications in the nanoencapsulation of the anti-tuberculosis drug rifampicin within flower-like polymeric micelles, *Colloids and Surfaces. B, Biointerfaces*, 79 (2010) 467.
[159] C. Rottman, G. Grader, Y. De Hazan, S. Melchior, D. Avnir, Surfactant-induced modification of dopants reactivity in sol−gel matrixes, *Journal of the American Chemical Society*, 121 (1999) 8533.
[160] K. Kuperkar, L. Abezgauz, D. Danino, G. Verma, P.A. Hassan, V.K. Aswal, *et al.*, Viscoelastic micellar water/CTAB/NaNO3 solutions: Rheology, SANS and cryo-TEM analysis, *Journal of Colloid and Interface Science*, 323 (2008) 403.
[161] Z. Lin, J.J. Cai, L.E. Scriven, H.T. Davis, Spherical-to-Wormlike micelle transition in CTAB solutions, *The Journal of Physical Chemistry*, 98 (1994) 5984.
[162] X. Zhang, Y. Hu, X. Yang, Y. Tang, S. Han, A. Kang, *et al.*, FÖrster resonance energy transfer (FRET)-based biosensors for biological applications, *Biosensors & Bioelectronics*, 138 (2019) 111314.
[163] P. Singh, S. Choudhury, V.K. Sharma, S. Mitra, R. Mukhopadhyay, R. Das, *et al.*, Modulation of solvation and molecular recognition of a lipid bilayer under dynamical phase transition, *ChemPhysChem*, 19 (2018) 2709.
[164] S. Saha, D. Majhi, K. Bhattacharyya, N. Preeyanka, A. Datta, M. Sarkar, Evidence of homo-FRET in quantum dot–dye heterostructured assembly, *Physical Chemistry Chemical Physics*, 20 (2018) 9523.

[165] S. Banerjee, N. Goswami, S.K. Pal, A potential carcinogenic pyrene derivative under Förster Resonance Energy Transfer to various energy acceptors in nanoscopic environments, *ChemPhysChem*, 14 (2013) 3581.
[166] R. Ghosh, S. Mondal, D. Mukherjee, A. Adhikari, S.A. Ahmed, R.I. Alsantali, *et al.*, Oral drug delivery using a polymeric nanocarrier: Chitosan nanoparticles in the delivery of rifampicin, *Materials Advances*, 3 (2022) 4622.
[167] D. Bagchi, V.S.S. Rathnam, P. Lemmens, I. Banerjee, S.K. Pal, NIR-Light-Active ZnO-Based Nanohybrids for Bacterial Biofilm Treatment, *ACS Omega*, 3 (2018) 10877.
[168] A. Bexfield, A.E. Bond, E.C. Roberts, E. Dudley, Y. Nigam, S. Thomas, *et al.*, The antibacterial activity against MRSA strains and other bacteria of a <500Da fraction from maggot excretions/secretions of Lucilia sericata (Diptera: Calliphoridae), *Microbes and Infection*, 10 (2008) 325.
[169] S.A. Ahmed, M.N. Hasan, H.M. Altass, A. Bera, R.I. Alsantali, N. Pan, *et al.*, Tetracycline encapsulated in Au nanoparticle-decorated ZnO nanohybrids for enhanced antibacterial activity, *ACS Applied Nano Materials*, 5 (2022) 4484.
[170] A. Bera, M.N. Hasan, A. Chatterjee, D. Mukherjee, S.K. Pal, Dual sensitization via electron and energy harvesting in a nanohybrid for improvement of therapeutic efficacy, *ACS Physical Chemistry Au*, 2 (2022) 171.
[171] A. Adhikari, V.K. Bhutani, S. Mondal, M. Das, S. Darbar, R. Ghosh, *et al.*, A nanoceutical agent for chemoprevention of bilirubin encephalopathy, *Pediatric Research*, 93 (2023) 827.
[172] T. Xu, J. Han, J. Zhang, J. Chen, N. Wu, W. Zhang, *et al.*, Absence of Protoheme IX Farnesyltransferase CtaB causes virulence attenuation but enhances pigment production and persister survival in MRSA, *Frontiers in Microbiology*, 7 (2016).
[173] B. Wang, T.W. Muir, Regulation of virulence in Staphylococcus aureus: Molecular mechanisms and remaining puzzles, *Cell Chemical Biology*, 23 (2016) 214.
[174] M.O. Clements, S.P. Watson, R.K. Poole, S.J. Foster, CtaA of Staphylococcus aureus is required for starvation survival, recovery, and cytochrome biosynthesis, *Journal of Bacteriology*, 181 (1999) 501.

[175] L. Dhungel, L. Burcham, J.Y. Park, H.D. Sampathkumar, A. Cudjoe, K.S. Seo, *et al.*, Responses to chemical cross-talk between the Mycobacterium ulcerans toxin, mycolactone, and Staphylococcus aureus, *Scientific Reports*, 11 (2021) 11746.
[176] S.V. Shahmirzadi, M.-T. Nguyen, F. Götz, Evaluation of Staphylococcus aureus Lipoproteins: Role in Nutritional Acquisition and Pathogenicity, *Frontiers in Microbiology*, 7 (2016) 1404.
[177] F. Götz, S. Mayer, Both terminal oxidases contribute to fitness and virulence during organ-specific Staphylococcus aureus colonization, *mBio*, 4 (2013) e00976.
[178] M. Elgrably-Weiss, S. Park, E. Schlosser-Silverman, I. Rosenshine, J. Imlay, S. Altuvia, A Salmonella enterica Serovar Typhimurium hemA Mutant Is Highly Susceptible to Oxidative DNA Damage, *Journal of Bacteriology*, 184 (2002) 3774.
[179] J. Desai, Y.-L. Liu, H. Wei, W. Liu, T.-P. Ko, R.-T. Guo, *et al.*, Structure, function and inhibition of Staphylococcus aureus heptaprenyl diphosphate synthase, *ChemMedChem*, 11 (2016) 1915.
[180] D.O. Chaffin, D. Taylor, S.J. Skerrett, C.E. Rubens, Changes in the Staphylococcus aureus transcriptome during early adaptation to the lung, *PLOS ONE*, 7 (2012) e41329.
[181] R. Banerjee, M. Gretes, C. Harlem, L. Basuino, H.F. Chambers, A mecA-Negative strain of Methicillin-Resistant Staphylococcus aureus with high-level β-Lactam resistance contains mutations in three genes, *Antimicrobial Agents and Chemotherapy*, 54 (2010) 4900.
[182] R. Deora, T.K. Misra, Characterization of the primary σ factor of Staphylococcus aureus, *Journal of Biological Chemistry*, 271 (1996) 21828.
[183] A. Weiss, B.D. Moore, M.H.J. Tremblay, D. Chaput, A. Kremer, L.N. Shaw, The ω subunit governs RNA polymerase stability and transcriptional specificity in Staphylococcus aureus, *Journal of Bacteriology*, 199 (2017) e00459.
[184] T.I. Moy, A. Daniel, C. Hardy, A. Jackson, O. Rehrauer, Y.S. Hwang, *et al.*, Evaluating the activity of the RNA polymerase inhibitor myxopyronin B against Staphylococcus aureus, *FEMS Microbiology Letters*, 319 (2011) 176.

[185] R.A. Forsyth, R.J. Haselbeck, K.L. Ohlsen, R.T. Yamamoto, H. Xu, J.D. Trawick, *et al.*, A genome-wide strategy for the identification of essential genes in Staphylococcus aureus, *Molecular Microbiology*, 43 (2002) 1387.

[186] R. Sierra, J. Prados, O.O. Panasenko, D.O. Andrey, B. Fleuchot, P. Redder, *et al.*, Insights into the global effect on Staphylococcus aureus growth arrest by induction of the endoribonuclease MazF toxin, *Nucleic Acids Research*, 48 (2020) 8545.

[187] D. Ince, D.C. Hooper, Quinolone resistance due to reduced target enzyme expression, *Journal of Bacteriology*, 185 (2003) 6883.

[188] K.L. Tomlinson, T.W.F. Lung, F. Dach, M.K. Annavajhala, S.J. Gabryszewski, R.A. Groves, *et al.*, Staphylococcus aureus induces an itaconate-dominated immunometabolic response that drives biofilm formation, *Nature Communications*, 12 (2021) 1399.

[189] J. Dordel, C. Kim, M. Chung, M. Pardos de la Gándara, M.T.J. Holden, J. Parkhill, *et al.*, Novel Determinants of Antibiotic Resistance: Identification of mutated loci in highly Methicillin-Resistant subpopulations of Methicillin-Resistant Staphylococcus aureus, *mBio*, 5 (2014) e01000.

[190] S.M. Edslev, M.-L. Clausen, T. Agner, M. Stegger, P.S. Andersen, Genomic analysis reveals different mechanisms of fusidic acid resistance in Staphylococcus aureus from Danish atopic dermatitis patients, *The Journal of Antimicrobial Chemotherapy*, 73 (2018) 856.

[191] J.G. Ondeyka, D. Zink, A. Basilio, F. Vicente, G. Bills, M.T. Diez, *et al.*, Coniothyrione, a Chlorocyclopentandienylbenzopyrone as a bacterial protein synthesis inhibitor discovered by antisense technology, *Journal of Natural Products*, 70 (2007) 668.

[192] S. Michalik, J. Bernhardt, A. Otto, M. Moche, D. Becher, H. Meyer, *et al.*, Life and death of proteins: A case study of glucose-starved Staphylococcus aureus, *Molecular & Cellular Proteomics*, 11 (2012) 558.

[193] L.H. Tsang, S.T. Daily, E.C. Weiss, M.S. Smeltzer, Mutation of traP in Staphylococcus aureus has no impact on expression of agr or biofilm formation, *Infection and Immunity*, 75 (2007) 4528.

[194] C. Wicker-Planquart, A.-E. Foucher, M. Louwagie, R.A. Britton, J.-M. Jault, Interactions of an essential Bacillus subtilis GTPase, YsxC, with Ribosomes, *Journal of Bacteriology*, 190 (2008) 681.

[195] P.D. Olson, L.J. Kuechenmeister, K.L. Anderson, S. Daily, K.E. Beenken, C.M. Roux, *et al.*, Small molecule inhibitors of Staphylococcus aureus RnpA alter cellular mRNA turnover, exhibit antimicrobial activity, and attenuate pathogenesis, *PLOS Pathogens*, 7 (2011) e1001287.

[196] C. Jensen, M.J. Fosberg, I. Thalso-Madsen, K.T. Bæk, D. Frees, Staphylococcus aureus ClpX localizes at the division septum and impacts transcription of genes involved in cell division, T7-secretion, and SaPI5-excision, *Scientific Reports*, 9 (2019) 16456.

[197] R.A. Keogh, R.L. Zapf, A. Frey, E.C. Marino, G.G. Null, R.E. Wiemels, *et al.*, Staphylococcus aureus trigger factor is involved in biofilm formation and cooperates with the chaperone PpiB, *Journal of Bacteriology*, 203 (2021) e00681.

[198] I.C. Saldarriaga Fernández, H.C.v.d. Mei, S. Metzger, D.W. Grainger, A.F. Engelsman, M.R. Nejadnik, *et al.*, In vitro and in vivo comparisons of staphylococcal biofilm formation on a cross-linked poly(ethylene glycol)-based polymer coating, *Acta Biomaterialia*, 6 (2010) 1119.

[199] J.V. Bugrysheva, A.V. Bryksin, H.P. Godfrey, F.C. Cabello, Borrelia burgdorferi rel is responsible for generation of Guanosine-3′-Diphosphate-5′-Triphosphate and growth control, *Infection and Immunity*, 73 (2005) 4972.

[200] Y. Xie, L. Yang, Calcium and Magnesium ions are membrane-active against stationary-phase Staphylococcus aureus with high specificity, *Scientific Reports*, 6 (2016) 20628.

[201] M.M. Pomposello, K. Nemes, K. Mosovsky, Dietary antioxidant seleno-L-methionine protects macrophages infected with Burkholderia thailandensis, *PLOS ONE*, 15 (2020) e0238174.

[202] A. Banerjee, R. Ghosh, T. Adhikari, S. Mukhopadhyay, A. Chattopadhyay, S.K. Pal, Development of nanomedicine from copper mine tailing waste: A pavement towards circular economy with advanced redox nanotechnology, *Catalysts*, 13 (2023) 369.

[203] B. Wang, X.-L. Wu, C.-Y. Shu, Y.-G. Guo, C.-R. Wang, Synthesis of CuO/graphene nanocomposite as a high-performance anode material for lithium-ion batteries, *Journal of Materials Chemistry*, 20 (2010) 10661.

[204] S. Asbrink, A. Waskowska, CuO: X-ray single-crystal structure determination at 196 K and room temperature, *Journal of Physics: Condensed Matter*, 3 (1991) 8173.

[205] A. Patterson, The Scherrer formula for X-ray particle size determination, *Physical Review*, 56 (1939) 978.

[206] M. Ahamed, H.A. Alhadlaq, M. Khan, P. Karuppiah, N.A. Al-Dhabi, Synthesis, characterization, and antimicrobial activity of copper oxide nanoparticles, *Journal of Nanomaterials*, 2014 (2014) 1.

[207] S. Moniri, M. Ghoranneviss, M.R. Hantehzadeh, M.A. Asadabad, Synthesis and optical characterization of copper nanoparticles prepared by laser ablation, *Bulletin of Materials Science*, 40 (2017) 37.

[208] S. Sen, K. Sarkar, Effective biocidal and wound healing cogency of biocompatible glutathione: Citrate-capped copper oxide nanoparticles against multidrug-resistant pathogenic enterobacteria, *Microbial Drug Resistance*, 27 (2021) 616.

[209] J.M. Cantu, Y. Ye, C. Valdes, K. Cota-Ruiz, J.A. Hernandez-Viezcas, J.L. Gardea-Torresdey, Citric acid-functionalized cuo nanoparticles alter biochemical responses in Candyland Red tomato (Solanum lycopersicum), *ACS Agricultural Science & Technology*, 2 (2022) 359.

[210] S. Pabisch, B. Feichtenschlager, G. Kickelbick, H. Peterlik, Effect of interparticle interactions on size determination of zirconia and silica based systems–A comparison of SAXS, DLS, BET, XRD and TEM, *Chemical Physics Letters*, 521 (2012) 91.

[211] Y. Abboud, T. Saffaj, A. Chagraoui, A. El Bouari, K. Brouzi, O. Tanane, *et al.*, Biosynthesis, characterization and antimicrobial activity of copper oxide nanoparticles (CONPs) produced using brown alga extract (Bifurcaria bifurcata), *Applied Nanoscience*, 4 (2014) 571.

[212] Y. Zhang, N. Li, Y. Xiang, D. Wang, P. Zhang, Y. Wang, *et al.*, A flexible non-enzymatic glucose sensor based on copper nanoparticles anchored on laser-induced graphene, *Carbon*, 156 (2020) 506.

[213] W. Zhu, $p < 0.05$, < 0.01, < 0.001, < 0.0001, < 0.00001, < 0.000001, or < 0.0000001, *Journal of Sport and Health Science*, 5 (2016) 77.

[214] M. Pirilä, M. Saouabe, S. Ojala, B. Rathnayake, F. Drault, A. Valtanen, *et al.*, Photocatalytic degradation of organic pollutants in wastewater, *Topics in Catalysis*, 58 (2015) 1085.

[215] A. Ajmal, I. Majeed, R.N. Malik, H. Idriss, M.A. Nadeem, Principles and mechanisms of photocatalytic dye degradation on TiO_2 based photocatalysts: A comparative overview, *RSC Advances*, 4 (2014) 37003.

[216] A.K. Sibhatu, G.K. Weldegebrieal, S. Sagadevan, N.N. Tran, V. Hessel, Photocatalytic activity of CuO nanoparticles for organic and inorganic pollutants removal in wastewater remediation, *Chemosphere*, (2022) 134623.

[217] I. Sharma, P. Ahmad, Catalase: A versatile antioxidant in plants, in: Oxidative damage to plants, Elsevier, Edinburgh, 2014, pp. 131.

[218] T. Wang, X. Xie, H. Liu, F. Chen, J. Du, X. Wang, *et al.*, Pyridine nucleotide-disulphide oxidoreductase domain 2 (PYROXD2): Role in mitochondrial function, *Mitochondrion*, 47 (2019) 114.

[219] J.F. Moran, Z. Sun, G. Sarath, R. Arredondo-Peter, E.K. James, M. Becana, *et al.*, Molecular cloning, functional characterization, and subcellular localization of soybean nodule dihydrolipoamide reductase, *Plant Physiology*, 128 (2002) 300.

[220] S. Marzi, W. Knight, L. Brandi, E. Caserta, N. Soboleva, W.E. Hill, *et al.*, Ribosomal localization of translation initiation factor IF2, *RNA*, 9 (2003) 958.

[221] M. Tarry, S.R. Arends, P. Roversi, E. Piette, F. Sargent, B.C. Berks, *et al.*, The Escherichia coli cell division protein and model Tat substrate SufI (FtsP) localizes to the septal ring and has a multicopper oxidase-like structure, *Journal of Molecular Biology*, 386 (2009) 504.

[222] Z. Freedman, C. Zhu, T. Barkay, Mercury resistance and mercuric reductase activities and expression among chemotrophic thermophilic Aquificae, *Applied and Environmental Microbiology*, 78 (2012) 6568.

[223] A. Banerjee, R. Ghosh, A. Bera, S. Mukhopadhyay, M.M. Al-Rooqi, I.I. Althagafi, *et al.*, "Nano-Copper": A potential remediation of antibiotic-resistant infections, *Journal of Nanomedicine*, 6 (2023) 1058.

[224] L.-F. Liao, C.-F. Lien, J.-L. Lin, FTIR study of adsorption and photoreactions of acetic acid on TiO_2, *Physical Chemistry Chemical Physics*, 3 (2001) 3831.
[225] E. Cheraghipour, S. Javadpour, A.R. Mehdizadeh, Citrate capped superparamagnetic iron oxide nanoparticles used for hyperthermia therapy, (2012).
[226] S. Nigam, K. Barick, D. Bahadur, Development of citrate-stabilized Fe_3O_4 nanoparticles: Conjugation and release of doxorubicin for therapeutic applications, *Journal of Magnetism and Magnetic Materials*, 323 (2011) 237.
[227] J. Jayaprakash, N. Srinivasan, P. Chandrasekaran, Surface modifications of CuO nanoparticles using Ethylene diamine tetra acetic acid as a capping agent by sol–gel routine, *Spectrochimica Acta Part A: Molecular and Biomolecular Spectroscopy*, 123 (2014) 363.
[228] D.D. Leipe, D. Landsman, Histone deacetylases, acetoin utilization proteins and acetylpolyamine amidohydrolases are members of an ancient protein superfamily, *Nucleic Acids Research*, 25 (1997) 3693.
[229] A.W. Smith, H. Roche, M.C. Trombe, D.E. Briles, A. Håkansson, Characterization of the dihydrolipoamide dehydrogenase from Streptococcus pneumoniae and its role in pneumococcal infection, *Molecular Microbiology*, 44 (2002) 431.
[230] M. Alfonso-Prieto, X. Biarnés, P. Vidossich, C. Rovira, The molecular mechanism of the catalase reaction, *Journal of the American Chemical Society*, 131 (2009) 11751.
[231] A.P. Batista, A. Kletzin, M.M. Pereira, The dihydrolipoamide dehydrogenase from the crenarchaeon Acidianus ambivalens, *FEMS Microbiology Letters*, 281 (2008) 147.
[232] H. Körner, H.J. Sofia, W.G. Zumft, Phylogeny of the bacterial superfamily of Crp-Fnr transcription regulators: Exploiting the metabolic spectrum by controlling alternative gene programs, *FEMS Microbiology Reviews*, 27 (2003) 559.

CHAPTER 5

Studies on Optical Multi-parameter Detection for Environmental Pollution Monitoring

5.1. INTRODUCTION:

The demand of fresh drinking water resources has increased dramatically across the globe as a result of population and economic expansion. Good quality of drinkable water is essential for human health, socio-economic development and ecosystems. Besides growing population and rapid urbanization, the high use of harmful chemicals in manufacturing, construction and other industries, fertilizers in farms and their direct disposal to nearby water bodies have significantly worsened the water quality available to people [1]. A minimum of 2 billion people worldwide consumes water for drinking, contaminated with faecal matter [2]. The root cause of many deadly diseases such as cholera, diarrhoea, dysentery as well as typhoid is consumption of contaminated water and the consumption results in more than half million deaths due to diarrhoea annually [3]. These statistics are indication of the urgent need for quantitative assessment of water quality including lakes [4] and large water bodies with online determination of results indicating the readiness of consumption of available drinking water. The quality of water is primarily determined by its physical, chemical, and biological content [5-7]. Traditional water drinkability assessments are generally performed manually where water samples are sent for examination to the laboratories, conventionally following chemical and other methods of analysis [8]. The processes are complex and require trained personnel [9]. Moreover, they are time-consuming and non-real time measurement techniques [10]. With the advent and development of sensor-based systems, substantial research has been carried out to automate and real-time monitor the water quality and Internet of Things (IoT) enabled devices are in demand for immediate intimation of human remedial interventions needed anywhere [11, 12]. But such sensor-based systems mainly focus on the total dissolved solvents (TDS) and pH properties of water and few such sensors have been made commercially available also. Some alternate

experimental methods [13] were also tried by researchers like using the bio-screen microbiological growth analyser [14] and underwater imaging systems [15, 16]. While online sensors ensure immediate data availability and trigger the need for urgent action, their calibration, reliability, and water-induced degradation or stains become an important concern [17]. Various methods of probing water quality have been tried and researched by various scientists. The contemporary research in this direction includes the measurement of ocean water colour and estimation of its effect on marine biology [18, 19]. RGB analysis has been used to determine the salinity index of water by using the ration of R to B and B to G was used to determine the chlorophyll content of water [20]. Although these methods are tried along with methods like airborne digital image photography has also been used to map water pollution and overcome the problem of cloud cover scenes [21] and recently, computer vision and artificial intelligence have witnessed their application in the measurement of water turbidity and related parameters [22, 23], an all in one real time water quality testing portable system is sparce in contemporary literature that can identify presence of any kind of suspended scatterer, harmful chemicals having emission and dissolved contaminants or bio-markers degrading the water quality. Table 5.1. shows a comparative analysis of existing water quality monitoring equipment.

Table 5.1. *Comparative analysis of existing water quality monitoring equipment*

Type	**ISE [12, 18]**	**Thermistor Technology [24]**	**Filter based colorimetry [25]**	**Image processing/ Microbial Assay based [26]**	**Spectro-scopy [27]**	**Our device**
Measure-ment parameters	Conductivity pH/ORP,Lu-minescent dissolved	Temperature	Multiple chemical pollutants (kit based)	Water Toxicity measureme-nt using	Bio-chemical species, such as	Contami-nants like dissolved organic

	oxygen, Turbidity, Depth, Chlorophyll a, Blue green algae, Rhodamine, Ammonium			microbial assay	proteins, viruses, bacteria, and spores	matter, dissolved organic chemicals, scatterer, bacteria etc.
Reagent dependence	No	No	Yes	Yes	Yes	No
Measurement resolution	High	Low	Moderate	High	High	High
Field Deployable	Yes	Yes	Yes	No	No	Yes
Cost Approx (USD)	High 3000	Low 150	Very High 2000	Very High 10000	High 8000	Low 400
IoT enabled	No	No	No	No	Yes	Yes

In this study, we have developed a prototype for the estimation of water quality using spectroscopic techniques. This proposed device can simultaneously measure the absorbance of water sample to give the information of dissolved colours, scattering parameters to estimate the suspended particulate matter and fluorescence to quantify

the harmful chemicals contaminating the water and degradation of the water quality. Detection of benzopyrene, a harmful carcinogenic common water pollutant [28], mainly contaminating water resources from industry effluents is a global concern of immense importance. In this study, the credentials of the developed proto-type have been established in identifying benzopyrene contamination in water samples. The limit of detection (LOD) of the device in terms of emission of benzopyrene contaminated water is found to be 0.503 ppb, much lower than the drinkable limit of 0.7 ppb [29] as per WHO guidelines which proves the efficacy of the device. Similarly, Crystal Violet (CV) is another dangerous and common mutagenic and teratogenic contaminant of water which enters into the aquatic systems from the effluents of textile or paint industry and also from medical and biotechnology industry and is well known for its mutagenic, teratogenic and mitotic poisoning nature [30]. The developed system is also capable of detecting the presence of such dissolved dyes in water by measuring absorbance. The designed device is found to have LOD 23.9 ppb whereas the safe limit of CV in drinking water is 100 ppb [31]. Simultaneously, the potential of the device in determining suspended particulate matters (SPM) in water is established by detecting Titanium di-oxide (TiO_2) as a model scatterer pollutant in water. The instrument yielded an LOD of 23.25 ppb (0.291 μM) in this case. The bacterial growth indication performance of the device in water was also studied using MRSA (Methicillin-resistant *Staphylococcus Aureus*) bacteria. Thus, this instrument, has the potential to replace the existing instruments for water quality measurement and has immense applications in the field of environmental research.

Arsenic is a naturally occurring toxic metalloid and is abundant in 'Earth's crust. Importantly, this is classified as a group I carcinogen in humans [32, 33]. Primary sources of ingested arsenic for humans are water and air, apart from some contribution from food. Contaminated groundwater with geogenic arsenic is the major source in various parts of the world, including a large part in the Ganga basin, and pose a major health risk to a large population worldwide [34, 35]. The toxicity of the most commonly occurring arsenic species in the environment decreases in the order As(III) (primarily as AsO_3^{3-}) > As (V) (primarily as AsO_4^{3-}) > As^0 (e.g. monomethyl arsonic acid ($MMAs^{III}$)) >As^{3-} (e.g.dimethylarsinic acid ($DMAs^{III}$)).

Among these, AsO_3^{3-} and AsO_4^{3-} are two primary arsenic species that occur in aqueous environments and contaminated water bodies with AsO_3^{3-} being more soluble than AsO_4^{3-} [36]. The epidemiological studies have revealed a distinct relation between a higher concentration of ingested arsenic in drinking water and the prevalence of several cancers [37-39]. Arsenate mimic inorganic phosphate in cellular or glycolytic respiration pathways and enters cells through the phosphate transport system [39]. AsO_3^{3-} induce toxicity by binding to sulfhydryl groups of proteins to inactivate several enzymes that are associated with cellular energy pathways, DNA synthesis, and repair [39-42]. Studies also establish that the hydration pattern for arsenite resembles glycerol hydration, which presumably favours its passage through membrane-bound aquaglyceroporins and cell membrane permeability [43-45]. Considering the acute and the high level of toxicity induced by iAs^{III} contamination, the World Health Organization (WHO) and U.S. Environmental Protection Agency (EPA) have set the maximum allowed contaminant level for arsenic in drinking water as ≤ 10 ppb [46, 47]. The groundwater of certain parts of many countries such as America, Thailand, England, Oregon, Bangladesh, India, Inner Mongolia, Taiwan, Vietnam, Pakistan, China and Canada, and so forth are reported to have the arsenic level that is well above the guideline value level (10 ppb/0.1 µg L^{-1}) specified by WHO [47-50]. According to a survey, it is estimated that more than150 million people around the globe are at risk because of arsenic contamination [47, 51]. To date, various conventional analytical techniques are commonly used for the detection of inorganic arsenic (iAs^{III}), those include inductively coupled plasma mass spectrometry, atomic absorption spectroscopy, high-performance liquid chromatography with optical spectrometric detection, atomic fluorescence spectrometry and voltammetry [52-59]. Although these techniques allow sensitive and accurate quantification of iAs^{III}, these methods require cumbersome sample processing, time, and highly trained personnel, which limit their applications for routine on-sight measurements [59, 60]. Considering such limitations, there is a conscious and focused effort for developing molecular sensors that could be integrated into an inexpensive optical device for specific, sensitive and instantaneous in-filed detection of the iAs^{III} with an associated optical read-out signal. Notably, such methodology with an associated switch ON optical

response helps in achieving a favorable signal-to-noise ratio and a trace level quantification. These criteria are ideally suited for the real-time on-sight application. To the best of our knowledge, examples of any molecular sensors that fulfill all these norms are scarce in contemporary literature. Further, literature reports also suggest that iAs^{III} (inorganic arsenic as AsO_3^{3-}) and its intermediate metabolites $MMAs^{III}$ and $DMAs^{III}$ are the most toxic to human physiology, with mitochondria being one of the primary target organelles [61-63]. Studies also reveal that iAs^{III} induced toxicity typically arises from the loss of mitochondrial membrane potential, inhibition of the electron transfer chain, the release of cytochrome c from mitochondria into the cytosol, and the overproduction of ROS of the malfunctioned mitochondria [61-63]. These findings further suggest the importance of a molecular sensor that could ideally allow us to visualize the real-time distribution of iAs^{III} in mitochondria. Luminescence-based switch ON response is principally preferred over other optical responses to suit the non-invasive intracellular imaging process, as well as for achieving higher sensitivity. To integrate all these requirements in the optical response of a single fluorescence-based molecular receptor, a new Ir(III)-based luminescent molecule (AS-1) is designed that shows specificity towards iAs^{III}. To further improve the solubility of the AS-1 in the aqueous medium, as well as the improved membrane binding-efficacy with a cationic biomimetic cetyltrimethylammonium bromide (CTAB) micelle and cell-membrane permeability with mitochondrial specificity [64, 65]. We have also utilized the switch ON luminescence response at ~ 466 nm for developing a hand-held micro-spectrometer-based prototype with an option for remote signal read-out using a smart mobile phone. The proposed device could be used for quantifying iAs^{III} at the sub 10ppb level in drinking water. The delicate balance between the lability of the N^O-donor derivative (HPBT) in AS-1 and the demonstrated affinity of As(III)-center towards S-donor receptors is effectively utilized for developing a ratiometric luminescence-based chemodosimetric receptor that is specifically localized in mitochondria of the live breast cancer cell lines (MCF-7). The newly developed chemodosimetric receptor, its specificity towards iAs^{III} for generating a ratiometric luminescence response, and integration for developing a hand-held device could be a solution for the population that is impacted with chronic As^{3+} toxicity.

5.2. RESULTS AND DISCUSSIONS:

5.2.1. A Portable Spectroscopic Instrument for Multiplexed Monitoring of Acute Water Toxicity: Design, Testing and Evaluation [66]:

0.5 mM, 0.5 mM and 0.21 mM stock solutions of Benzopyrene, Crystal Violet and TiO_2 were prepared in aqueous solution and filtered for the current work. To evaluate the efficacy of the device, the stock solutions were sufficiently diluted in Mili Q water. For real water samples, tap water were collected and filtered using 0.22 µm filter. The used tap water samples were analysed in a National Accreditation Board for Testing and Calibration Laboratory.

5.2.1.1. Construction of Instrument:

5.2.1.1.1. Hardware Design:

The optical spectroscopic device reported in this work comprises of mainly two compartments, one optical and other electronic, which together integrates data collection, data processing, and wireless transmission. The light weight, portable and IoT enabled device is designed in two vertical compartments to confirm complete space utilization of the form factor and stability of the device as shown in Figure 5.1.

5.2.1.1.1.1. Optical Chamber:

A customized cuvette holder mounted internally surrounded by three light sources and one spectrometer detector is the heart of the upper optical compartment of the system. The micro-spectrometer (Hamamatsu C12880ma, wavelength range: 304 nm - 1024 nm) along with One white LED (DC 3V, 20mA, 400-700 nm), one UV LED (wavelength 361 nm, DC 3V, 500mA) and one LASER source (wavelength 667 nm (5V, 5mW)) are placed at 90° angle to each other of the square cuvette holder. The white LED for absorbance measurements is placed at 180° position of the micro-spectrometer. The UV LED and the LASER are positioned at 90° of the micro-spectrometer for fluorescence and scattering measurements respectively as depicted in Figure 5.1.b. The micro-spectrometer is directly mounted on defined pins of one micro-controller (Arduino UNO) board that controls the automatic data acquisition (DAQ) and visualization of the acquired spectra. The UNO board along with all light

sources are controlled from the lower electronic section by wire connections passing down through designated slots in the base plate of the upper chamber.

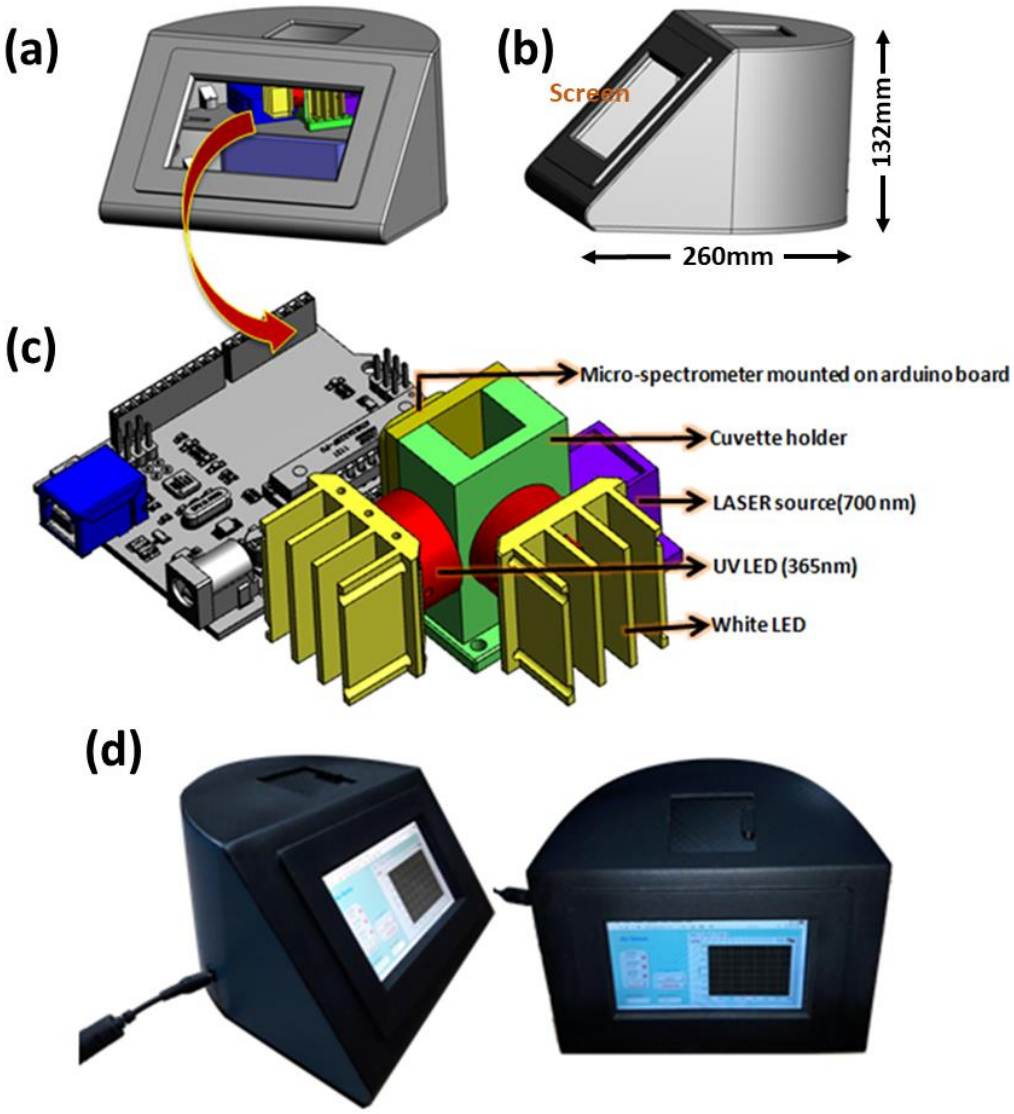

Figure 5.1. *Schematic of the developed device (a) Front view (b) Side view (c) Internal arrangements of optical compartment (d) Real images of device.*

5.2.1.1.1.2. Electronic Chamber:

The lower electronic section primarily consists of a box type mini-computer (intel NUC 8i3BEH), two micro-controller (Arduino UNO) boards and a rechargeable battery for power supply. Two cooling fans (5V, DC) fixed at diagonally opposite positions of the wall maintains constant temperature inside the device eliminating heating effects. An LCD display (7 inch, Waveshare) is attached in front of the device in a slanting position (Figure 5.1.d) for showing results. The lower micro-controller

board is for the controlling the light sources. The switching chronology, illumination time, automatic intensity adjustments by PWM (Pulse Width Modulation) etc. are controlled through this Arduino board. The in-built Bluetooth and Wi-Fi modules in the PC take care of the data and report uploading procedures. The device technical details are also tabulated in the following Table 5.2.

Table 5.2. *Technical details of the developed device*

Serial Number	**Parameters of developed device**	**Specifications**
1	Battery life	60 hours
2	Re-calibration required after	5000 hrs
3	Cost	400 USD
4	Working principle	Spectroscopic detection (Absorbance, Emission, Scattering)
5	Standard deviation in measurements (ppb) (From Bland-Altman statistical analysis, Figure 5.10.)	(a)0.6953 for absorbance, (b)0.4227 for emission (c)0.0867 for scattering
6	LOD	(a)23.9 ppb for absorbance (b)0.50 ppb for emission (c)23.2 ppb (0.29µM) for scattering
7	LOQ	(a)72.4 ppb for absorbance (b)1.52 ppb for emission (c) 0.882µM for scattering
8	Mode of operation	Static and Kinetics
9	Weight	2.54 kgs
10	Dimension	260 X 132 mm

5.2.1.1.2. Software Development:

Figure 5.2.a illustrates the simple sequential program flow diagram of the software for accurate assessment of drinkability of water. The device is IoT enabled which signifies that the developed device has both Bluetooth and Wi-Fi to transmit the data obtained directly to cloud as well as experts. Immediate necessary actions can be employed if required, from miles away depending on the severity of the pollution level. The entire algorithm has been indigenously developed in LabVIEW (by National Instruments) platform with easy user interface for automated data acquisition and visualization of spectra as well as drinkability condition of the water sample. After getting powered up, health check-up and initialization of the device takes place. In case of any discrepancy, the instrument auto-corrects different conditions and restarts automatically, followed by a pop-up window asking for sample water details including date, source etc. to be saved along with data in individual folders. Then as directed by the GUI, 2ml of water sample to be tested is to be placed in cuvette inside the designated cuvette holder slot and click on the 'start' button in the software. The UV LED, White LED and LASER sources are turned ON by the program one by one through micro-controller serial communications and spectrometer captures data as per pre-determined parameters along with integration time of 800ms. After reading the optical signal intensity array for three cases i.e., absorbance, emission and scattering, the corresponding wavelength (1D array) for each detector pixel number is calculated. Wavelength vs absorbance, emission and scattering intensity plots are shown live in separate panels in the display. From a pre-loaded file location, the baseline spectra of pure water are read and from calibration equations already fed to the algorithm, water drinkability examinations are performed. As per the pre-calibration, if any contaminants are found above the pre-defined stipulated limits in terms of emission, absorbance or scattering, the sample water is indicated as "unsafe to drink". If the water passes the eligibility criteria to be drinkable, a green symbol displayed in the screen indicates the water is safe. The data measured by our developed device may compare the existing data base from several authorities and guide the user for potential remediation. The measured data could also be a part of the existing data base for future use.

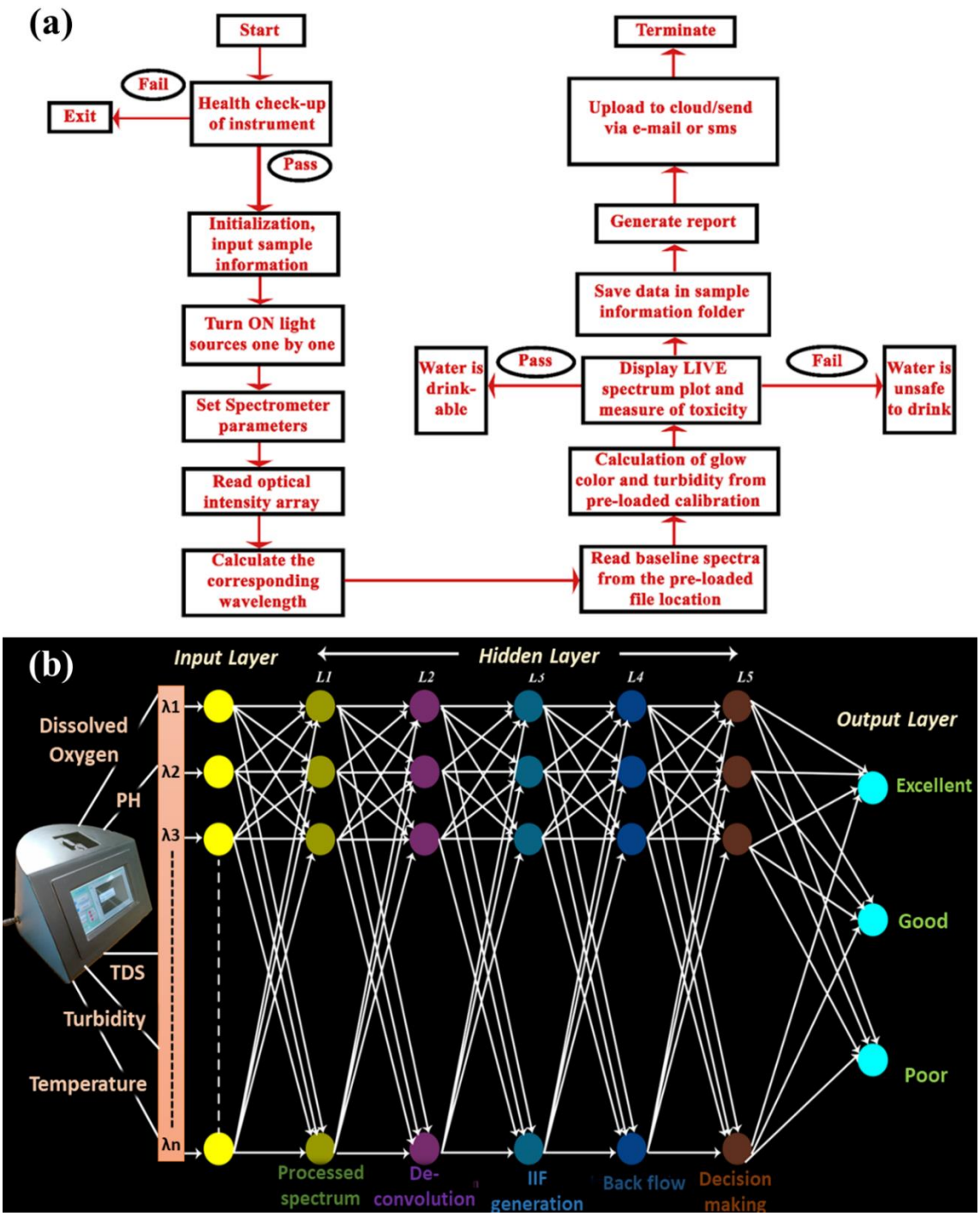

Figure 5.2. *(a) Sequential program flow diagram of the developed prototype (b) Framework of Artificial Neural Network (ANN algorithms) to predict Water Quality Index (WQI). IIF = Instrument Index Function.*

In this study, Figure 5.2.a shows the sequential program flow diagram of the indigenously developed software in LabVIEW platform for data acquisition and analysis for the drinkability testing spectroscopic device. However, the scope of the developed prototype can be extended to monitor other markers of the Water Quality

Index (WQI) [67] i.e., dissolved oxygen (DO), temperature, total dissolved solids (TDS), pH, turbidity and presence of biological organism, like bacteria. To measure the amount of dissolved oxygen in water, the popular choice is an optical sensor which works on the principle of fluorescence quenching [68]. In this context, it is worth mentioning that our group has already developed multiple optical sensors using the fluorescence quenching mechanism for measurement of harmful salts of fluoride, iron, arsenic and mercury present in the water [69-72]. The presence of these heavy metals and their salts are the indicators of the amount of TDS as well. Similarly, pH of water could be monitored by using UV-visible spectroscopy based sensors [73] and for measurement of temperature, electronic sensors [74] can also be integrated to the developed prototype. Such well-equipped sensing system has a huge potential to construct an efficient artificial intelligence (AI)-based water monitoring framework as depicted in Figure 5.2.b. It was estimated that, by 2030, in USA alone, the AI expenditures in the water industry will cost around $9 billion [75]. To implement a competent AI-based water monitoring system from the sensor clusters, the machine learning (ML) protocol must be incorporated. According to the US Food and Drug Administration (FDA), AI has been defined as the scientific and technological development associated with intelligent machine-making process and ML is a data-driven intuitive training software algorithm to obtain AI-based network [76]. For processing and analysing the enormous amount of data, collected from the developed sensor, Artificial Neural Networks (ANN), a well-known ML technique, would be integrated with the system. ANN is a well-established ML methodology which has ability to handle complex, non-linear data-set like, monitoring of water quality index [77]. The ANN algorithm tries to mimic the network of a human brain, where input layers and output layers are connected by single or multiple hidden layers and interconnecting nodes with variable 'weight factor' [78]. For analysing the data through ANN algorithm, the feed-forward pathway should be considered as shown in Figure 5.2.b. The Input Layer will collect various spectroscopic parameters with respect to wavelengths. The first hidden layer (HL) HL1 deconvolutes the acquired data and compound-specific peaks would be generated. HL2 is responsible for instrument index factor generation by formulating the appropriate prototype-specific

weight factor. A comparative analysis of the concentrations of water sample parameters with the permissible levels (Table 5.3.) are carried out in layer HL3.

Table 5.3. *Permissible limits of the parameters used for calculating the WQI* [67, 79]

Parameters	**Permissible Limits**
Dissolved oxygen (mg/L)	10
pH	8.5
Biological oxygen demand (mg/L)	5
Turbidity (FNU)	120

HL4 is the decision-making layer, which identifies good data and bad data. The bad data points which lie beyond the error margin will be back-propagated for reacquisition. Finally, the water quality is displayed in the output layer.

The present study addresses data validation as well as data acquisition for the developed prototype and also investigates the scope of ANN on the present model. The ANN can predict the water quality index by creating a comprehensive library from the acquired, real world sample data-set, and executing feed-forward and back-propagation algorithm on neural network. This directs our future course of research for further exploration and implementation of ANN.

In this section, the performances of the proposed prototype for water quality monitoring and management in distributed, dynamic, and complex scenarios such as water distribution systems (WDSs) is analysed. The performance of the instrument in detecting benzopyrene, crystal violet and TiO_2 as model contaminants in drinking water using emission, absorbance and scattering properties are elaborated. The device performance can be extended to other emissive, absorptive and scattering water contaminants with calibration for each species. Once the device is calibrated, it remains valid for 5000 hours unless the geometrical aspect of the device, such as the

positions of the various components and light sources remain unhindered. Implementation of the device in depicting bacterial growth in water is also discussed. All quality factors like precision, accuracy, limits of detection and quantification etc. associated with the integrated system are finally presented.

5.2.1.2. Detection of Dissolved Organic Matter:

The developed spectroscopic instrument is capable of detecting the presence of trace amount of emissive organic pollutants in the water sample. In the present work, identification of Benzopyrene contamination in drinking water is considered. Upon excitation of the sample water contaminated with benzopyrene with 361 nm UV radiation by the device, emission peak at 406 nm is found to increase considerably with increase in the concentration of benzopyrene. Primarily a shift in wavelength for the peak positions was observed in our developed device with respect to the standard one, which was corrected by wavelength recalibration of the micro-spectrometer used in the developed device with the standard instrument (JASCO spectrofluorometer, FP-8200). Figure 5.3.a illustrates the full emission spectrum of benzopyrene contaminated water for different concentration of Benzopyrene (BP) from 0 ppb to 11.35 ppb for excitation at 361 nm in standard instrument.

Figure 5.3.b simultaneously shows the spectra obtained in our developed device for the same concentrations of benzopyrene and under same excitation condition. These spectra are found exactly consistent with the full spectra obtained in standard fluorometer after the baseline correction. Next, to calibrate the device and to determine the direct correlation of emission intensity at 406 nm with the measured benzopyrene concentrations, the intensities at 406 nm are plotted against the different concentrations of benzopyrene. Figure 5.3.c elaborates the calibration of the device with concentration of benzopyrene. The exponential calibration equation is obtained as $y=A1\ \exp(x/t1)+y0$ with adj. $r^2=0.9967$. This curve is then included to the device algorithm for predicting emissive contaminant level in drinking water. The performance of the device is also evaluated by the validation curve obtained in Figure 5.3.d ($y=1.062x+0.08$, $r=0.986$) with six different concentrations of BP.

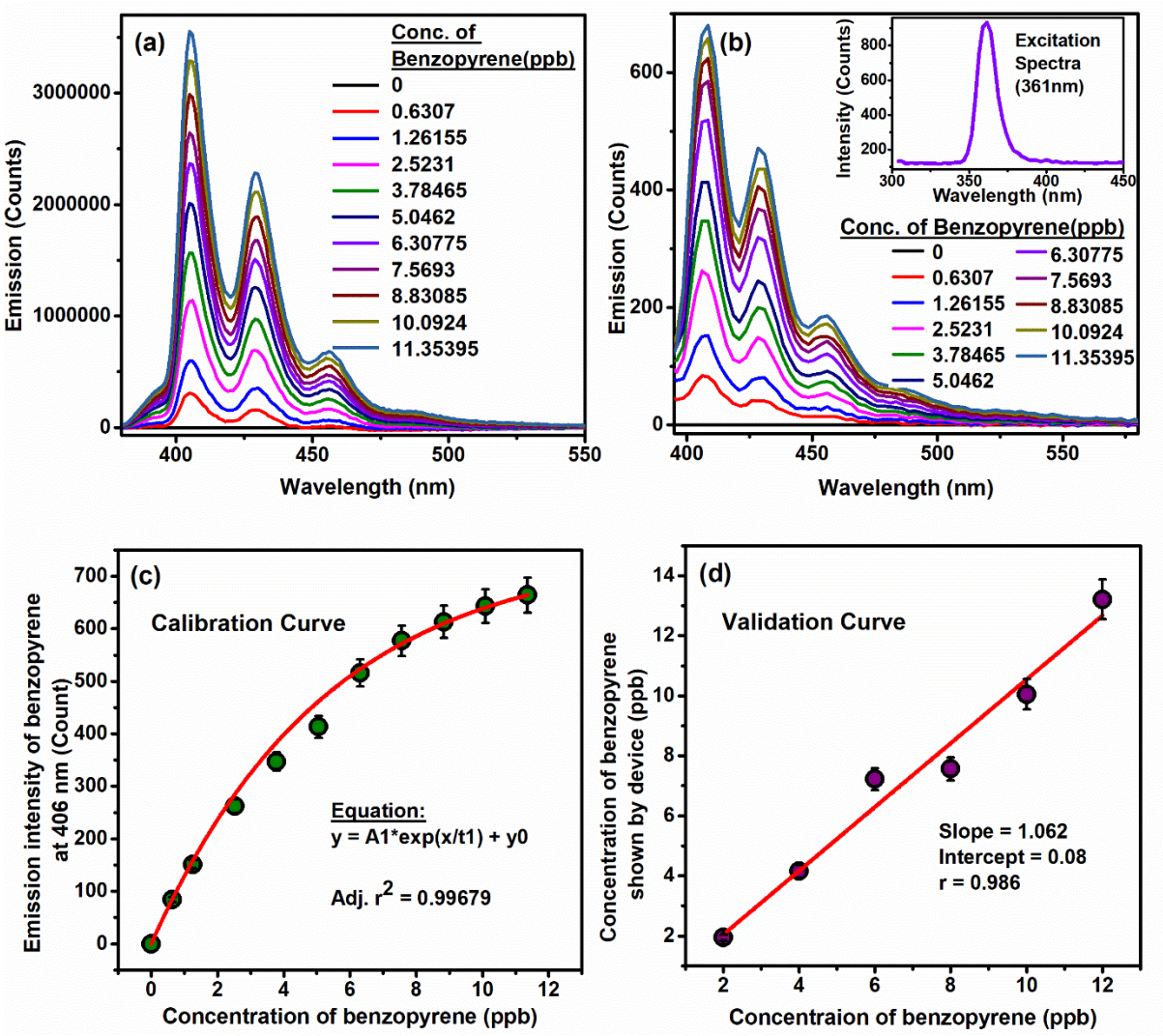

Figure 5.3. *(a) Emission spectra of different concentration of Benzopyrene (BP) from 0 ppb to 11.35 ppb for excitation at 361nm in standard instrument. (b) Emission spectra of different concentration of Benzopyrene (BP) from 0 ppb to 11.35 ppb for excitation at 361nm in our developed device. The inset shows the excitation spectrum of UV LED with peak at 361nm. (c) Calibration curve of emission(counts) at 406nm (peak) vs concentration of BP in ppb (d) Validation curve of the device with known concentrations of Benzopyrene.*

The linear regression analysis resulted in a correlation of proposed measurement technique with the standard one with Pearson's correlation coefficient(r) 0.986 (p <;0.0001, one way ANOVA). The standard deviation between two measurements is 0.695 (p<0.0001, one way ANOVA), which necessarily means that the quantity measured by the instrument may have a tentative variation of + 0.69ppb. Furthermore, the Bland Altman analysis shows a positive bias of +0.3552, (p<0.0001) signifying the tendency of the device to overestimate the values by +0.355ppb. The limits of agreement lie in a range of -1.0076ppb to +1.717ppb (Figure 5.10.), which essentially

signifies that all the values measured by our device will have a maximum difference of 2.72ppb.

However, for the measurements of DOMs outside the wavelength range (304-1024nm) of the micro-spectrometer of the developed set-up, it is planned to use some sensors or dyes whose absorbance or fluorescence fall within the detectable range of our device. For example: fluoride ions are not detectable with standard visible absorbance or fluorescence measurements, however some nano-sensors (Hematoporphyrin in SDS micelles) shows promising performance in detecting fluoride whose spectral response (quenching of emission peak at 605nm) lies in the range of our developed instrument [70]. Similarly, for detection of protein like fractions in drinking water as per some monitoring requirement, 'Bradford Assay' can be used where the transformed blue colour of the dye in presence of protein is easily measurable in our developed system. Thus, using dyes or sensors the device is capable of measuring different dissolved chemicals or organic matters whose absorbance or emission apparently lies outside the measurement range of the spectrometer.

5.2.1.3. Detection of Dissolved Chemicals:

Following Lambert-Beer's Law, the device can detect the dissolved contaminations in test sample of water affecting the absorbance of water. Crystal violet (CV) is detected in the current work as the absorbance changing contaminant of drinking water. Absorbance measured in standard spectrometer and in the designed instrument for various concentrations of crystal violet (0.1- 15.2 ppm) in water are depicted in Figure 5.4.a and 5.4.b. As elaborated in the previous section, the calibration of the device in terms of absorbance is done by wavelength (nm) vs maximum absorbance at 589nm plot (Figure 5.4.c). The calibration equation obtained from the exponential regression curve was $y_i = A_1 \exp(x_i/t_1)+y_0$, where y_i represents the absorbance(a.u.) of CV at 589nm and x_i represents the concentration of CV in ppm. We used this equation in the LabVIEW software to estimate the unknown concentration of absorbing pollutants in test sample from the spectral information obtained using our device. In the corresponding validation curve($y_i=0.98x_i+0.19$) shown in Figure 5.4.d, linear regression analysis results (Pearson's correlation coefficient r = 0.995, P

value < 0.0001, F value= 2562.86, slope=0.98, and intercept = 0.19 one way ANOVA) indicate a correlation between the two methods for same samples simultaneously measured in standard spectrophotometer as well as our proposed device.

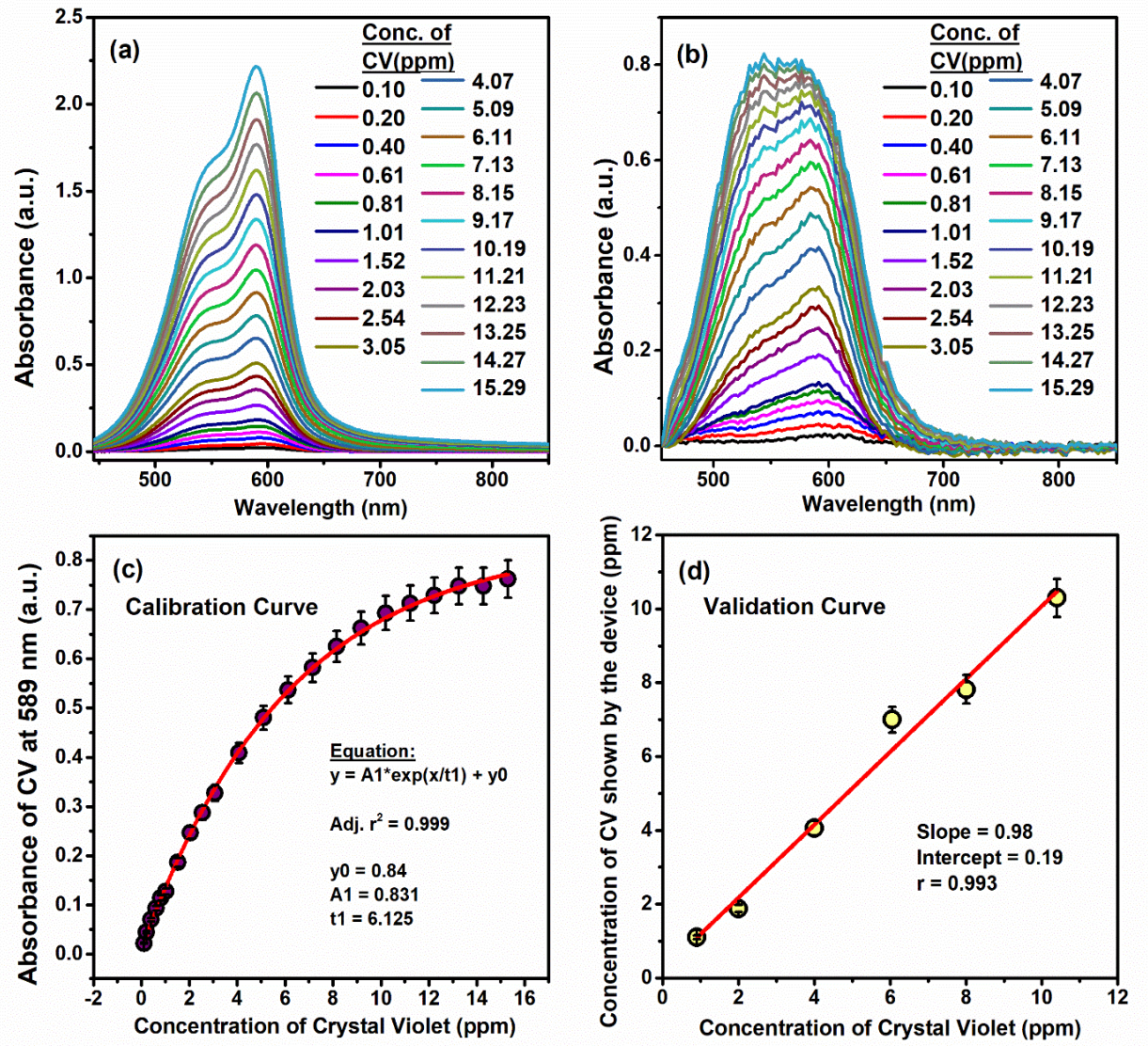

Figure 5.4. *(a) Absorbance spectra of different concentration of Crystal Violet (CV) from 0.101 ppm to 15.29 ppm in standard instrument (b) Absorbance spectra of different concentrations of Crystal Violet (CV) from 0.101 ppm to 15.29 ppm in our developed device. (c) Calibration curve of absorbance at 589 nm (peak) vs concentration of CV in ppm(d) Validation curve of the device with known concentrations of Crystal Violet.*

The standard deviation between two measurements is 0.42 ($p<0.0001$, one way ANOVA), which necessarily means that the quantity measured by the instrument will have a difference of + 0.4 Furthermore, the bland Altman analysis shows a positive

bias of + 0.135, ($p<0.0001$) signifying the tendency of the device to overestimate the values by 0.1 (Figure 5.10.).

5.2.1.4. Detection of Suspended Particulate Matter:

The presence of undissolved suspended particulate matters in water can be detected by the device through the change in scattered light intensity of the laser source placed at right angular position of the spectrometer. Titanium di-oxide (TiO_2) particles are used in this study to make a clear water turbid and measure the amount of turbidity by the developed equipment. Figure 5.5.a shows the DLS (Dynamic Light Scattering) data indicating the presence of TiO_2 particles mainly of two sizes, 295nm and 5.56 μm. It is clear from the DLS study that the bigger particles are present more in the sample. Now from the formula of Rayleigh scattering (equation 5.1), considering the scattered intensities the calculated particle size comes out to be around 6.2 micrometre.

$$I = I_0 \frac{1+cos^2\theta}{2R^2}\left(\frac{2\pi}{\lambda}\right)^4\left(\frac{n^2-1}{n^2+1}\right)^2\left(\frac{d}{2}\right)^6 \quad (5.1)$$

where 'R' is the distance of spectrometer sensor from the scattering medium, 'θ' is the scattering angle (here 90°), 'n' is the refractive index, 'I' and 'I_0' are scattered intensities in presence and absence of scatterer in medium respectively.This result is evident from the fact that the scattered intensity is proportional to the sixth power of particle diameter, so the larger particles have the main contribution in scattered intensity detected by the spectrometer. For the estimation of diameter of particles in colloidal suspension from the above well-known Rayleigh scattering equation (equation 5.1), the refractive index 'n' was considered as 1.33 and the wavelength to be 667nm. Figure 5.5.b reveals the increase in scattering intensity with increase in TiO_2 concentration from 0.125 μM to 2.504 μM (0.03-0.6NTU) in the device. Figure 5.5.c and 5.5.d are the calibration curve ($y=138.36x+481.83$, $r=0.998$) of scattered intensity (counts) at 667nm (peak) vs concentration of TiO_2 in μM and validation ($y=1.006x+0.028$, $r=0.997$) of the device respectively. The standard deviation between two measurements is 0.086 ($p<0.0001$, one way ANOVA), which necessarily means that the quantity measured by the instrument will have a tentative difference of +0.08.

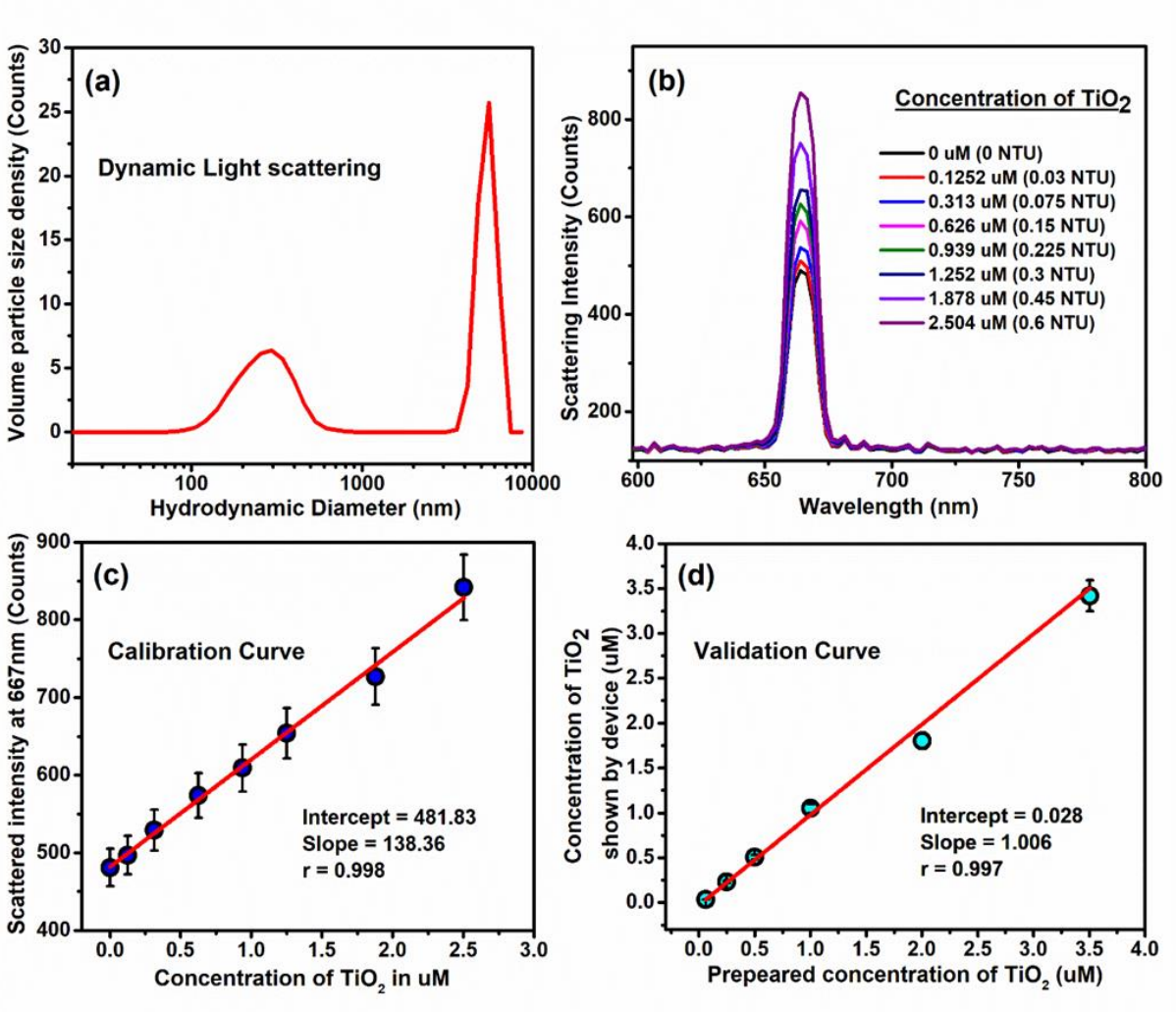

Figure 5.5. *(a) Hydrodynamic diameter of TiO_2 from Dynamic Light Scattering (b) Scattering spectra of different concentration of TiO_2 from 0.125 µM to 2.504 µM in our developed device. (c) Calibration curve of scattered intensity (counts) at 667nm (peak) vs concentration of TiO_2 in µM (d) Validation of the device with known concentrations of TiO_2.*

Furthermore, the Bland Altman analysis(Figure 5.10.) shows a negative bias of -0.047 ppb, ($p<0.0001$) signifying the tendency of the device to underestimate the values by 0.04 ppb. The limits of agreement lie in a range of -0.2175ppb to +0.1223ppb (Figure 5.10.).

5.2.1.5. Detection of Microbial Growth:

The device is found suitable in detecting bacterial presence in drinking water. The bactericidal activity was performed using MRSA bacteria cells as depicted in Figure 5.6. The cells were cultured in a Luria Broth (LB) medium under an incubator shaker at 37°C for 24 h. The optical density of freshly grown overnight culture was

fixed to 0.1 n LB medium initially. The culture was then put in a cuvette and incubated at 37°C with shaking for 9 hours.

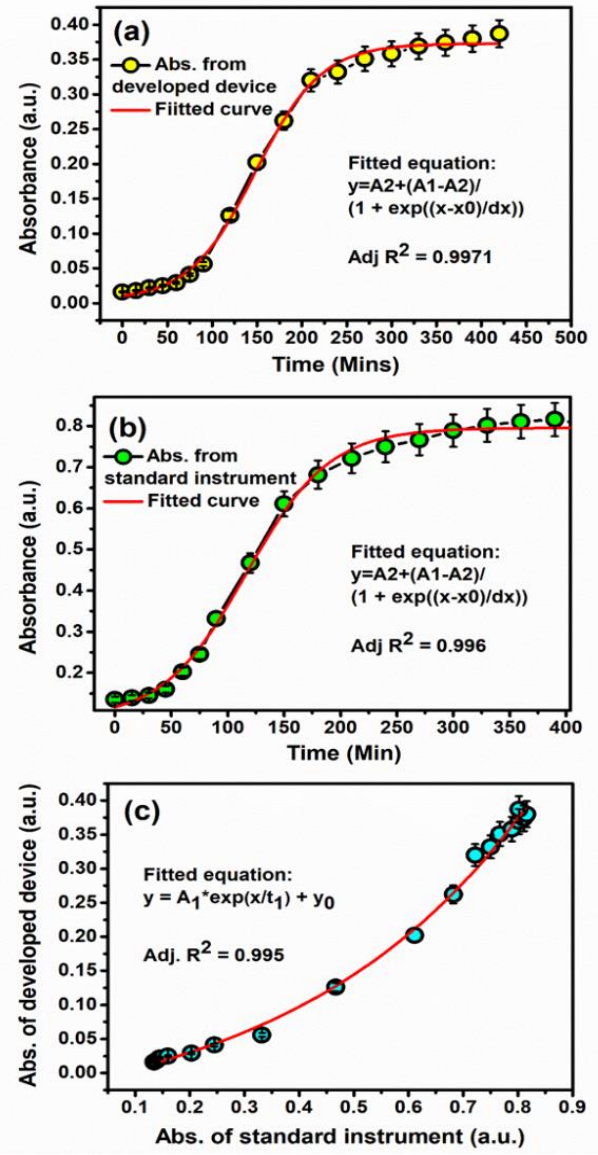

Figure 5.6. *MRSA growth curve in standard and developed instrument along with calibration*

The absorbance is taken at every hour interval and plotted against time with baseline correction for both standard spectrophotometer and our developed device (Figure 5.6.a and 5.6.b). The minimum detectable concentration of MRSA was determined using the onset of the growth curve. To estimate the limit of detection (LOD) of the suspended micro-organism (MRSA), we have converted the concentration of the micro-organism in the media from CFU/ml to ppm unit. The calibration curve of our device is finally shown in Figure 5.6.(c) with respect to standard commercially available spectrophotometer.

5.2.1.6. Repeatability and Reproducibility and Quality Factors of Device:

The reproducibility of the device (Figure 5.7.a, b and c) was checked for detecting BP, CV and TiO_2 in terms of three of the optical parameters i.e. emission, absorbance and scattering intensities individually.

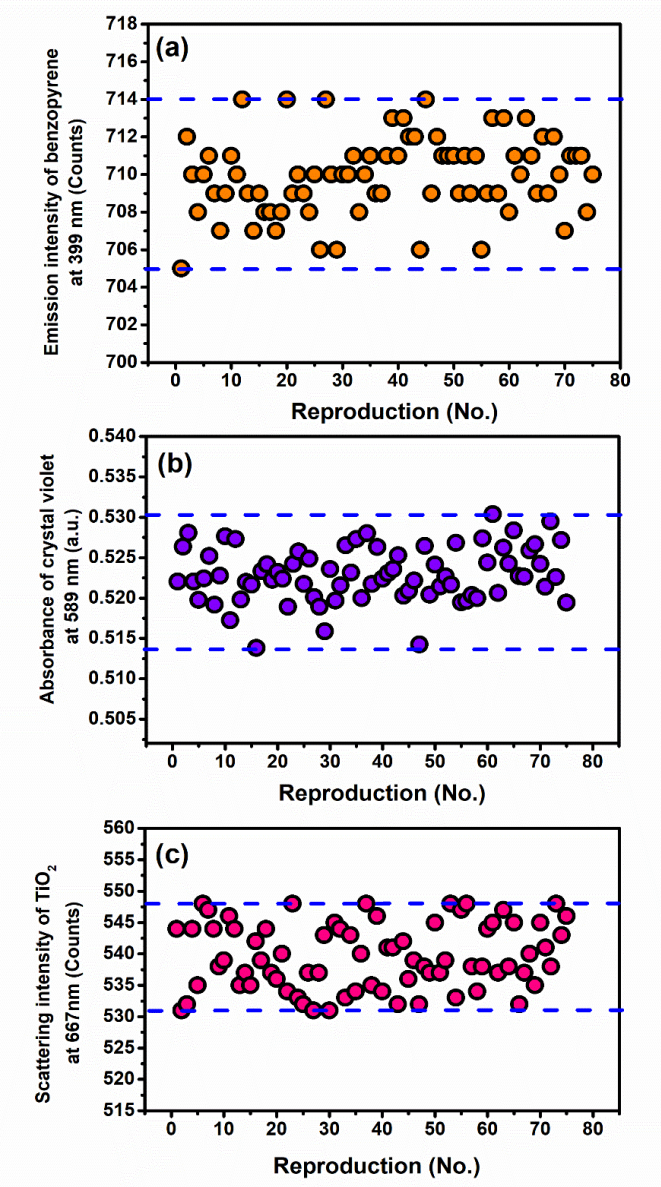

Figure 5.7. *Reproducibility of the device in terms of (a) Emission (b) absorbance (c) Scattering.*

The device was programmed in 'kinetics' mode for reproducibility checking, where 75 data were collected for each in the interval of 10 minutes (total time required = 12.33 hours) for the same sample. The emission intensity readings (Figure 5.7.a) of BP at 406 nm were found to fluctuate between 705 to 714 counts for a particular concentration. Simultaneously, Figure 5.7.b shows the fluctuation in absorbance at 589nm for CV is

from 0.5135 to 0.5305 only. The scattered intensity readings for a constant concentration of TiO_2 were observed to fluctuate between 531 to 548 counts. The repeatability of the device is also performed as shown in Figure 5.8.a, b and c, for BP, CV and TiO_2 detection, establishing the consistency of the device by preparing 20 samples of same concentrations for each of the three spectroscopic parameters.

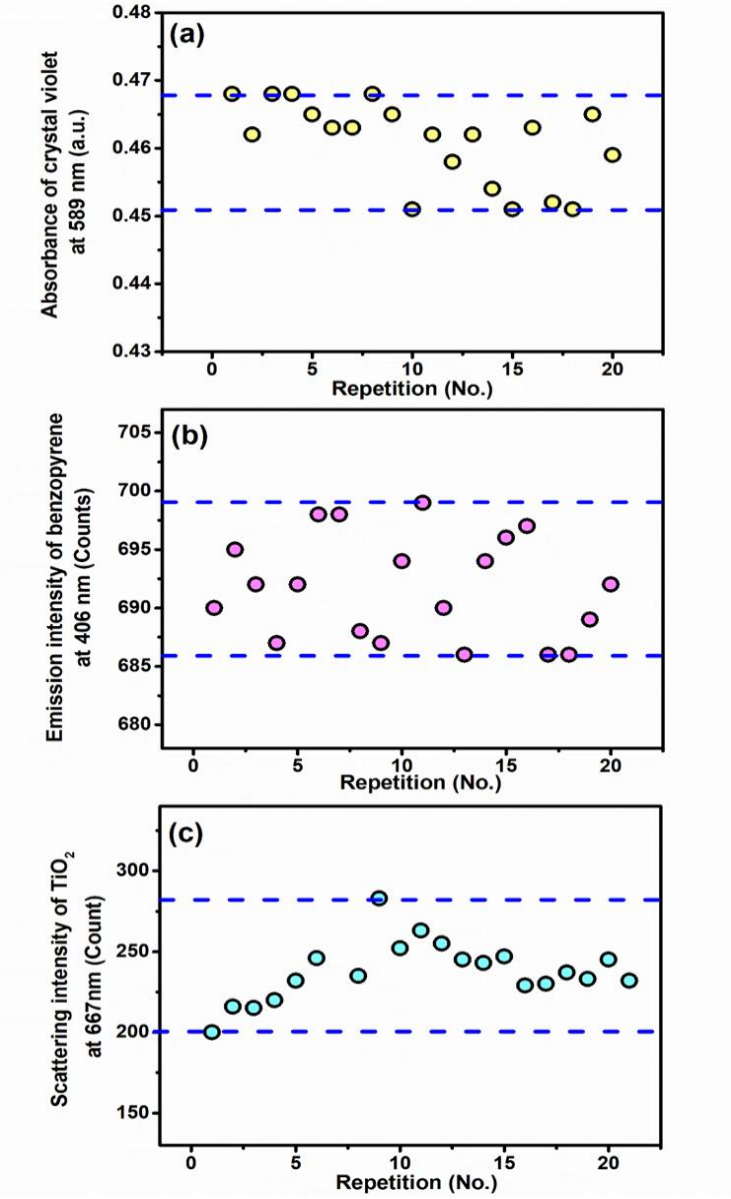

Figure 5.8. *Repeatability of the device in terms of (a) Emission (b) absorbance (c) Scattering.*

For 2 consecutive days, under same conditions, 3 experimentalists prepared samples of identical specifications and tested the repeatability of the device.

Limit of Detection (LOD) and Limit of Quantification (LOQ) are two important terminologies used to describe the smallest concentration of a measurand that can be

reliably measured by an analytical procedure [80]. More precisely, the smallest amount or concentration of the analyte in the test sample that can be reliably distinguished from zero [81] is termed as LOD and the lowest concentration of the analyte that can be determined with an acceptable repeatability and trueness is defined as LOQ [82]. Mathematically they can be expressed by equations 3.9 and 3.10 as described in Chapter 3. In Figures 5.3.c and 5.4.c, the slopes of the linear region of the calibration curves for low concentrations of benzopyrene and crystal violet were considered respectively for LOD and LOQ calculations. In the current study, the LODs for emission, absorbance and scattering measurements were obtained as 0.50 ppb or 500 ppt, 23.9 ppb and 0.291μM (0.069NTU) respectively for detection of Benzopyrene, Crystal Violet and TiO_2. LOQ values for the same were found to be 1.52 ppb, 72.4 ppb and 0.882μM (0.211NTU) respectively.

The device performance in terms of precision was calculated. The precision of an instrument indicates the fluctuation of readings for same test sample giving consistency or reproducibility of the measurement. Precision is primarily obtained by the range or difference between maximum and minimum values of readings. In this study, the fluorescence intensity readings (Figure 5.7.a) of Benzopyrene (6 ppb) at 406nm were observed to fluctuate between 705 to 714 counts giving precision as 9 counts. The fluctuation in absorbance readings (Figure 5.7.b) at 589nm for a particular concentration of Crystal Violet is from 0.5135 to 0.5305 resulting in absorbance precision of 0.017. The device is very precise (17 counts) in terms of scattering also as shown in Figure 5.7.c.

Sensitivity of an instrument is defined as the ratio of the changes in the output of a device to a change in the value of the quantity being measured or simply the slope of the calibration curve. From Figures 5.4.c, 5.5.c and 5.6.c the sensitivity of the set-up was obtained as 90.31, 0.0919 and 1.6076 counts/ppb respectively for measuring BP, CV and TiO_2 concentrations.

Use of the highly sensitive micro-spectrophotometer C12880ma (Spectral range, 304-1020 nm) improves the resolution of the device manifold than photo-diode or other sensors. For fluorescence measurements the instrument achieves resolution

of 17.093 ppt which reveals that the device is capable to distinguish concentration variation of as small as 17.09 ppt/count. Absorbance and scattering resolutions were found to be 20.53 ppb and 0.0084 μM (0.002NTU) respectively.

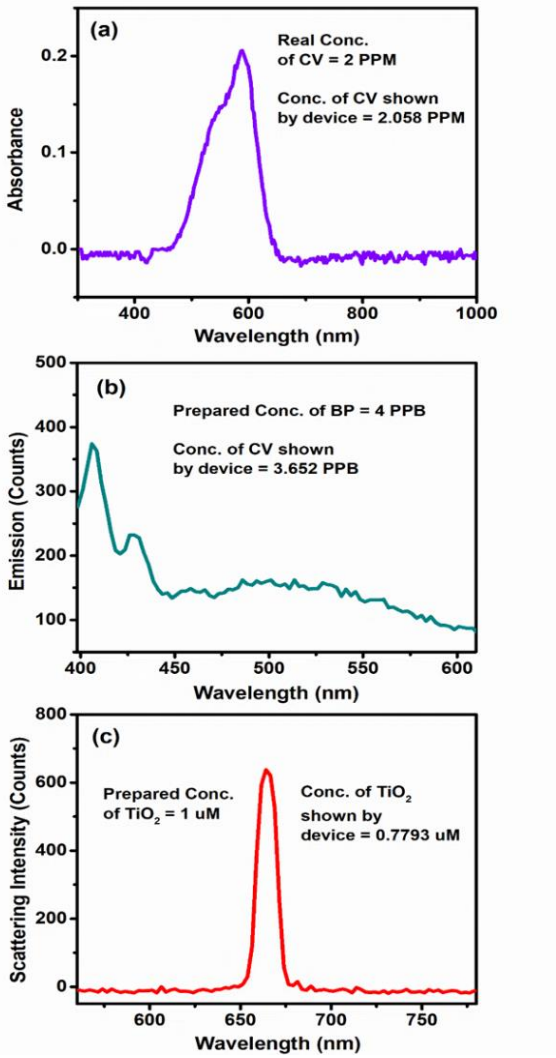

Figure 5.9. *Measurement of concentrations of contaminants (having absorbtion, emission and scattering) from a mixture in a mimic of real world water sample by the developed device (a) Absorbtiometric detection of Crystal Violet (b) Detection of Benzopyrene by emission (c) Detection of TiO_2 by scattering.*

The accuracy of a device is calculated by following the equation 3.8 of Chapter 3. In the present work, the accuracy for measurement of Benzopyrene concentration through emission was found to be 92.807% from the validation data obtained in Figure 5.3.d. Simultaneously, the accuracy of measuring Crystal Violet and TiO_2 concentrations in water samples through absorbance and scattering information resulted in 93.56% and 88.152% from validations of Figure 5.4.d and 5.5.d respectively, confirming the high level of accuracy of the proposed device.

Finally, in Figure 5.9., it is shown that, the developed device is capable of measuring the concentrations of contaminants having absorption, emission and scattering when they are present together in a water sample. A mimic of real-world water sample was prepared by spiking Crystal Violet, Benzopyrene and TiO_2 in 2ml water where the effective concentrations of CV, BP and TiO_2 were 2 ppm, 4 ppb and 1 µM respectively. The values shown by the device for the aforementioned three contaminants were 2.058 ppm, 3.652 ppb and 0.7793 µM respectively which proves the promising nature of the proto-type in monitoring water quality with a mixture of contaminants. The Bland-Altman statistical analysis of the validation data for emission, absorbance and scattering as discussed earlier and shown in Figure 5.10. establishes the high level of accuracy of the developed device.

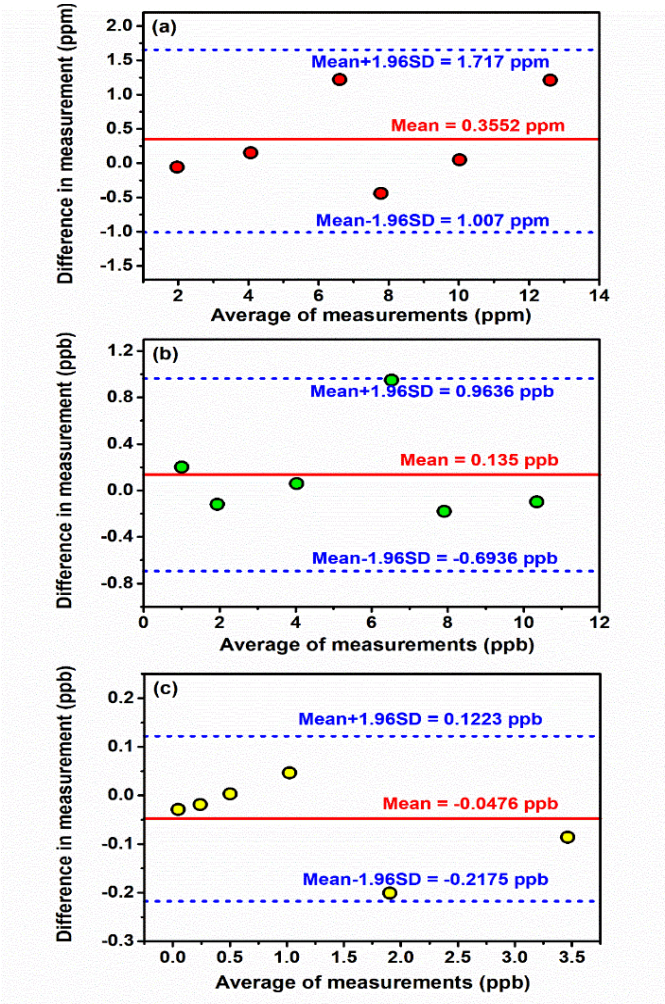

Figure 5.10. *Relationship of measurements between the developed device and the conventional techniques using emission, absorption and scattering: Bland-Altman plots (mean and 95% limits of agreement) between the developed device and values obtained from the three conventional techniques viz. (a) Emission (b) Absorbance and (c) Scattering are shown respectively.*

5.2.2. An Ultrasensitive Reagent for Ratiometric Detection and Detoxification of iAsIII in Water and Mitochondria [83]:

The meta acid (H_2AsO_2) is known to exist as a polymer with a very delicate As-O-As bond that undergoes hydrolysis to yield ortho arsenous acid (H_3AsO_3) [84]. Importantly, sodium arsenite is expected to exist primarily (~ 99.9 %) as H_3AsO_3 in an aqueous medium at neutral pH, owing to its high pKa^1 value (9.25) [45, 84]. Chromogenic sensor AS-1 was synthesized following the methodology shown in (Figure 5.14.a) and isolated as a pure compound in a reasonably good yield (60%). Details of the procedures adopted for synthetic of AS-1 and its characterization data are presented in Supporting Information. Characterization of the desired Ir(III)-complex was achieved using nuclear magnetic resonance (^1H and ^{13}C NMR) (Figure 5.11. and 5.12.) spectroscopy and MS spectral analysis. Desired purity of AS-1 was ascertained using data obtained from high-resolution mass spectrometric (HRMS) (Figure 5.13.) analysis. Additionally, the molecular structure for AS-1was confirmed by single-crystal X-ray structural analysis (Figure 5.14.b).

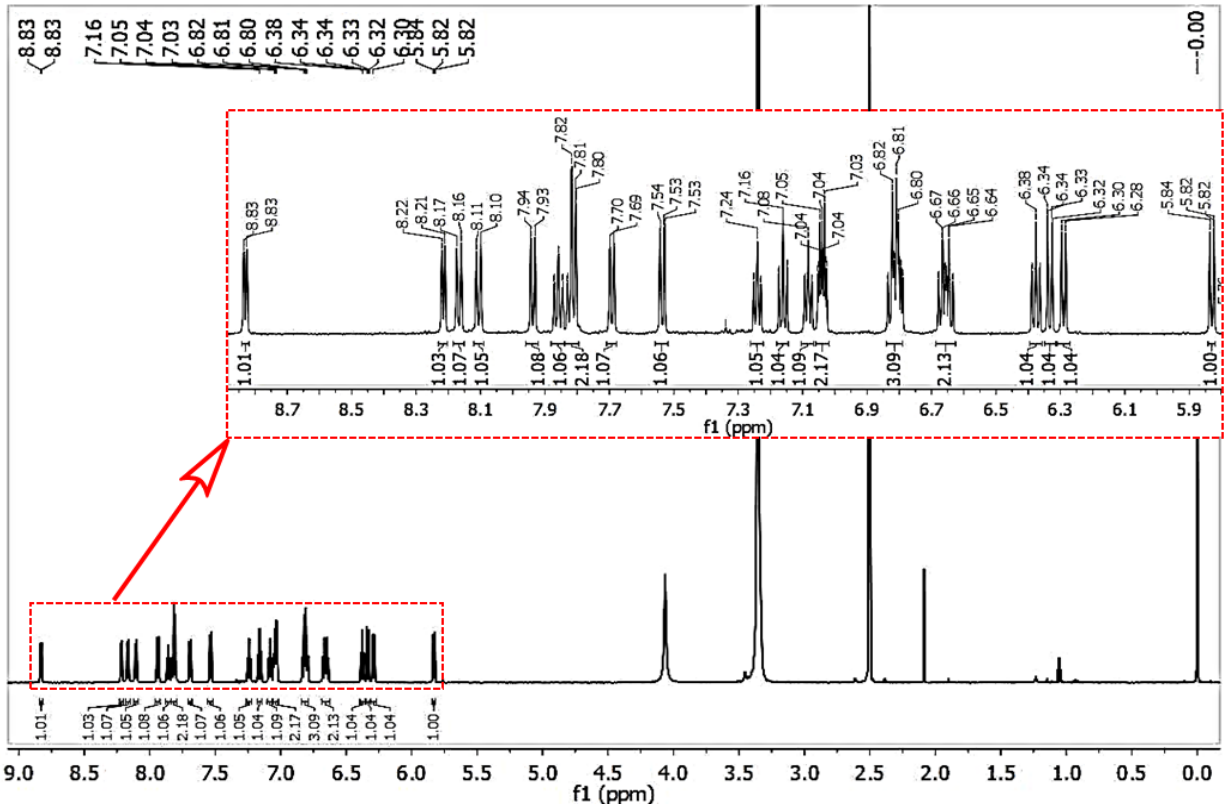

Figure 5.11. *^1H NMR spectrum of AS-1 recorded in DMSO-d^6.*

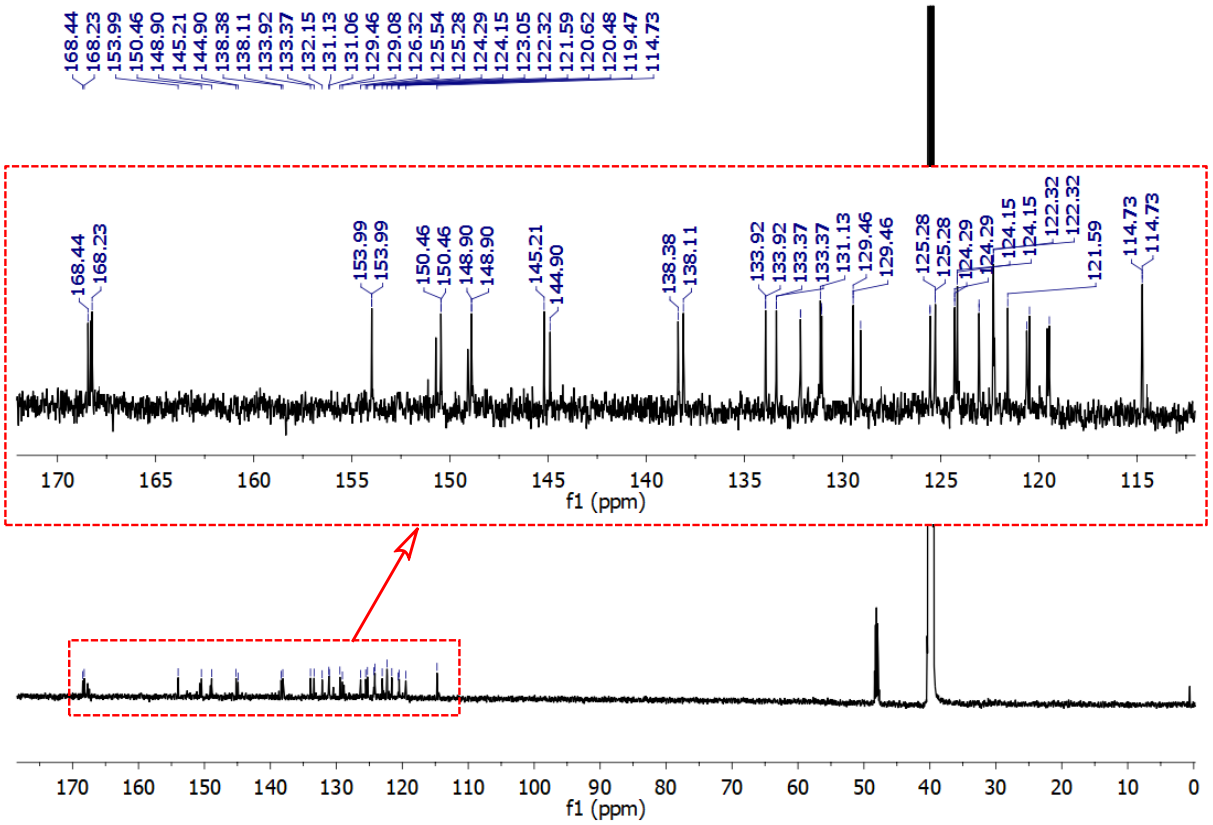

Figure 5.12. *^{13}C NMR spectrum of **AS-1** recorded in DMSO-d^6.*

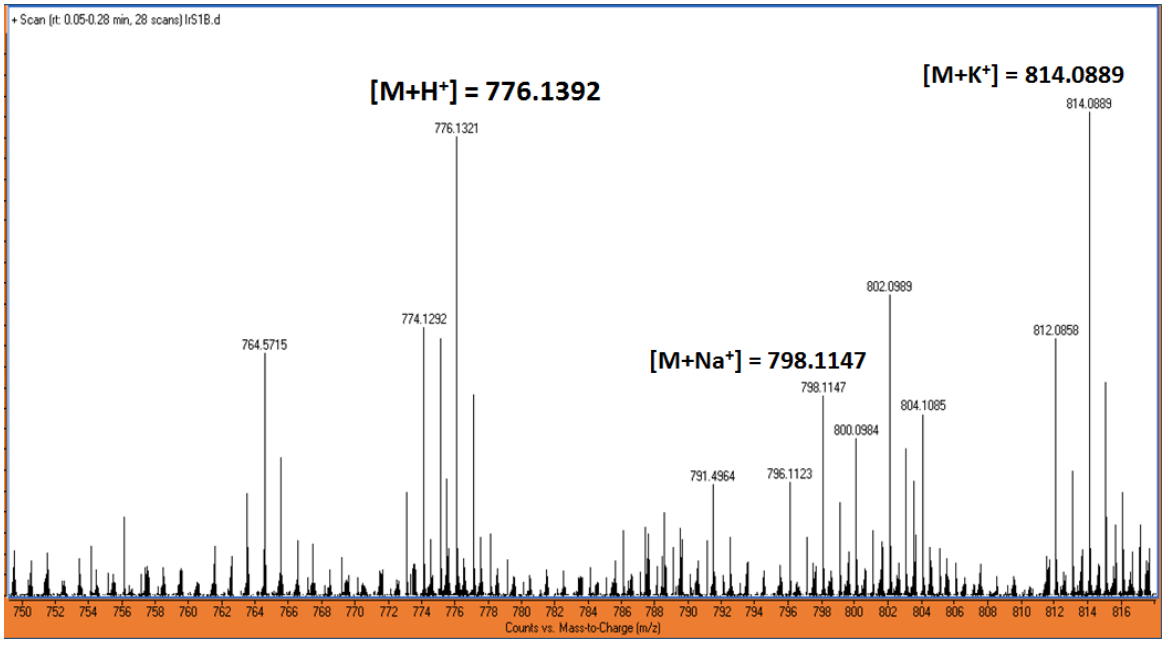

Figure 5.13. *HRMS spectrum of **AS-1** recorded in Methanol. The calculated value for [M+H$^+$] = 776.1392; [M+H$^+$] = 798.1167 and for [M+H$^+$] = 814.0896.*

The crystallographic refinement parameters (Table 5.4.) of AS-1 and the selected bond length (Å) and bond angle (degree) parameters (Table 5.5.) are provided here.

Structural analysis reveals that the Ir(III) centre in AS-1 adopts an anticipated distorted octahedral coordination geometry with cis metallated carbons and trans nitrogen atoms, as revealed by previous structural studies on mononuclear complexes comprising the cyclometalated C-N ligands [85-88].

Table 5.4. *Crystallographic Data for AS-1*

Chemical formula	**$C_{39}H_{24}IrN_3OS$**
F_w	774.9
Crystal system	Triclinic
Space group	$P\bar{1}$
Hall group	*-P 1*
a (Å)	9.3774(6)
b (Å)	10.0175(7)
c (Å)	17.6829(12)
α (deg)	84.881(2)
β (deg)	83.611(2)
γ (deg)	71.432(2)
V	1562.30(18)
Z	2
T (K)	100
S	1.131
μ (mm^{-1})	4.376
$2\theta_{max}$ (deg)	56.56
no. of reflns	7043
Npar	406
T_{min}	0.534
T_{max}	0.785
R	0.0361
wR2	0.0887
h,k,lmax	12,13,23

Table 5.5. *Selected Bond Length (Å) and Angles (deg) for As-1*

Ir(1)-C(13)	2.005(4)	Ir(1)-C(26)	1.998(4)
Ir(1)-N(3)	2.198(4)	Ir(1)-N(2)	2.028(4)
Ir(1)-O(1)	2.128(3)	Ir(1)-N(1)	2.046(4)
C13-Ir1-N1	81.8(2)	N2-Ir1-N3	90.9(1)
C13-Ir1-C26	84.7(2)	N3-Ir1-C26)	99.8(2)
C26-Ir1-N2	81.5(2)	N2-Ir1-O1	93.5(1)
C13-Ir1-N2	92.9(2)	C26-Ir1-N1	95.4(2)
N1-Ir1-O1	89.0(1)	C13-Ir1-O1	90.1(2)
N3-Ir1-O1	85.7(1)	N3-Ir1-N1	94.6(1)

A comparison of the Ir-N bond lengths of AS-**1** with those of the reported octahedral Ir-N bonds (1.85-2.07Å) indicates that the Ir-N3 bond length (2.198 Å) is substantially long (Table 5.5.) [89-91]. On the other hand, the Ir-O bond length in AS-1 (2.128 Å) is on the shorter side (Ir-O ~ 2.2 Å) (Table 5.5.), reflecting the possibility of the dissociation of the Ir-N bond first in presence of a nucleophile with subsequent dissociation of the Ir-O bond.

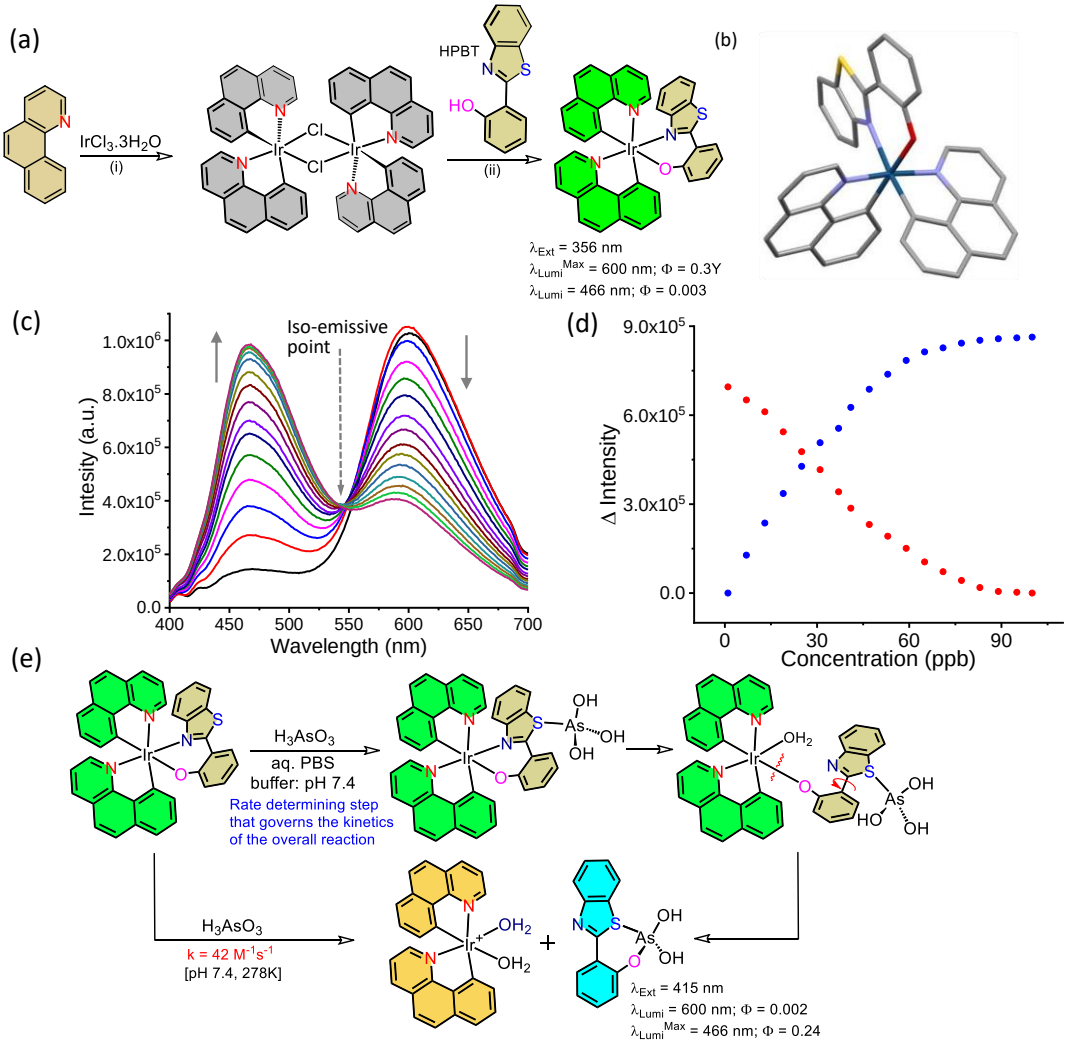

Figure 5.14. *(a) Synthetic route and molecular structure of AS-1; (i) EtOH, H_2O, 90°C, 24h. (ii) EtOH, Na_2CO_3, 90°C, 4h. (b) Single-crystal X-ray structure of As-1with thermal ellipsoids are drawn at the 40% probability level. (c) Emission spectral profile of AS-1 (λ_{Ext} = 415 nm) in aq. PBS buffer solution (pH = 7.4) upon the gradual increase in [iAs^{III}] (0 - 100 ppb). (d) A plot of change in luminescence intensity at 466 nm (blue) and 600 nm (red) with subsequent changes in [iAs^{III}] (0 - 100 ppb) having an iso-emissive point at 547 nm following excitation at 415 nm, respectively, to confirm the ratiometric response of AS-1; emission spectral measurements were performed in a aq. PBS buffer solution (pH = 7.4). (e) Proposed binding of the $S_{Imidazole}$ moiety to the iAs^{III}-centre in a rate-determining step to form a transient species, which undergo dissociation process to yield iAs^{III}-HPBT with a characteristic emission spectrum having emission maximum at 466 nm (λ_{Ext} = 415 nm).*

The electronic spectrum for AS-1 was recorded in aqueous phosphate buffer saline (PBS; pH 7.4) medium, and this showed an absorption maximum at 453 nm, along with a hump at ~425 nm (Figure 5.15.). These absorption bands/shoulders are attributed to predominantly intra ligand π-π* charge transfer transitions.

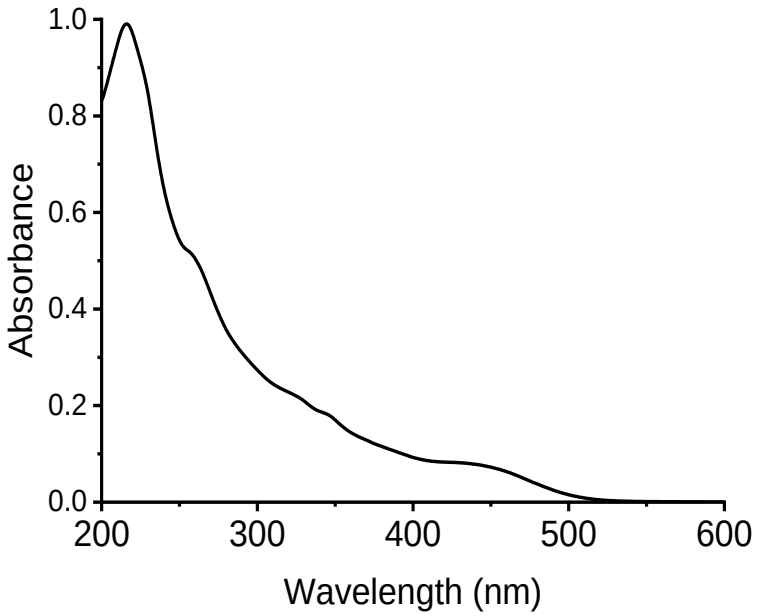

Figure 5.15. *The absorbance spectra of AS-1 in aqueous phosphate buffer saline (PBS; pH 7.4) medium at a concentration of 10^{-6} M.*

Luminescence spectrum for AS-1 was recorded in aqueous phosphate buffer saline (PBS; pH 7.4) following excitation at 415 nm. A distinct luminescence maximum at 600 nm was observed (Φ^{600} = 0.28). On a gradual increase in [iAs^{III}], a new luminescence band having a maximum at 466 nm was observed with a concomitant decrease in the 600 nm band intensity (Figure 5.14.c). A systematic luminescence titration was performed following excitation at 415 nm in aq. PBS buffer solution (pH = 7.4) of AS-1(50 ppm) and varying [iAs^{III}] (0 - 100 ppb) confirmed a ratiometric change in the spectral luminescence pattern having an isoemissive point at 547 nm (Figure 5.14.c). Luminescence quantum yield for the new band at 466 nm (Φ^{466}/λ_{ext} 415 was evaluated as 0.24. A switch ON enhancement in luminescence intensity at ~466 nm is evaluated on the addition of iAs^{III} (Figure 5.14.c and 5.14.d). Presumably, the formation of iAs^{III}-HPBT accounts for the changes in emission responses of AS-1 on reaction with iAs^{III} vide infra).

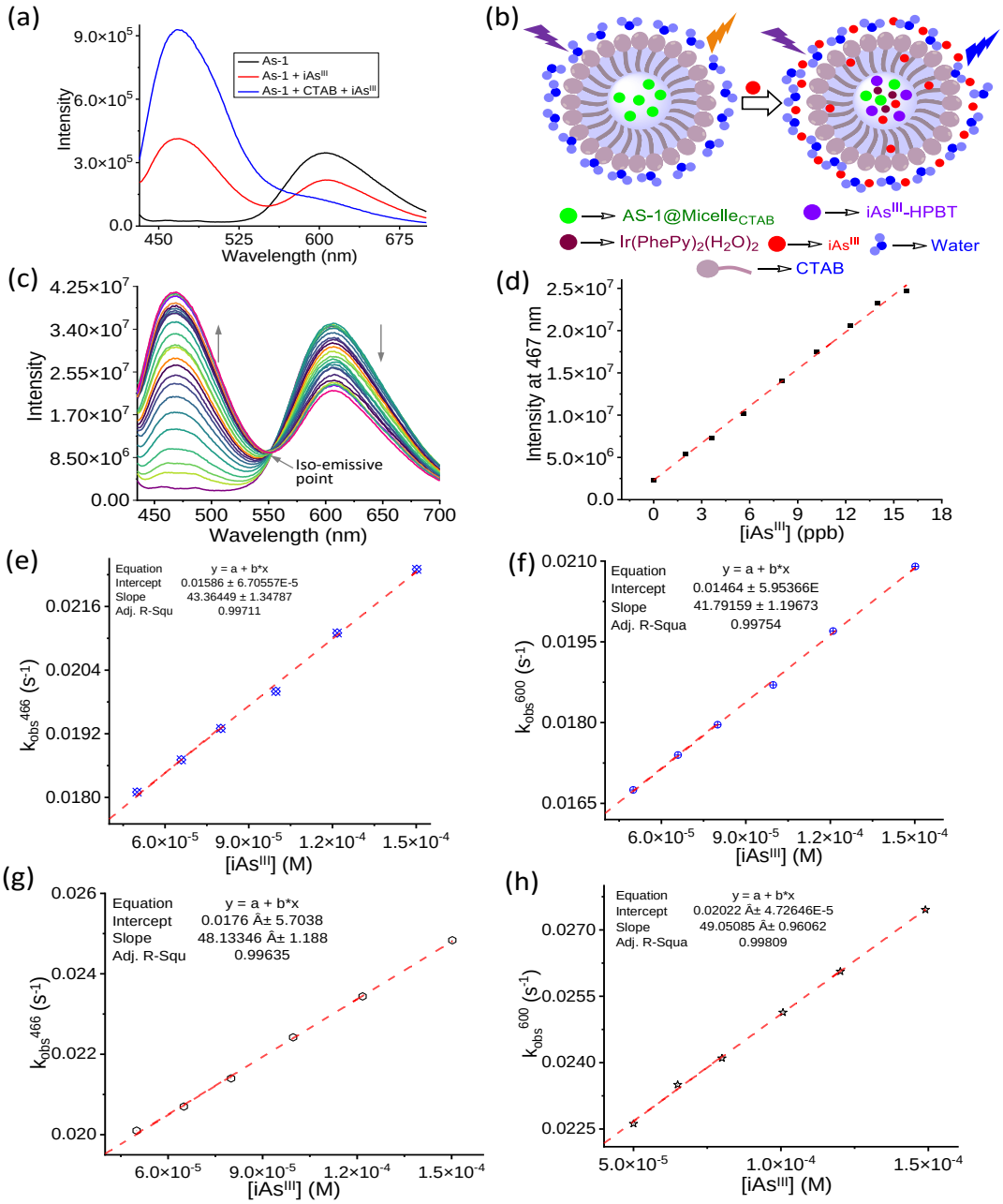

Figure 5.16. *(a) Emission spectra (λ_{Ext} = 415 nm) for* ***AS-1*** *(1X10^{-5} M);* ***AS-1*** *(1.0 x 10^{-5} M) in presence of* ***iAs^{III}*** *(1.0 x10^{-4} M); and* ***AS-1*** *(1.0 x 10^{-5} M), [CTAB] (10.0 x 10^{-4} M) and* ***iAs^{III}*** *(1.0 x 10^{-4} M) showing the improved emission response under micellar condition. A PBS buffer solution having pH 7.4 was used for experiment. (b) A schematic diagram illustrating micellar-enhanced detection of* ***iAs^{III}****. k_{obs} vs* ***[iAs^{III}]*** *plot for (c) $\lambda_{Ext}/\lambda_{Em}$: 415/466 nm and (d) $\lambda_{Ext}/\lambda_{Em}$: 415/600 nm). The experiment was performed with 10 μM of* ***AS-1*** *in presence of varying* ***[iAs^{III}]*** *(5.0 ×10^{-5} M – 15.0 x 10^{-5} M) at 298 K. k_{obs} vs* ***[As-1]*** *plot in the presence of 1.0 x 10^{-4} M CTAB for (e) $\lambda_{Ext}/\lambda_{Em}$: 415/466 nm and (f) $\lambda_{Ext}/\lambda_{Em}$: 415/600 nm). The experiment was performed with 10 μM of* ***AS-1*** *in presence of a various concentration of* ***iAs^{III}*** *(5.0 ×10^{-5} M – 15.0 x 10^{-5} M) at 298 K. Aq. PBS buffer having a solution having pH 7.4 was used for studies. All kinetic studies were performed at (298 ± 1) ℃. (g) Emission spectral profile (λ_{Ext} = 415 nm) of* ***AS-1*** *(1.0 x 10^{-5} M) in CTAB (10.0 x 10^{-4} M) with varying* ***iAs^{III}*** *(5.0 × 10^{-5} M – 15.0 x 10^{-5} M) in aq. PBS buffer solution (pH = 7.4). (h) a plot of change in luminescence intensity at 466 nm with subsequent changes in* ***[iAs^{III}]*** *(0 - 20 ppb).*

The presence of a distinct iso-emissive point at 547nm signifies the presence of two luminescent species that exist in equilibrium with characteristic luminescence maxima at 466 and 600 nm, respectively (Figure 5.14.c). According to 'Pearson's hard and soft acid-base theory, soft-soft interaction is favoured over hard-soft interaction. As^{3+} being a "soft" metal ion, typically shows a strong affinity to the 'soft' S-donor ligands, and this is also primarily the reason for iAs^{III} to bind preferentially to the proteins having Cys-residue with a free sulfhydryl functionality [39]. Presumably, this also accounts for the no interaction between the S-donor HPBT and iAs^{V} (vide infra). To ascertain this, we synthesized and isolated the complex iAs^{III}-HPBT by reacting iAs^{III} and HPBT. After all necessary characterization for ensuring the desired purity of the isolated iAs^{III}-HPBT complex, different spectra (electronic, luminescence, ESI-Ms, and ^{1}H NMR spectra) were recorded.

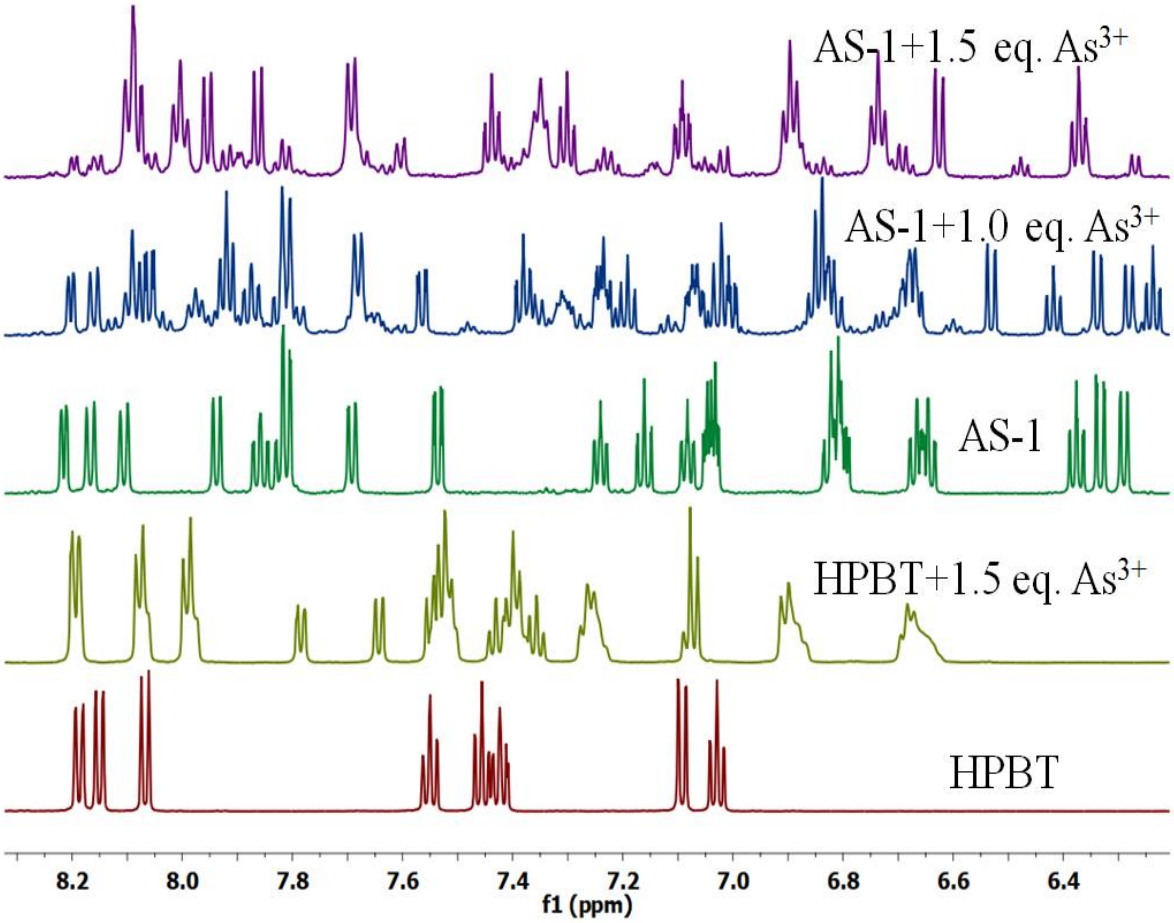

Figure 5.17. *^{1}H NMR spectra between ligand HPBT and* ***AS-1*** *with various concentration of* ***iAs^{III}*** *in DMSO-d^{6}.*

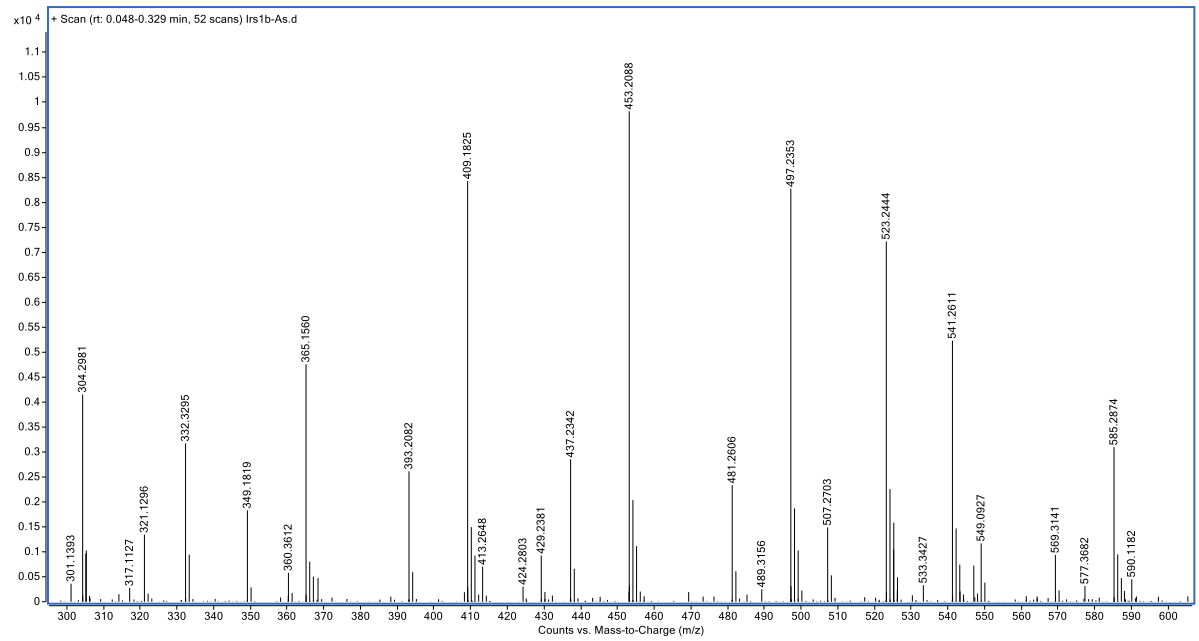

Figure 5.18. *HRMS spectrum of AS-1 + 3 eq. of iAs^{III} recorded in Methanol.*

Luminescence spectrum of this presynthesized and isolated iAs^{III}-HPBT in aq. PBS buffer medium (pH 7.4) showed a maximum at 466 nm. Importantly, ^{1}H NMR titration with a fixed [AS-1] and varying [iAs^{III}], clearly shows the appearance of the signals that correspond to the formation of iAs^{III}-HPBT (Figure 5.17.). MS spectrum recorded for the reaction mixture for AS-I and iAs^{III} revealed the presence of the molecular ion (M^+/z) signal for iAs^{III}-HPBT and $Ir(H_2O)_2$, which further corroborate our proposition for the formation of iAs^{III}-HPBT (Figure 5.14.e). High-resolution mass spectrometry (HRMS) shows signals at 332.3295 and 585.2874 (Figure 5.18.), which correspond to iAs^{III}-HPBT (calculated mass: 332.3394) and [$Ir(BZQ)_2(H_2O)_2$] (calculated mass: 585.2176), respectively. Literature reports also reveal that $Ir(BZQ)_2(H_2O)_2$ is non-luminescent. Thus, all these data corroborate our proposition for the formation of iAs^{III}-HPBT and [$Ir(BZQ)_2(H_2O)_2$][BZQ: benzo h quinoline] (Figure 5.14.e).

To further improve the solubility of AS-1 in aq. buffer medium and considering its hydrophobicity, we explored the possibility of using a surfactant, CTAB above the critical micellar concentration (CMC) for achieving improved solubilization of AS-1 in aq. buffer medium. The hydrophobic tail, the hydrophilic (ammonium ion derivative) head group of the self-assembled micellar structures help in trapping AS-1 in the hydrophobic micellar core. The dynamic nature of the micellar structures allows the

diffusion of iAs^{III} from the bulk of the aq. solution to the core. These micellar cores act as a microreactor and favour the reaction between AS-1 and iAs^{III} and help in achieving the improved performance of the AS-1 molecule in sensing iAs^{III} (Figure 5.16.a and 5.16.b).

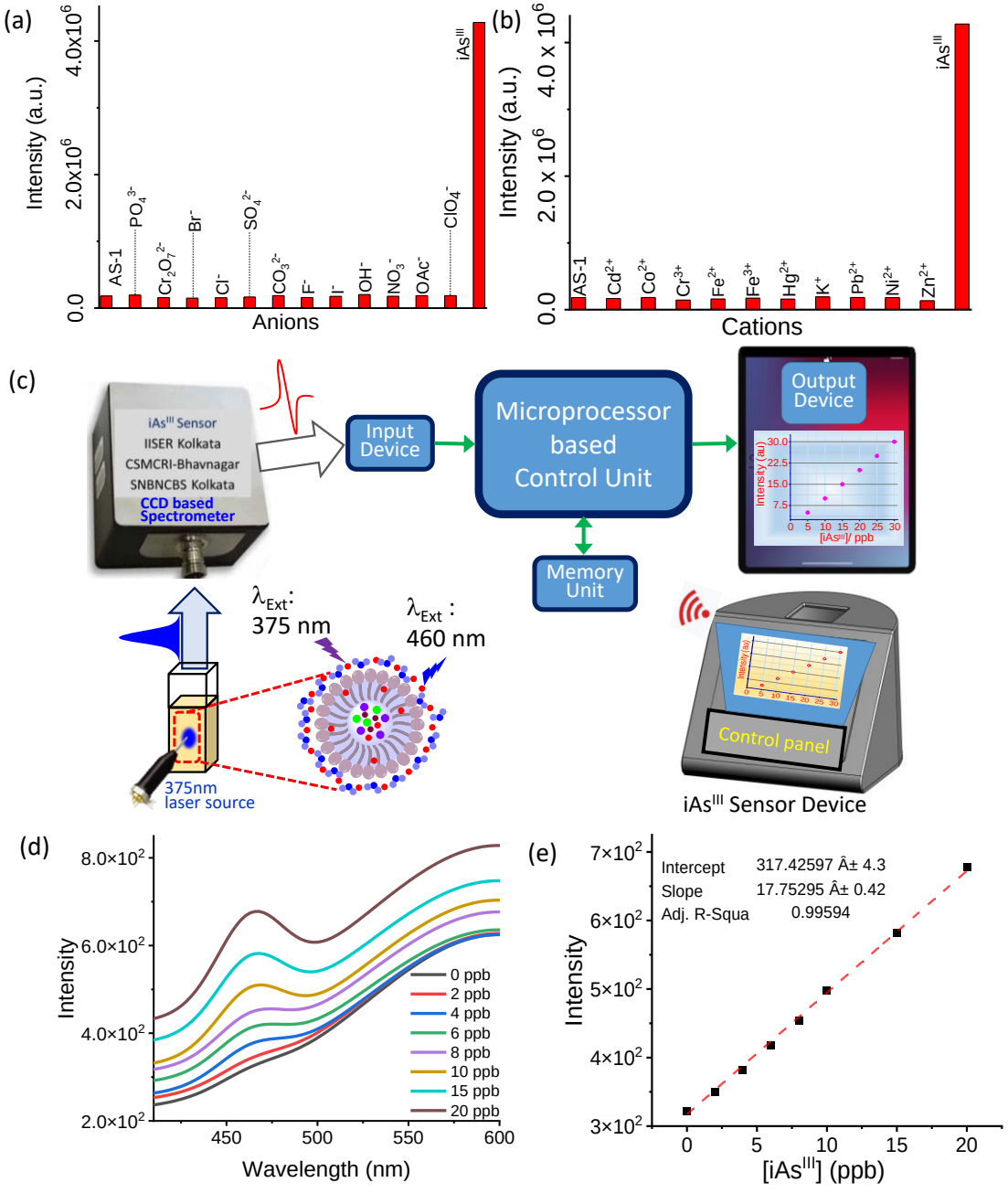

Figure 5.19. *(a) & (b). Relative fluorescence intensity changes on addition of 10 equiv. various anions and metal ions to 10 μM AS-1. (c) Schematic diagram of Arsenic Sensing device and the sensing mechanism of the sensor in CTAB, "Enhancement of fluorescence" occurs in the presence of iAs^{III} ions in solution having AS-1@Micelle^{CTAB}. (d) Full spectra of iAs^{III} contaminated having AS-1@Micelle^{CTAB} (e) The calibration curve derived using indigenously developed device shown in (c).*

Importantly, solution (aq. PBS buffer; pH 7.4) luminescence for AS-1 remained unchanged when spectra were recorded at 298 K over a period of time (Figure 5.20.). However, a sharp decrease in luminescence intensity at 600 nm with a concomitant increase in luminescence intensity at 466 nm was observed when spectra were recorded in presence of 10-mole equivalence of iAs^{III} (Figure 5.21.). To confirm that both these changes at 466 nm and 600 nm signify the same reaction, kinetics were studied for a fixed [AS-1] (1M) and a varying [iAs^{III}] (5.0×10^{-5} M – 15.0×10^{-5} M) in aq. PBS buffer (pH 7.4) at 298 K by monitoring the changes in luminescence at two specified wavelengths as a function of time.

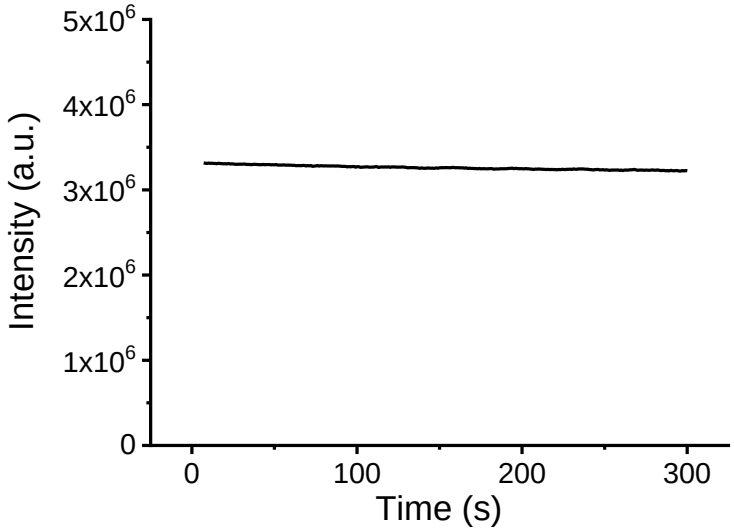

Figure 5.20. *Plot emission intensity at 600nm Vs. Time of AS-1 recorded at 298 K.*

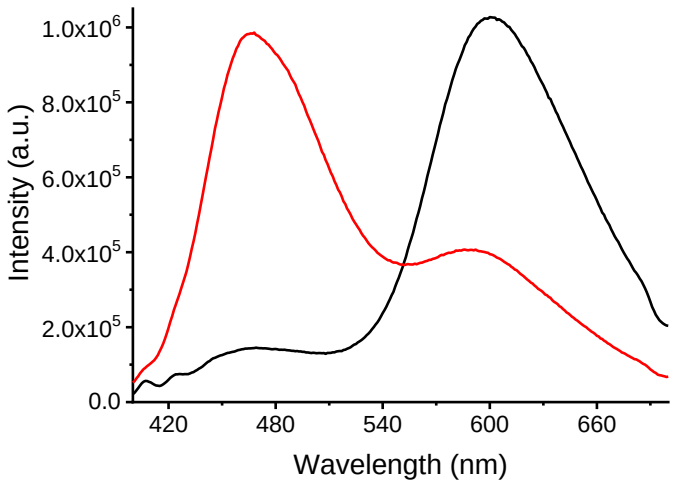

Figure 5.21*. Emission spectra of AS-1 before (black) and after (red) the addition of 10 equivalents of* iAS^{III}*.*

Observed pseudo-first-order rate constant (k_{obs} (s^{-1})) for respective [iAs^{III}] was evaluated for each kinetic run. A plot of k_{obs}^{466} or k_{obs}^{600} vs. [iAs^{III}] yielded a linear plot with a negligible intercept (Figure 5.16.c and 5.16.d). Minimal intercept signifies negligible dissociation of the complex AS-1 under the experimental condition. The first-order dependence on [iAs^{III}] with intrinsic rate constant (k^{466} = (43 ±1.3) $M^{-1}s^{-1}$; k^{600} = (42 ± 1.12) $M^{-1}s^{-1}$) for the substitution reaction of HPBT in AS-1 by iAs^{III} confirms that iAs^{III} is associated with the slow step of the reaction (Figure 5.14.e). This confirms an associative substitution reaction. Importantly, similarities of the values for the intrinsic rate constants (k^{466} and k^{600}) also confirm that luminescence changes associated at 466 nm and 600 nm signify the same chemical transformation. (Figure 5.16.c and 5.16.d).

Kinetic studies were repeated by probing the luminescence changes either at 466 nm or at 600 nm in presence of 10.0 x 10^{-4} M CTAB (*Vide infra*). It is worth mentioning that this is higher than the critical micelle concentration (CMC) for amphiphilic CTAB (CMC_{CTAB} ~ 8.5 x 10^{-4}M) [92] in aq. PBS buffer solution having pH 7.4. For studying these reactions, 10.0 x 10^{-4} M CTAB was added to a solution of AS-1 (100 µ M) in aq. PBS buffer (pH = 7.4). AS-1, being hydrophobic, was favorably partitioned inside the hydrophobic core of the micelle and this was expected to provide a nano-reactor type option with a relatively higher localized concentration of reactants as compared to the bulk aq buffer media [93-96]. Rate constants of $k^{466}_{CTAB\text{-}M}$ = (48 ± 1.2) $M^{-1}s^{-1}$ and $k^{600}_{CTAB\text{-}M}$ = (49 ± 0.96) $M^{-1}s^{-1}$ at 298K for the reaction between AS-1 and HPBT were evaluated using otherwise analogous conditions for kinetic studies (Figure 5.16.e and Figure 5.16.f). Importantly, a comparison of the rate constants evaluated from kinetic studies in the presence of 10.0 x 10^{-4} M CTAB (> CMC_{CTAB}) shows that the respective rate constant is higher by 17% as compared to the one studied in the absence of CTAB. This further confirms that the orientation of the reactants within the hydrophobic core of the micellar structure favored the reaction, presumably through a higher localized concentration of the reactants. Studies (Figure 5.22.) with other surfactants (anionic: sodium dodecyl sulfate, SDS; neutral: Triton-X-100) yielded no improvement in the kinetic parameters.

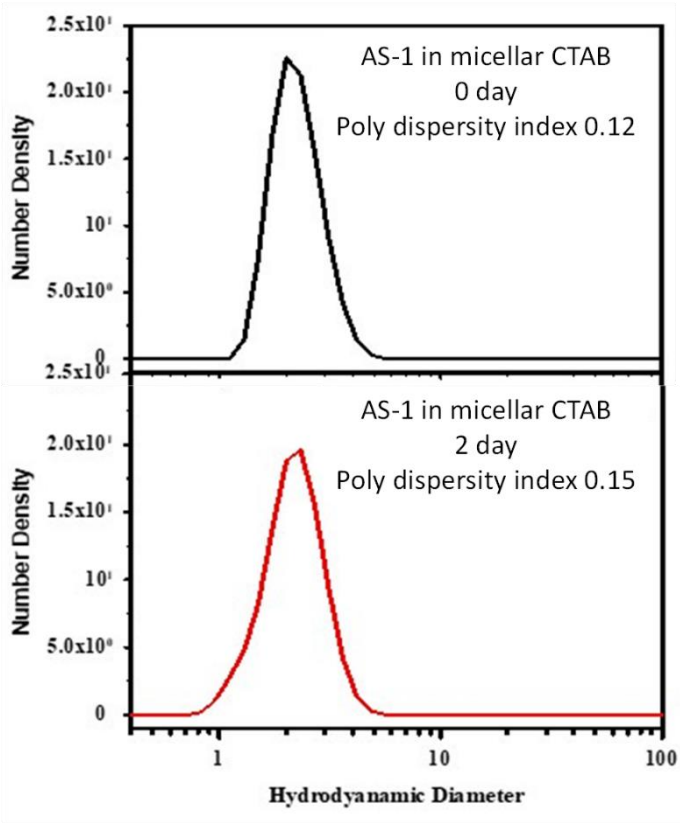

Figure 5.22. *DLS data of AS-1@Micelle^{CTAB}. After immediate preparation (top) and after 2 days (bottom).*

Presumably, the formation of a stable coordination complex between iAs^{III} and HPBT accounts for the thermodynamic driving force for the formation of a bis-solvated complex of Ir(III). A moderately high binding constant for iAs^{III}-HPBT [$K_{iAs^{III}\text{-}HPBT}$ = (3.0 ± 0.1) × 10^5 $M^{-2}L^2$ at 298 K] complex formation was also evaluated based on data obtained from a luminescence titration.

This proposition was further confirmed by a systematic ^{1}H NMR titration on a mixture of AS-1 and iAs^{III} in D_2O medium. As shown in Figure 5.17., the chemical shifts of protons of HPBT were found to change significantly upon binding to iAs^{III} and no further change was observed beyond a 1.5 mole equivalence of iAs^{III}. Once the kinetic pathway and the basis for the luminescence response for the reaction between AS-1 and iAs^{III} were ascertained, luminescence response was utilized for quantitative estimation of iAs^{III} in aq. PBS buffer medium having physiological pH (7.4). A plot of the differences ($-\Delta I_C = -(I_0-I_C)$) in the initial luminescence intensity (I_0) and final luminescence intensity (I_C) at 466 nm as a function of [iAs^{III}] was obtained from the

luminescence titration using a fixed [AS-1] (1 μM) with a varying [iAs^{III}] (5.0×10^{-5} M – 15.0×10^{-5} M) in aq. PBS buffer (pH 7.4) (Figure 5.23.). The limit of quantification (LOQ) of 9.38 ppb and 20 ppb was experimentally evaluated by using a detectable change in luminescence with signal to noise ratio of 3:1 and 10:1, respectively, for a certain [iAs^{III}]. However, LOD value calculated following the 3σ method is 9.38 ppb, which is in the borderline of the WHO recommended allowed limit of 10 ppb for iAs^{III} in potable water.

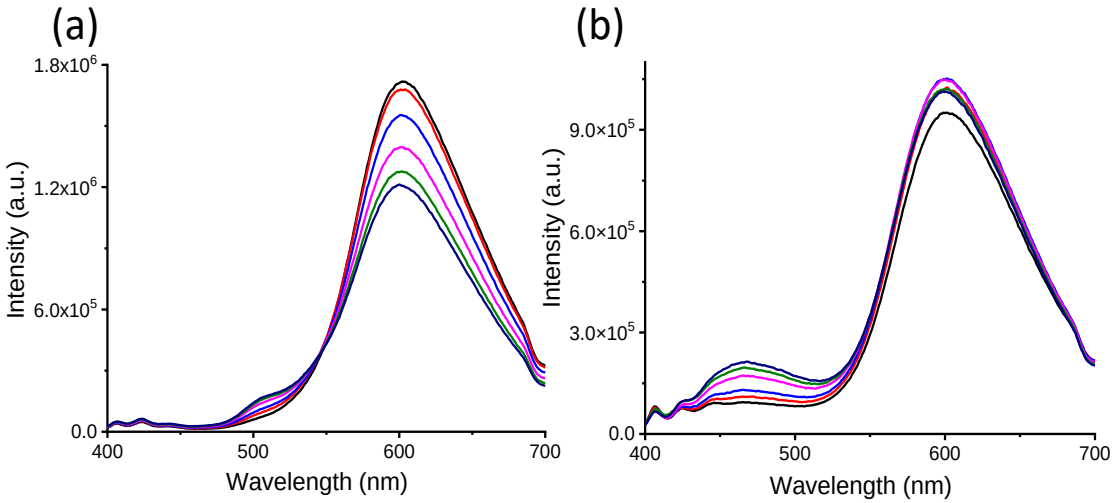

***Figure 5.23**. The fluorescence spectral changes of AS-1 (λ_{ext} 365 nm) in micellar (a) SDS, (b) Triton-X with gradual increasing concentration of iAs^{III} (0 to 5 μM).*

To achieve a more efficient detection and quantification, analogous luminescence titration was performed in presence of 10.0×10^{-4}M of CTAB (Figure 5.16.g and 5.16.h). As discussed earlier, entrapment of the neutral molecule AS-1 inside the hydrophobic core of the micellar structure helped in improving the local concentration of AS-1, as well as lowering the solvation influence of the iAs^{III} within the hydrophobic core as compared to one that one would expect in the bulk aq. buffer media. For evaluating the LOD in micellar medium, a solution of 10.0×10^{-4} M CTAB was stirred with AS-1 (10 μM) in aq. PBS buffer (pH = 7.4) for 1 hour at 298K. To this, varying [iAs^{III}] (0 - 10ppb) was added, and the changes in the steady-state luminescence values were measured for the respective solution for a certain [iAs^{III}]. For AS-1@$Micelle^{CTAB}$ LOD (3σ) and LOQ (S/N = 3), values evaluated were 0.2 ppb and 0.5 ppb, respectively, which was much lower than the lowest allowed detection limit for iAs^{III} for potable water. To the best of our knowledge, this is one of the most

efficient molecular probes reported for the detection of iAs^{III} in potable water as per the WHO norms.

The specificity of chemodosimetric molecule AS-1 for the detection of iAs^{III} was also examined. The fluorescence responses of 10 µM AS-1 in the presence of 50 µM various metals ions (Na^{+}, K^{+}, Ag^{+}, Zn^{2+}, Fe^{2+}, Pb^{2+}, Cd^{2+}, Co^{2+}, Cu^{2+}, Ni^{2+}, Hg^{2+}, Mn^{2+}, Ca^{2+}, Mg^{2+}, Fe^{3+}, Cr^{3+}, Al^{3+}, As^{3+}, As^{5+} etc.) and anions and ROS species (F^{-}, Cl^{-}, Br^{-}, I^{-}, NO_3^{-}, PO_4^{3-}, OAc^{-}, SO_4^{2-} , $Cr_2O_7^{2-}$, OH^{-}, ClO_4^{-}, CO_3^{2-}) were recorded under identical experimental condition (Figure 5.19.a and 5.19.b). A ~ 300 fold enhancement of luminescence was observed only when the studies were performed with iAs^{III} and this confirmed the desired specificity of the chemodosimetric molecule AS-1 for its quantitative estimation.

After confirming the selective detection of iAs^{III} in an aqueous solution having concentration as low as 2 ppb, a network-enabled portable device was conceived and constructed (Figure 5.19.c) to miniaturize a complete iAs^{III} sensing system that was capable to linking the fluorescence output to a real-time digital read-out signal. The device contains a customized cuvette holder mounted internally surrounded by a light source and one micro-spectrometer detector (Hamamatsu C12880ma). At 90^{o} position of this micro-spectrometer, one UV LED of wavelength 365 nm (DC 3V, 500mA) is mounted for measuring fluorescence. This arduino driven set-up can directly measure the concentration of iAs^{III} in water. The prototype is powered by a 19.5 V source and comprises a liquid crystal display (LCD) linked to two Arduino UNO boards. The software has been indigenously developed in LabVIEW (by National Instruments) platform for easy user interface and displays the calculated concentration of the arsenic present in the groundwater sample. This software captures the change in luminescence intensity upon the excitation of UV LED of wavelength 365 nm and translates into its corresponding As^{3+} concentration from the previous calibration (Figure 5.19.d and Figure 5.19.e) and is displayed on the LCD screen. We found using the AS-1@$Micelle^{CTAB}$ probe, the device could be able to detect the iAs^{III} concentration within 10 seconds with a detection limit of 2 ppb. Using this prototype, water samples from River Ganges and Gulf of Khambhat, spiked with known concentration of iAs^{III}

were tested (Table 5.4.). The concentrations of iAs^{III} in these samples were monitored using our developed sensor, which shows noteworthy agreement with the results obtained from standard instrument. This data highlights the method performance and reliability of the AS-1@Micelle^{CTAB} probe coupled with the internet-enabled portable prototype which may provide an easy solution for water testing in remote areas where frequent monitoring of the As^{3+} level is crucial. Further work is in progress to enable the real-time data upload to the cloud or transmission to experts a thousand miles away for analysis and taking immediate necessary actions within another 7 to 10 seconds from a remote place by virtue of the IOT association with the instrument. Simultaneously large scale testing of real groundwater samples from different areas of West Bengal, which is one of the most iAs^{III} contaminated places in India, is in progress to extend the potentiality of the device.

As discussed earlier, mitochondria are the primary target organelle for iAs^{III} induced toxicity for human physiology. After establishing its specific recognition of iAs^{III} with an associated switch ON luminescence response, its utility in mapping the uptake and distribution of iAs^{III} in human live breast cancer cell line (MCF-7) was explored. The toxicity of this molecule AS-1 and the micellar system (AS-1@Micelle^{CTAB}) on MCF-7 cells (Figure 5.24.) was established using an MTT (3-(4,5-dimethylthiazol-2-yl)-2,5-diphenyltetrazolium bromide) assay, and no significant toxicity was observed.

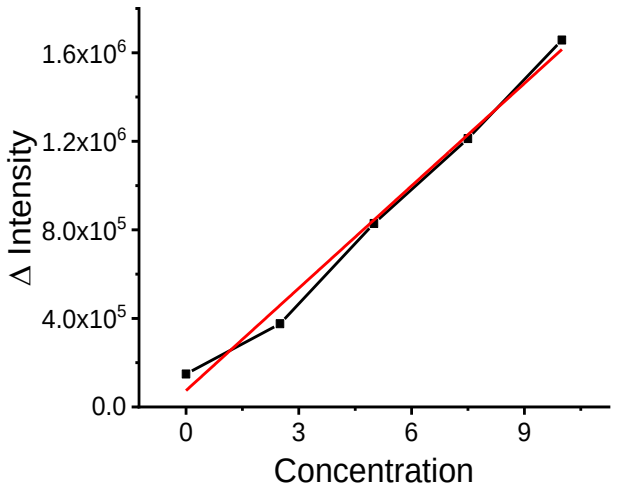

Figure 5.24. *Plot of change in luminescence intensity of AS-1 at 466 nm with subsequent changes in [iAs^{III}] (0 - 10 ppb).*

Seo, Kwon, and co-worker have successfully demonstrated that cationic Ir(III)-core and lipophilic coordinating ligands helps in designing appropriate reagent for crossing the inner mitochondrial membrane (IMM) and localization in mitochondria [97]. Further, recent reports have also established that the use of cationic surfactants helps in enhanced permeation and retention of Drug@Micelle^{Cation} in mitochondria [98-101]. The mitochondria membrane potential for tumor cells ($\Delta\Psi_T{}^{Mitochondria} \sim -180$ mV) is much higher than the $\Delta\Psi_{NE}{}^{Mitochnodria}$ (NE: normal epithelial cells), and this favors the localization of cationic micelles in mitochondria [102, 103]. We examined the subcellular location of AS-1@Micelle^{CTAB} and, eventually, the iAs^{III}-HPBT using confocal laser scanning microscopy (CFLSM). A commercial fluorescent staining agent, MitoTracker Deep Red, is also used for staining inner mitochondrial membrane (IMM) and intermembrane space (IMS) and co-localization studies. To examine the real-time uptake of iAs^{III} in live cancer MCF-7 cells in presence of AS-1 or AS-1@Micelle^{CTAB}, the confluent MCF 7 cells were incubated with 5 μM of AS-1 or AS-1@Micelle^{CTAB} for 60 min and followed by exposure to 10 μM iAs^{III} for 30 min at 37 °C and pH 7.4 (Figure 5.25.a). The positively charged AS-1@Micelle^{CTAB} are rapidly get internalized into cells via clathrin- and caveolae-mediated endocytosis pathways [104, 105]. Luminescence studies reveal that luminescence maximum, characteristic for AS-1 appears at 600 nm, while that for iAs^{III}-HPBT appears at 466 nm following excitation at 415 nm. On incubation with AS-1@Micelle^{CTAB}, bright intracellular emission was observed when a long-pass filter of 500 nm was used (Figure 5.25.a-iii), while no such emission was detected when a short-pass filter of 500 nm was used (Figure 5.25.a-ii). In presence of AS-1@Micelle^{CTAB} and iAs^{III}, a significant intracellular luminescence was observed when images were collected using a bandpass filter of 450-550 nm (Figure 5.25.a-iv) due to the formation of iAs^{III}-HPBT in the cytoplasmic region. These confirmed the cell membrane permeability of AS-1 or AS-1@Micelle^{CTAB}, their localization in cytoplasm, and the ratiometric response of the molecular probe AS-1. The punctuated nature of the images (Figure 5.25.a-iii) indicates that the probe AS-1 localize in specific regions within the cytoplasm. This was investigated in more detail through co-localization studies. This was investigated in more detail through co-localization studies. For co-localization studies, the intensity profile of CFLSM images

recorded with Mito Tracker Red overlapped closely with that of the iAs^{III}-HPBT complex with a significantly high value for the Pearson's coefficient (90%) (Figure 5.25.b).

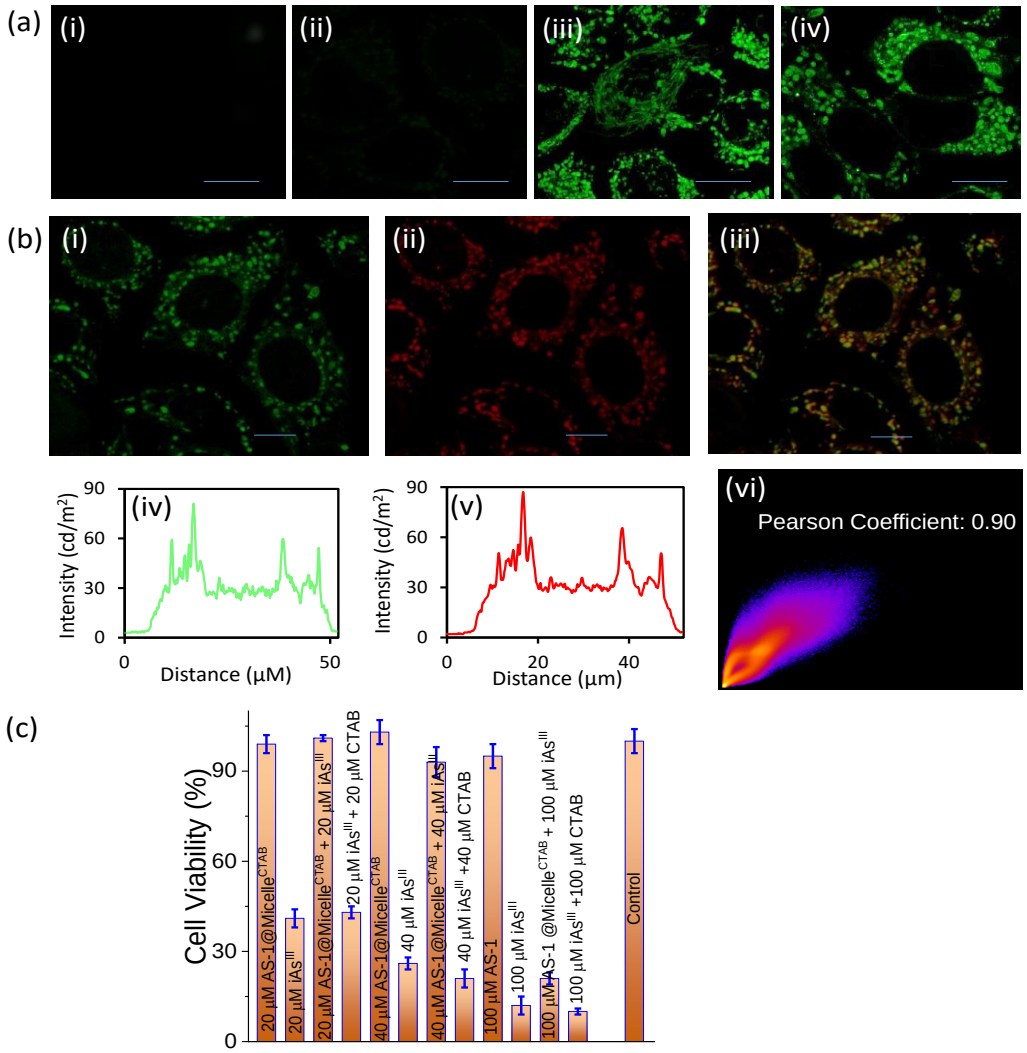

Figure 5.25*. (a) Confocal Laser Scanning Microscopy images of AS-1 treated MCF-7 cells. The cells were incubated with (i) iAs^{III}, (ii) AS-1 short-pass filter of 500 nm (< 500nm), (iii) AS-1 long-pass filter of 500 nm (> 500nm), (iv) iAs^{III} + AS-1. Scale bar 10 μm. (b) Co-localization experiments of intracellular localization of AS-1@Micelle^{CTAB} (panel i) using Mito Traker probes with intensity along traced line shown (iv) underneath. Emission from Mito Traker Deep Red (panel ii) and intensity along the same line shown (v) below. The overlap of the intensity is shown in panel (iii). Panel (iii) shows the overlap of the green and red fluorescence, indicating mitochondrial localization of AS-1@Micelle^{CTAB}. Panel (vi) shows the Pearson co-efficient = 0.90. Scale bar 10 μm and λ_{400nm}. (c) Cell viability assay in the presence of iAs^{III} and AS-1@Micelle^{CTAB}. The bar diagram represents the effect on cell viability when MCF 7 cells were exposed to various concentrations (20, 40, and 100 μM) of AS-1@Micelle^{CTAB}, iAs^{III}, and iAs^{III} + AS-1@Micelle^{CTAB}, wherein the case of iAs^{III} and AS-1@Micelle^{CTAB}, cells were pre-incubated with iAs^{III} for 30 min trailed by AS-1@Micelle^{CTAB} treatment for 24 h. The cell viability was evaluated colorimetrically by using cell CCK-8 counting kit-8. Cell viability is stated as the relative percentage of the control cell line assuming 100% cell viability for DMEM treated control cells. Values represent the mean ± SD.*

Importantly, co-localization experiments with LysoTracker Deep Red (LTDR) confirmed that initially AS-1 or AS-1@Micelle^{CTAB} and eventually iAs^{III}-HPBT were not localised in the lysosome of the MCF-7 cells (Figure 5.26). All these results confirmed the localization of AS-1 in the mitochondrial region of MCF-7 cells, as well as the lysosome/endosome escape of AS-1 or AS-1@Micelle^{CTAB} conjugates through membrane rupture [106].

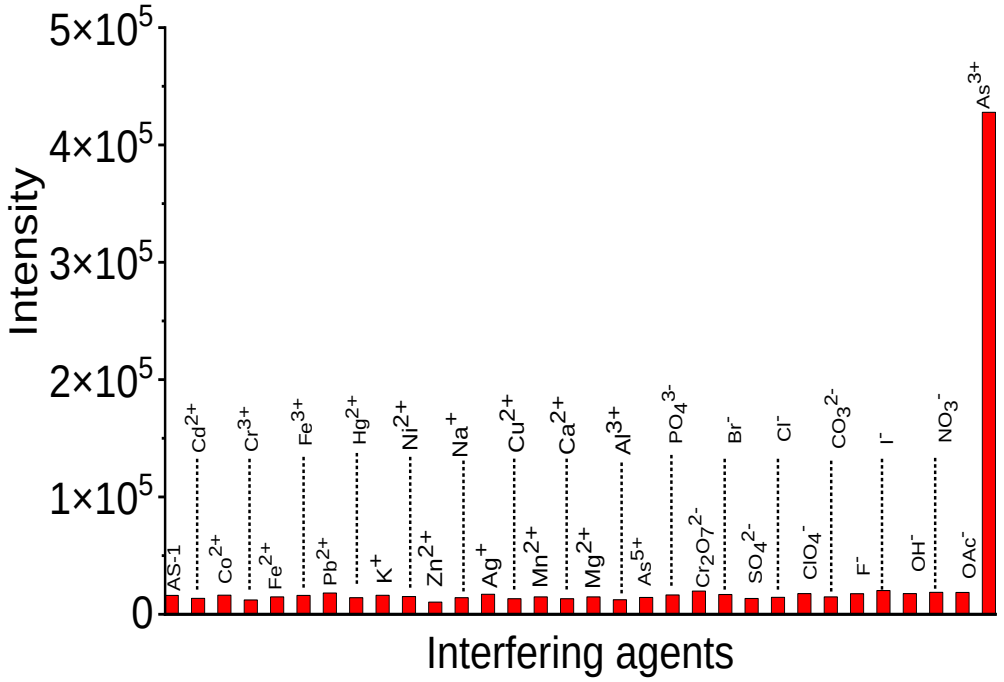

Figure 5.26. *Relative fluorescence intensity changes on addition of 10 equiv. various metal ions and anions to 0.1 μM AS-1.*

Earlier studies have revealed that iAs^{III} has a strong affinity towards S-donor thiophene functionality of HPBT moiety in AS-1. Thus this kinetically controlled process is further favoured with associated gain in thermodynamic stability due to the chelate formation, which eventually leads to the formation of the iAs^{III}-HPBT. Considering this, we explored the possibility of using AS-1 as a next-generation luminescent molecular probe for simultaneous recognition and detoxification of iAs^{III} in cellular conditions [107]. To substantiate this hypothesis, the cell viability at different concentrations of iAs^{III} and AS-1 was tested in cultured MCF-7 cells and assessed using the cell counting kit (CCK-8). The samples (iAs^{III}, AS-1, a mixture of iAs^{III} and AS-1; in case of iAs^{III} and AS-1 co-incubation, iAs^{III} was incubated first for

30 min followed by AS-1) were dissolved in Dulbecco's Modified Eagle's Medium (DMEM) cell culture medium to obtain the anticipated desired concentrations. The MCF-7 cells were seeded at a density of 1.0×10^5 cells and were plated in 6-well cell culture plates at 37 °C under 5% CO_2 for 24 h. The cells were then treated with 100 µL of various concentrations of the samples. After 24 h of treatment, the CCK-8 was added to each of the wells (treated and control), and the wells were incubated further for 4 h. The absorbance was measured at 450 nm. From the cell viability assay (Figure 5.25.c), it is observed that iAs^{III} alone at 20µM for 24 h is toxic to MCF-7 cells (41 ± 3). This cell viability decreases further with an increase in the concentration of iAs^{III}. Interestingly, in presence of AS-1, the toxic effect of iAs^{III} was substantially neutralized. This is evident from the increase in cell viability (100 ± 4 at 20µM iAs^{III} + AS-1; 93 ± 5 at 40 µMAs^{III} + AS-1). However, for an even higher concentration of iAs^{III} (100 µM) no further improvement in the cell viability (12 ± 2 at 100 µM iAs^{III} ; 21 ± 3 for 100 µMiAs^{III} + AS-1) is observed. Presumably, for a limited number of cells in a specific well, [iAs^{III}] of 100 µM may be too high for the cells to survive. Thus, experimental data confirm that AS-1 induces dose-dependent detoxification of iAs^{III} in live cells.

5.3. CONCLUSION:

In this work, analytical performance of a developed field deployable, low cost (USD 400), real-time, reagent-free spectroscopic device for water quality monitoring is demonstrated and established. The data have been collected and analysed by the device using an indigenously developed software for online analysis of the model contaminated water medium in terms of absorbance, fluorescence and scattering. The set-up is found to be effective in measuring suspended scatterer ($TiO_{2)}$, harmful chemicals having emission (Benzopyrene) and bacteria (MRSA), dissolved contaminants (Crystal Violet) or bio-markers degrading the water quality in real time without the use of any reagent. The very low concentration detection capability (LOD like 0.5 ppb) and sensitivity (90 counts/ppb) by spectroscopic means ensures the promising credentials of the developed device for field application as an all-in-one unique water quality monitoring system.

In the work of this chapter, we have also synthesised a new fluorogenic Ir(III)-based molecular probe (AS-1) for the specific and ultrasensitive detection of iAs^{III} in an aqueous medium and mitochondria, which is commonly argued as the target organelle for iAs^{III}-induced toxicity. Spectroscopic investigations on AS-1 and its interaction with iAs^{III} reveal a remarkable specificity of the thioimidazole-moiety towards iAs^{III}, which eventually leads to the formation of iAs^{III}-HPBT. The higher affinity of the S-donor ligands towards iAs^{III} favours the formation of a kinetically controlled intermediate product, which eventually follows a dsscoiative reaction to yield a thermodynamically controlled product, iAs^{III}-HPBT. AS-1 and more specifically AS-1@Micelle^{CTAB} are found to be localized at the mitochondria of the MCF-7 cells, which are reported to have a substantially higher negative membrane potential. The use of AS-1@Micelle^{CTAB} as the probe reagent further enhances the LOQ and enables us to quantify iAs^{III} as low as 0.2 ppb in bulk water medium. Confinement of AS-1 in micellar nano-reactor and efficient diffusion of iAs^{III} to the hydrophobic micelle core due to the dynamic nature of such micelles favour a more efficient reaction. Mitochondrial localization of AS-1 or AS-1@Micelle^{CTAB}, as well as detection of mitochondrial iAs^{III} are confirmed from the CFLSM studies. Most importantly, the reaction between iAs^{III} and AS-1 or AS-1@Micelle^{CTAB} led to the formation of iAs^{III}-HPBT. CCK-8 assay studies reveal that this helps in curbing the toxic influence of iAs^{III} and improving the cell viability of MCF-7 cells. The remarkable selectivity of AS-1 and AS-1@Micelle^{CTAB} towards iAs^{III} and no detectable interference from environmentally relevant cations/ anions encouraged us to build a fluorescence-based prototype for a real-time infield arsenic detection. A prototype is developed in-house using AS-1@Micelle^{CTAB} as the molecular probe. A ratiometric fluorescence ON response at 466 nm on excitation at 415 nm, and appropriate electronics for converting the fluorescence response to a read-out digital signal offer a distinct advantage over other such devices, including devices that use ISE method. To the best of our knowledge, an example of such an ultra-sensitive and mitochondria-specific smart molecular sensor for iAs^{III} and a microprocessor-based device that allows direct quantification of iAs^{III} in a water body in the form of a digital read-out signal is scarce in the contemporary literature. Further, device fabrication also allows an option to

design an IOT based system for remote monitoring of iAs^{III} in any water body for better monitoring of the treated water for distribution and human consumption.

REFERENCES

[1] N.A. Cloete, R. Malekian, L. Nair, Design of smart sensors for real-time water quality monitoring, *IEEE Access*, 4 (2016) 3975.

[2] E.W. Kimani-Murage, A.M. Ngindu, Quality of water the slum dwellers use: The case of a Kenyan slum, *Journal of Urban Health*, 84 (2007) 829.

[3] R.H. Dwight, L.M. Fernandez, D.B. Baker, J.C. Semenza, B.H. Olson, Estimating the economic burden from illnesses associated with recreational coastal water pollution—a case study in Orange County, California, *Journal of Environmental Management*, 76 (2005) 95.

[4] R. Li, M. Dong, Y. Zhao, L. Zhang, Q. Cui, W. He, Assessment of water quality and identification of pollution sources of plateau lakes in Yunnan (China), *Journal of Environmental Quality*, 36 (2007) 291.

[5] E. Lawson, Physico-chemical parameters and heavy metal contents of water from the Mangrove Swamps of Lagos Lagoon, Lagos, Nigeria, *Advances in Biological Research*, 5 (2011) 8.

[6] R. Ramalho, J. Cunha, P. Teixeira, P.A. Gibbs, Improved methods for the enumeration of heterotrophic bacteria in bottled mineral waters, *Journal of Microbiological Methods*, 44 (2001) 97.

[7] G. Sadeghi, M. Mohammadian, M. Nourani, M. Peyda, A. Eslami, Microbiological quality assessment of rural drinking water supplies in Iran, *Journal of Agriculture & Social Sciences*, 3 (2007) 31.

[8] M. Farré, D. Barceló, Toxicity testing of wastewater and sewage sludge by biosensors, bioassays and chemical analysis, *TrAC Trends in Analytical Chemistry*, 22 (2003) 299.

[9] T.H.Y. Tebbutt, Principles of water quality control, *Elsevier*, London, 2013.

[10] D.R. Lenat, Water quality assessment of streams using a qualitative collection method for benthic macroinvertebrates, *Journal of the North American Benthological Society*, 7 (1988) 222.

[11] B. O'Flynn, R. Martínez-Català, S. Harte, C. O'Mathuna, J. Cleary, C. Slater, *et al.*, SmartCoast: A wireless sensor network for water quality monitoring, *32nd IEEE Conference on Local Computer Networks (LCN 2007)*, *IEEE*, Ireland, 2007.

[12] N.C. Munksgaard, D.L. Parry, Monitoring of labile metals in turbid coastal seawater using diffusive gradients in thin-films, *Journal of Environmental Monitoring*, 5 (2003) 145.
[13] S. Zhou, Z. Yuan, Q. Cheng, Z. Zhang, J. Yang, Rapid in situ determination of heavy metal concentrations in polluted water via portable XRF: Using Cu and Pb as example, *Environmental Pollution*, 243 (2018) 1325.
[14] M.D. Johnston, A simple and rapid test for quality control of liquid media, using the bioscreen microbiological growth analyser, *Journal of Microbiological Methods*, 32 (1998) 37.
[15] B. Ouyang, F.R. Dalgleish, F.M. Caimi, T.E. Giddings, J. Shirron, A.K. Vuorenkoski, *et al.*, Compressive sensing underwater laser serial imaging system, *Journal of Electronic Imaging*, 22 (2013) 021010.
[16] D. Selmo, F. Sturt, J. Miles, P. Basford, T. Malzbender, K. Martinez, *et al.*, Underwater reflectance transformation imaging: A technology for in situ underwater cultural heritage object-level recording, *Journal of Electronic Imaging*, 26 (2017) 011029.
[17] T.P. Lambrou, C.C. Anastasiou, C.G. Panayiotou, M.M. Polycarpou, A low-cost sensor network for real-time monitoring and contamination detection in drinking water distribution systems, *IEEE Sensors Journal*, 14 (2014) 2765.
[18] A. Rymszewicz, J. O'sullivan, M. Bruen, J. Turner, D. Lawler, E. Conroy, *et al.*, Measurement differences between turbidity instruments, and their implications for suspended sediment concentration and load calculations: A sensor inter-comparison study, *Journal of Environmental Management*, 199 (2017) 99.
[19] P.D.L.S.L. Shujing, M. Zhihua, The application of watercolor remote sensing in generalmanagement of coast zone, *Spacecraft Recoery & Remote Sensing*, (2001).
[20] L. Goddijn, M. White, Using a digital camera for water quality measurements in Galway Bay, *Estuarine, Coastal and Shelf science*, 66 (2006) 429.
[21] K. Kallio, T. Kutser, T. Hannonen, S. Koponen, J. Pulliainen, J. Vepsäläinen, *et al.*, Retrieval of water quality from airborne imaging spectrometry of various lake types in different seasons, *Science of the Total Environment*, 268 (2001) 59.
[22] B. Zion, The use of computer vision technologies in aquaculture–a review, *Computers and Electronics in Agriculture*, 88 (2012) 125.

[23] C.C. Lee, M.-V. Tran, C.W. Choo, C.P. Tan, Y.S. Chiew, Evaluation of air quality in Sunway City, Selangor, Malaysia from a mobile monitoring campaign using air pollution micro-sensors, *Environmental Pollution*, 265 (2020) 115058.

[24] J.F. Orwin, C. Smart, Short-term spatial and temporal patterns of suspended sediment transfer in proglacial channels, small river glacier, Canada, *Hydrological Processes*, 18 (2004) 1521.

[25] S.K. Varigala, M. Hegarty-Craver, S. Krishnaswamy, P. Madhavan, M. Basil, P. Rosario, *et al.*, Field testing of an onsite sanitation system on apartment building blackwater using biological treatment and electrochemical disinfection, *Environmental Science: Water Research & Technology*, 6 (2020) 1400.

[26] J. Yu, C. Zhang, P. Dai, S. Ge, Highly selective molecular recognition and high throughput detection of melamine based on molecularly imprinted sol–gel film, *Analytica Chimica Acta*, 651 (2009) 209.

[27] M.C. Hacıfazlıoğlu, I. Parlar, T.Ö. Pek, N. Kabay, Evaluation of chemical cleaning to control fouling on nanofiltration and reverse osmosis membranes after desalination of MBR effluent, *Desalination*, 466 (2019) 44.

[28] G. Lux, A. Langer, M. Pschenitza, X. Karsunke, R. Strasser, R. Niessner, *et al.*, Detection of the carcinogenic water pollutant benzo [a] pyrene with an electro-switchable biosurface, *Analytical Chemistry*, 87 (2015) 4538.

[29] F. Edition, Guidelines for drinking-water quality, *WHO chronicle*, 38 (2011) 104.

[30] M.R. Kulkarni, T. Revanth, A. Acharya, P. Bhat, Removal of Crystal Violet dye from aqueous solution using water hyacinth: Equilibrium, kinetics and thermodynamics study, *Resource-Efficient Technologies*, 3 (2017) 71.

[31] I. Šafařík, M. Šafaříková, Detection of low concentrations of malachite green and crystal violet in water, *Water Research*, 36 (2002) 196.

[32] S. Wei, H. Zhang, S. Tao, A review of arsenic exposure and lung cancer, *Toxicology Research*, 8 (2019) 319.

[33] V.D. Martinez, E.A. Vucic, D.D. Becker-Santos, L. Gil, W.L. Lam, Arsenic exposure and the induction of human cancers, *Journal of Toxicology*, 2011 (2011) 431287.

[34] W.G. Burgess, M.A. Hoque, H.A. Michael, C.I. Voss, G.N. Breit, K.M. Ahmed, Vulnerability of deep groundwater in the Bengal Aquifer system to contamination by arsenic, *Nature Geoscience*, 3 (2010) 83.

[35] M. Amini, K.C. Abbaspour, M. Berg, L. Winkel, S.J. Hug, E. Hoehn, *et al.*, Statistical modeling of global geogenic arsenic contamination in groundwater, *Environmental Science & Technology*, 42 (2008) 3669.

[36] K. Henke, Arsenic: Environmental chemistry, health threats and waste treatment, *Environmental Chemistry*, *Wiley*, New Jersey, 2009.

[37] L.L. Arnold, M. Eldan, A. Nyska, M. van Gemert, S.M. Cohen, Dimethylarsinic acid: Results of chronic toxicity/oncogenicity studies in F344 rats and in B6C3F1 mice, *Toxicology*, 223 (2006) 82.

[38] H.V. Aposhian, M.M. Aposhian, Arsenic toxicology: Five questions, *Chemical Research in Toxicology*, 19 (2006) 1.

[39] S. Shen, X.-F. Li, W.R. Cullen, M. Weinfeld, X.C. Le, Arsenic binding to proteins, *Chemical Reviews*, 113 (2013) 7769.

[40] R.N. Ratnaike, Acute and chronic arsenic toxicity, *Postgraduate Medical Journal*, 79 (2003) 391.

[41] N. Poddar, C. Badilla, S. Maghool, T.H. Osborne, J.M. Santini, M.J. Maher, Structural and functional investigation of the periplasmic arsenate-binding protein ArrX from Chrysiogenes arsenatis, *Biochemistry*, 60 (2021) 465.

[42] A.M. Spuches, H.G. Kruszyna, A.M. Rich, D.E. Wilcox, Thermodynamics of the As(III)−Thiol interaction: Arsenite and monomethylarsenite complexes with glutathione, dihydrolipoic acid, and other thiol ligands, *Inorganic Chemistry*, 44 (2005) 2964.

[43] H.-C. Yang, H.-L. Fu, Y.-F. Lin, B.P. Rosen, Pathways of arsenic uptake and efflux, *Current Topics in Membranes*, 69 (2012) 325.

[44] J. Hernández-Cobos, M.C. Vargas, A. Ramírez-Solís, I. Ortega-Blake, Aqueous solvation of $As(OH)_3$: A Monte Carlo study with flexible polarizable classical interaction potentials, *The Journal of Chemical Physics*, 133 (2010) 114501.

[45] J. Mähler, I. Persson, R.B. Herbert, Hydration of arsenic oxyacid species, *Dalton Transactions*, 42 (2013) 1364.

[46] J. Li, C. Packianathan, T.G. Rossman, B.P. Rosen, Nonsynonymous polymorphisms in the human AS3MT arsenic methylation gene: Implications for arsenic toxicity, *Chemical Research in Toxicology*, 30 (2017) 1481.

[47] L. Ramsay, M.M. Petersen, B. Hansen, J. Schullehner, P. van der Wens, D. Voutchkova, *et al.*, Drinking water criteria for arsenic in high-income, low-dose countries: The effect of legislation on public health, *Environmental Science & Technology*, 55 (2021) 3483.

[48] A.H. Smith, E.O. Lingas, M. Rahman, Contamination of drinking-water by arsenic in Bangladesh: A public health emergency, *Bull World Health Organ*, 78 (2000) 1093.

[49] R. Saha, N.C. Dey, M. Rahman, P. Bhattacharya, G.H. Rabbani, Geogenic arsenic and microbial contamination in drinking water sources: Exposure risks to the coastal population in Bangladesh, *Frontiers in Environmental Science*, 7 (2019) 00057.

[50] S.A. Ahmad, M.H. Khan, M. Haque, Arsenic contamination in groundwater in Bangladesh: Implications and challenges for healthcare policy, *Risk Management and Healthcare Policy*, 11 (2018) 251.

[51] C.M. Steinmaus, C.M. George, D.A. Kalman, A.H. Smith, Evaluation of two new arsenic field test kits capable of detecting arsenic water concentrations close to 10 µg/L, *Environmental Science & Technology*, 40 (2006) 3362.

[52] X. Ge, Y. Ma, X. Song, G. Wang, H. Zhang, Y. Zhang, *et al.*, β-FeOOH Nanorods/Carbon foam-based hierarchically porous monolith for highly effective arsenic removal, *ACS Applied Materials & Interfaces*, 9 (2017) 13480.

[53] M.-K. Ke, G.-X. Huang, S.-C. Mei, Z.-H. Wang, Y.-J. Zhang, T.-W. Hua, *et al.*, Interface-promoted direct oxidation of p-arsanilic acid and removal of total arsenic by the coupling of peroxymonosulfate and Mn-Fe-mixed oxide, *Environmental Science & Technology*, 55 (2021) 7063.

[54] T. Gupte, S.K. Jana, J.S. Mohanty, P. Srikrishnarka, S. Mukherjee, T. Ahuja, *et al.*, Highly sensitive As3+ detection using electrodeposited nanostructured MnOx and phase evolution of the active material during sensing, *ACS Applied Materials & Interfaces*, 11 (2019) 28154.

[55] N.-U.-A. Babar, K.S. Joya, M.A. Tayyab, M.N. Ashiq, M. Sohail, Highly sensitive and selective detection of arsenic using electrogenerated nanotextured gold assemblage, *ACS Omega*, 4 (2019) 13645.
[56] T. Wang, R.D. Milton, S. Abdellaoui, D.P. Hickey, S.D. Minteer, Laccase inhibition by arsenite/arsenate: Determination of inhibition mechanism and preliminary application to a self-powered biosensor, *Analytical Chemistry*, 88 (2016) 3243.
[57] S. Deshmukh, D. Banerjee, G. Bhattacharya, S.J. Fishlock, A. Barman, J. McLaughlin, *et al.*, Red mud-reduced graphene oxide nanocomposites for the electrochemical sensing of arsenic, *ACS Applied Nano Materials*, 3 (2020) 4084.
[58] N. Priyadarshni, P. Nath, Nagahanumaiah, N. Chanda, DMSA-functionalized gold nanorod on paper for colorimetric detection and estimation of arsenic (III and V) contamination in groundwater, *ACS Sustainable Chemistry & Engineering*, 6 (2018) 6264.
[59] L. Zeng, D. Zhou, J. Gong, C. Liu, J. Chen, Highly sensitive aptasensor for trace arsenic(iii) detection using DNAzyme as the biocatalytic amplifier, *Analytical Chemistry*, 91 (2019) 1724.
[60] B.M. Sonkoue, P.M.S. Tchekwagep, C.P. Nanseu-Njiki, E. Ngameni, electrochemical determination of arsenic using silver nanoparticles, *Electroanalysis*, 30 (2018) 2738.
[61] H. Naranmandura, N. Suzuki, K.T. Suzuki, Trivalent arsenicals are bound to proteins during reductive methylation, *Chemical Research in Toxicology*, 19 (2006) 1010.
[62] N.C. Sumedha, S. Miltonprabu, Cardiac mitochondrial oxidative stress and dysfunction induced by arsenic and its amelioration by diallyl trisulphide, *Toxicology Research*, 4 (2015) 291.
[63] R. Jahangirnejad, M. Goudarzi, H. Kalantari, H. Najafzadeh, M. Rezaei, Subcellular organelle toxicity caused by arsenic nanoparticles in isolated rat hepatocytes, *International Journal of Occupational and Environmental Medicine*, 11 (2020) 41.
[64] S.A. Durazo, U.B. Kompella, Functionalized nanosystems for targeted mitochondrial delivery, *Mitochondrion*, 12 (2012) 190.

[65] T.A. Trendeleva, E.I. Sukhanova, A.G. Rogov, R.A. Zvyagilskaya, I.I. Seveina, T.M. Ilyasova, *et al.*, Role of charge screening and delocalization for lipophilic cation permeability of model and mitochondrial membranes, *Mitochondrion*, 13 (2013) 500.
[66] A. Banerjee, S. Singh, R. Ghosh, M.N. Hasan, A. Bera, L. Roy, *et al.*, A portable spectroscopic instrument for multiplexed monitoring of acute water toxicity: Design, testing, and evaluation, *Review of Scientific Instruments*, 93 (2022) 115105.
[67] M. Hmoud Al-Adhaileh, F. Waselallah Alsaade, Modelling and prediction of water quality by using artificial intelligence, *Sustainability*, 13 (2021) 4259.
[68] Y. Wei, Y. Jiao, D. An, D. Li, W. Li, Q. Wei, Review of dissolved oxygen detection technology: From laboratory analysis to online intelligent detection, *Sensors*, 19 (2019) 3995.
[69] A. Halder, D. Shikha, A. Adhikari, R. Ghosh, S. Singh, T. Adhikari, *et al.*, Development of a nano-sensor (fensor) based device for estimation of iron ions in biological and environmental samples, *IEEE Sensors Journal*, 20 (2019) 1268.
[70] A. Halder, S. Singh, A. Adhikari, P. Singh, P.K. Sarkar, U. Pal, *et al.*, Selective and fast responsive sensitized micelle for detection of fluoride level in drinking water, *ACS Sustainable Chemistry & Engineering*, 7 (2019) 16355.
[71] S.S. Pasha, A. Banerjee, S. Sreedharan, S. Singh, N. Kandoth, K.A. Vallis, *et al.*, ultrasensitive reagent for ratiometric detection and detoxification of iAs III in water and mitochondria, *Inorganic Chemistry*, 61 (2022) 13115.
[72] P.K. Sarkar, A. Halder, N. Polley, S.K. Pal, Development of highly selective and efficient prototype sensor for potential application in environmental mercury pollution monitoring, *Water, Air, & Soil Pollution*, 228 (2017) 1.
[73] Z. Liu, F. Luo, T. Chen, Phenolphthalein immobilized membrane for an optical pH sensor, *Analytica Chimica Acta*, 510 (2004) 189.
[74] M. Mansoor, I. Haneef, S. Akhtar, A. De Luca, F. Udrea, Silicon diode temperature sensors—A review of applications, *Sensors and Actuators A: Physical*, 232 (2015) 63.
[75] W.F. Management, Report: Data demand will drive $92 billion in investment by 2030, 2020 (https://waterfm.com/report-data-demand-will-drive-92-billion-in-investment-by-2030/).

[76] FDA, Artificial Intelligence and Machine Learning in Software as a Medical Device (https://www.fda.gov/medical-devices/artificial-intelligence-and-machine-learning-software-medical-device).

[77] Y. Khan, C.S. See, Predicting and analyzing water quality using Machine Learning: A comprehensive model, *2016 IEEE Long Island Systems, Applications and Technology Conference (LISAT)*, *IEEE*, New York, 2016.

[78] Y. Park, K.H. Cho, J. Park, S.M. Cha, J.H. Kim, Development of early-warning protocol for predicting chlorophyll-a concentration using machine learning models in freshwater and estuarine reservoirs, Korea, *Science of the Total Environment*, 502 (2015) 31.

[79] R. Afriyie Mensah, J. Xiao, O. Das, L. Jiang, Q. Xu, M. Okoe Alhassan, Application of adaptive neuro-fuzzy inference system in flammability parameter prediction, *Polymers*, 12 (2020) 122.

[80] D.A. Armbruster, T. Pry, Limit of blank, limit of detection and limit of quantitation, *The Clinical Biochemist Reviews*, 29 (2008) S49.

[81] M. Thompson, S.L. Ellison, R. Wood, Harmonized guidelines for single-laboratory validation of methods of analysis (IUPAC Technical Report), *Pure and Applied Chemistry*, 74 (2002) 835.

[82] B. Magnusson, The fitness for purpose of analytical methods: A laboratory guide to method validation and related topics (2014), *Eurachem*, UK, 2014.

[83] S.S. Pasha, A. Banerjee, S. Sreedharan, S. Singh, N. Kandoth, K.A. Vallis, *et al.*, Ultrasensitive reagent for ratiometric detection and detoxification of iAs III in water and Mitochondria, *Inorganic Chemistry*, 61 (2022) 13115.

[84] T.M. Loehr, R.A. Plane, Raman spectra and structures of arsenious acid and arsenites in aqueous solution, *Inorganic Chemistry*, 7 (1968) 1708.

[85] F. Neve, M. La Deda, A. Crispini, A. Bellusci, F. Puntoriero, S. Campagna, Cationic Cyclometalated Iridium luminophores: Photophysical, redox, and structural characterization, *Organometallics*, 23 (2004) 5856.

[86] Z.-q. Chen, Z.-q. Bian, C.-h. Huang, Functional IrIII complexes and their applications, *Advanced Materials*, 22 (2010) 1534.

[87] B. Happ, A. Winter, M.D. Hager, U.S. Schubert, Photogenerated avenues in macromolecules containing Re(i), Ru(ii), Os(ii), and Ir(iii) metal complexes of pyridine-based ligands, *Chemical Society Reviews*, 41 (2012) 2222.

[88] H. Xu, R. Chen, Q. Sun, W. Lai, Q. Su, W. Huang, *et al.*, Recent progress in metal–organic complexes for optoelectronic applications, *Chemical Society Reviews*, 43 (2014) 3259.

[89] D. Sieh, J. Schöffel, P. Burger, Synthesis of a chloro protected iridium nitrido complex, *Dalton Transactions*, 40 (2011) 9512.

[90] P. Zhao, S. Tofighi, R.M. O'Donnell, J. Shi, P.Y. Zavalij, M.V. Bondar, *et al.*, Electronic nature of new Ir(III) complexes: Linear spectroscopic and nonlinear optical properties, *The Journal of Physical Chemistry C*, 121 (2017) 23609.

[91] Y. You, W. Nam, Photofunctional triplet excited states of cyclometalated Ir(iii) complexes: Beyond electroluminescence, *Chemical Society Reviews*, 41 (2012) 7061.

[92] S. Wu, F. Liang, D. Hu, H. Li, W. Yang, Q. Zhu, Determining the critical micelle concentration of surfactants by a simple and fast titration method, *Analytical Chemistry*, 92 (2020) 4259.

[93] G. La Sorella, G. Strukul, A. Scarso, Recent advances in catalysis in micellar media, *Green Chemistry*, 17 (2015) 644.

[94] Y. Liu, Y. Wang, Y. Wang, J. Lu, V. Piñón, M. Weck, Shell cross-linked micelle-based nanoreactors for the substrate-selective hydrolytic kinetic resolution of epoxides, *Journal of the American Chemical Society*, 133 (2011) 14260.

[95] X. Lang, U. Thumu, L. Yuan, C. Zheng, H. Zhang, L. He, *et al.*, Chemical fuel-driven transient polymeric micelle nanoreactors toward reversible trapping and reaction acceleration, *Chemical Communications*, 57 (2021) 5786.

[96] F. Ali, S. Saha, A. Maity, N. Taye, M.K. Si, E. Suresh, *et al.*, Specific reagent for Cr(III): Imaging cellular uptake of Cr(III) in Hct116 cells and theoretical rationalization, *The Journal of Physical Chemistry B*, 119 (2015) 13018.

[97] C. Lee, J.S. Nam, C.G. Lee, M. Park, C.-M. Yoo, H.-W. Rhee, *et al.*, Analysing the mechanism of mitochondrial oxidation-induced cell death using a multifunctional iridium(III) photosensitiser, *Nature Communications*, 12 (2021) 26.

[98] Y. Ni, L. Zhang, Z. Cheng, X. Zhu, Iodine-mediated reversible-deactivation radical polymerization: A powerful strategy for polymer synthesis, *Polymer Chemistry*, 10 (2019) 2504.

[99] G. Battogtokh, Y.-Y. Cho, J.Y. Lee, H.S. Lee, H.C. Kang, Mitochondrial-targeting anticancer agent conjugates and nanocarrier systems for cancer treatment, *Frontiers in Pharmacology*, 9 (2018) 922.

[100] W.Q. Li, J.Y. Wu, D.X. Xiang, S.L. Luo, X.B. Hu, T.T. Tang, *et al.*, Micelles loaded with puerarin and modified with triphenylphosphonium cation possess mitochondrial targeting and demonstrate enhanced protective effect against isoprenaline-induced H9c2 cells apoptosis, *International Journal of Nanomedicine*, 14 (2019) 8345.

[101] H. Wang, S. Ding, Z. Zhang, L. Wang, Y. You, Cationic micelle: A promising nanocarrier for gene delivery with high transfection efficiency, *The Journal of Genetic Medicine*, 21 (2019) e3101.

[102] E.A. Liberman, V.P. Topaly, L.M. Tsofina, A.A. Jasaitis, V.P. Skulachev, Mechanism of coupling of oxidative phosphorylation and the membrane potential of mitochondria, *Nature*, 222 (1969) 1076.

[103] L. Milane, M. Trivedi, A. Singh, M. Talekar, M. Amiji, Mitochondrial biology, targets, and drug delivery, *Journal of Control Release*, 207 (2015) 40.

[104] S. Behzadi, V. Serpooshan, W. Tao, M.A. Hamaly, M.Y. Alkawareek, E.C. Dreaden, *et al.*, Cellular uptake of nanoparticles: Journey inside the cell, *Chemical Society Reviews*, 46 (2017) 4218.

[105] C. Peetla, S. Jin, J. Weimer, A. Elegbede, V. Labhasetwar, Biomechanics and Thermodynamics of Nanoparticle Interactions with Plasma and Endosomal Membrane Lipids in Cellular Uptake and Endosomal Escape, *Langmuir*, 30 (2014) 7522.

[106] B.H. Kang, J. Plescia, H.Y. Song, M. Meli, G. Colombo, K. Beebe, *et al.*, Combinatorial drug design targeting multiple cancer signaling networks controlled by mitochondrial Hsp90, *The Journal of Clinical Investigation*, 119 (2009) 454.

[107] A. Malek, K. Bera, S. Biswas, G. Perumal, A.K. Das, M. Doble, *et al.*, Development of a next-generation fluorescent turn-on sensor to simultaneously detect and detoxify mercury in living samples, *Analytical Chemistry*, 91 (2019) 3533.

CHAPTER 6

Development of Optical Spectroscopy-based Techniques for Food-quality Assessment

6.1. INTRODUCTION:

Tea, the most widely consumed aromatic, non-alcoholic stimulating beverage in the world [1] is the infusion prepared from the processed leaves of *Camellia Sinensis*. A native plant of southwestern China and eastern India, tea plants are now being harvested in countries like South America, Africa, the Middle East [1] not only for its medicinal values, but also for its substantial export revenue generation. India being the home to world's premium tea, is responsible for 20% of global tea production and has earned INR 5500 crore or 700 million US Dollar through tea export per year [2]. Amongst all the tea variants in India, Darjeeling tea, a special variety of tea grown and produced in the defined area of the Darjeeling District of India, is famous for its distinct aroma and premium quality. To implement and protect the Geographical Indications (GI) of the Darjeeling Tea under Trade-Related Aspects of Intellectual Property Rights (TRIPS Agreement, WTO) [3], a robust identification validity technique of this variety of tea is highly sought after. Usually, GI associates a renowned product with a specific place, corresponding microclimatic environment, and post-processing techniques and hence establishing the authenticity, reputation and goodwill of the product in the market [3]. Despite GI validation, the quality assessment of Darjeeling tea has remained in the primitive stage, with no available automated instrumental validation technique. The existing method for tea identification by tea testers depends solely on a person's sensory skill, and hence it is associated with a higher risk of human errors. It also lacks evidence-based measurement techniques, which could assure the accuracy of tea identification. Furthermore, the economically motivated adulteration (EMA) [4] has become a growing concern all over the world, not only for its economic impact, but primarily because of associated health hazards. It has been predicted that the negative impact of

global food-fraud would cost the food industry about $10-$15 billion a year [4]. The tea industry, being no exception, faces severe damage due to such types of fraudulent activities. The most common adulteration technique is to mix low quality tea with premium quality tea for substantial profit margin [5]. According to the Food Safety and Standards Authority of India (FSSAI), the other hazardous, non-edible adulterations may include artificial colours like, tartrazine, carmoisine and sunset yellow or substances like, saw dust, iron fillings. Considerable amount of efforts have been made in past for tea identification and characterization, most of which involve expensive and laborious processes, for example gas chromatography (GC) [6], mass spectroscopy [7], HPLC [8] or NMR spectroscopy [9]. GC/MS combined with chemometric analysis techniques are still being used in recent times for the identification of the geographic origins of black tea [10]. Yongjiang Dong et. al. [11, 12] adopted an approach to identify Chinese tea variants based upon the principle of fluorescence technique, where they fixed the emission wavelength around 650 nm, which is the signature emission wavelength of chlorophyll as well. Hence, this technique cannot detect any other variety of green leaves in the tea. Another detailed study was reported [13] to characterize the Sri Lankan black teas, employing fluorescence spectroscopy along with the linear discriminant analysis and principal component analysis techniques. But this study would require further precise standardization for quantitative classification of the tea. Near-infrared reflectance (NIR) spectroscopy was also explored to establish a rapid, non-invasive, and non-destructive instrumental technique [14, 15]. Although, this technique was reported to lack adequate sensitivity, accuracy and stability [16]. The main limitation of these laboratory-based research works is the lack of their suitability for the prompt, online detection of tea quality for industrial usage. For a sustainable industrial infrastructure, it is necessary to supervise the whole production line to safeguard the high quality and the desired attributes of a specific tea. Electronic sensor technologies, e.g., electronic nose, tongue and eye-based technologies were also investigated extensively for tea quality evaluation [17-19]. These non-invasive, online sensors generally use metal oxide semiconductor (MOS), electrochemical, quartz crystal microbalance, conducting polymers, amperometry for sensing the quality of tea [20]. In a pioneering

study, Dutta et al used the electronic nose system, to analyse black tea aroma and flavour in different part of production line [17]. Yu et al employed E-nose system for discrimination of LongJing green-teas with different quality grades [18]. MOS sensors based e-nose was used by [19] for black tea quality assessment. The requirement of a high operating temperature (150–400°C) for the MOS sensor array in e-nose, makes it disadvantageous for prompt use of tea sensing [20]. In e-tongue system the electrodes require frequent washing because of adsorption of the components present in the solution on the membrane potential [21, 22]. For an e-eye system, insufficient lighting cause uncertain instrumental resolution and may generate unreliable reports on the quality of tea [23]. Some onsite attempts [24, 25] were made using optical visible and near-infrared (VIS-NIR) reflectance spectroscopy to detect the content of total polyphenols in tea [24], and an in situ monitoring system for measuring the total polyphenols content during tea oxidation [25]. These systems rely heavily on proper algorithm development and are therefore not suitable for monitoring the overall traits of a specialty tea. A comprehensive analysis of the reported tea-sensors and testing methods are given in Table 6.1.

Table 6.1. *A comparative analysis of the reported tea-sensors and testing methods*

Tea type	**Origin**	**Detectable element**	**Name of the sensor**	**Sensing technique**	**Data analysis algorithm**	**Refere -nce**
Green Tea	Shifeng Longjing tea samples, China	Fluorescence spectra	LED based fluorescence correlation spectroscopy	Electronic	Partial Least Square Regression	[12]
Six different comer-cial tea product (oolong,	Black, green and white tea from Vahdam Teas, India; Oolong tea	Processed-tea image	Hyperspectr al imaging camera	Hyper-spectral imaging (HSI)	Principal Component Analysis (PCA), Isometric mapping (ISOMAP), t-	[14]

green, yellow, white, black and Pu-erh)	was from Yamamoto yama, USA; Pu-erh tea from UK				distributed Stochastic Neighbour Embedding (t-SNE), Support Vector Machines (SVMs)	
Black Tea	Assam, India	Volatile organic compounds (VOC)	Electronic-nose	Electronic	Self-organizing map (SOM) method, Radial Basis Function (RBF) network and Probabilistic Neural Network (PNN)	[17]
Black Tea	Vellore, India	Polyphenols	6B pencil lead	Electro-chemical	Linear regression and standard addition approach	[26]
Black Tea	Darjeeling Tea Research and Developme nt Centre (DTR&DC), Kurseong	Geraniol, VOC	Quartz Crystal Microbalance Sensor	Electronic	Plot Correlation Factor	[27]
Green Tea	China	Grade of green tea by detecting Volatile organic	Colorimetric sensor array-based artificial olfactory	Electronic	Principal Component Analysis (PCA), Back Propagation	[28]

		compounds (VOC)	system (E-nose)		Artificial Neural Network (BP-ANN)	
Green Tea	China	Total polyphenols	array of seven chemical sensors with Ag/AgCl reference electrode and organic material coated silicon transistor sensors	Chemical	Principal component analysis (PCA)-artificial neural network (ANN) model	[29]
Oolong Tea, Black Tea, Green tea, Scented tea	Chongqing, China	Amino acids	Colorimetric indicator displacement assays (IDA) sensor	Chemical	Hierarchy Cluster Analysis (HCA) & Principal Component Analysis (PCA)	[30]
Black Tea	Huoshan County, Anhui Province, China	Polyphenol and catechin	Smartphone-based miniature NIR spectrometry and image processing	Optical	linear partial least squares (PLS)	[31]
Green Tea	Mee Tea and Yellow Mountain Fuzz Tip	Polyphenols	Color sensitive sensor	Optical	Extreme learning machine (ELM), Ant colony	[32]

					optimization (ACO) algorithm	
Semi-fermented Oolong (SFO) Teas and Unfermented Green Tea (UGT)	SFO - (Gong-mei (GM), Da-hong-pao (DHP), Tie-guan-yin (TGY), Bai-mu-dan (BMD), Gui-hua-wu-long (GHWL) UGT - (Piao-xue (PX), Mao-feng (MF), Zhu-ye-qing (ZYQ), Longjing (LJ)	Six tea polyphenols, including EC, GA, EGC, ECG, MG and EGCG	Indicators Displacement Assay (IDA) based optical colorimetric sensor array	Optical	Unsupervised Hierarchical Cluster Analysis (HCA), supervised Partial Least-Squares Discriminant Analysis (PLS-DA)	[33]
Green Tea	China	Green tea aroma during fixation procedure and image formation with machine vision	Electronic nose and Machine vision	Electronic and optical	Adaptive fuzzy logic control	[34]
Black Tea	Gengxiang Organic Tea Co.,	Volatile organic	colorimetric sensor	Chemical, optical	K-Nearest Neighbour and	[35]

	Ltd (Wuyi, Zhejiang), China	compounds [VOCs] occurred during black tea fermentation	array-based artificial olfaction system		adaptive boosting, namely KNN-AdaBoost,	
Green Tea	Damin Foodstuff Co., Ltd	Polyphenols	Optical sensors system	Chemical, optical	Partial Least-Squares (PLS) models along with Si-PLS, GA or CARS, correlation coefficient of calibration set (Rc), root mean square error of cross validation (RMSECV), correlation coefficient of prediction (Rp) and root mean square error of prediction (RMSEP)	[24]
Black Tea	Sunriver Keemun Black Tea Co., Ltd., and Yunnan Dianhong Group Co., Ltd., China	Aroma quality	A lab-made color sensitive sensor array with eleven porphyrins and one pH indicator for data	Chemical, optical	Back propagation neural network (BPNN) and Particle swarm optimization (PSO) algorithm	[36]

			acquisition and color components extraction.			
Black Tea	Xiang Yuan Tea Factory (Jinzhai County, Lu 'an City, Anhui Province), China	Aroma capture	High-sensitivity hyperspectral coupled self-assembled nanoporphyrin Sensor along with computer vision systems (CVS) and hyperspectral imaging systems (HSI)	Chemical, optical	Principal component analysis (PCA) and hierarchical cluster analysis (HCA)	[37]
Green Tea	Tea leaves Zhongcha108 and Longjing43 from Fuyang Tea Factory, Hangzhou, Zhejiang Province, China	Catechin, gallic acid, polyphenol and caffeine contents of green tea	The foliar Vis-NIR spectra, recorded in the reflectance mode	Optical	Principal Component Analysis (PCA)	[38]

Although, the above-mentioned studies have used several effective tea-testing mechanisms, but a compact, field-deployable prototype which could analyse the

quality of tea in real-time is yet to be available in the market. In this context, developing an inexpensive, portable, field-deployable instrument for detection, validation and quality control of tea is essential. The present study aims to cater the need for a sustainable tea-industry, where a unique, novel, highly sensitive device would not only efficiently measure, analyse and identify the specific spectral signature of tea variants, e.g. Darjeeling tea, Assam tea and Nepal tea, but also would be able to detect the seasonal variation (first flash/autumn flash etc.) from a particular garden and adulteration in tea samples. After performing the photophysical studies associated with the working principle of the prototype, the development and validation of the device were attempted. The fluorescence quantum yield (QY) along with absorbance was found to be a unique marker for individual pure tea variant which resemble significantly with the spectroscopic signature of the biomarker quercetin produced from rutin upon enzymatic activity of β-glucosidase. The device utilizes the distinct difference in 360 nm absorbance peak and fluorescent quantum yield at 450 nm (λ_{ex}=360 nm) to precisely identify not only the attributes of the Darjeeling tea over the other variants of tea, but also the potential tea adulteration, seasonal variation, shelf life and health benefits of tea extracts. The precision and accuracy of the instrument have proven to be high enough to distinguish the variation in the quality of the Darjeeling tea among various tea gardens under the same GI by virtue of implemented machine learning algorithm associated with multivariate analysis. This cost-efficient device has a huge potential to serve as a smart spectroscopic sensor for detection of the adulterations in tea. The apparatus has also proven its capability to detect the possible health benefits of tea additives e.g. milk, sugar etc, on the quality of tea in terms of anti-oxidant property. The simple user interface and almost zero maintenance cost of the device will make it useful and attractive to minimally trained manpower at low resource setting. To analyse the role of tea as a healthy beverage, the quercetin-protein interaction was also reported in detail using computational biology.

In another work, the interaction of chlorophyll with artificial colourants in restricted nanoscopic environment was explored to find the key insights on the toxicity from electronic spectroscopy. The protective role of fruits and vegetables

consumption against chronic lifestyle diseases, like cancer and cardiovascular disease has been established quite a few decades back in several studies [39-42]. The potential defensive mechanism of fruits and vegetables are strongly associated with their constituents, namely, antioxidants, vitamins, pigments like chlorophylls, flavonoids etc [43]. However, in recent decades, adulteration of food items, especially in vegetables, fruits, spices, and beverages has become a major concern to public health. According to the U.S. Food and Drug Administration (FDA), the main incentive behind the irresponsible adulteration is financial gain, known as economically motivated adulteration (EMA). In EMA, the actual components and ingredients of foods are either deliberately substituted by some cheaper products, or its real appearance gets more attractive and fresher by external modifications [44]. Before reaching to the consumer, an untrusted entity can cause adulteration of food at any of the stages of growth, processing, transportation, and supply of food by multiple entities in the delivery chain [45]. Human health is food-sensitive, and thus acute or chronic exposure to adulterated products can have a long-term adverse health impact. Adulterated food consumption is directly associated to major health risks such as liver, vision, skin, and stomach disorders [46]. To make the appearance of fruits and vegetables more fresh, dangerous industrial dyes, like sudan dyes I-IV, metanil yellow, malachite green, copper sulphate, rhodamine B are often used, which can create severe damage to public health in the long run [47]. Additionally, there are evidence that the dye additives cause genotoxicity, carcinogenicity and hypersensitivity [48]. Among common inedible and harmful chemical dyes used to make vegetables look fresh and vibrant [47], for the current work, three widely-used dyes were chosen viz., copper sulphate, malachite green, and sudan red to study their interactions with chlorophyll. Copper sulphate, a toxic chemical known for its ability to affect liver [49] is widely used in food industry for its re-greening properties on vegetables. $CuSO_4$ is toxic for humans if an amount of >1 gm is ingested [50], with symptoms ranging from mild nausea to severe gastrointestinal infections along with other disorders [51]. On the other hand, copper is a common non-biodegradable heavy metal which can accumulate in soils for a long period of time due to anthropogenic activity such as the use of chemical fertilizers, adulterant dyes, sewage, industrial and

smelting wastes [52], and can be taken up by the root system of plants via diffusion, endocytosis or metal transporters [53-64]. Although Cu is an important micronutrient that constitute plastocyanin and cytochrome oxidase essential for photosynthesis and respiration which have a crucial function in plant carbon assimilation and ATP generation [65, 66] excessive levels of Cu intake in plants can lead to oxidative stress that causes severe damage to membranes and macromolecules, as well as having a severe negative impact on many metabolic pathways [67]. Cu-stressed plants exhibit a variety of visible symptoms, including chlorosis, stunted development, ion leakage and reduced growth of roots [68]. Thus, elaborate study of the interaction of copper and its compounds with chlorophyll is essential to explore the potential risks for plants and animals. To enhance the freshness and appearance of green vegetables like gourds, peas and beans [69], malachite green is also used, which acts as a tumour promoter, by inducing the formation of reactive oxygen species [70]. Malachite Green (MG) is a triphenylmethane dye, is a multiple use compound that is mainly used in textile industries and partly used in aquaculture in fungicides and ectoparasiticides [71, 72]. It also possesses carcinogenic and genotoxic properties which pose a potential risk to humans and therefore, this dye has been banned in Europe, the USA and several countries [71]. Therefore, on the other hand, the MG dye in water may be accumulated in plant tissue and inhibit growth of the plants [73, 74]. Use of the sudan dyes was also reported to pose serious threat, as its excessive use may lead to liver cancer like severe diseases [75]. Animal studies have already predicted the neurotoxic and hepatotoxic nature of metanil yellow [76]. The detailed interaction of Chlorophyll with the harmful dyes, viz, copper sulphate, malachite green and sudan red III are studied in the current study using absorption and emission spectroscopy along with Time-Correlated Single Photon Counting (TCSPC) technique. The dyes may directly interact with the chlorophyll of fruits and vegetables, either by unethical fraudulent practices of adulteration to keep them fresh, or through intake of dye contaminated soils with industrial or agricultural effluents through the root of plants. In plants, chlorophylls are not freely available, they are encapsulated in granum. To create the similar restrictive nanoscopic environment in our study, Sodium Dodecyl Sulfate (SDS) micelles was used, which, like granum, confine the chlorophyll. To establish the

harmful effects of these dangerous dyes at the molecular level, computational biology technique was also employed in this study.

6.2. RESULT AND DISCUSSION:

6.2.1. Spectroscopic Studies on a Natural Biomarker for the Identification of Origin and Quality of Tea Extracts for the Development of a Portable and Field Deployable Prototype [77]:

6.2.1.1. Collection of Tea Samples and Preparation for Testing:

74 tea samples from various sources or tea gardens were examined for the current study, of which 25 samples were of the Darjeeling variety, 32 samples were of the Assam variety, and 17 samples were of the Nepal type. The samples of distinct geographical location of tea gardens were collected following standard procedure reported in literature [78]. The latitude and longitude of each tea garden have also been provided in details in Table 6.2. in order to reveal the idea regarding the microclimatic environments associated with the GI. All the samples were collected during August 2016 to March 2019. The samples were dried in an electric blast drying oven (WGLL-230BE, FAITHFUL Instrument, Hebei, Co., Ltd) at 80°C until they reached a constant weight. The dry samples were crushed and put through a 60 Tyler mesh sieve. Before further examination, the tea powder was sealed in a self-sealing bag and preserved at -20°C.

Table 6.2. *List of tea samples tested in this study and their geographical indices*

SL. NO.	Sample code of tea garden	Latitude and longitude of tea garden	Region	Type
1	A1	26.5869, 93.3602	Assam	Organic tea
2	A2	26.6538, 94.1232	Assam	Black tea
3	A3	27.1514, 95.3518	Assam	Black tea
4	A4	26.7940, 94.2800	Assam	Black tea
5	A5	26.5780, 93.8202	Assam	Black tea
6	A6	28.5998, 98.8365	Assam	Organic tea

7	A7	26.6241, 93.8443	Assam	Black tea
8	A8	26.8330, 94.6990	Assam	Black tea
9	A9	27.2208, 95.1331	Assam	Black tea
10	A10	26.6538, 94.1232	Assam	Black tea
11	A11	27.2540, 95.3769	Assam	Black tea
12	A12	26.4994, 93.9187	Assam	Black tea
13	A13	26.7361, 94.3885	Assam	Black tea
14	A14	25.9211, 93.7162	Assam	Black tea
15	A15	26.7767, 93.2741	Assam	Black tea
16	A16	26.6871, 94.3979	Assam	Black tea
17	A17	26.7736, 94.3927	Assam	Black tea
18	A18	27.4412, 94.8754	Assam	Black tea
19	A19	27.1945, 95.0310	Assam	Black tea
20	A20	26.9495, 93.0898	Assam	Black tea
21	A21	26.7966, 94.6916	Assam	Leaf tea
22	A22	27.0736, 95.0121	Assam	Black tea
23	A23	26.61225, 94.2700	Assam	Black tea
24	A24	26.6862, 94.2851	Assam	Black tea
25	A25	26.6488, 94.3608	Assam	Black tea
26	D1	27.1027, 88.2661	Darjeeling	Black tea
27	D2	26.8658, 88.2769	Darjeeling	Black tea
28	D3	27.0948, 88.2992	Darjeeling	Black tea
29	D4	27.0597, 88.2590	Darjeeling	Black tea
30	D5	26.9271, 88.1691	Darjeeling	Black tea
31	D6	26.8271, 88.2590	Darjeeling	Black tea
32	D7	26.9526, 88.7296	Darjeeling	Black tea
33	D8	26.8754, 88.3006	Darjeeling	Black tea
34	D9	26.9762, 88.2350	Darjeeling	Black tea
35	D10	27.0415, 88.1841	Darjeeling	Black tea
36	D11	27.0137, 88.3701	Darjeeling	Green tea

37	D12	26.8395, 88.3206	Darjeeling	Black tea
38	D13	26.9007, 88.3227	Darjeeling	Black tea
39	D14	26.86983, 88.2633	Darjeeling	Black tea
40	D15	26.8465, 88.2026	Darjeeling	Black tea
41	D16	26.8587, 88.3217	Darjeeling	Black tea
42	D17	27.0927, 88.3668	Darjeeling	Black tea
43	D18	27.0425, 88.1984	Darjeeling	Black tea
44	D19	26.9335, 88.2313	Darjeeling	Black tea
45	D20	26.9401, 88.2037	Darjeeling	Black tea
46	D21	26.9174, 88.2084	Darjeeling	Black tea
47	D22	26.9493, 88.2538	Darjeeling	Black tea
48	D23	27.0378, 88.2762	Darjeeling	Black tea
49	D24	27.2006, 88.1684	Darjeeling	Black tea
50	D25	26.9861, 88.1966	Darjeeling	Black tea
51	D26	27.05860, 88.6509	Darjeeling	Black tea
52	D27	26.8795, 88.2116	Darjeeling	Black tea
53	D28	26.9446, 88.3187	Darjeeling	Black tea
54	D29	26.910, 88.1926	Darjeeling	Black tea
55	D28	27.0948, 88.2593	Darjeeling	Black tea
56	D29	26.9610, 88.7089	Darjeeling	Black tea
57	N1	26.9785, 87.9218	Nepal	Organic tea
58	N2	27.8009, 85.4821	Nepal	White tea
59	N3	26.9201, 87.8578	Nepal	Black tea
60	N4	26.9083, 87.8405	Nepal	Black tea
61	N5	27.0190, 87.3170	Nepal	Black tea
62	N6	26.9113, 87.9236	Nepal	Black tea
63	N7	27.9926, 85.0869	Nepal	Green tea
64	N8	26.5441, 87.9583	Nepal	Black tea
65	N9	27.0184, 88.3737	Nepal	Black tea
66	N10	26.9259, 87.8576	Nepal	Black tea

67	N11	27.1339, 87.7743	Nepal	Black tea
68	N12	26.5174, 87.9493	Nepal	Black tea
69	N13	26.6570, 87.6655	Nepal	Leaf tea
70	N14	26.8724, 88.1402	Nepal	Green tea
71	N15	26.9194, 87.8585	Nepal	Black tea
72	N16	26.9224, 87.9248	Nepal	Black tea
73	N17	26.6488, 88.0139	Nepal	Black tea
74	N18	26.5051, 87.8544	Nepal	Black tea

10 milligrams of each tea sample were boiled with 100 ml of double distilled water (concentration 10 mg/ml) at 80°C under continuous stirring for 1 hour. After extraction the aqueous extract was filtered through whatman filter papers and the filtrate was collected.

6.2.1.2. Photophysical Studies:

In the initial photophysical studies, some of the tea variants from east part of Himalayan region, India, were analyzed employing their spectral signature. Figure 6.1.a depicts the absorbance, excitation and emission of the biomarker quercetin measured in standard instruments. Figure 6.1.b highlights the mechanism of conversion of rutin to quercetin and other flavouring molecules by the activity of β-glucosidase enzyme. Figure 6.1.c shows the absorbance and fluorescence spectra (λ_{ex} = 360 nm) of different tea extracts, i.e, Darjeeling, Nepal and Assam tea in a standard instrument as mentioned in Chapter 3 (section 3.1.1). Here, all the measurements were carried out at room temperature (27 °C). Fluorescence quantum yields of different tea variants were calculated using the following equation with quercetin as a reference [79, 80]:

$$QY = QY_{ref}\frac{\eta^2}{\eta_{ref}^2}\frac{I}{A}\frac{A_{ref}}{I_{ref}} \quad (6.1)$$

where, 'QY_{ref}' is the quantum yield of the reference compound, 'η' is the refractive index of the solvent, 'I' is the integrated fluorescence intensity and 'A' is the absorbance at the excitation wavelength 360 nm. The resemblance of quercetin's

spectral signatures with that of the tea variants are conspicuously revealed in Figure 6.1.a and Figure 6.1.c From the spectra, fluorescence quantum yields were calculated for Darjeeling, Nepal and Assam tea variants using the equation 6.1 and quercetin was considered as a reference. Figure 6.1.d clearly indicates the distinct difference in absorbance normalized fluorescence intensity as well as quantum yield (Figure 6.1.d inset) for the three tea variants.

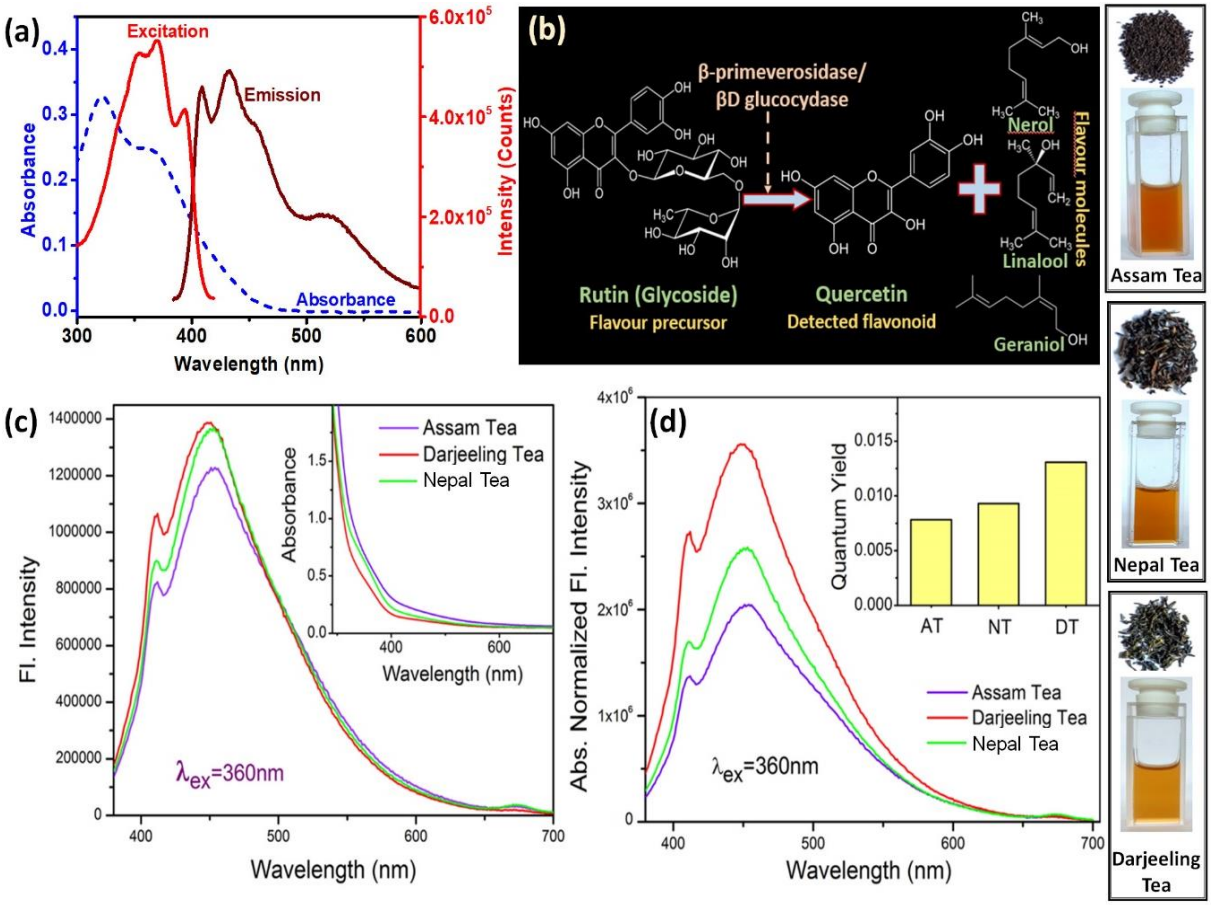

Figure 6.1. *(a) The absorbance, excitation and emission (for excitation at 360 nm) spectra of the biomarker quercetin (b) Conversion of rutin present in tea samples into quercetin and other flavoring molecules in presence of β-primeverosidase enzyme (c) Fluorescence and absorbance (inset) spectra for excitation at 360 nm of Assam, Darjeeling and Nepal tea extracts (d) Comparison of fluorescence spectra after absorbance normalization and quantum yield (inset) of three tea variants (Assam, Darjeeling and Nepal tea).*

From the Figure 6.1.c and 6.1.d, the distinct differences in the 360 nm absorbance peak and corresponding fluorescent quantum yield at 450 nm (λ_{ex}=360 nm) among different tea varieties are evident. Thus in principle, the quality of Darjeeling tea can also be estimated from the quantum yield. Considering the unique spectroscopic signatures

in terms of fluorescent quantum yield and absorbance for individual tea variant, a prototype is further developed for monitoring tea quality. In our study, the spectroscopic signature of tea, in the region of interest exactly resembles that of quercetin (absorption peak at 360 nm; and emission maxima, λ_{em} at 450 nm, when λ_{ex}=360 nm), a co-product during aroma formation of tea by the activity of β-glycosidase or β-primeverosidase. The quercetin in the extract comes from precursor molecule, rutin (a primeveroside) which is one of the aroma precursors of tea. The experimental procedure does not include direct spectroscopy of the leaf or any plant tissue of the *Camellia Sinensis* variety. Rather we have extracted the substrate rutin from tea leaves which is converted to quercetin upon the enzymatic activity of β-glucosidase. The spectroscopic studies of quercetin are performed in the study. The activity of β-glycosidase or β-primeverosidase increases with temperature, as it is a thermolabile enzyme. We have optimized the preparation of tea sample boiling at 80°C for 1 hour to get the maximum activity of β-primeverosidase along with the complete conversion of rutin to quercetin. The conversion mechanism is depicted in Figure 6.1.c. Floral tea aroma is one of the most important factors to determine the character and quality of each variety of tea, and Darjeeling tea is well known for its flavour. Previous studies demonstrated that the fresh tea leaves are virtually odourless or slightly smells of green note, and endogenous enzymes (β-glycosidase or β-primeverosidase) synthesise the majority of floral aroma compounds during tea preparation [81]. The enzyme β-primeverosidase catalyzes the hydrolysis of different kind of disaccharide β-primeverosides to release a primeverose unit and various aroma compounds (2-phenylethanol, benzyl alcohol, geraniol, nerol, methyl salicylate, cis-linalool 3,7-oxide, linalool, cis-linalool 3,6-oxide, trans-linalool 3,6-oxide, and (Z)-3-hexenol etc.) by a retaining mechanism but does not sequentially hydrolyse β-primeverosides to monosaccharide units [81, 82]. It is clear from previous studies on fundamental biochemical processes of tea aroma formation that the amount of rutin formed is proportional to the amount of aroma compounds converted [83]. Thus, Darjeeling tea having high aroma compounds, has the highest amount of rutin, which is reflected in higher fluorescence quantum yield in our study making it distinctly different from the other tea variants. The device has been developed based

on the findings of the primary photophysical studies which is capable to distinguish among different tea samples according to their characteristic spectroscopic features.

6.2.1.3. Instrumentation:

In the present study, we have developed a spectroscopy based affordable, easy to use device and technique for quick validation of the Darjeeling Tea. The schematic diagram of the proposed device is depicted in Figure 6.2.a. The developed prototype primarily is constructed in two sections, optical and electronic. The upper optical chamber comprises of a customized square cuvette holder mounted internally surrounded by three light sources and one spectrometer detector as shown in Figure 6.1.b. A white LED source (DC 3V, 20 mA, 400-700 nm) is positioned at 180° with respect to the micro-spectrophotometer (Hamamatsu C12880ma) for measuring absorbance of samples placed inside the cuvette holder. One UV LED (wavelength 365 nm, DC 3V, 500 mA) and one LASER source (wavelength 667 nm (5V, 5mW)) are placed at 90° angle of the spectrometer for taking care of the fluorescence and scattering measurements. The micro-spectrometer is mounted directly on defined pins of a micro-controller (Arduino UNO) board that dictates the automatic data acquisition (DAQ) and visualization of the acquired spectra. The UNO board along with all light sources are controlled from the lower electronic chamber by wire connections passing down through designated slots in the base plate of the upper compartment. The micro-spectrometer used in this study for developing the prototype costed ~220USD. However, the installation charges are one time and testing of numerous tea samples can be performed in almost zero cost along with zero maintenance costing for the device.

The heart of the lower electronic section is a computing device (intel NUC 8i3BEH). Along with this mini-PC another micro-controller (Arduino UNO) boards and a rechargeable battery for power supply are other important components in the chamber. The frontside of the instrument contains a slanting touchscreen LCD display (7 inch, Waveshare) (Figure 6.1.b) for showing results. Proper cooling arrangements (cooling fans,5V DC) are incorporated in this section also for elimination of heating effects from different components. The second micro-controller board is for the

controlling the light sources. The switching chronology, automatic intensity adjustments by PWM (Pulse Width Modulation), illumination time, etc. are controlled

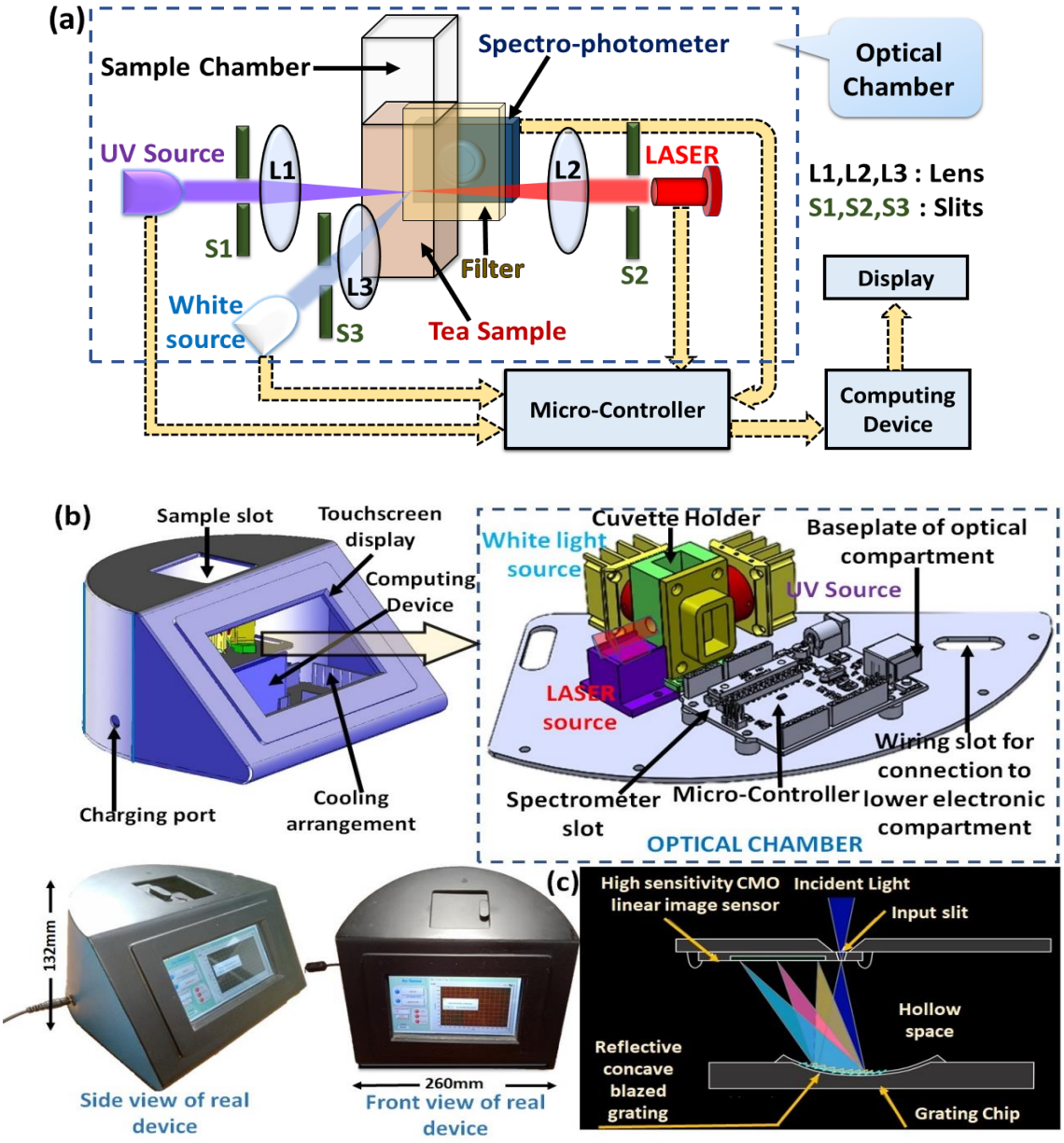

Figure 6.2. *(a) The schematic diagram of the developed instrument. The optical chamber (inside blue dotted rectangle) consists of an UV source and a LASER light source at 90˚ positions to the spectrometer. A white LED source is also positioned at 180˚ to the spectrometer. It has three converging lenses (L1, L2 and L3) positioned in front of the three light sources to focus the light into the sample chamber. The three slits (S1, S2 and S3) are placed in front of the three light sources to modulate the intensity of light incident into the sample chamber. The optical chamber is connected directly to the micro-controller unit, computing device and display. (b) CAD diagram of the foot print of the real proto-type showing the sample slot, touch-screen display, charging spot and the computing device. The zoomed image of the optical chamber shows the design of the cuvette holder, the spectrometer slot and the three windows along the sample chamber for placing light sources. The side view and the front view of the real prototype with physical dimensions are also shown. (c) Schematic diagram of the spectrometer used to show its internal configuration with grating.*

through this Arduino board. The in-built Bluetooth and Wi-Fi modules in the PC take care of the data and report transmission procedures of the light weight, portable and IoT enabled device. The different components of the real prototype and its dimensions are shown in Figure 6.1.b. Figure 6.1.c represents the schematic diagram of the micro-spectrophotometer used.

To operate the device, the entire machine learning algorithm was indigenously developed in LabVIEW platform for automatic data acquisition and visualization of spectra for tea quality and category assessment. Figure 6.3. illustrates the simple sequential program flow diagram of the software.

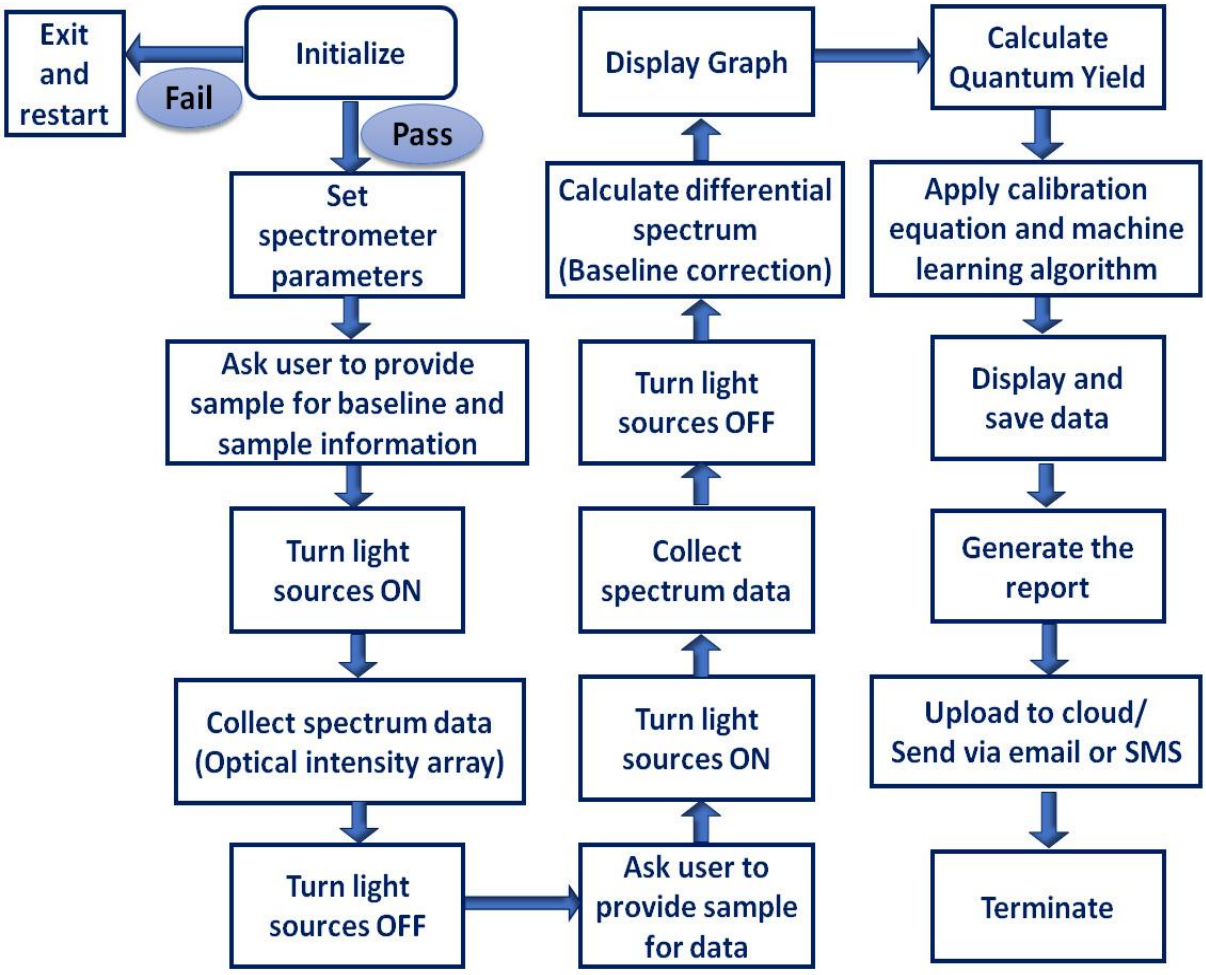

Figure 6.3. *Sequential program flow diagram of the developed device showing the process of initialization followed by setting up the parameters of the spectrometer. After the process of initialization, and taking the baseline data, the QY of the tea sample is calculated based on its absorbance and fluorescence properties. Finally, a report is generated stating the geographical location of the tea sample along with the presence of any adulteration. The data is saved and uploaded to a cloud or sent to the user via email.*

After getting power, the device checks functionality of all sections first in the initialization phase and in case of any discrepancy it corrects them automatically (e.g., tuning light source intensities with PWM under fluctuating current conditions) or restarts. After a proper initialization, a user-friendly interface guides the user to enter sample details like sample name or details, date etc. in a pop-up window which eventually is saved in a separate folder created for the sample along with the data. Then as directed by the GUI, 3ml of water sample is to be placed in cuvette inside the designated cuvette holder slot and click on the 'BASELINE' button in the software for making baseline corrections. After successful baseline correction, the machine directs to "INSERT sample". 300ul tea sample that is to be tested is then to be put in the water already present in the cuvette and touch the "START" option displayed in the screen to start test. The white LED, UV LED and LASER sources are turned ON by the program one by one through micro-controller serial communications and spectrometer captures data as per pre-determined parameters along with integration time of 800 ms. The device algorithm compares the test sample data with pre-loaded data of tea variants from the library and automatically detects deviation if any and displays results in the screen.

6.2.1.4. Distinction of the Variety of Tea:

In the current study, 74 tea samples were analyzed from different sources or gardens among which 25 were Darjeeling variety, 32 were Assam variety and 17 Nepal variety as tabulated in Table 6.2. To get an idea regarding the microclimatic environments associated with the GI, the values of latitude and longitude of each tea garden have also been provided. The principal component analysis (PCA), a well-known unsupervised machine learning (ML) technique [84] was employed to interpret the collected data. As pointed out by Ren et al [78], PCA analysis proven to be a useful statistical tool to establish the geographic source of an agricultural produce. In our study also, it was observed that PCA, which was based on absorption, fluorescence QY, geographical locations like latitude and longitude can detect the spatial variation of the tea samples quite effectively (Figure 6.4.a, b, c). This technique can differentiate between Assam and Darjeeling tea, along with Assam and Nepal tea.

However, this technique did not identify the distinction between Darjeeling and Nepal tea, where the samples (D and N) share almost the same latitude and longitude values (Table 6.2.).

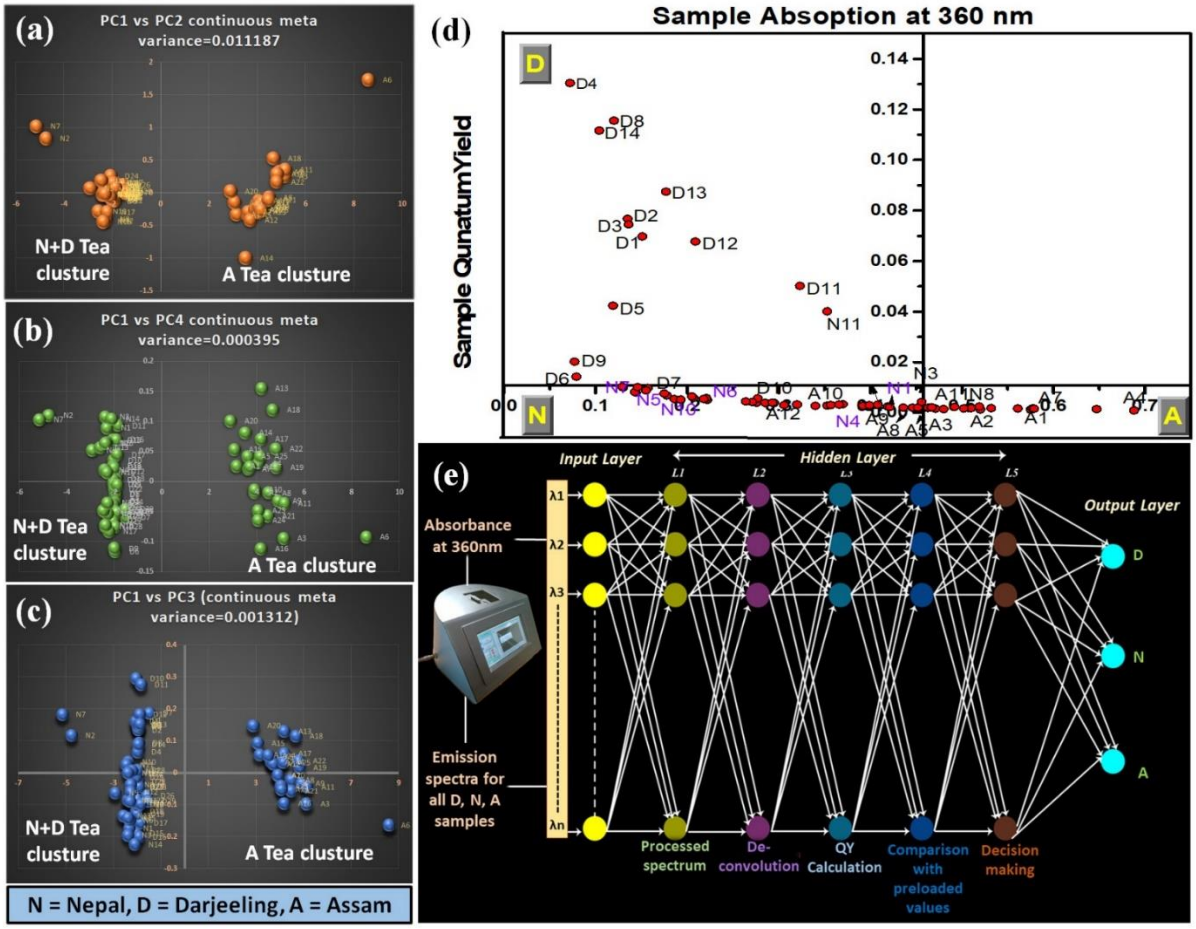

Figure 6.4. *Principal Component Analysis (PCA) (a) PC1 vs PC2 (b) PC1 vs PC3 (c) PC1 vs PC4 (d) Framework for ANN (Artificial Neural Network) to predict tea quality.*

To discretely identify the Nepal and Darjeeling tea samples, famous for their unique aroma, quadrant-analysis technique was employed as depicted in Figure 6.4.d. This technique effectively finds out the characteristic traits of Darjeeling tea, where Darjeeling tea mostly falls in the second quadrant, third quadrant belongs to Nepal tea and fourth one is for Assam tea (DNA quadrant). Our device can also display the quadrant-specific multivariate analysis effectively. It was observed from the Figure 6.4.d that some Darjeeling tea samples are overlapped with Nepal samples. However, Assam samples only fall into the fourth quadrant. Thus, Darjeeling tea has low absorbance with high fluorescence quantum yield, Assam tea has the opposite

property and Nepal tea has low absorbance and low quantum yield. The overlap between Darjeeling and Nepal tea in some areas may be due to the similar microclimatic conditions that may have helped them to possess similar characteristic features. The developed instrument was able to distinguish the variation in quality of Darjeeling Tea among various tea gardens under the same GI of Darjeeling Tea. Generally, it was observed that the high-quality Darjeeling tea variants shows high quantum yield and low absorbance, thus falls in the top-left corner of the second quadrant (Figure 6.4.d) whereas the low-quality ones show high absorbance and low quantum yield.

6.2.1.5. Implementation of Artificial Neural Network (ANN) for Automated Data Analysis:

Artificial-intelligence controlled tea production line for quality monitoring could be easily implemented by integrating the developed prototype with an ANN network (Figure 6.4.d). The data for absorption and emission spectra for all D, N, A samples would be provided in input layer. The emission spectra are deconvoluted and absorption peak value are determined at hidden layer (HL)1. Quantum yield calculations are carried out in HL2. HL3 is responsible for computation of instrument index. Quadrant specific preloaded values compare the dataset with existing values of D, N, A samples, already stored in the algorithm library. This decision-making layer HL4 dictates the identity of the tea samples (D, N, A) along with the presence of adulteration and sample shelf-life.

6.2.1.6. Distinguishment of Darjeeling Tea and Nepal Tea:

The instrument was quite able to distinguish between high quality Darjeeling and Nepal tea, as depicted in Figure 6.5.a, b and c. The Darjeeling tea showed high quantum yield and low absorbance. In comparison, Nepal tea samples showed low quantum yield and low absorbance, and thus has occupied the third quadrant. However, some low-quality Darjeeling tea overlapped with that of Nepal ones. The overlap between Darjeeling and Nepal tea (particularly those that are at the Nepal-Darjeeling border area) may be due to the similar microclimatic conditions that may have helped them to grow similar characteristics.

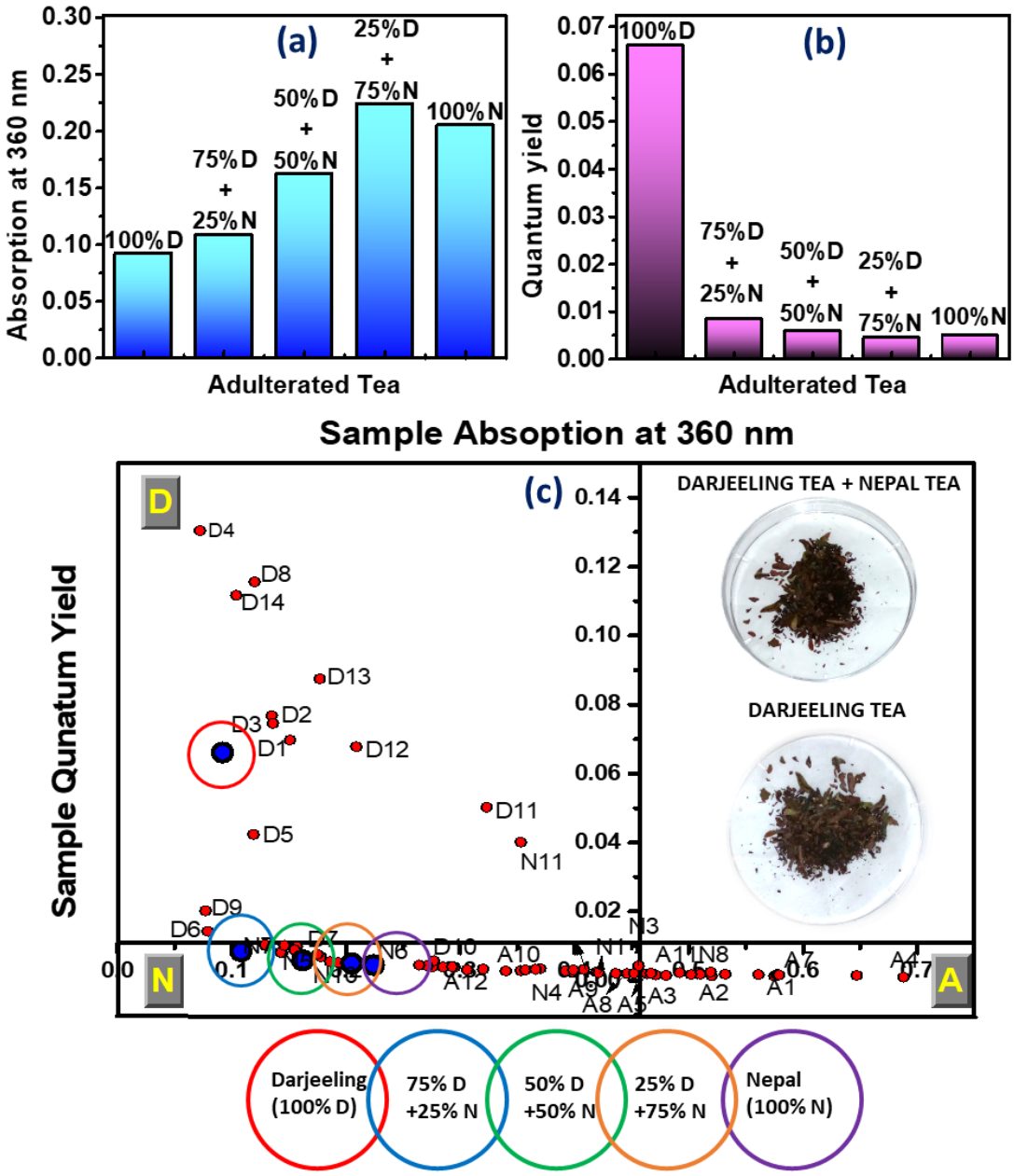

Figure 6.5. *Detection of adulteration in Darjeeling tea with mixing of low-quality tea (a) Variation in absorbance of Darjeeling tea with mixture of different percentages of low-grade Nepal Tea (b) Variation in Quantum Yield of Darjeeling tea with mixture of different percentages of low-grade Nepal Tea (c) Positions of pure Darjeeling tea and adulterated samples in DNA quadrants (Insets show visually indistinguishable samples of pure Darjeeling tea and adulterated Darjeeling tea with low grade Nepal tea).*

6.2.1.7. Detection of Adulteration, Seasonal Variation from a Particular Garden and Shelf Life of Tea:

The tea industry will be benefited immensely as the developed instrument is capable of detecting adulterations in tea, which is a major problem in the tea industry. The instrument was perfectly able to detect adulterations of saw dust in Darjeeling

tea. Saw dust is a well-known non-edible tea adulterant as mentioned in FSSI regulations [85]. Such adulterations are non-emissive and thus cause a decrease in fluorescence of the Darjeeling tea, which reduces the quantum yield or quality which is clearly detected in the developed instrument. Figure 6.6.a shows, how the instrument detected and displayed the adulterations in tea sample which are visually indistinguishable (Inset of Figure 6.6.a).

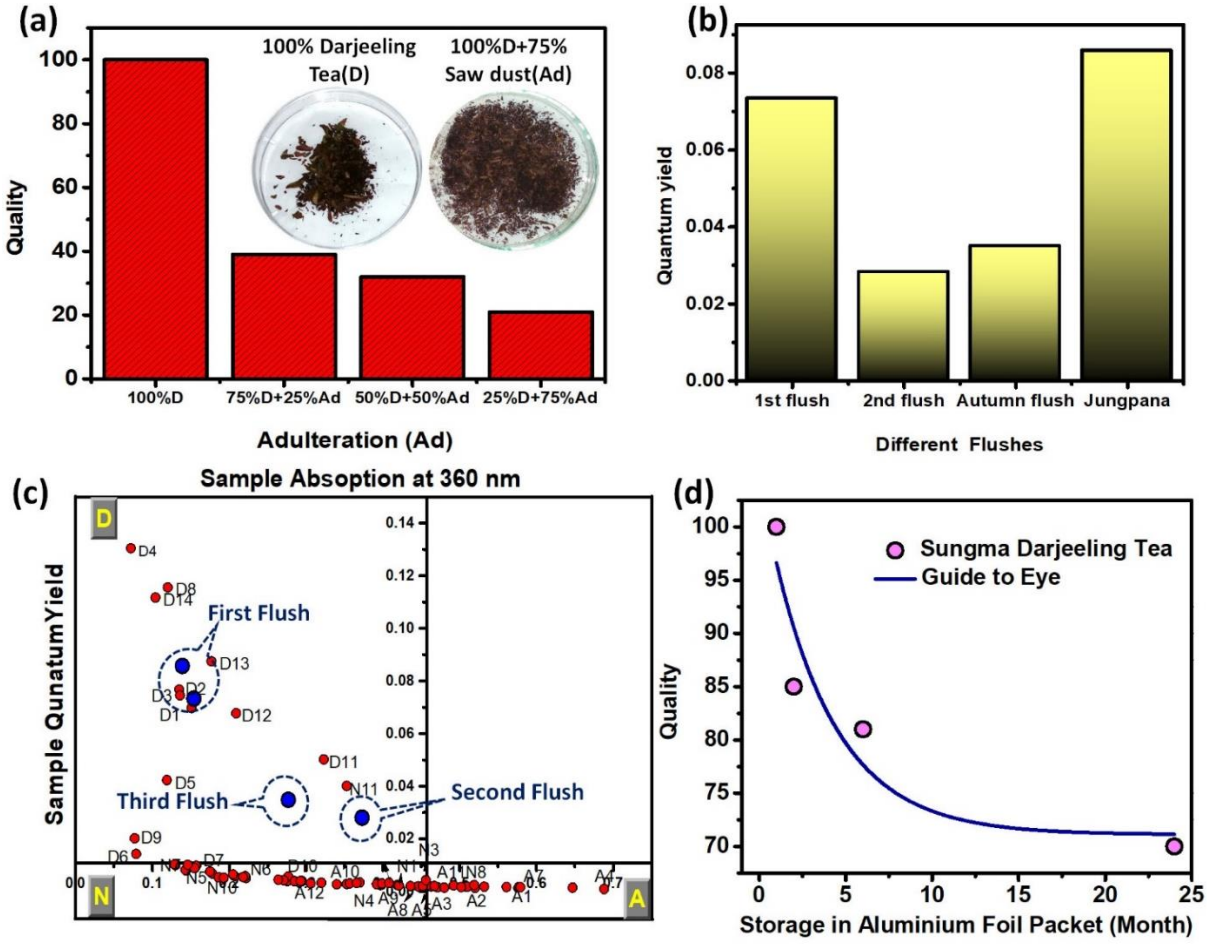

Figure 6.6. *(a) Detection of adulteration with mixing of saw dust (Insets show visually indistinguishable pure and adulterated tea samples) (b) Variation in quantum yield with seasonal variation of Jungpana Darjeeling tea (c) Variation in position on 'D' quadrant for different flushes of tea from a particular garden (d) Effect of shelf life on a Darjeeling tea detected by the developed device (Sungama).*

The instrument was able to detect seasonal variations of a particular tea garden. This is also particularly of great importance for tea industry. Three different flushes viz., first flush, second flush and autumn flush of Darjeeling tea from the Jungpana tea garden were investigated in this study. The results are depicted in Figure 6.6.b and

6.6.c. The quantum yields for the individual flushes were observed to be distinctly different and acquired different positions in the 'D' quadrant. Independent mapping for a single garden with unique GI may enable the device to predict seasonal variations precisely.

The instrument has the capability to detect the shelf life of a finished product (made tea) as revealed in Figure 6.6.d. We have used the Darjeeling tea variant from Sungma tea garden (packed in aluminium foil pack) and monitored it up to 25 months. The fluorescence quantum yield decreased in a time dependent manner as shown in Figure 6.6.d. The apparent reduction in quantum yield may be because of the spontaneous conversion of quercetin present in the tea leaves to various other products like protocatechuic acid, phloroglucinic acid, phlorogucinol etc., which have different spectral characteristics than quercetin.

6.2.1.8. Effects of Tea Additives on Quality of Tea and Quercetin-Protein Interaction Network:

Oxidative stress has been identified as the root cause of the development and progression of several diseases. The supplementation of exogenous antioxidants or boosting endogenous antioxidant defences of the body is a promising way of combating the undesirable effects of reactive oxygen species (ROS) induced oxidative damage. Plants have a natural capacity to attenuate the ROS- induced oxidative damage by using the non-enzymatic antioxidants. Hence, *in vitro* antioxidant activities of the tea samples and the effects of the additives like milk, sugar etc. were studied. The standard DPPH (2,2-diphenyl-1-picrylhydrazyl) free radical scavenging assay method was used to measure the antioxidant potential [86]. DPPH is a well-known radical and a scavenger for other radicals. The violet-coloured solution containing DPPH radicals with absorption peak at 535 nm, becomes colourless or light yellow after neutralization. This is a useful property to get an idea of initial radical numbers by monitoring the reaction mechanism [86]. The tea samples are found to donate a proton/electron to the radical DPPH, eventually reducing the radical to $DPPH_2$ form, revealing decolourization (from violet to yellow) of the medium [87, 88].

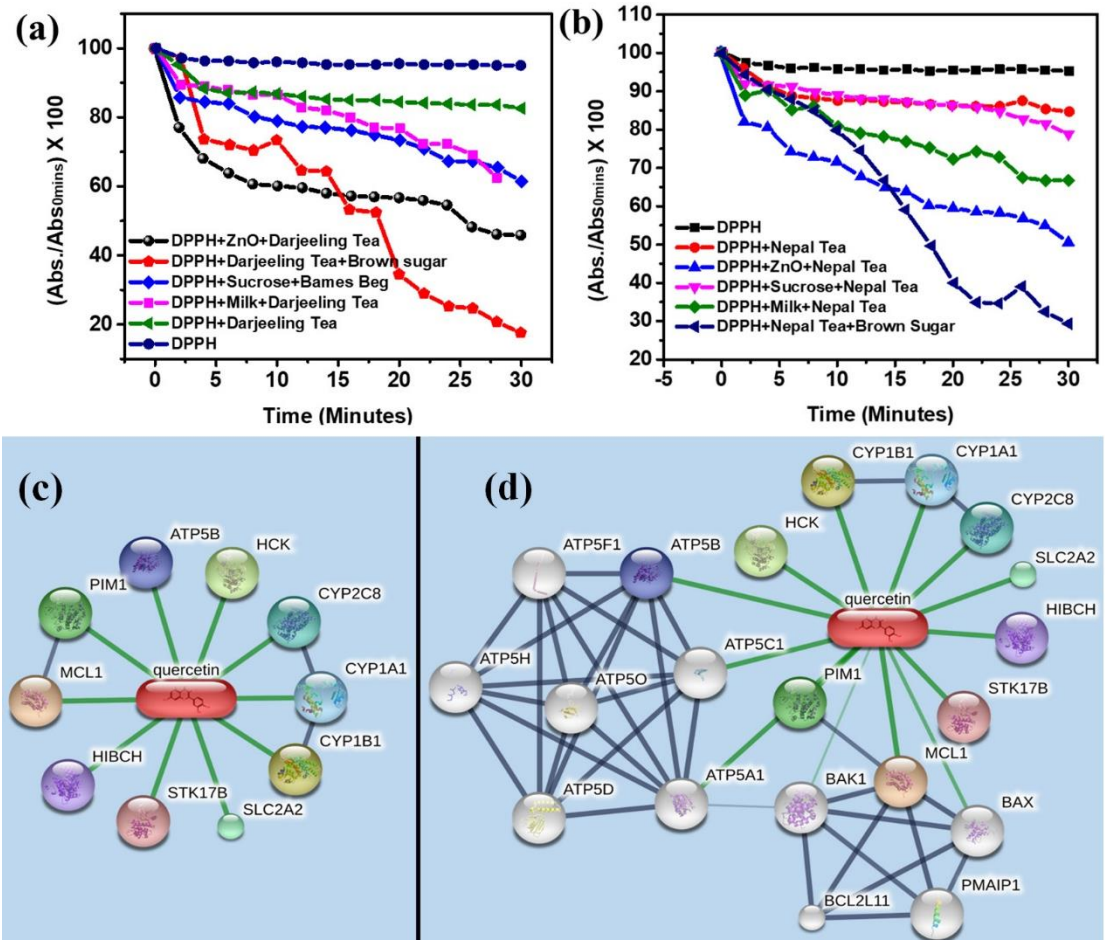

Figure 6.7. *(a) DPPH free radical scavenging activity of Darjeeling tea (Bames Beg) and tea additives (b) DPPH free radical scavenging activity of Nepal tea and tea additives; Quercetin-protein interaction network (c) Primary (d) Secondary.*

The results (Figure 6.7.) show that the Darjeeling tea possesses some amount of free radical scavenging activity. The addition of well-known tea additives like sugar or milk does not significantly alter the antioxidant potential. However, adding brown sugar significantly increases the antioxidant activity (~60% increase; $p<0.05$). This may be due to presence of high amounts of polyphenols in brown sugar which enhance the free radical scavenging property of tea. The ZnO nanoparticle (30 nm), which we have used as an alternative to milk (artificial dairy whitener) for those allergic to milk, also enhances the anti-oxidative property of tea. Similar trends were observed in the case of Nepal teas also (Figure 6.7.b). However, Darjeeling tea has higher antioxidant effect than Nepal tea.

To analyze the impact of quercetin on human health, a detailed network analysis was conducted following the compound-protein interaction mechanism [89]

(Table 6.3.). A comprehensive score output was also generated (Table 6.4.) which describes the scores of individual interactions along with their combined scores considered for this analysis. The combined score was produced according to the method as described by Christian von Mering et al. [89]. Figures 6.7.c and 6.7.d show the primary and secondary interactions of quercetin, respectively.

Table 6.3. *Impact of quercetin on human proteins*

Name of protein/compound	**Mode of action**	**Biological function**
ATP5B	Direct	It was reported that ATP5B plays an essential role in tumour progression and metastasis, especially in case of breast cancer [90].
PIM1	Direct	For prostate cancer, PIM1 acts as a cancer drug target [91].
MCL1	Direct	MCL1 protein is recognised for its anti-apoptotic (apoptic- cell death mechanism, sometimes responsible for cancer growth) activity [92].
HIBCH	Direct	HIBCH deficiency is a rare disorder which shows the symptoms of motor delay, hypotonia, ataxia, dystonia, seizures poor feeding, and organic aciduria [93].
STK17B	Direct	STK17B is upregulated in Hepatocellular carcinoma (HCC), a type of malignancy with very poor prognosis [94].
SLC2A2	Direct	biallelic SLC2A2 mutations may cause Fanconi–Bickel syndrome (FBS) [95].
CYP1B1	Direct	CYP1B1 has been reported to be up-regulated in many types of cancer including renal cell carcinoma [96].

CYP1A1	Direct	CYP1A1 is one of the main enzymes, with the ability to activate compounds with carcinogenic properties. Long term exposure to hazardous chemicals and environmental carcinogens may increase the level of CYP1A1. Surprisingly, CYP1A1 has a crucial cancer preventative role in metabolic activation of dietary compounds [97].
CYP2C8	Direct	CYP2C8 enzyme is responsible for the metabolism of the anti- cancer drug paclitaxel [98].
HCK	Direct	In Mantle cell lymphoma, HCK has been reported to be upregulated in cell lines [99].

Table 6.4. *The score values of various interactions along with combined scores*

node1	**node2**	**Phylogenetic cooccurrence**	**homology**	**Co-expression**	**Experimentally determined interaction**	**Database annotated**	**Automated text mining**	**Combined score**
MCL1	quercetin	0	0	0	0	0.7	0.959	0.987
CYP1B1	quercetin	0	0	0	0.52	0.7	0.838	0.975
HCK	quercetin	0	0	0	0.851	0.8	0	0.969
PIM1	quercetin	0	0	0	0.851	0.8	0	0.969
SLC2A2	quercetin	0	0	0	0	0.7	0.887	0.965
CYP2C8	quercetin	0	0	0	0	0.8	0.826	0.964
CYP1A1	quercetin	0	0	0	0.22	0.7	0.853	0.963
ATP5B	quercetin	0	0	0	0.794	0.8	0.114	0.961
STK17B	quercetin	0	0	0	0.8	0.8	0	0.958
HIBCH	quercetin	0	0	0	0.8	0.8	0	0.958

CYP1A1	CYP2C8	0.527	0.813	0	0	0.9	0.822	0.923
CYP1A1	CYP1B1	0	0.903	0.17 1	0	0.9	0.922	0.921
PIM1	MCL1	0	0	0	0	0	0.835	0.835

6.2.2. Interaction of Chlorophyll with Artificial colorants in Restricted Nanoscopic Environment: Exploration of Toxicity from Electronic Spectroscopy [100]:

For the current work, fresh Neem (*Azadirachta Indica*) leaves (100 gm) were cut into small pieces (approximately 1 cm ×1 cm). The pieces were ground in a mortar (5 mins), 95% Iso-propyl alcohol (IPA) (50 mL) was added and the mixture was homogenized for 3-5 mins or until a light green solution was obtained (Figure 6.8.). The solution was kept overnight and after extraction the solution was filtered through whatman filter papers and the filtrate was collected.

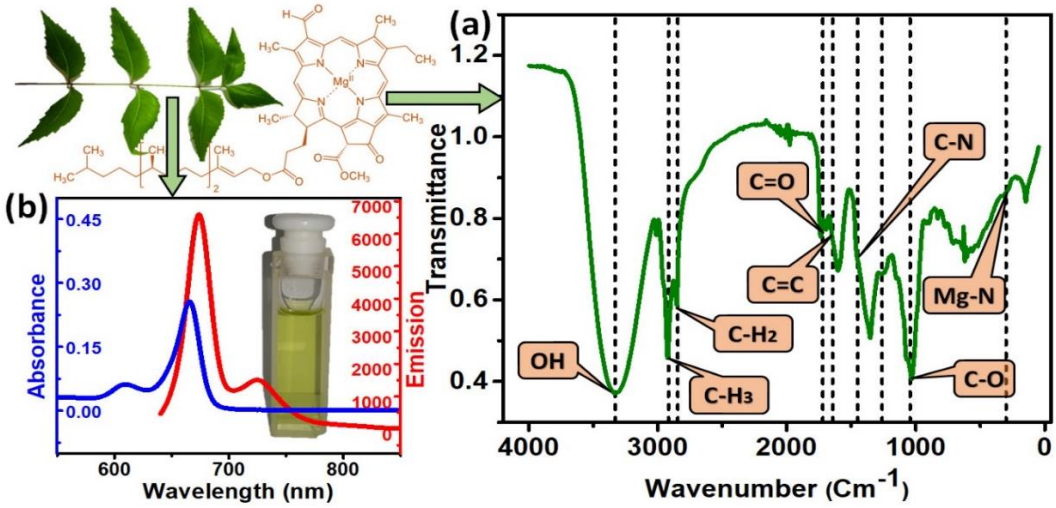

Figure 6.8. *Extraction and characterization of chlorophyll from leaves (a) FTIR spectrum of the extracted chlorophyll in the range 0-4000cm^{-1} (b) Absorbance (blue) and emission (red) spectra of the extracted chlorophyll. The recorded emission is for excitation at the isosbestic point of chlorophyll a and b (629nm). Inset shows the physical appearance of the extracted chlorophyll after filtration.*

FTIR spectra of the extract from leaves in the spectral range of 4000-0 cm^{-1} revealed the presence of chlorophyll as depicted in Figure 6.8.a. As observed from the functional groups of the chlorophyll dye extracted from *Azadirachta Indica* in Figure 6.8.a, the vibrations of C-H_3 and C-H_2 bonds are obtained at 2916.2 cm^{-1} and 2844.7 cm^{-1}[101, 102] respectively. Moreover, absorption band occurring at around 1721

cm^{-1}[101, 103] is attributed due to the C=O bond and the C–O vibration at 1045 cm^{-1}[101] is prominent also. The C–N vibration of porphyrins at 145 cm^{-1} are also observed [104]. The signature of the OH bond stretching can be witnessed at 3330cm^{-1}[103, 105]. The Mg-N peak is visible at 301cm^{-1} [106]. Finally, the absorption band at 1644 cm^{-1} is due to the presence of the C=C bond [107].

Interactions of extracted chlorophyll (chl) from leaves with different dyes commonly used to adulterate fruits and vegetables are investigated in a restricted nanoscopic environment of SDS micelles analogous to granum where chlorophylls are naturally restricted. The isosbestic point at 629 nm for chlorophyll a and b [108] is considered for excitation in this study. 20 mM, 3 mM, 5 mM and 4 mM stock solutions of SDS, MG and $CuSO_4$ in DI water (Milli-Q) and SR in DMSO were prepared. The solutions were further diluted according to the experimental study. All the measurements were performed at room temperature. The absorbance and emission of the extracted chlorophyll along with its physical appearance are shown in Figure 6.8.b. The absorbance maxima at 664 nm and 611nm and emission 672nm are exactly matching with that of pure chlorophyll [103] confirming the proper extraction of chlorophyll.

6.2.2.1. Spectroscopic Investigations of The Nature of Interactions of Chl–Cu(II) Systems Within the Micellar Cavity:

The main absorption bands in the Chl–Cu(II) (Figure 6.9.a) spectra are mainly generated due to electronic transitions between π and π* orbitals of the macrocycle of the Metallochlorophylls complex, quite similar to that of metalloporphyrins. The effect of metal binding on the spectral properties of the chlorophyll has been systematically investigated by Gouterman [109, 110], which is later backed by the theoretical calculations of Orzeł et.al. and Sundholm's [111, 112]. In our study, Chl is attached to the negatively charged surface of the SDS micelle. During gradual addition of the $CuSO_4$ at increasing concentrations to the Chl-SDS complex, significant changes in absorption spectra has been observed, among them the most significant are (1) hypsochromic shift at around 660 to 670 nm of the Q_Y band from its original position; (2) significant hypsochromisms in the UV-Vis absorption of the low intensity bands at

around 500 nm; (3) hypsochromisms in the highest intensity bands around 400 nm. Substitution of the Mg^{2+} metal ion into the tetrapyrrolic cavity by other ions depends on the competitive binding affinity which brings a strong impact mainly on the electronic state of the macrocycle and consequent absorption spectra as well. Hypsochromic shift of the Q_Y band clearly indicates the formation of a complex with the added metal ion. The features of the Q_Y bands at several concentrations of $CuSO_4$ are quite dramatic and do not follow the regular pattern. It follows an initial decrease followed by further reconstruction of the absorption band, but the reconstructed band is not identical in terms of absorption intensity as well as wavelength as that of starting one by which it discards the possibility of the reversible interaction. Reduction of the absorption intensity around the 400 nm central band as well as hypochromicity around 500 nm are the clear signature of the formation of an intermediate complex where both the metals ions (Mg^{2+} and Cu^{2+}) are held by the macrocyclic ring. Irreversibility of the 650 nm absorption band at highest $CuSO_4$ concentration discards the complete substitution of the Mg^{2+} by the Cu^{2+}. The corresponding fluorescence spectra of the chlorophyll display no considerable shift of the peak position with increasing concentration of $CuSO_4$, however the intensity decreases gradually (Figure 6.9.b). This quenching of fluorescence intensity might be due to the formation of SDS-Chl-Cu^{2+} ion pair, which progressively associate to form an aggregated type of structure. The same nature of fluorescence quenching has also been observed with increasing concentration of Cu^{2+} in absence of Chl alone in water.

To interpret the nature of quenching, we have monitored the fluorescence lifetime since both $\frac{I_0}{I}$ or $\frac{\tau_0}{\tau}$ directly related to the quenching ability of a quencher. At 50 μM concentration of $CuSO_4$, the excited state lifetime of the Chl in SDS reduces from 1.13 ns to 0.347 ns and the change of (τ_0/τ) matches well with that of intensity (I_0/I) confirming the dynamic nature of the quenching (Figure 6.9.c). In contrary, Chl in water in presence of Cu^{2+} shows no changes in excited state lifetime which is the signature of the static nature of the quencher where the ground state population of Chl has been perturbed by the quenchers (Figure 6.9.c inset).

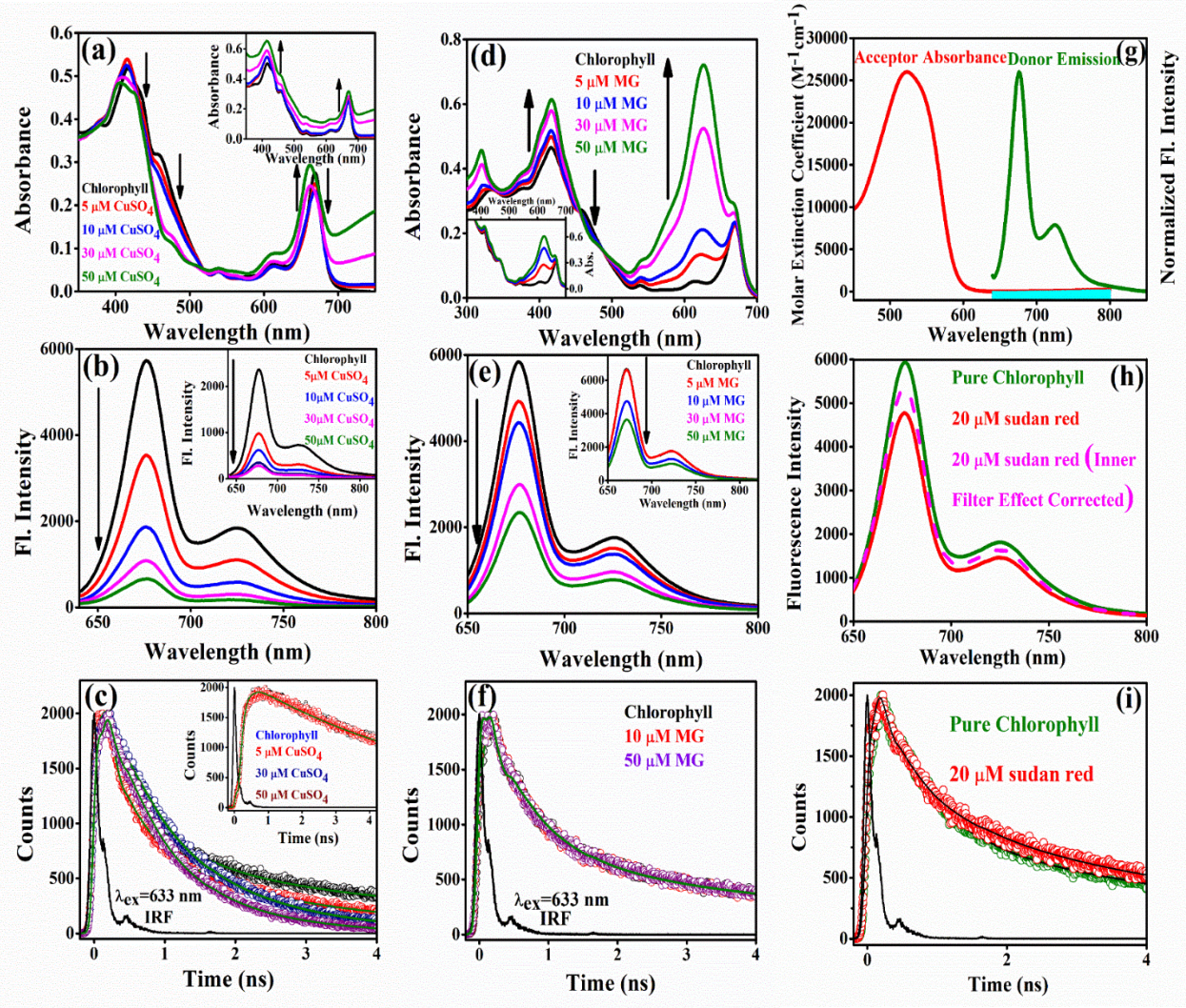

Figure 6.9. *Interaction of chlorophyll with $CuSO_4$ in terms of (a) Absorbance (b) Emission and (c) TCSPC in SDS micelles for 5-50uM concentrations of $CuSO_4$ (insets show absorbance, emission and TCSPC in water respectively). Interaction of chlorophyll with malachite green in terms of (d) Absorbance (e) Emission and (f) TCSPC in SDS micelles for 5-50 uM concentrations of MG (insets show absorbance, emission and TCSPC in water respectively). (g) Spectral overlap of chl fluorescence (green) and SR absorbance (red) when both are incorporated in SDS micelle. (h) Forster Resonance Energy Transfer (FRET) process is of chl ligand to SR within the SDS micelle is evident from the quenching of the steady-state fluorescence intensity after inner filter effect correction (i) Picosecond-resolved fluorescence transients of the chl ligand as donor in SDS micelle in absence and in presence of SR as an acceptor.*

To investigate the electronic property and charge transfer mechanism in the hybrid system, we have performed first principles density functional theory calculations. Figure 6.10.a and b show the ionically relaxed structure of Chl and Chl-Cu(II) using a Γ-point centred single k-point calculation. The Chl-Cu(II) has replaced the Mg ion of Chl by Cu ion [113].

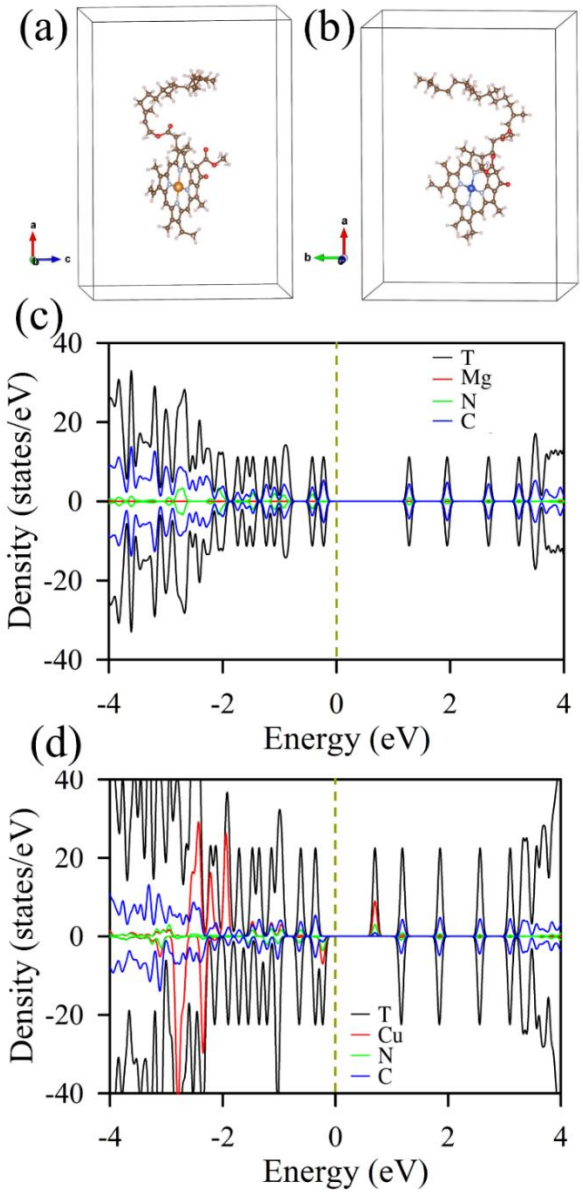

Figure 6.10. *Ionic relaxed structure of (a) chlorophyll and (b) chlorophyll-Cu(II). The partial density of states (PDOS) (c) chlorophyll and (d) chlorophyll-Cu(II).*

The formation energy of the Chl-Cu(II) system is -0.15 eV/atom which indicates the feasibility of formation and structural stability of Chl-Cu(II). Figure 6.10.c shows the atom-projected partial density of states (APDOS) of pure Chl and Figure 6.10.d shows the APDOS of Chl-Cu(II). Pristine Chl is seen to have an energy-gap of ~1.4 eV between valence band maxima (VBM) and conduction band minima (CBM). The CBM has mostly constituted by N-2*p* and C-2*p* orbital. There is a significant reduction of energy bandgap for Chl-Cu(II) due to presence of some additional ligand levels states (Figure 6.9.d) of constituting N-2p and C-2p orbitals. There is a structural

reconstruction around the metal ion associated with the replacement of Mg with Cu because of the difference in the radii of Mg^{2+} (0.65 A) and Cu^{2+} (0.73 A) as well as the additional spin-polarization incorporated within the system due to the substitution of the non-magnetic atom Mg with magnetic atom Cu. This reconstruction of the structure leads to the modification of the ligand levels and are thereby responsible due to the modification of band gap [114]. The theoretically predicted results support the experimental findings of modification of the optical properties due to the change of the electronic interaction.

6.2.2.2. Spectroscopic Investigations of the Nature of Interactions of Chl–MG Systems Within the Micellar Cavity:

Absorption spectra of the Chl-SDS upon interaction with MG at various concentrations are shown in Figure 6.9.d. As observed from the Figure, Chl in SDS produces an absorption band around 400 nm and 600 nm, which progressively increases in terms of intensity upon addition of MG at various concentrations. Intensifying the peak at position 600 nm in the spectrum indicates the formation of an adduct of MG with Chl-surfactant complex. Shukla et. al. [115] earlier reported such interaction between a cationic dye, crystal violet and Chl, resulting in the formation of a new band in the blue region of the absorption spectrum. Such an interaction might also lead to the formation of dimers of the dye. The absorption peak at the blue end is strengthened most at highest MG concentration, at the expense of the weakening of the 470 nm absorption band. Isosbestic point at 500 nm reveals coexistence of two different species in the medium.

The fluorescence spectrum of Chl in SDS strongly corroborates with the spectral nature of Chl in water. The observed decrease in fluorescence intensity of Chl in the presence of MG can (Figure 6.9.e) arise either due to the various quenching mechanisms or even through non-molecular mechanisms where self-absorption of the fluorophores may screen the emissive light. To find out the possibility we have corrected the emission spectra by considering the absorption of the absorbing species (equation 6.2) [116]:

$$F_{Corr} = F_{Obs} \times \exp\left((A_{ex} + A_{em})/2\right) \quad (6.2)$$

where F_{cor} and F_{obs} are the corrected and observed fluorescence intensities, respectively; A_{ex} and A_{em} are the absorbance of the system at excitation and emission wavelength, respectively. After correction we observe MG induce significant quenching of the Chl which further discards the possibility of inner filter effect of fluorescence quenching. To understand the quenching mechanism, we have further monitored excited state lifetime of Chl-SDS complex at various MG concentrations since alternatively the quenching process can be expressed in terms of $\frac{\tau_0}{\tau}$. The constant value of τ_0/τ confirms the static nature of the quenching (Figure 6.9.f and Table 6.5.).

Table 6.5. *Time-resolved decay parameters of chlorophyll in SDS in absence and in presence of copper sulphate, malachite green and sudan red dyes at different concentrations. Reactant (R) stands for 2 ml 20 mM SDS +300 uM chlorophyll.*

System	**τ1 (ns)/%**	**τ2 (ns)/%**	**τ3 (ns)/%**	**τ_{avg} (ns)**	**χ^2**
Reactant (R)	0.327 (53%)	1.40 (20%)	5.67 (27%)	2.19	1.17
R+20 uM Sudan Red	0.192 (51%)	0.930 (21%)	5.82 (28%)	1.94	1.01
R+40 uM Sudan Red	0.156 (52%)	0.879 (17%)	5.89 (31%)	2.03	1.02
Reactant(R)	0.141 (60%)	0.763 (24%)	5.50 (16%)	1.13	1.04
R+5 uM $CuSO_4$	0.140 (70%)	0.877 (17%)	3.29 (13%)	0.678	0.987
R+20 uM $CuSO_4$	0.037 (59%)	0.572 (20%)	1.55 (21%)	0.463	0.988
R+40 uM $CuSO_4$	0.030 (58%)	0.426 (20%)	1.13 (21%)	0.349	0.888
Reactant(R)	0.223 (59%)	1.00 (21%)	5.56 (20%)	1.46	1.00
R+20 uM MG	0.149 (58%)	0.817 (24%)	5.70 (18%)	1.25	1.05
R+40 uM MG	0.060 (66%)	0.674 (22%)	5.68 (12%)	0.856	1.09

6.2.2.3. Spectroscopic Investigations of the Nature of Interactions of Chl with a Foreign Dye Sudan Red Within the Micellar Cavity:

In our study, we have made an attempt to capture the interaction of sudan red as a food adulterant [117] with Chl. Since sudan red has an absorption tail around the emission tail of Chl (Figure 6.9.g), it is assumed that there is a possibility of FRET (Forster Resonance Energy Transfer) between Chl-SDS and sudan red. After spectral correction in steady state emission spectra, energy transfer efficiency has been obtained at ~ 15% (Figure 6.9.h). Energy transfer efficiency has been calculated as $E = 1 - \frac{F_{DA}}{F_D}$; F_{DA} and F_D are the fluorescence intensity of the donor in presence and in absence of acceptor. To further verify the energy transfer efficiency, we have monitored the excited state lifetime in absence and in presence of sudan red. By using τ_D and $\tau_{DA,}$ the calculated energy transfer efficiency obtained as ~ 18% which clearly supports the observed fluorescence quenching in steady state (Figure 6.9.i). It is evident that by monitoring FRET efficiency, one can monitor the presence of other foreign molecules like sudan red as an adulterant specially in vegetables.

6.2.2.4. Computational Studies to Predict the Harmful Effects of Dyes on Human Health:

Chlorophyll, the primary pigment responsible for the green colour in vegetables and plants, with their limited bioavailability, reported to have oxidative stress regulating capacity, hence has a preventative role in cancer initiation and progression [118]. Studies [119, 120] have shown that plant pigments, including chlorophyll are able to bind mutagens, also inhibit the absorption, and stop mutagens to interact with DNA. However, when the vegetables are adulterated with harmful industrial chemical and dyes like copper sulphate, malachite green and sudan red, the dyes may create serious health hazards. Table 6.6. provides a comprehensive analysis regarding the chemical-protein interaction for the current study, as depicted in Figure 6.11.

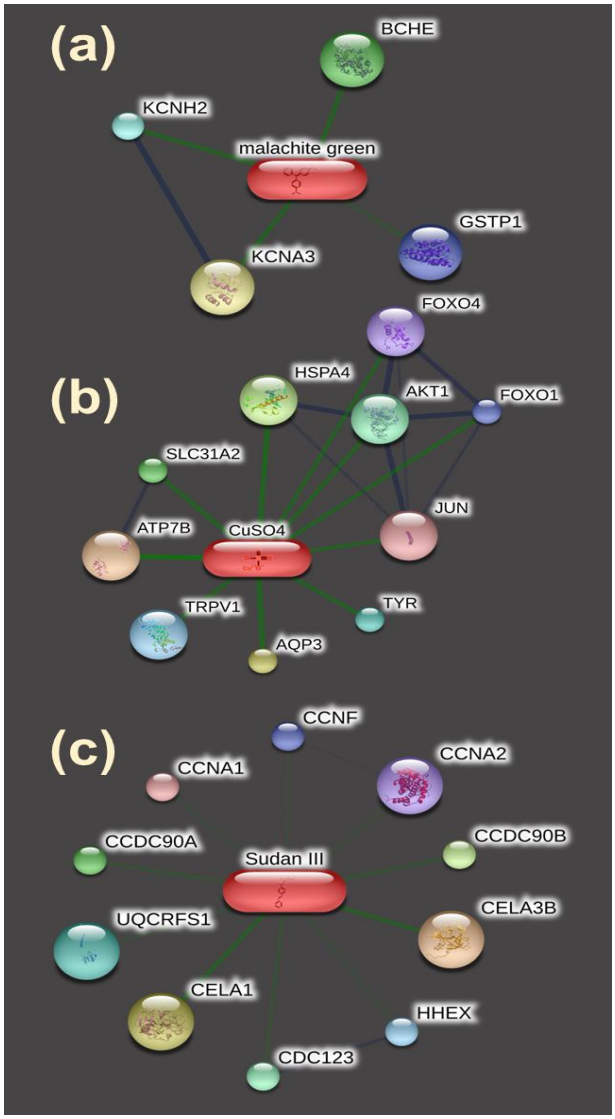

Figure 6.11. *Chemical protein interaction of (a) Malachite green (b) Copper sulphate and (c) Sudan Red using Computational Biology*

Table 6.6. *Chemical-protein interaction and activity of copper sulphate, sudan red and malachite green.*

Name of the chemical	Name of the interacting protein	Activity
Copper sulphate	HSPA4 /heat shock 70kDa protein 4	In vivo and in vitro studies have shown that heat shock proteins (HSPs), detected in both the prokaryotic and eukaryotic cells, enhances its level after environmental stresses, infection, normal physiological processes, gene transfer,

		thus plays a crucial role in the survival of organisms.
	SLC31A2(CTR2) / solute carrier family 31 (copper transporters), member 2;	CTR2 plays an important role in mammalian Cu homeostasis and is involved in low-affinity copper uptake (Potential)
	ATP7B / ATPase, Cu++ transporting, beta polypeptide;	It is involved in the export of copper out of the cells, such as the efflux of hepatic copper into the bile. Almost 60 diseases have now been reported in connection with specific mutations of ATP7B in patients with Wilson's disease, a genetic disorder of copper metabolism.
	TRPV1 / transient receptor potential cation channel, subfamily V, member 1;	It is involved in detection of noxious chemical and thermal stimuli. TRPV1 may provide connection between the process of inflammation, cancer and immunity, which can be useful to cultivate new treatment pathways.
	AQP3 / aquaporin 3 (Gill blood group);	Water channel promotes glycerol permeability and water transport across cell membranes and acts as a glycerol transporter in skin and plays an important role in regulating stratum corneum and epidermal glycerol content and involved in skin hydration, wound healing, and tumorigenesis.
	TYR / tyrosinase	This is a copper-containing oxidase that functions in the formation of pigments such as melanin and other polyphenolic compounds and have the potential applications like design of inhibitors of undesirable fruit browning in

		vegetables or of colour skin modulators in animals.
	JUN / jun proto-oncogene	Although it is not identified as a cancer-specific chromosomal translocation, but its dominant negative mutants weaken the growth of various tumour cells.
	AKT1/ v-akt murine thymoma viral oncogene homolog 1	AKT1 is one of 3 closely related serine/threonine- protein kinases which regulate many processes including metabolism, cancer proliferation, cell survival, growth and angiogenesis.
	FOXO1 / forkhead box O1 and FOXO4 / forkhead box O4	Transcription factor that is the main target of insulin signalling and regulates metabolic homeostasis in response to oxidative stress. It is also involved in processes like apoptosis, cell cycle arrest, stress resistance, cellular differentiation and development, and tumor suppression
Sudan Red	CCNA1 / cyclin A1	Loss of cyclin A1 may lead to disruption of male sterility due to cell arrest in the late diplotene stage of the meiotic cell cycle
	CCDC90A / coiled-coil domain containing 90A	Key regulator of mitochondrial calcium uniporter (MCU) required for calcium entry into mitochondrion. Plays a direct role in uniporter-mediated calcium uptake, possibly via a direct interaction with MCU
	UQCRFS1 / ubiquinol-cytochrome c reductase, Rieske	Component of the ubiquinol-cytochrome c reductase complex (complex III or cytochrome b-c1 complex), which is a respiratory chain that generates an electrochemical potential coupled to ATP synthesis. Isolated complex III (CIII)

	iron-sulfur polypeptide 1	deficiency symptoms range from isolated myopathy to severe multi-systemic disorders, even early death and disability.
	CELA1 / chymotrypsin-like elastase family, member 1	Acts upon elastin
	CDC123 / cell division cycle 123 homolog (S. cerevisiae)	It has a crucial role in protein biosynthesis by supplying methionylated initiator tRNA to the ribosomal translation initiation complex.
	HHEX / hematopoietically expressed homeobox	Its enforced expression may induces T-cell leukaemia.
	CCDC90B / coiled-coil domain containing 90B	It is important agent for fusion, signalling, and scaffolding.
	CCNA2 / cyclin A2	It is essential for the control of the cell cycle at the G1/S (start) and the G2/M (mitosis) transitions. It is also a potential target for prevention of tamoxifen resistance.
Malachite green	BCHE / butyrylcholinesterase	Contributes to the inactivation of the neurotransmitter acetylcholine. Can degrade neurotoxic organophosphate esters. It is a perfect indicator of pesticide poisoning and nerve agent exposure.
	KCNH2 / potassium voltage-gated channel, subfamily H	Its dysfunction may lead to intrauterine fetal death, sudden infant death syndrome, cardiac arrhythmia, and sudden cardiac death

	(eag-related), member 2	
	KCNA3 / potassium voltage-gated channel, shaker-related subfamily, member 3	Mediates the voltage-dependent potassium ion permeability of excitable membranes. It also regulates neurotransmitter release, insulin secretion, neuronal excitability, immune response, apoptosis, and cell proliferation.
	GSTP1 / glutathione S-transferase pi 1	This enzyme can detoxify the cell from endogenous and exogenous toxic compounds by using glutathione (GSH).

6.3. CONCLUSION:

In this chapter, a portable and easy to use spectroscopic device has been developed as a viable alternative to the conventional qualitative and manual tea testing technique for identification of the geographical indication and quality of tea. The developed device is also capable of detecting adulterations in Darjeeling tea with other low-grade tea like Nepal variants or inedible adulterants like saw dust by simply measuring the absorbance and fluorescence quantum yield of a tea sample. The seasonal variation in different flushes, the shelf life and health benefits of variety of tea can also be measured by the device. The performance of the device shows huge potential for application in tea industry. Anti-oxidant activities of tea variants are also explored along with computational biology studies. The interaction of quercetin with protein reveals tremendous health benefits of the Darjeeling tea.

In this chapter, the present work has also demonstrated, the detailed mechanism of interactions of chlorophyll with some harmful dyes. The dyes can be interlinked directly with chlorophyll of fruits and vegetables either by unscrupulous business practices of adulteration for making items fresh and vibrant or by consumption through root of plants from dye contaminated soils with industry or agricultural effluents. The experimental findings reveal the interaction of chlorophyll with three commonly used illegal dyes, namely copper sulphate, malachite green, and

sudan red in a restricted nanoscopic environment of SDS micelles. For copper sulphate, the hypsochromic shift of 10nm in the absorbance band of chlorophyll confirms the metal binding and fluorescence quenching as well as TCSPC studies revealed the nature of dynamic quenching. The intensification of absorbance peak in presence of the dye malachite green is indicative of probable formation of dimers of the dye. The absorption peak at the blue end is strengthened most at the highest concentration of the MG dye, at the expense of weakening of the 470 nm absorption band. Further significant fluorescence quenching of chlorophyll after inner filter effect correction and picosecond time resolved analysis with addition of malachite green indicate the static quenching mechanism. The possibility of FRET between the chlorophyll-SDS and sudan red dye due to their overlapped emission and absorbance spectral signatures was explored and around 15% energy transfer efficiency was obtained between the doner and acceptor establishing a mild interaction. The hazardous effects of the dyes on human are also thoroughly investigated using predictive computational biology technique.

REFERENCES

[1] J.A. Novotny, D.J. Baer, Tea, Encyclopedia of Human Nutrition, *Elsevier*, Edinburgh, 2013.

[2] statistica.com, Main export countries for tea worldwide 2021, *Statistica*.

[3] K. Das, International protection of India's Geographical Indications with special reference to "Darjeeling" tea, *The Journal of World Intellectual Property*, 9 (2006) 459.

[4] FDA, Applied, Economically Motivated Adulteration (Food Fraud), *FDA*, 2021.

[5] S. Ghosal, Darjeeling planters seek anti-dumping duty on Nepal tea, *The Economic Times*, India, 2022.

[6] M. Kawakami, S.N. Ganguly, J. Banerjee, A. Kobayashi, Aroma composition of Oolong tea and Black tea by brewed extraction method and characterizing compounds of Darjeeling tea aroma, *Journal of Agricultural and Food Chemistry*, 43 (1995) 200.

[7] N. Togari, A. Kobayashi, T. Aishima, Pattern recognition applied to gas chromatographic profiles of volatile components in three tea categories, *Food Research International*, 28 (1995) 495.

[8] W. Shao, C. Powell, M.N. Clifford, The analysis by HPLC of green, black and Pu'er teas produced in Yunnan, *Journal of the Science of Food and Agriculture*, 69 (1995) 535.

[9] G. Le Gall, I.J. Colquhoun, M. Defernez, Metabolite profiling using 1H NMR spectroscopy for quality assessment of green tea, Camellia sinensis (L.)., *Journal of Agricultural and Food Chemistry*, 52 (2004) 692.

[10] J. Yun, C. Cui, S. Zhang, J. Zhu, C. Peng, H. Cai, *et al.*, Use of headspace GC/MS combined with chemometric analysis to identify the geographic origins of black tea, *Food Chemistry*, 360 (2021) 130033.

[11] Y. Dong, X. Liu, L. Mei, C. Feng, C. Yan, S. He, LED-induced fluorescence system for tea classification and quality assessment, *Journal of Food Engineering*, 137 (2014) 95.

[12] Y. Dong, H. Lu, Z. Yong, C. Yan, S. He, Fast two-dimensional fluorescence correlation spectroscopy technique for tea quality detection, *Applied Optics*, 54 (2015) 7032.

[13] L.N. Seetohul, S.M. Scott, W.T. O'Hare, Z. Ali, M. Islam, Discrimination of Sri Lankan black teas using fluorescence spectroscopy and linear discriminant analysis, *Journal of the Science of Food and Agriculture*, 93 (2013) 2308.

[14] P. Mishra, A. Nordon, J. Tschannerl, G. Lian, S. Redfern, S. Marshall, Near-infrared hyperspectral imaging for non-destructive classification of commercial tea products, *Journal of Food Engineering*, 238 (2018) 70.

[15] P. Firmani, S. De Luca, R. Bucci, F. Marini, A. Biancolillo, Near infrared (NIR) spectroscopy-based classification for the authentication of Darjeeling black tea, *Food Control*, 100 (2019) 292.

[16] M.-Z. Zhu, B. Wen, H. Wu, J. Li, H. Lin, Q. Li, *et al.*, The quality control of tea by Near-Infrared Reflectance (NIR) spectroscopy and chemometrics, *Journal of Spectroscopy*, 2019 (2019) e8129648.

[17] R. Dutta, E.L. Hines, J.W. Gardner, K.R. Kashwan, M. Bhuyan, Tea quality prediction using a tin oxide-based electronic nose: An artificial intelligence approach, *Sensors and Actuators B: Chemical*, 94 (2003) 228.

[18] H. Yu, J. Wang, Discrimination of LongJing green-tea grade by electronic nose, *Sensors and Actuators B: Chemical*, 122 (2007) 134.

[19] N. Bhattacharyya, S. Seth, B. Tudu, P. Tamuly, A. Jana, D. Ghosh, *et al.*, Detection of optimum fermentation time for black tea manufacturing using electronic nose, *Sensors and Actuators B: Chemical*, 122 (2007) 627.

[20] S.M.T. Gharibzahedi, F.J. Barba, J. Zhou, M. Wang, Z. Altintas, Electronic sensor technologies in monitoring quality of tea: A review, *Biosensors*, 12 (2022) 356.

[21] M. Xu, J. Wang, L. Zhu, The qualitative and quantitative assessment of tea quality based on E-nose, E-tongue and E-eye combined with chemometrics, *Food Chemistry*, 289 (2019) 482.

[22] W. He, X. Hu, L. Zhao, X. Liao, Y. Zhang, M. Zhang, *et al.*, Evaluation of Chinese tea by the electronic tongue: Correlation with sensory properties and classification according to geographical origin and grade level, *Food Research International*, 42 (2009) 1462.

[23] Y. Wang, Y. Liu, Q. Cui, L. Li, J. Ning, Z. Zhang, Monitoring the withering condition of leaves during black tea processing via the fusion of electronic eye (E-eye), colorimetric sensing array (CSA), and micro-near-infrared spectroscopy (NIRS), *Journal of Food Engineering*, 300 (2021) 110534.

[24] S. Qi, Q. Ouyang, Q. Chen, J. Zhao, Real-time monitoring of total polyphenols content in tea using a developed optical sensors system, *Journal of Pharmaceutical and Biomedical Analysis*, 97 (2014) 116.
[25] W. Pan, J. Zhao, Q. Chen, L. Yuan, In situ monitoring of total polyphenols content during tea extract oxidation using a portable spectroscopy system with variables selection algorithms, *RSC Advances*, 5 (2015) 60876.
[26] N. Vishnu, M. Gandhi, S. Badhulika, A.S. Kumar, Tea quality testing using 6B pencil lead as an electrochemical sensor, *Analytical Methods*, 10 (2018) 2327.
[27] P. Sharma, A. Ghosh, B. Tudu, L.P. Bhuyan, P. Tamuly, N. Bhattacharyya, *et al.*, A quartz crystal microbalance sensor for detection of geraniol in black tea, *IEEE Sensors Journal*, 15 (2015) 1178.
[28] L. Li, S. Xie, F. Zhu, J. Ning, Q. Chen, Z. Zhang, Colorimetric sensor array-based artificial olfactory system for sensing Chinese green tea's quality: A method of fabrication, *International Journal of Food Properties*, 20 (2017) 1762.
[29] Q. Chen, J. Zhao, Z. Guo, X. Wang, Determination of caffeine content and main catechins contents in green tea (Camellia sinensis L.) using taste sensor technique and multivariate calibration, *Journal of Food Composition and Analysis*, 23 (2010) 353.
[30] J. Li, B. Fu, D. Huo, C. Hou, M. Yang, C. Shen, *et al.*, Discrimination of Chinese teas according to major amino acid composition by a colorimetric IDA sensor, *Sensors and Actuators B: Chemical*, 240 (2017) 770.
[31] Y. Wang, L. Li, Y. Liu, Q. Cui, J. Ning, Z. Zhang, Enhanced quality monitoring during black tea processing by the fusion of NIRS and computer vision, *Journal of Food Engineering*, 304 (2021) 110599.
[32] H. Jiang, W. Xu, Q. Chen, Determination of tea polyphenols in green tea by homemade color sensitive sensor combined with multivariate analysis, *Food Chemistry*, 319 (2020) 126584.
[33] M. Jia, Y. Pan, J. Zhou, M. Zhang, Identification of Chinese teas by a colorimetric sensor array based on tea polyphenol induced indicator displacement assay, *Food Chemistry*, 335 (2021) 127566.
[34] F. Song, J. Wu, B. Liu, J. Jiang, Z. Li, C. Song, *et al.*, Intelligent green tea fixation with sensor fusion technology, *Journal of Food Engineering*, 317 (2022) 110846.

[35] H. Li, B. Zhang, W. Hu, Y. Liu, C. Dong, Q. Chen, Monitoring black tea fermentation using a colorimetric sensor array-based artificial olfaction system, *Journal of Food Processing and Preservation*, 42 (2018) e13348.
[36] H. Jiang, W. Xu, Q. Chen, Evaluating aroma quality of black tea by an olfactory visualization system: Selection of feature sensor using particle swarm optimization, *Food Research International*, 126 (2019) 108605.
[37] L. Li, M. Li, Y. Liu, Q. Cui, K. Bi, S. Jin, *et al.*, High-sensitivity hyperspectral coupled self-assembled nanoporphyrin sensor for monitoring black tea fermentation, *Sensors and Actuators B: Chemical*, 346 (2021) 130541.
[38] S. Alireza, H. Xinyao, Z. Zhangfeng, J. Yifan, L. Xiaoli, H. Yong, *et al.*, Nondestructive monitoring of polyphenols and caffeine during green tea processing using Vis-NIR spectroscopy, *Food Science & Nutrition*, 8 (2020) 5860.
[39] K. Steinmertz, J. Potter, Vegetables, fruit and cancer epidemiology, *Cancer Causes Cont*, 2 (1991) 325.
[40] G.R. Howe, T. Hirohata, T.G. Hislop, J.M. Iscovich, J.-M. Yuan, K. Katsouyanni, *et al.*, Dietary factors and risk of breast cancer: Combined analysis of 12 case—control studies, *JNCI: Journal of the National Cancer Institute*, 82 (1990) 561.
[41] K.J. Joshipura, F.B. Hu, J.E. Manson, M.J. Stampfer, E.B. Rimm, F.E. Speizer, *et al.*, The effect of fruit and vegetable intake on risk for coronary heart disease, *Annals of internal medicine*, 134 (2001) 1106.
[42] B.N. Rao, Bioactive phytochemicals in Indian foods and their potential in health promotion and disease prevention, *Asia Pacific Journal of clinical nutrition*, 12 (2003).
[43] A. Laura, E. Alvarez-Parrilla, G.A. González-Aguilar, Flavonoids and their relation to human health, *Fruit and Vegetable Phytochemicals: Chemistry, Nutritional Value and Stability*, *Wiley*, New jersey, 2009.
[44] F. Casino, V. Kanakaris, T. K. Dasaklis, S. Moschuris, S. Stachtiaris, M. Pagoni, N. P. Rachaniotis, Blockchain-based food supply chain traceability: A case study in the dairy sector, *International Journal of Production Research*, 59 (2021) 5758.
[45] L.M. Schell, M.V. Gallo, K. Cook, What's NOT to eat—food adulteration in the context of human biology, *American Journal of Human Biology*, 24 (2012) 139.

[46] S. Bansal, A. Singh, M. Mangal, A.K. Mangal, S. Kumar, Food adulteration: Sources, health risks, and detection methods, *Critical Reviews in Food Science and Nutrition*, 57 (2017) 1174.

[47] M. Oplatowska-Stachowiak, C.T. Elliott, Food colors: Existing and emerging food safety concerns, *Critical Reviews in Food Science and Nutrition*, 57 (2017) 524.

[48] S. Kobylewski, M.F. Jacobson, Toxicology of food dyes, *International Journal of Occupational and Environmental Health*, 18 (2012) 220.

[49] M.J. Scotter, L. Castle, D. Roberts, Method development and HPLC analysis of retail foods and beverages for copper chlorophyll (E141 [i]) and chlorophyllin (E141 [ii]) food colouring materials, *Food Additives and Contaminants*, 22 (2005) 1163.

[50] C.S. Gamakaranage, C. Rodrigo, S. Weerasinghe, A. Gnanathasan, V. Puvanaraj, H. Fernando, Complications and management of acute copper sulphate poisoning; a case discussion, *Journal of Occupational Medicine and Toxicology*, 6 (2011) 1.

[51] S. Shomaji, N.V.R. Masna, D. Ariando, S. Deb Paul, K. Horace-Herron, D. Forte, *et al.*, Detecting dye-contaminated vegetables using low-field NMR relaxometry, *Foods*, 10 (2021) 2232.

[52] C. Aydinalp, S. Marinova, The effects of heavy metals on seed germination and plant growth on alfalfa plant (Medicago sativa), *Bulgarian Journal of Agricultural Science*, 15 (2009) 347.

[53] M.A. Öztürk, Plants and pollutants in developped and developing countries: International symposium held in Izmir, Turkey; Botany Department, Science Faculty, Ege University, *Ege University Press*, Bornova, 1989.

[54] I. Ali, C.K. Jain, Advances in arsenic speciation techniques, *International Journal of Environmental Analytical Chemistry*, 84 (2004) 947.

[55] M. Krzesłowska, The cell wall in plant cell response to trace metals: Polysaccharide remodeling and its role in defense strategy, *Acta Physiologiae Plantarum*, 33 (2011) 35.

[56] I. Ali, V.K. Gupta, T.A. Khan, M. Asim, Removal of arsenate from aqueous solution by electro-coagulation method using Al-Fe electrodes, *International Journal of Electrochemical Science*, 7 (2012) 1898.

[57] I. Ali, Z.A. ALOthman, M.M. Sanagi, Green synthesis of iron nano-impregnated adsorbent for fast removal of fluoride from water, *Journal of Molecular Liquids*, 211 (2015) 457.
[58] M. Suhail, I. Ali, Advanced spiral periodic classification of the elements, *Chemistry International,* 3 (2017) 220.
[59] I. Ali, O.M. Alharbi, Z.A. Alothman, A.Y. Badjah, A. Alwarthan, Artificial neural network modelling of amido black dye sorption on iron composite nano material: kinetics and thermodynamics studies, *Journal of Molecular Liquids*, 250 (2018) 1.
[60] M. Sabir, E.A. Waraich, K.R. Hakeem, M. Öztürk, H.R. Ahmad, M. Shahid, Phytoremediation: Mechanisms and adaptations, *Soil Remediation and Plants: Prospects and Challenges*, 85 (2014) 85.
[61] M.H. Dehghani, D. Sanaei, I. Ali, A. Bhatnagar, Removal of chromium (VI) from aqueous solution using treated waste newspaper as a low-cost adsorbent: Kinetic modeling and isotherm studies, *Journal of Molecular Liquids*, 215 (2016) 671.
[62] O.M. Alharbi, R.A. Khattab, I. Ali, Health and environmental effects of persistent organic pollutants, *Journal of Molecular Liquids*, 263 (2018) 442.
[63] A.A. Basheer, New generation nano-adsorbents for the removal of emerging contaminants in water, *Journal of Molecular Liquids*, 261 (2018) 583.
[64] E.A. Burakova, T.P. Dyachkova, A.V. Rukhov, E.N. Tugolukov, E.V. Galunin, A.G. Tkachev, *et al.*, Novel and economic method of carbon nanotubes synthesis on a nickel magnesium oxide catalyst using microwave radiation, *Journal of Molecular Liquids*, 253 (2018) 340.
[65] H. Singh, D. Kumar, V. Soni, Copper and mercury induced oxidative stresses and antioxidant responses of Spirodela polyrhiza (L.) Schleid, *Biochemistry and Biophysics Reports*, 23 (2020) 100781.
[66] S. Raj, H. Singh, R. Trivedi, V. Soni, Biogenic synthesis of AgNPs employing Terminalia arjuna leaf extract and its efficacy towards catalytic degradation of organic dyes, *Scientific Reports*, 10 (2020) 9616.
[67] S. Yadav, Heavy metals toxicity in plants: An overview on the role of glutathione and phytochelatins in heavy metal stress tolerance of plants, *South African Journal of Botany*, 76 (2010) 167.

[68] H. Bouazizi, H. Jouili, A. Geitmann, E. El Ferjani, Copper toxicity in expanding leaves of Phaseolus vulgaris L.: Antioxidant enzyme response and nutrient element uptake, *Ecotoxicology and Environmental Safety*, 73 (2010) 1304.

[69] V. Ashok, N. Agrawal, A. Durgbanshi, J. Esteve-Romero, D. Bose, Determination of adulteration of malachite green in green pea and some prepared foodstuffs by micellar liquid chromatography, *Journal of AOAC International*, 97 (2014) 1387.

[70] A. Panandiker, C. Fernandes, K. Rao, The cytotoxic properties of malachite green are associated with the increased demethylase, aryl hydrocarbon hydroxylase and lipid peroxidation in primary cultures of Syrian hamster embryo cells, *Cancer Letters*, 67 (1992) 93.

[71] S. Srivastava, R. Sinha, D. Roy, Toxicological effects of malachite green, *Aquatic Toxicology*, 66 (2004) 319.

[72] X.-Y. Fu, W. Zhao, A.-S. Xiong, Y.-S. Tian, B. Zhu, R.-H. Peng, *et al.*, Phytoremediation of triphenylmethane dyes by overexpressing a Citrobacter sp. triphenylmethane reductase in transgenic Arabidopsis, *Applied Microbiology and Biotechnology*, 97 (2013) 1799.

[73] P.A. Herklotz, P. Gurung, B. Vanden Heuvel, C.A. Kinney, Uptake of human pharmaceuticals by plants grown under hydroponic conditions, *Chemosphere*, 78 (2010) 1416.

[74] M. Szczygłowska, A. Piekarska, P. Konieczka, J. Namieśnik, Use of Brassica Plants in the Phytoremediation and Biofumigation Processes, *International Journal of Molecular Sciences*, 12 (2011) 7760.

[75] T.M. Fonovich, Sudan dyes: Are they dangerous for human health?, *Drug and Chemical Toxicology*, 36 (2013) 343.

[76] T.N. Nagaraja, T. Desiraju, Effects of chronic consumption of metanil yellow by developing and adult rats on brain regional levels of noradrenaline, dopamine and serotonin, on acetylcholine esterase activity and on operant conditioning, *Food and Chemical Toxicology*, 31 (1993) 41.

[77] A. Banerjee, R. Ghosh, S. Singh, A. Adhikari, S. Mondal, L. Roy, *et al.*, Spectroscopic studies on a natural biomarker for the identification of origin and quality of tea extracts for the development of a portable and field deployable

prototype, *Spectrochimica Acta Part A: Molecular and Biomolecular Spectroscopy*, 299 (2023) 122842.

[78] Y.-f. Ren, C. Feng, Z.-h. Ye, H.-y. Zhu, R.-y. Hou, D. Granato, *et al.*, Keemun black tea: Tracing its narrow-geographic origins using comprehensive elemental fingerprinting and chemometrics, *Food Control*, 133 (2022) 108614.

[79] P. Drössler, W. Holzer, A. Penzkofer, P. Hegemann, Fluoresence quenching of riboflavin in aqueous solution by methionin and cystein, *Chemical Physics*, 286 (2003) 409.

[80] N. Goswami, S. Chaudhuri, A. Giri, P. Lemmens, S.K. Pal, Surface engineering for controlled nanocatalysis: Key dynamical events from ultrafast electronic spectroscopy, *The Journal of Physical Chemistry C*, 118 (2014) 23434.

[81] M. Mizutani, H. Nakanishi, J.-i. Ema, S.-J. Ma, E. Noguchi, M. Inohara-Ochiai, *et al.*, Cloning of β-Primeverosidase from tea leaves, a key enzyme in tea aroma formation, *Plant Physiology*, 130 (2002) 2164.

[82] S. Bhattacharya, R. Gachhui, P.C. Sil, Hepatoprotective properties of kombucha tea against TBHP-induced oxidative stress via suppression of mitochondria dependent apoptosis, *Pathophysiology: The Official Journal of the International Society for Pathophysiology*, 18 (2011) 221.

[83] V.S.P. Chaturvedula, I. Prakash, The aroma, taste, color and bioactive constituents of tea, *Journal of Medicinal Plants Research*, 5 (2011) 2110.

[84] C.-y. Peng, Y.-f. Ren, Z.-h. Ye, H.-y. Zhu, X.-q. Liu, X.-t. Chen, *et al.*, A comparative UHPLC-Q/TOF-MS-based metabolomics approach coupled with machine learning algorithms to differentiate Keemun black teas from narrow-geographic origins, *Food Research International*, 158 (2022) 111512.

[85] S. Srivastava, Food adulteration affecting the nutrition and health of human beings, *Journal of Biological Sciences and Medicine*, 1 (2015) 65.

[86] S.B. Kedare, R.P. Singh, Genesis and development of DPPH method of antioxidant assay, *Journal of Food Science and Technology*, 48 (2011) 412.

[87] M. Ismail, M. Ibrar, Z. Iqbal, J. Hussain, H. Hussain, M. Ahmed, *et al.*, Chemical constituents and antioxidant activity of Geranium wallichianum, *Records of Natural Products*, 3 (2009) 193.

[88] O.A. Chat, M.H. Najar, A.A. Dar, Evaluation of reduction kinetics of 2, 2-diphenyl-1-picrylhydrazyl radical by flavonoid glycoside Rutin in mixed solvent based micellar media, *Colloids and Surfaces A: Physicochemical and Engineering Aspects*, 436 (2013) 343.

[89] C. von Mering, L.J. Jensen, B. Snel, S.D. Hooper, M. Krupp, M. Foglierini*, et al.*, STRING: Known and predicted protein-protein associations, integrated and transferred across organisms, *Nucleic Acids Research*, 33 (2005) D433.

[90] M. Liu, Y. Xu, Y. Zhou, R. Lang, Z. Shi, J. Zhao*, et al.*, Integrated analyses reveal the multi-omics and prognostic characteristics of ATP5B in breast cancer, *Frontiers in Genetics*, 12 (2021) 652474.

[91] Y. Tursynbay, J. Zhang, Z. Li, T. Tokay, Z. Zhumadilov, D. Wu*, et al.*, Pim-1 kinase as cancer drug target: An update, *Biomedical Reports*, 4 (2016) 140.

[92] H. Widden, W.J. Placzek, The multiple mechanisms of MCL1 in the regulation of cell fate, *Communications Biology*, 4 (2021) 1029.

[93] K.R. Casano, M.E. Ryan, A.R. Bicknese, D.S. Mithal, MRI of 3-hydroxyisobutyryl-CoA hydrolase (HIBCH) deficiency, *Radiology Case Reports*, 16 (2021) 807.

[94] Y. Lan, J. Han, Y. Wang, J. Wang, G. Yang, K. Li*, et al.*, STK17B promotes carcinogenesis and metastasis via AKT/GSK-3β/Snail signaling in hepatocellular carcinoma, *Cell Death & Disease*, 9 (2018) 236.

[95] F. Sansbury, S. Flanagan, J. Houghton, F. Shuixian Shen, A. Al-Senani, A. Habeb*, et al.*, SLC2A2 mutations can cause neonatal diabetes, suggesting GLUT2 may have a role in human insulin secretion, *Diabetologia*, 55 (2012) 2381.

[96] Y. Mitsui, I. Chang, S. Fukuhara, M. Hiraki, N. Arichi, H. Yasumoto*, et al.*, CYP1B1 promotes tumorigenesis via altered expression of CDC20 and DAPK1 genes in renal cell carcinoma, *BMC Cancer*, 15 (2015) 1.

[97] V.P. Androutsopoulos, A.M. Tsatsakis, D.A. Spandidos, Cytochrome P450 CYP1A1: Wider roles in cancer progression and prevention, *BMC Cancer*, 9 (2009) 1.

[98] M. Johansson, E. Strahm, A. Rane, L. Ekström, CYP2C8 and CYP2C9 mRNA expression profile in the human fetus, *Frontiers in Genetics*, 5 (2014) 58.

[99] H.C. Lantermans, M. Minderman, A. Kuil, M.-J. Kersten, S.T. Pals, M. Spaargaren, Identification of the SRC-family tyrosine kinase HCK as a therapeutic target in mantle cell lymphoma, *Leukemia*, 35 (2021) 881.

[100] A. Banerjee, D. Mukherjee, M.N. Hasan, S. Mukhopadhyay, D. Karmakar, R. Das, *et al.*, Interaction of chlorophyll with artificial colorants in restricted nanoscopic environment: Key insights on the toxicity from electronic spectroscopy, *Nanoscience and Nanotechnology: Open Access,* 2(1) (2023) 1012.

[101]. H. Chang, M.-J. Kao, T.-L. Chen, C.-H. Chen, K.-C. Cho, X.-R. Lai, Characterization of natural dye extracted from wormwood and purple cabbage for dye-sensitized solar cells, *International Journal of Photoenergy*, 2013 (2013) 159502

[102] Merck, IR spectrum table by frequency range, *Sigma Aldrich,* United States.

[103] J.K. Ahmed, Z.J.A. Amer, M.J.M. Al-Bahate, Effect of chlorophyll and anthocyanin on the secondary bonds of poly vinyl chloride (PVC), *International Journal of Materials Science and Applications*, 4 (2015) 21.

[104] I.R. Suica-Bunghez, A.A. Sorescu, S.M. Doncea, M. Constantin, I. Raut, I. Rodica Mariana, Phytochemical, antioxidant and antimicrobial characterization of Hedera helix L. extract, *Journal of Plant Development*, 27 (2020) 47.

[105] S. Hemmalakshmi, S. Priyanga, K. Devaki, Fourier Transform Infra-Red Spectroscopy Analysis of Erythrina variegata L, *Journal of Pharmaceutical Sciences and Research*, 9 (2017) 2062.

[106] S. Mojumdar, M. Melnik, E. Jona, Thermal decomposition and IR spectra of Mg (II) compounds with caffeine, *Chemical Papers-slovak Academy of Sciences*, 53 (1999) 309.

[107] H. Darmokoesoemo, A.R. Fidyayanti, H. Setyawati, H.S. Kusuma, Synthesis of complex compounds Ni (II)-chlorophyll as dye sensitizer in dye sensitizer solar cell (DSSC), *Korean Chemical Engineering Research*, 55 (2017) 19.

[108] L. Guidi, M. Tattini, M. Landi, How does chloroplast protect chlorophyll against excessive light, *Chlorophyll*, 21 (2017) 21.

[109] M. Gouterman, Optical spectra and electronic structure of porphyrins and related rings, *The porphyrins*, 3 (1978) 1.

[110] M. Gouterman, G.H. Wagni re, L.C. Snyder, Spectra of porphyrins, *Journal of Molecular Spectroscopy*, 11 (1963) 108.

[111] Ł. Orzeł, B. Szmyd, D. Rutkowska-Żbik, L. Fiedor, R. van Eldik, G. Stochel, Fine tuning of copper (II)–chlorophyll interactions in organic media: Metalation versus oxidation of the macrocycle, *Dalton Transactions*, 44 (2015) 6012.
[112] D. Sundholm, Comparison of the electronic excitation spectra of chlorophyll a and pheophytin a calculated at density functional theory level, *Chemical Physics Letters*, 317 (2000) 545.
[113] H. Küpper, I. Šetlík, M. Spiller, F.C. Küpper, O. Prášil, Heavy metal-induced inhibition of photosynthesis: Targets of in vivo heavy metal chlorophyll formation1, *Journal of Phycology*, 38 (2002) 429.
[114] R. Bechaieb, A.B. Fredj, A.B. Akacha, H. Gérard, Interactions of copper (II) and zinc (II) with chlorophyll: Insights from density functional theory studies, *New Journal of Chemistry*, 40 (2016) 4543.
[115] D. Shukla, F.P. Pandey, P. Kumari, N. Basu, M.K. Tiwari, J. Lahiri, *et al.*, Label-free fluorometric detection of adulterant malachite green using carbon dots derived from the medicinal plant source ocimum tenuiflorum, *Chemistry Select*, 4 (2019) 4839.
[116] D. Mukherjee, P. Singh, S. Singh, D.S. Roy, S. Singha, U. Pal, *et al.*, Host assisted molecular recognition by human serum albumin: Study of molecular recognition controlled protein/drug mimic binding in a microfluidic channel, *International Journal of Biological Macromolecules*, 176 (2021) 137.
[117] G.J. Trentanni Hansen, J. Almonacid, L. Albertengo, M.S. Rodriguez, C. Di Anibal, C. Delrieux, NIR-based Sudan I to IV and Para-Red food adulterants screening, *Food Additives & Contaminants: Part A*, 36 (2019) 1163.
[118] M. Hayes, M.G. Ferruzzi, Update on the bioavailability and chemopreventative mechanisms of dietary chlorophyll derivatives, *Nutrition Research*, 81 (2020) 19.
[119] M.T. Simonich, P.A. Egner, B.D. Roebuck, G.A. Orner, C. Jubert, C. Pereira, *et al.*, Natural chlorophyll inhibits aflatoxin B 1-induced multi-organ carcinogenesis in the rat, *Carcinogenesis*, 28 (2007) 1294.
[120] C. Jubert, J. Mata, G. Bench, R. Dashwood, C. Pereira, W. Tracewell, *et al.*, Effects of chlorophyll and chlorophyllin on low-dose aflatoxin B1 pharmacokinetics in human volunteers, *Cancer Prevention Research*, 2 (2009) 1015.

List of Publications

1. **A. Banerjee**, N. Bhattacharyya, R. Ghosh, S. Singh, A. Adhikari, S. Mondal, L. Roy, A. Bajaj, N., Ghosh, A. Bhushan, M. Goswami, A. S. A. Ahmed, Z. Moussa, P. Mondal, S. Mukhopadhyay, D. Bhattacharyya, A. Chattopadhyay, S. A. Ahmed, A. K. Mallick and S. K. Pal,
   "Non-invasive estimation of hemoglobin, bilirubin and oxygen saturation of neonates simultaneously using whole optical spectrum analysis at point of care",
   ***Scientific Reports,* 13 (2023) 2370.**

2. **A. Banerjee**, D. Mukherjee, A. Bera, R. Ghosh, S. Mondal, S. Mukhopadhyay, R. Das, H. M. Altass, S. S. A. Natto, Z. Moussa, S. A. Ahmed, A. Chattopadhyay and S. K Pal,
   "Molecular co-localization of multiple drugs in a nanoscopic delivery vehicle for potential synergistic remediation of multi-drug resistant bacteria",
   ***Scientific Reports,* 12 (2022) 18881.**

3. **A. Banerjee**, R. Ghosh, T. Adhikari, S. Mukhopadhyay, A. Chattopadhyay, S K Pal,
   "Development of nanomedicine from copper mine tailing waste: A pavement towards circular economy with advanced redox nanotechnology",
   ***Catalysts,* 13 (2023) 369.**

4. **A. Banerjee**, R. Ghosh, A. Bera, S. Mukhopadhyay, M. M. Al-Rooqi, I. I. Althagafi A. S. Khder, S. A. Ahmed, A. Chattopadhyay and S. K. Pal,
   " "Nano-Copper": A potential remediation of antibiotic-resistant infections",
   ***Journal of Nanomedicine,* 6 (2023) 1058.**

5. **A. Banerjee**, S. Singh, R. Ghosh, M. N. Hasan, A. Bera, L. Roy, N. Bhattacharya, A. Halder, A. Chattopadhyay, S. Mukhopadhyay, A. Das, H. M. Altass, Z. Moussa, S. A. Ahmed and S. K. Pal,

"A portable spectroscopic instrument for multiplexed monitoring of acute water toxicity: Design, testing and evaluation",
Review of Scientific Instruments, **93 (2022) 115105.**

6. **A. Banerjee**, S. S. Pasha, S. Sreedharan, S. Singh, N. Kandoth, K. A. Vallis, S. K. Pal, S. K. Pramanik and A. Das,
"An ultrasensitive reagent for ratiometric detection and detoxification of iAsIII in water and mitochondria",
ACS Inorganic Chemistry, **61 (2022) 13115.**

7. **A. Banerjee**, R. Ghosh, S. Singh, A. Adhikari, S. Mondal, L. Roy, S. Midya, S. Mukhopadhyay, S. S. Chowdhury, S. Chakraborty, R. Das, J. H. Al-Fahemi, Z. Moussa, A. K. Mallick, A. Chattopadhyay, S. A. Ahmed and S. K. Pal,
"Spectroscopic studies on a natural biomarker for the identification of origin and quality of tea extracts for the development of a portable and field deployable prototype",
Spectrochimica Acta Part A: Molecular and Biomolecular Spectroscopy, **299 (2023) 122842**.

8. **A. Banerjee**, D. Mukherjee, M. N. Hasan, S. Mukhopadhyay, D. Karmakar, R. Das, A. Chattopadhyay and S. K. Pal,
"Interaction of chlorophyll with artificial colorants in restricted nanoscopic environment: Key insights on the toxicity from electronic spectroscopy",
Nanoscience and Nanotechnology Open Access, **2 (2023) 1012**.

9. * L. Roy, D. Mukherjee, S. Singh, **A. Banerjee**, N. Bhattacharyya, A. Halder, P. Singh, S. Mukhopadhyay, K. Bhattacharya, R. Das and S. K. Pal,
"Pico-second resolved Förster resonance energy transfer (FRET) differentiates self-assembled biological macromolecules in aqueous medium",
Chemical Physics Impact, **4 (2022) 100081**.

10. * N. Bhattacharyya, S. Singh, **A. Banerjee**, R. Ghosh, O. Sinha, N. Das, R. Gayen, S. S. Pal, S. Ganguly, T. Dasgupta, T. Dasgupta, P. Mondal, A. Adhikari, S. Sarkar, D. Bhattacharyya, A. K. Mallick, O. P. Singh and S. K. Pal,
"Integration of electroencephalogram (EEG) and motion tracking sensors for objective measure of attention-deficit hyperactivity disorder (MAHD) in pre-schoolers",
***Review of Scientific Instruments*, 93 (2022) 054101**.

11. * N. Pan, N. Bhattacharyya, **A. Banerjee**, P. Biswas, L. Roy, A. Chatterjee, R. Bhattacharjee, S. Singh, S. A. Ahmed, A. Chattopadhyay, M. Mitra and S. K. Pal,
"Paper-based plasmonic nanosensor monitors environmental lead pollution in real field",
***New Journal of Chemistry*, 46 (2022) 8177**.

12. * N. Bhattacharyya, S. Singh, R. Ghosh, **A. Banerjee**, A. Adhikari, A. Halder, M. Goswami, A. Chattopadhyay, P. Mondal, S. S. Natto, S. A. Ahmed, A. Mallick, and S. K. Pal,
"Development of a smart active respirator for comfortable and hygienic breathing",
***Physics of Fluids*, 34 (2022) 051901**.

13. * S. Singh, A. Halder, **A. Banerjee**, M. N. Hasan, A. Bera, O. Sinha, S.K. Ghosh, A. Mitra, S. K. Pal,
"An optical scattering based cost-effective approach towards quantitative assessment of turbidity and particle size estimation in drinking water using image analysis",
***Journal of Environmental Science & Engineering*, 10 (2021) 32942.**

14. * S. Singh, A. Halder, O. Sinha, N. Chakrabarty, T. Chatterjee, A. Adhikari, P. Singh, D. Shikha, R. Ghosh, **A. Banerjee**, P. Das Mahapatra, A. Mandhar, M. Bhattacharyya, S. Bose, S. A. Ahmed, A. Alharbi, A. M. Hameed and S. K. Pal,

"Spectroscopic studies on the biomolecular recognition of toluidine blue: Key information towards development of a non-contact, non-invasive device for oral cancer detection",
Frontiers in Oncology, **10 (2020) 529132**.

15. * S. Singh, A. Halder, Sk. A. Mohid, D. Bagchi, O. Sinha, **A. Banerjee**, P. K. Sarkar, A. Bhunia, S. K. Ghosh, A. Mitra and S. K. Pal,
"Non-thermal atmospheric plasma (NTAP) induced cellular envelope damage of Staphylococcus aureus and Candida albicans biofilms: Spectroscopic and bio-chemical investigations",
IEEE Transactions in Plasma Science, **48 (2020) 2768**.

16. * A. Halder, A. Adhikari, R. Ghosh, S. Singh, **A. Banerjee**, N. Ghosh, A. M. Bhattacharya, S. Mandal, P. Chakrabarti, D. Bhattacharyya, H. M. Altass, M. Morad, S. A. Ahmed, A. K. Mallick and S. K. Pal,
"Large scale validation of a new non-invasive and non-contact bilirubinometer in neonates with risk factors",
Scientific Reports, **10 (2020) 11149**.

17. * S. Singh, A. Halder, O. Sinha, P. K. Sarkar, P. Singh, **A. Banerjee**, S. A. Ahmed, A. Alharbi, R. J. Obaid, S. K. Ghosh, A. Mitra and S. K. Pal,
"Nanoparticle-based 'turn-on' scattering and post-sample fluorescence for ultrasensitive detection of water pollution in wider window",
PLOS ONE, **5 (2020) e0227584**.

18. * R. Ghosh, N. Bhattacharyya, **A. Banerjee**, L. Roy, D. Mukherjee, S. Singh, A. Chattopadhyay, T. Adhikari and S. K. Pal,
"Sensing bioavailable water content of granulated matrices: A combined experimental and computational study",
Biosensors, **13 (2023) 185.**

19. * N. Pan, R. Ghosh, D. Mukherjee, N. Bhattacharyya, L. Roy, **A. Banerjee**, S. Singh, R. T. Goswami, M. Mitra, A. Chattopadhyay and S. K. Pal,
"A nanosensor-based prototype development for heavy metal detection: A combined spectroscopic and theoretical study",
IEEE Sensors Letters, **7 (2023) 3**.

20. * M. S. Malik, S. Faazil, M. A. Alsharif, Q. M. S. Jamal, J. H. Al-Fahemi, **A. Banerjee**, A. Chattopadhyay, S. K. Pal, A. Kamal and S. A. Ahmed,
"Antibacterial properties and computational insights of potent novel linezolid-based Oxazolidinones",
Pharmaceuticals, **16 (2023) 516.**

21. * L. Roy, **A. Banerjee**, N. Bhattacharyya, S. Mondal, R. Ghosh, M. Das, R. T. Goswami, K. Bhattacharya, A. K. Mallick, A. Chattopadhyay and S. K. Pal,
"Radiolucency in conventional X-ray imaging leads potential diagnosis of hypoxia in human organ",
Journal of Clinical Images & Medical Case Reports, **4 (2023) 2261**.

22. * N. Pan, L. Roy, M. N. Hasan, **A. Banerjee**, R. Ghosh, M. A. Alsharif, B. A. Asghar, R. J. Obaid, A. Chattopadhyay, R. Das, S. A. Ahmed and S. K. Pal,
"Unraveling an ultrafast electron transport mechanism in a photocatalytic 'Micromachine' for their potential light harvesting applications",
Micromachines, **14 (2023) 980**.

*** Not included in the thesis.**

Patent

1. Device for the detection of arsenic level in drinking water and its method for preparation thereof, Sheik Saleem Pasha, Deepak Tayde, **Amrita Banerjee**, Soumendra Singh, Sumit Kumar Pramanik, Samir Kumar Pal, Amitava Das, US Patent, 202011045584, Appl. (2020).

International conference

1. **A. Banerjee**, A. Chattopadhyay, S. K. Pal, "Repurposing materials for circular economy", **Advanced Materials and Characterization (AMC2023), Mumbai, India (2023).**